
**Développement d'un procédé micro-plasma micro-onde pour l'élaboration
de nano-carbonés hybridés sp^3**

*Development of a microwave microplasma process for the synthesis of sp^3 hybridized
nanocarbons*

THÈSE DE DOCTORAT

présentée par

Abdoulaye SIBY

Laboratoire des Sciences des Procédés et des Matériaux (LSPM)

Pour l'obtention du grade de

DOCTEUR EN SCIENCE DE L'INGÉNIEUR

Soutenue le 11 juin 2025 devant le jury d'examen constitué de :

LOMBARDI Guillaume	Université Paris XIII — Président du jury
NAUDE Nicolas	Université Toulouse III — Rapporteur
COUEDEL Lenaïc	University of Saskatchewan — Rapporteur
GRANIER Agnès	Université de Nantes — Examinatrice
MICHAU Armelle	Université Paris XIII — Examinatrice
HASSOUNI Khaled	Université Paris XIII — Directeur de thèse
PRASANNA Swaminathan	Université Paris XIII — Co-encadrant

Abstract

This work focuses on the use of a microwave plasma torch based on a coaxial transmission line (CTRL) for the synthesis of nanodiamonds under mbar pressure conditions using H_2/CH_4 (\pm Ar) mixtures. Optical diagnostics of the plasma, including optical emission spectroscopy (OES) and picosecond two-photon laser-induced fluorescence (ps-TALIF), reveal that the torch produces high electron densities ($2 \times 10^{13} \text{ cm}^{-3}$), high atomic hydrogen densities (up to 10^{17} cm^{-3}) and gas temperatures ranging from 1000 to 1700 K. These parameters favor nanodiamond nucleation by stabilizing the diamond sp^3 phase. Deposition studies confirmed the formation of nanodiamonds with a crystal structure and size distribution of around 10 nm. Deposition quality, assessed by the sp^3/sp^2 ratio, shows an optimum value at 4% methane at 100 mbar and 90 W. The addition of argon (up to 25 sccm) further enhanced nanostructure performance by increasing gas temperatures and promoting favorable radical densities. The nucleation process was found to occur mainly in the gas phase, driven by key radicals such as CH_3 , CH , C and C_2 , which form via hydrogen dissociation and hydrocarbon reactions. High concentrations of acetylene, however, led to the formation of amorphous carbon via the HACA mechanism.

Key words : microwave plasma torch, coaxial transmission line, nanodiamond, gas-phase nucleation, plasma diagnostics.

Résumé

Ce travail porte sur l'utilisation d'une torche à plasma micro-ondes basée sur une ligne de transmission coaxiale (CTRL) pour la synthèse de nanodiamants dans des conditions de pression mbar en utilisant des mélanges H_2/CH_4 (\pm Ar). Les diagnostics optiques du plasma comprenant la spectroscopie d'émission optique (OES) et la fluorescence picoseconde induite par laser à deux photons (ps-TALIF), révèlent que la torche produit une grande densité d'électrons ($2 \times 10^{13} \text{ cm}^{-3}$), de grandes densités d'hydrogène atomiques (jusqu'à 10^{17} cm^{-3}) et températures du gaz allant de 1000 à 1700 K. Ces paramètres favorisent la nucléation de nanodiamants en stabilisant la phase sp^3 du diamant. Les études de dépôt ont confirmé la formation de nanodiamants avec une structure cristalline et une distribution de tailles d'environ 10 nm. La qualité du dépôt évalué par le rapport sp^3/sp^2 montre une valeur optimale à 4% de méthane à 100 mbar et 90 W. L'ajout d'argon (jusqu'à 25 sccm) a encore amélioré le rendement de la nanostructure en augmentant les températures du gaz et en favorisant des densités de radicaux favorables. On a constaté que le processus de nucléation se produisait principalement en phase gazeuse, sous l'impulsion de radicaux clés tels que CH_3 , CH , C et C_2 , qui se forment par dissociation de l'hydrogène et par des réactions d'hydrocarbures. Des concentrations élevées d'acétylène ont toutefois conduit à la formation de carbone amorphe par le biais du mécanisme HACA.

Mots clés : torche à plasma micro-ondes, ligne de transmission coaxiale, nanodiamant, nucléation en phase gazeuse, diagnostics plasma.

Acknowledgments

“Ad astra per aspera.”
To the stars through difficulties.

This thesis marks the end of several intense years of work, doubts, discoveries, and, above all, meaningful human and scientific encounters.

First and foremost, I would like to express my deepest gratitude to **Prasanna Swaminathan**, my co-supervisor, with whom I truly shared this journey on a daily basis. Thank you, Prasanna, for your patience, your constant availability, your sharp insight, and your unique way of making things simple without oversimplifying them. Thank you for the technical discussions, the long conversations, the encouragements, and the trust you placed in me from the very beginning. I could not have wished for a better guide throughout this adventure.

I also warmly thank my PhD supervisor, **Khaled Hassouni**, for his guidance, his advice, and for allowing me to take part in this ambitious project. Thank you for your scientific rigor and high standards, which have taught me a great deal.

To my family, my father **Siby Mamadou** and my mother **Traoré Krotimi**, I don't have enough words to express my gratitude. Thank you for your unwavering support, your prayers, your messages, and your confidence. You've always encouraged me to aim high without ever doubting me.

And to **Salimata Sanogo**, thank you for your presence, your strength, your love, and your endless support. You have been my anchor in the storms, my safe haven in times of doubt, and my guiding light throughout this journey.

Finally, I would like to thank all members of the **LSPM laboratory**, with whom I shared moments of science, coffee, laughter, and friendship. Thank you for your warm welcome, your kindness, and the small gestures that made everyday life more human.



List of Acronyms and Abbreviations

AIT	Axial Injection Torch
ADT	Axial Dielectric Tube
AFM	Atomic Force Microscopy
BDD	Boron-Doped Diamond
BEN	Bias-Enhanced Nucleation
CCD	Charge-Coupled Device
CHI	CH Instruments software
CMOS	Complementary Metal–Oxide–Semiconductor
CTRL	Coaxial Transmission Line Resonator
CVD	Chemical Vapor Deposition
DND	Detonation Nanodiamonds
DNP	Diamond Nanoparticles
ECR	Electron Cyclotron Resonance
EEDF	Electron Energy Distribution Function
EM	Electromagnetic
FTIR	Fourier Transform Infrared Spectroscopy
FWHM	Full Width at Half Maximum
GHz	Gigahertz
HACA	Hydrogen-Abstraction Carbon Addition
HAVA	Hydrogen-Abstraction Vinyl Radical Addition
HPHT	High Pressure High Temperature
IR	Infrared
I_D/I_G	Intensity ratio of D and G Raman bands
LIF	Laser-Induced Fluorescence
MAC	Methyl Addition Cyclization
MCP	Microchannel Plate
MHz	Megahertz
M-NDs	Milled Nanodiamonds
MW	Microwave
MWCNT	Multiwalled Carbon Nanotube
MWPECVD	Microwave Plasma Enhanced CVD
NCD	Nanocrystalline Diamond

NDs	Nanodiamonds
NEMS	NanoElectroMechanical Systems
NV center	Nitrogen-Vacancy center
OES	Optical Emission Spectroscopy
ORCA-Flash4.0	CMOS camera model
PAH	Polycyclic Aromatic Hydrocarbon
PAC	Phenyl Addition Cyclization
PECVD	Plasma Enhanced CVD
PCD	Polycrystalline Diamond
P_{inj}	Injected Microwave Power
P_{ref}	Reflected Microwave Power
P_{abs}	Absorbed Microwave Power
PLAL	Pulsed Laser Ablation in Liquid
PMWD	Microwave power density
ps-TALIF	Picosecond Two-photon Absorption LIF
RF	Radio Frequency
ROI	Region of Interest
RSR	Resonance-Stabilized Radical reactions
S/N	Signal-to-Noise Ratio
S₁₁	Reflection coefficient
SCD	Single-Crystal Diamond
SEM	Scanning Electron Microscopy
sp, sp², sp³	Carbon hybridizations
SWCNT	Single-Walled Carbon Nanotube
TALIF	Two-photon Absorption LIF
TE₁₀, TE₁₁	Waveguide TE modes
TEM	Transmission Electron Microscopy
UNCD	Ultrananocrystalline Diamond
XPS	X-ray Photoelectron Spectroscopy

Table of contents

Abstract	i
Résumé	ii
Acknowledgments	iii
List of Acronyms and Abbreviations	iv
Table of contents	vi
List of Figures	ix
1 Introduction	1
1.1 Carbon and its allotropes	1
1.1.1 sp^2 carbon: Graphite, graphene, fullerene, carbon nanotubes	2
1.1.2 sp^3 carbon phase or diamond	3
1.2 Nanodiamond: a high impact nanomaterial	5
1.2.1 Technological importance of nanodiamonds	6
1.2.1.1 Imaging and Biological Applications	6
1.2.1.2 Quantum Computing Applications	7
1.2.1.3 Sensor and Electronic Applications	8
1.2.1.4 Energy Storage Applications	8
1.2.1.5 Nanomechanical Sensors and Nanoelectromechanical Sys- tems (NEMS)	8
1.2.1.6 Mechanical and tribology	8
1.2.2 Synthesis of Nanodiamonds	9
1.2.2.1 Top-down approach	9
1.2.2.2 Bottom-up Approach	13
1.3 Motivation and objectives of the thesis	17
1.4 Organization of the thesis	18
2 Review of related literature	20
2.1 Plasma assisted processes	20
2.1.1 MW plasmas	21
2.1.2 Growth of diamond in CVD reactors	26

2.1.3	Nucleation of diamond on non-diamond surfaces	28
2.1.4	Homogeneous Nucleation of carbon nanostructures	30
2.1.5	Gas-phase nucleation of nanodiamonds	34
2.2	Conclusion	36
3	Experimental setups and instruments	37
3.1	Introduction	37
3.2	Description of the MW-torch	38
3.3	Deposition Experiments	38
3.3.1	Heating/biasing system	39
3.3.2	Substrate cooling system or cold finger	39
3.4	Plasma diagnostics	40
3.4.1	Optical emission spectroscopy (OES)	40
3.4.2	Two-photon Absorption Laser Induced Fluorescence (TALIF)	42
3.4.2.1	Principle	42
3.4.2.2	Optical setup for TALIF	44
3.5	Material characterization technique	46
3.5.1	Raman spectroscopy	47
3.5.1.1	Principle	47
3.5.1.2	Instrumentation	47
3.5.2	X-ray Photoelectron Spectroscopy	49
3.5.2.1	Principle	49
3.5.2.2	Instrumentation	50
3.5.3	Atomic force microscopy	51
3.5.3.1	Principle	51
3.5.3.2	Instrumentation	51
3.5.4	Scanning Electron Microscopy	52
3.5.4.1	Principle	52
3.5.4.2	Instrumentation	52
3.5.5	Transmission Electron Microscopy	54
3.5.5.1	Principle	54
3.5.5.2	Different operating modes	54
3.5.5.3	Instrumentation	55
4	Characterization of MW torch	57
4.1	Introduction	57
4.2	Working principle of the MW torch	58
4.3	MW-plasma coupling and electrical characterization of plasma	61
4.4	Gas temperature (T_g) measurement from OES	65
4.4.1	Gas temperature from rotational distribution of molecule	65
4.4.2	Methodology used	67
4.4.3	Results	68

4.5	Measurement of electron density n_e	69
4.5.1	Principle	69
4.5.2	Plasma parameters	72
4.6	Measurement of atomic Hydrogen density	76
4.6.1	Measurement of atomic Hydrogen density by actinometry	76
4.6.2	Measurement of H-atom density using ps-TALIF	77
4.6.3	Data post-processing	78
4.6.4	Results	79
4.7	Gas temperature measurement from ps-TALIF	80
4.7.1	Analysis of propagation of errors	81
4.7.2	Validation of the novel proposed approach	83
4.7.3	Spatial distribution of T_g and n_H	84
4.8	Conclusion	86
5	Carbon nps in H-rich CH₄ plasmas	87
5.1	Introduction	87
5.2	Characterization of carbon nanostructures	88
5.2.1	Morphological and structural analysis of carbon nanostructures	88
5.2.2	Evaluation of the abundance of sp ³ phase	90
5.3	Carbon NPs produced in H ₂ /CH ₄ plasmas	92
5.3.1	Characterization of H ₂ /CH ₄ plasmas	93
5.3.2	Effect of MW power on carbon NPs	95
5.3.3	Effect of pressure and methane on carbon NPs	96
5.3.4	Influence of Argon on nanodiamond yield	99
5.4	Investigation of NDs nucleation mechanisms	102
5.4.1	Consistency Across Substrates	104
5.4.2	Effect of substrate temperature	105
5.4.3	Application of substrate bias	106
5.4.4	Time-Dependent Deposition Studies	107
5.4.5	Carbon nanostructures collection in different deposition zones	108
5.4.6	Transfer of nanodiamonds to solution	110
5.5	Discussion on nucleation of nanodiamonds	110
5.6	Conclusions	115
6	Conclusion and perspectives	117
6.1	General conclusions	117
6.2	Perspectives on optimization of plasma-nucleation process	119
	Bibliography	121

List of Figures

1.1	Schematic representation of sp^2 and sp^3 hybridizations in carbon	2
1.2	Graphite Structure	3
1.3	Carbon sp^2 allotropes: Graphite (3D), Graphene (2D), Carbon nanotubes (1D) and Fullerenes (0D)	3
1.4	(a) Diamond mesh and (b) Crystallographic representation of the structure	4
1.5	Carbon phase diagram	4
1.6	Illustration of Diamond Structures: Single-Crystal Diamond, Polycrystalline Diamond, and Nanocrystalline Diamond	5
1.7	Structure of the Nanodiamond	6
1.8	Crystalline structure of an NV center	7
1.9	Carbon phase diagram including temperature and pressure zones for the main diamond synthesis methods	10
1.10	Synthesis techniques for nanodiamonds	10
1.11	(a) Cross-section diagram of Sumitomo's high-pressure, high-temperature growth framework, (b) HPHT diamond single crystals obtained under conditions favoring the formation of oriented faces (100), and (c) conditions favoring the formation of oriented faces (111)	11
1.12	(a) Illustration of nanodiamond synthesis by detonation. (b) Carbon phase diagram showing the Jouguet point (point A) and red pressure-temperature trajectory during cooling. (c) Summary of the stages of ND growth during detonation	13
1.13	Procedure for purifying and deagglomerating detonation nanodiamonds	14
1.14	Schematic of the setup of ND synthesis by PLAL	15
1.15	Raman spectra of carbon nanostructures produced using MW plasma torch at 100 mbar and $CH_4 = 3\%$, $H_2 = 97\%$ (a) 80 W and (b) 70 W.	18
2.1	Schematic diagram of MPT showing two types of applicators: surfaguide and surfatron	23
2.2	AIT schematic diagram and zones in a plasma jet produced by the AIT	24
2.3	Schematic diagram of tubular, ASTEX metal wall, bell jar, and ellipsoidal reactors	25
2.4	Simplified diagram of diamond growth using the MWPECVD process	26
2.5	Gas phase nucleation process	31
2.6	Chemical structure of the smallest aromatic ions predicted by Calcote mechanism .	32
2.7	PAH formation through HACA mechanism	33
2.8	Mechanism of detonation nanodiamond proposed by Dolmatov et al.	35

3.1	MW microplasma torch	39
3.2	Experimental set-up for carbon particle deposition using the MW microplasma torch	40
3.3	Experimental set-up of the deposition with substrate cooling system	41
3.4	Schematic of the experimental setup for performing OES	42
3.5	Spectral response of the 1-m spectrometer	43
3.6	Scheme of H-atoms TALIF	43
3.7	Diagram showing the path of a photon through the streak camera	45
3.8	Schematic of the experimental setup showing the layout of MW plasma reactor, ps-laser and streak camera.	45
3.9	Representation of the different light scattering phenomena including Raman scattering	47
3.10	HR-800 spectrometer at LSPM was used for characterizing the carbon nanostructures	48
3.11	Typical Raman peaks considered	49
3.12	Principle of photoelectron generation	50
3.13	High-resolution XPS analysis system at ITODYS laboratory	50
3.14	The main components of an atomic force microscope	51
3.15	AFM instrument	52
3.16	Different types of emissions produced by SEM	53
3.17	SEM instrument	53
3.18	Schematic flow diagram of a transmission electron microscope	54
3.19	TEM Instrument	56
4.1	Design of MW-torch and its equivalent circuit	60
4.2	Evolution of microplasma as a function of absorbed power at 50 mbar. Inset (top right): Spots of the plasmas formed.	62
4.3	Representation of critical power as a function of pressure	62
4.4	Representation of reflected power as a function of absorbed power for different pressures	63
4.5	(a)Resistance and Inductance as a function of power and coefficient reflection at 100 mbar and (b) Evolution of n_e as a function of absorbed power at different pressures	64
4.6	Spectra of the (a) first R-branch lines of the transition $G^1 \sum_g^+, \nu' = 0 \rightarrow B^1 \sum_u^+, \nu'' = 0$ and (b) the transition $d^3 \Pi_u^+ \rightarrow a^3 \sum_g^+ (0,0)$ at 50 mbar operating pressure . . .	67
4.7	Boltzmann diagram for the determination of rotational temperature from R branch of $G^1 \sum_g^+, \nu' = 0 \rightarrow B^1 \sum_u^+, \nu'' = 0$ (THR100, 80W 100 sccm H_2 , 100 mbar) . . .	69
4.8	Representation of T_{rot} (G) (a) and T_{rot} (X) of Fulcher- α (b) as a function of absorbed power and pressure	70
4.9	H_β line profile	71
4.10	Method for determination of electron density	72
4.11	Representation of electron density as a function of absorbed power	73
4.12	Representation of plasma length as a function of absorbed power at different operat- ing pressures and at 90W	75
4.13	Representation of PMWD (a) and plasma volume (b) as a function of absorbed power at different pressures	75

4.14	Illustration of the fluorescence captured by the streak camera.	79
4.15	(a) Variations of S_{Fi} as a function of laser energy for H and Kr and (b) H-atom densities measured using actinometry and ps-TALIF as a function of pressure and power.	80
4.16	Relative errors for the different terms of the gas temperature equation at 100 mbar and 100W.	82
4.17	Variation of τ_H extracted from ps-TALIF signals and corresponding γ_H as a function of pressure and power for the experimental conditions considered	83
4.18	Parity plot comparing gas temperature measurement from ps-TALIF using $\sigma_{H/H_2} = 98 \text{ \AA}^2$ with rotational temperatures (a) $T_{rot}(G)$ and (b) $T_{rot}(d)$	84
4.19	Constructed 2D contour plots of H-atom density and T_g for different pressures. The x-axis is in pixels, and the y-axis refers to z with 0 referring to the first possible laser measurement about 0.5 mm from the base of the torch.	85
5.1	Experimental conditions: Gas composition 96:4 H ₂ /CH ₄ , Pressure = 100 mbar, MW power = 90 W.	88
5.2	Particle size distribution using (a) SEM and (b) AFM	89
5.3	(a)TEM image of carbon nanoparticles at a resolution of 1.8 Å, its corresponding (b) selected area electron diffraction with blue circle refers to the (111) plane and red circle to the (311) plane of diamond phase and (c) EELS spectra of carbon nanoparticles. Experimental conditions: CH ₄ = 4 sccm, H ₂ = 96 sccm, pressure of reactor = 100 mbar, MW power = 90 W.	90
5.4	An example of (a) Raman spectra and (b) XPS C1s line observed for carbon nanostructures produced in the torch. Also shown are the deconvolution of the raw spectra to identify individual Raman bands and deconvolution of XPS C1s line to sp ³ /sp ² configuration.	91
5.5	Variation of the sp ³ /sp ² ratio as a function of methane concentration measured by XPS (black) and Raman (red). Experimental conditions: Total flow-rate = 100 sccm with mixture H ₂ and CH ₄ , Pressure = 100 mbar, substrate = silicon, distance plasma-substrate = 1 cm and deposition time = 1h.	93
5.6	(a) Example of CN profile obtained with the conditions : CH ₄ = 6% , H ₂ = 94% , Pressure = 100 mbar and Power= 90W and (b) Variation of gas temperature with methane concentration in the CH ₄ /H ₂ mixture. Experimental conditions : CH ₄ +H ₂ = 100 sccm, Pressure= 100 mbar, Power = 90 W.	93
5.7	(a) Variations of SFi as a function of laser energy for H. Experimental conditions: CH ₄ = 7% and H ₂ = 93% , (b) n _H as a function of CH ₄ concentration at 100 mbar and 90W from ps-TALIF.	94
5.8	(a) The Raman spectra of the samples and (b) its corresponding sp ³ /sp ² (left) and I _D /I _G (right) ratio as a function of input power. Experimental conditions: CH ₄ = 4 sccm, H ₂ = 96 sccm, Pressure = 100 mbar, substrate = silicon, distance plasma-substrate = 1 cm and deposition time = 1h.	96

5.9	Distribution of (a) I_{dia}/I_G ratio , (b) I_D/I_G ratio, (c) I_{trans}/I_G and (d) sp^3 fraction as a function of pressure and methane concentration.	97
5.10	Evolution of C_2 and CH as a function of methane concentration at 100 mbar and 90W by OES as a function of methane concentration. Experimental conditions : Pressure = 100 mbar, Power = 90W and the total flowrate $CH_4+H_2 = 100$ sccm.	98
5.11	Representation of reflected power as a function of absorbed power at 100 mbar with different Ar/ H_2 mixture. The total flowrate $Ar+H_2 = 100$ sccm.	99
5.12	(a) Variation of T_g as a function of Ar flow rate and (b) n_H as a function of CH_4 concentration and argon flowrate (sccm) at 100 mbar and 90 W.	100
5.13	Distribution of (a) I_{dia}/I_G ratio , (b) I_D/I_G ratio, (c) I_{trans}/I_G as a function of Ar and methane concentration and (d) Ternary contour of mixture $H_2 +CH_4+Ar$. Experimental conditions : Pressure = 100 mbar, Power = 90 W and the total flowrate $CH_4/H_2 = 100$ sccm.	101
5.14	2D Contour plot showing the evolution of (a) CH and (b) C_2 species as a function of methane concentration and argon flowrate. Experimental conditions : Pressure = 100 mbar, Power = 90W and flowrate of $CH_4+H_2 = 100$ sccm.	102
5.15	Schematic of gas-phase processes: molecular growth and nucleation and subsequent collection of NPs on the substrate	103
5.16	Raman spectra for (a) different plasma-substrate distances and (b) different type of substrate. Experimental conditions: $CH_4 = 4$ sccm, $H_2 = 96$ sccm, Pressure = 100 mbar, power = 90W and deposition time : 1h	104
5.17	TEM image of carbon nanoparticles (left) and its corresponding selected area electron diffraction (right) for 5 min of deposition in the cold finger(experimental conditions: $CH_4 = 4$ sccm, $H_2 = 96$ sccm, pressure of reactor = 100 mbar, injected power = 90 W)105	
5.18	Raman spectra for different substrate temperature . Experimental conditions: $CH_4 = 4$ sccm, $H_2 = 96$ sccm, Pressure = 100 mbar, power = 90W and deposition time : 1h106	
5.19	SEM image of carbon deposit obtained on a substrate with bias of 200 V.	107
5.20	(a) Raman spectra and (b) its corresponding sp^3/sp^2 (left) and I_D/I_G (right) ratio for different deposition time. Experimental conditions: $CH_4 = 4$ sccm, $H_2 = 96$ sccm, Pressure = 100 mbar, power = 90W, distance plasma-substrate = 1cm	108
5.21	Particle size distribution for different deposition time. Insets of the respective images are shown. (b) Experimental conditions: $CH_4 = 4$ sccm, $H_2 = 96$ sccm, Pressure = 100 mbar, power = 90W, distance plasma-substrate = 1cm	109
5.22	Raman spectra at different zones of deposition	109
5.23	(a) Solution of iso-proponal containing NDs, and their (b) HR-TEM image and corresponding (c) SAED pattern. Experimental conditions: $CH_4 = 4$ sccm, $H_2 = 96$ sccm, Pressure = 100 mbar, power = 90W and deposition time : 1h	110
5.24	Mechanism reaction for production of primary radicals in H_2/CH_4 plasmas at intermediate pressures	111
5.25	Density of main species produced in CH_4/H_2 mixture with 4% of CH_4 for a total flowrate of 100 sccm at 100 mbar pressure and 90 W power.	113

5.26	2D contour plot showing the evolution of (a) C , (b) C ₂ H ₃ and (c) C ₂ H as a function of methane concentration and pressure using the 0D model. Experimental conditions : Power = 90W and flowrate of CH ₄ +H ₂ = 100 sccm.	114
5.27	2D contour plot showing the evolution of (a) CH ₃ and (b) C ₂ species as a function of methane concentration and pressure using the 0D model. Experimental conditions : Power = 90W and flowrate of CH ₄ +H ₂ = 100 sccm.	114
6.1	Raman spectrum with presence of ethanol. Conditions: Pressure = 100 mbar , Power = 90W, H ₂ = 96sccm and 500 mg/L of ethanol	120

Chapter 1

Introduction

Contents

1.1	Carbon and its allotropes	1
1.1.1	sp^2 carbon: Graphite, graphene, fullerene, carbon nanotubes	2
1.1.2	sp^3 carbon phase or diamond	3
1.2	Nanodiamond: a high impact nanomaterial	5
1.2.1	Technological importance of nanodiamonds	6
1.2.2	Synthesis of Nanodiamonds	9
1.3	Motivation and objectives of the thesis	17
1.4	Organization of the thesis	18

1.1 Carbon and its allotropes

The carbon atom is the first element in column IV of Mendeleev's periodic table, and its atomic number is $Z=6$ ¹. The most stable isotopic form of carbon is ^{12}C , which contains 6 protons and 6 neutrons. The electronic configuration of this atom is $1s^2 2s^2 2p^2$. Its two valence electrons should a priori give it a divalent character in its chemical bonds. Actually, the electrons of the peripheral layers, i.e. 2s and 2p, are distributed over atomic orbitals called sp hybrids. They then become unpaired and can create four chemical bonds, making it a tetravalent atom. There are also three hybridization states of these valence orbitals: sp, sp^2 , sp^3 , leading to the formation of σ and π -type covalent and van der Waals bonds, binding and anti-binding, respectively. This generates allotropic structures of different dimensionalities with a wide variety of physical and chemical properties² (diamond, graphite, graphene, etc.). In addition to these allotropic forms, carbon can also be found in amorphous form, leading to another very large family of carbon-materials with different physical and chemical properties¹.

Carbon exists in many forms, including sp^2 phases such as nanotubes, graphite, graphene, fullerenes, sp^3 phase of diamond and the amorphous state. The two main allotropic forms are graphite (sp^2 hybridization) and diamond (sp^3 hybridization), shown in Figure 1.1.

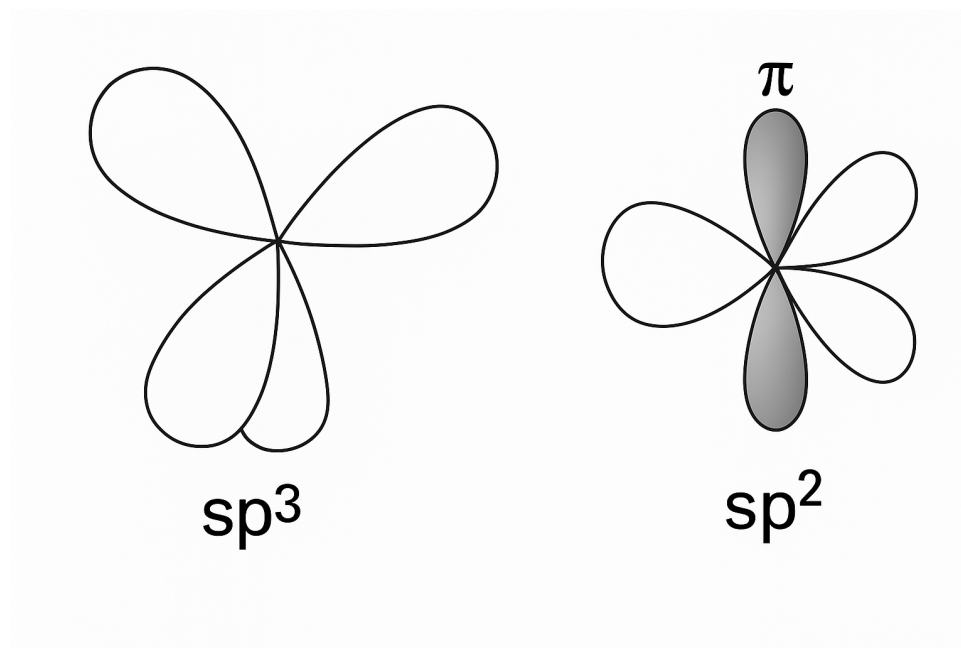


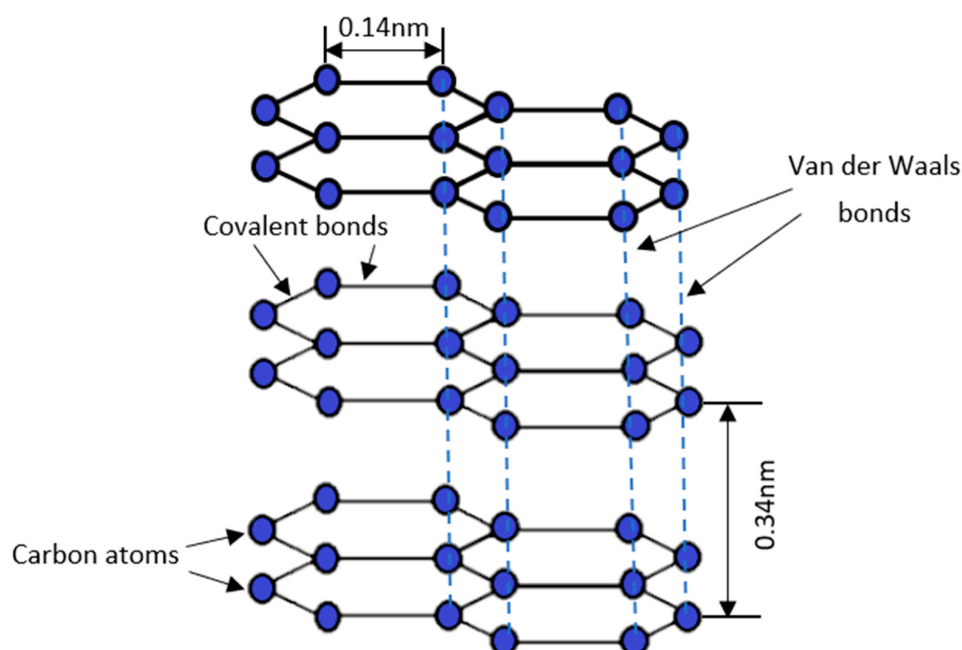
Figure 1.1: Schematic representation of sp^2 and sp^3 hybridizations in carbon³

1.1.1 sp^2 carbon: Graphite, graphene, fullerene, carbon nanotubes

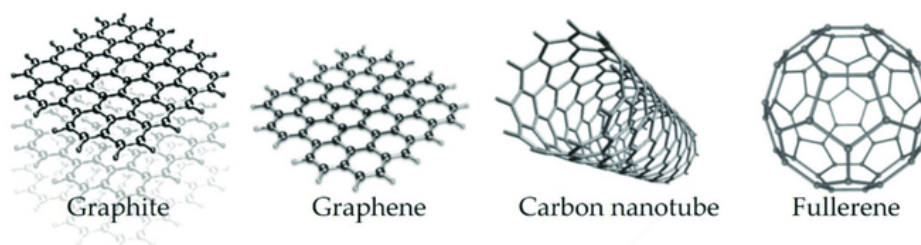
Based on the various forms of carbon, we first examine the structure of graphite, the most common and thermodynamically stable form of carbon at standard temperature and pressure (298 K and 1 atm). It is found in metamorphic sediments, often close to organic coal. Graphite is made up of sheets in which each carbon atom is located at the vertex of a regular hexagon. These sheets, called "graphenes", are superimposed on each other, leaving a spacing of around 0.34 nm^4 . Within a sheet, each carbon atom is linked to three other ones by covalent σ bonds, the angle between these bonds being 120° . The electrons not engaged in the σ bonds (one per carbon atom) form delocalized π bonds, which are perpendicular to plane form by the σ bonds. These π bonds contribute to electrical conductivity within the plane of the graphite sheets. The sheets themselves are held together by van der Waals forces, which are much weaker than the covalent σ and π bonds within the sheets (cf. Figure 1.2).

Because of the layered structure of graphite, its physical properties are anisotropic. In particular, electrical conductivity shows two different values in directions parallel and perpendicular to the laminate planes. Graphite also shows interesting frictional properties. In fact, graphene sheets can align in parallel with the direction of relative motion and thus slide relatively easily over each other³.

Figure 1.3 shows the different sp^2 allotropes of carbon in addition to graphite. Graphene is a two-dimensional crystal of sp^2 carbon atoms regularly distributed on a hexagonal honeycomb lattice. A single layer of graphene is just one atom thick, at around 0.335 nanometers. Concerning fullerenes, they are hollow molecular structures in the nanometer range, composed solely of sp^2 -hybridized carbon atoms, forming a closed sphere or ellipse. The best known fullerene is C_{60} , which resembles a football (buckminsterfullerene). Fullerenes are obtained from graphite vaporized in an atmosphere of neutral gas, helium, or argon^{6,7}. Carbon nanotubes are sheets

Figure 1.2: Graphite Structure⁵

of graphene wound on themselves, forming hollow cylinders, with at least one dimension at the nanoscale. A distinction is made between: (i) single-walled carbon nanotubes (SWCNT), which consist of a sheet of graphene wound into a cylindrical tube, and (ii) multiwalled carbon nanotubes (MWCNT), which consist of several concentric tubes. Their average diameter ranges from nanometers (SWCNT) to tens of nanometers (MWCNT), up to 100 nm.

Figure 1.3: Carbon sp^2 allotropes: Graphite (3D), Graphene (2D), Carbon nanotubes (1D) and Fullerene (0D)⁸

1.1.2 sp^3 carbon phase or diamond

Diamond is a pure allotropic crystalline form of carbon, which is metastable under standard conditions (298 K and 1 atm) and stable under high pressure and temperature conditions ($P > 10$ GPa and $T > 2000\text{K}$)⁹. Diamonds are known as the hardest material and consist of an assembly of carbon atoms in sp^3 hybridization, where each atom is bonded to four other carbon atoms by strong σ covalent bonds; which results in a tetrahedral structure. This confers exceptional physical properties on the diamond, which is described in greater detail later in the manuscript. Diamond shows a face-centered cubic crystallographic structure. In this structure, the unit cell

contains eight atoms, four of which are located at the centers of four small cubes, each one occupying the eighth of the unit cell's volume. Diamond is said to have a blende-like structure¹⁰. These face-centered cubic cells are interpenetrated and offset by a quarter of the unit cube diagonal length (Figure 1.4), with a distance between two neighboring atoms of 0.154 nm, and a lattice parameter $a=0.356$ nm.

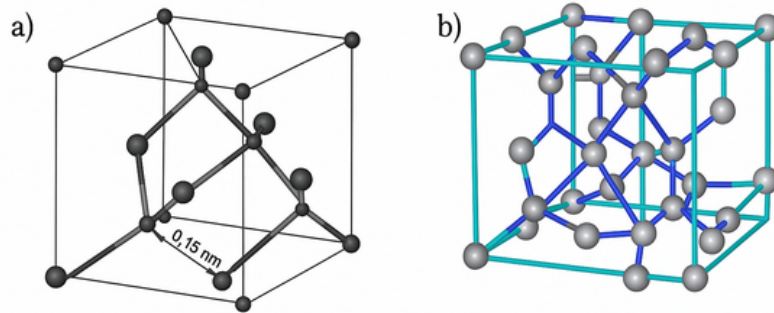


Figure 1.4: (a) Diamond mesh and (b) Crystallographic representation of the structure¹¹

The carbon phase diagram (cf. Figure 1.5) shows that diamond only forms at extremely high pressures. Consequently, diamond can only exist as a metastable phase of carbon under normal temperature and pressure conditions. The formation of a natural diamond is the result of the extreme conditions that prevailed during the formation of the earth's crust.

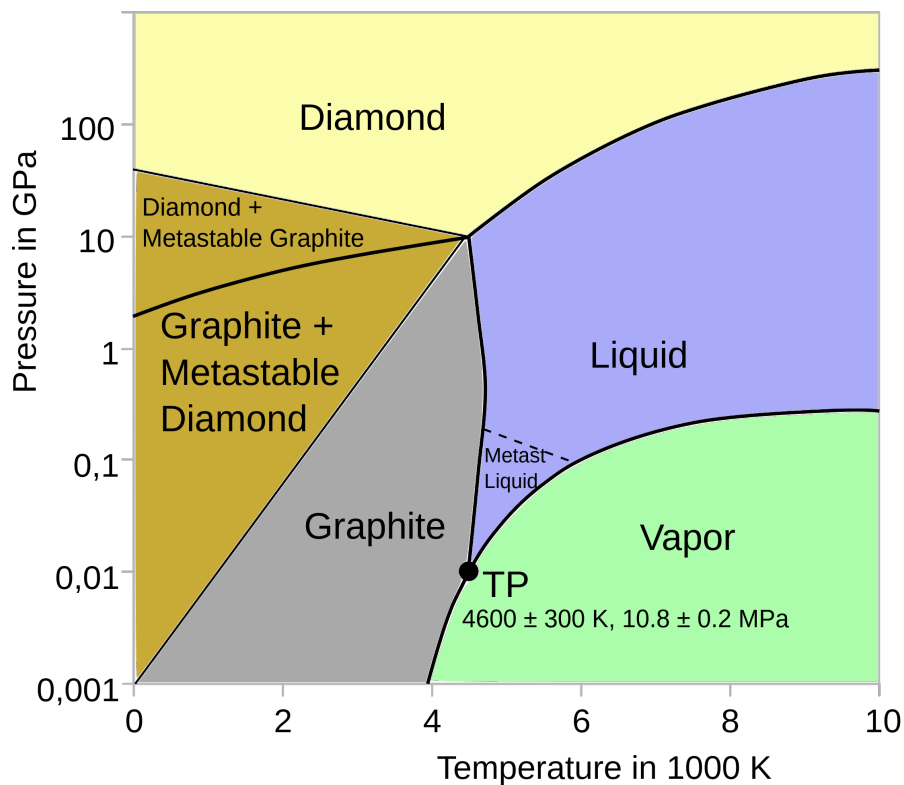


Figure 1.5: Carbon phase diagram¹²

These high pressure conditions can be reproduced in the laboratory where diamond can be synthesized from a graphitic precursor in the presence of a catalyst¹³. This so-called High Pressure High Temperature (HPHT) process has been extensively used to produce a synthetic diamond. It provides stable and homogeneous quality materials with good reproducibility, making them highly suitable for industrial applications.

Diamond exists in various forms, including monocrystalline, polycrystalline, and nanocrystalline diamond films (cf. Figure 1.6) as well as nanodiamond particles. Single-crystal diamond (SCD) or monocrystalline diamond consists of a single crystal with a perfectly ordered crystal lattice. It is a natural form of diamond and can also be synthesized by HPHT or Chemical Vapor Deposition (CVD). This type of diamond has been used mainly in jewellery, but in applications in power electronics as heat spreader and after doping as sensors, and quantum computing. Polycrystalline diamond (PCD) consists of numerous disoriented crystalline diamond grains (micrometric size), usually synthesized by HPHT or CVD on non-diamond substrates. Like PCD, nanocrystalline diamond (NCD) is composed of nanometric diamond grains (grain size between 5 and 100 nm), often coated with amorphous or non-diamond carbon, giving a mixed structure. Ultrananocrystalline diamond (UNCD) is composed of even smaller diamond grains with grain size typically less than 10 nm, resulting in an extremely dense and uniform structure.

The diamond phase can also exist as isolated nanoparticles of size < 100 nm, usually referred to as nanodiamonds (NDs), or diamond nanoparticles (DNPs). A brief review of the literature shows that the term “nanodiamond” is often used to refer to nanocrystalline diamond films deposited on a silicon substrate using CVD processes and made up of nano-sized diamond grains. In this thesis, the term nanodiamonds refers to isolated diamond nanoparticles of sizes smaller than 100 nm that are not necessarily obtained by a CVD process. We will look at the properties and applications of nanodiamonds in detail in the next section.

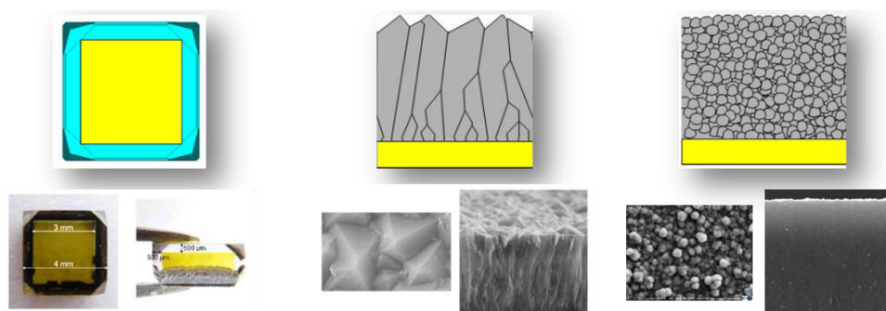


Figure 1.6: Illustration of Diamond Structures from Left to Right Respectively: Single-Crystal Diamond (a), Polycrystalline Diamond (b), and Nanocrystalline Diamond (c)¹⁴

1.2 Nanodiamond: a high impact nanomaterial

They are a carbon allotrope composed of sp^3 hybridized carbon atoms that assemble into nanoscale crystals¹⁵. Three essential elements make up the structure of diamond nanoparticles: the overall shape, the core, and the surface (Figure 1.7). The overall shape of diamond nanoparticles is generally either spherical or elliptical, through numerous diffraction experiments. The

core of nanodiamonds is similar to the structure of a conventional diamond (sp^3 -hybridization), but their surface is more graphite-like (sp^2 hybridization), with dangling bonds at the edges containing functional groups. Most of the diamond phase is present in the inner core. The intermediate sheet, which is usually examined as an inhomogeneous translational carbon shell, is detached from the innermost shell face by onion-shaped carbon rings. The next subsections will discuss the technological importance and synthesis of nanodiamonds.

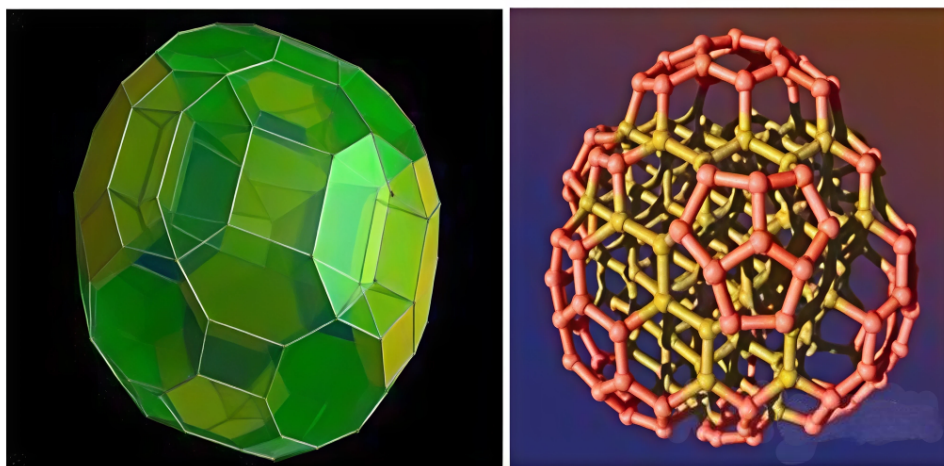


Figure 1.7: Structure of the Nanodiamond¹⁶

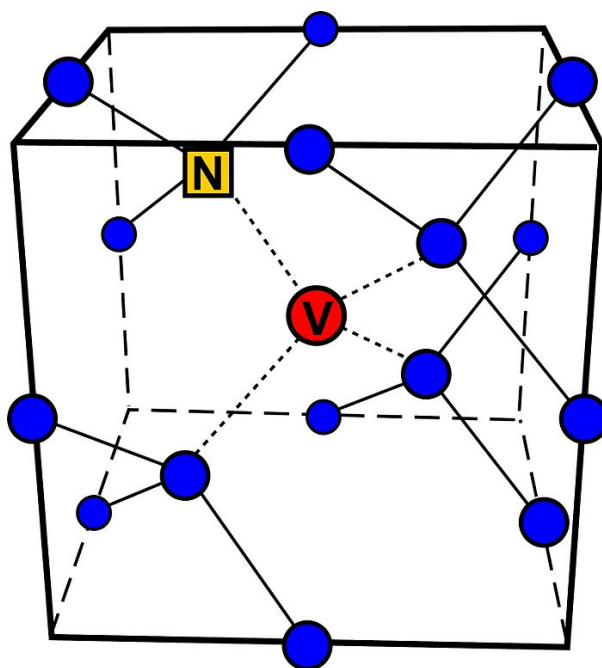
1.2.1 Technological importance of nanodiamonds

NDs possess remarkable characteristics such as exceptional hardness, high chemical stability, chemical inertness, high thermal conductivity, excellent biocompatibility, and ease of surface functionalization. These properties make them particularly suitable for numerous applications in fields such as medicine, tribology, catalysis, electronics, and energy^{17–20}.

1.2.1.1 Imaging and Biological Applications

Diamond is transparent across a wide range of the electromagnetic spectrum and has a high refractive index, around 2.4 in the visible range. However, on the nanoscale, NDs can exhibit different optical properties depending on their size, becoming progressively transparent in the ultraviolet when their size is less than 100 nm²¹. The most interesting optical properties arise from the presence of color centers resulting from impurities in the diamond matrix²². Among these, the nitrogen-vacancy (NV) center, formed by the presence of a nitrogen atom near a vacancy in the diamond lattice (as illustrated in Figure 1.8), is the most studied.

When excited by a green laser (typically between 488 and 575 nm), NV centers emit red light with near-unity efficiency and very stable photoemission²⁴. These centers are systematically present in high-pressure high-temperature (HPHT) NDs, and their number can be increased by irradiating NDs with He⁺ ion beams or high-energy electrons, which create vacancies. Thermal treatments then allow these vacancies to migrate towards nitrogen atoms that are often naturally present as impurities in the diamond lattice^{25,26}.

Figure 1.8: Crystalline structure of an NV center²³

Fluorescent NDs, particularly those with NV centers, are used as markers to track cells in vitro due to their photostability and biocompatibility^{26–29}. However, for in vivo applications, the use of NV centers is limited to surface tissues, such as skin or mucous membranes, due to high tissue absorption in the visible range where the excitation and emission wavelengths occur. In addition, the luminescence of NDs is highly dependent on their surface chemistry and may be inhibited, for example, in the case of a hydrogenated surface³⁰. Although NV centers have been observed in detonation NDs, their luminescence is too weak for effective cellular imaging³¹. It is important to note that structural surface defects in detonation NDs can induce luminescence properties that are not associated with NV centers, yet still allow the tracking of NDs within cells³¹. The 1332 cm^{-1} Raman signal of diamond can also be used to track NDs in vitro²⁷. Coupling the optical and magnetic properties of NV centers significantly enhances the imaging capabilities of NDs, allows for determining their orientation, and enables the measurement of magnetic fields directly within cells³². Furthermore, NDs show promise in enhancing the effectiveness of drug delivery systems in the treatment of skin cancer due to their high biocompatibility and high adsorption capacity, allowing them to carry more active compounds and penetrate deeper into the skin layers than conventional formulations³³. Their role in wound healing and tissue repair is also promising, with potential applications in developing gene transfer systems for wound healing³³.

1.2.1.2 Quantum Computing Applications

Nanodiamonds with NV centers are an alternative to trapped ions for room-temperature quantum computing³⁴. Their stability and high-temperature operation make them interesting for quantum simulations. The spin properties of NV centers allow qubit manipulation with magnetic fields, potentially replacing or complementing ion-trap technology.

1.2.1.3 Sensor and Electronic Applications

Unlike bulk diamond, the electronic and electrochemical properties of NDs are less studied due to the insulating nature of undoped diamond. In bulk diamonds, doping with boron atoms can create a p-type semiconductor or even a metallic material at boron concentrations greater than $5 \times 10^{20} / \text{cm}^3$, which is particularly interesting for high-power electronic and electrochemical applications^{35,36}. Boron-doped nanodiamonds (BDD), fabricated using plasma-enhanced chemical vapor deposition (PECVD) methods, have shown promise for detecting dopamine, a key neurotransmitter involved in several neurological functions. Dopamine detection is crucial in studies on neuropsychiatric disorders and diseases such as Parkinson's disease. These sensors can be optimized for better sensitivity through post-synthetic treatments, such as anodization or deposition of polymer films on the BDD surface³⁷.

NV centers enable monitoring of magnetic fields^{38,39} or electric fields⁴⁰ at the nanoscale by optically measuring the spin properties of NV centers, which are sensitive to ambient magnetic fields. ND-based sensors can operate at room temperature and, being entirely composed of carbon, can be safely injected into living cells³⁸.

1.2.1.4 Energy Storage Applications

NDs, due to their high surface area, stability, and wide electrochemical potential windows, are attractive candidates for energy storage systems. Boron-doped nanodiamond electrodes, fabricated using PECVD, exhibit exceptional stability across a wide range of operating potentials in aqueous solutions⁴¹. Moreover, the surface functionalization of NDs can enhance their ion storage capacity by introducing additional pseudocapacitive processes⁴². When used as a dispersed phase in nanocomposites, NDs can also modify certain electronic characteristics of polymer matrices, probably due to functional groups on their surface, which facilitates ion exchange and reduces the system's impedance⁴³. These properties can be used in the development of electrochemical sensors and energy storage systems.

1.2.1.5 Nanomechanical Sensors and Nanoelectromechanical Systems (NEMS)

Nanodiamonds demonstrate an exceptional capability to withstand high mechanical stresses, with a maximum local elastic stress of over 9% and a corresponding maximum tensile stress exceeding 100 GPa, making them ideal for high performance nanomechanical sensors and NEMS applications⁴⁴.

1.2.1.6 Mechanical and tribology

Nanodiamonds, much like bulk diamond, have impressive mechanical properties, such as a hardness of 10 on the Mohs scale and a Young's modulus over 1000 GPa. These features make them highly promising for applications in nanoscale mechanical systems. For example, adding diamond nanoparticles to engine oils can greatly improve their lubricating abilities, cutting the friction coefficient by 80-90%⁴⁵. Additionally, when nanodiamonds are mixed into polymer matrices, they create new nanocomposites with far better mechanical strength, such as 200

times more hardness and 10 times the Young's modulus compared to regular polymers⁴⁶. These nanocomposites also perform better in terms of friction, making them potential replacements for micrometer-sized diamonds in cutting or polishing materials⁴⁷. What's more, when combined with biodegradable polymers, they could even be used to make bone prostheses⁴⁸.

1.2.2 Synthesis of Nanodiamonds

A close look at the carbon phase diagram drawn up by F.P. Bundy⁴⁹ and presented in Figure 1.9, shows the stable carbon phases (i.e. a phase with minimum free energy) as a function of temperature and pressure.

Zones 1 and 2 on this diagram represent the most stable thermodynamic conditions at high pressure and high temperature (HPHT), where graphite can be transformed into a diamond. The first strategy of producing diamond is to achieve these extreme conditions as in the case of HPHT process under equilibrium conditions while detonation or laser ablation, etc. under non-equilibrium conditions. However, the high temperatures and pressures required by the processes make them difficult and expensive. The second strategy looks for growing diamond at softer non-equilibrium conditions (a few tens to few hundreds of mbar) through chemical vapour deposition (CVD), where one can achieve conditions where diamond is metastable. This corresponds to Zone 3 in the Figure 1.9. This process synthesizes diamond from the interactions of active species produced by chemical reactions taking place in the vapor phase with the growing diamond substrate. Metastable conditions are achieved using an H-atom rich environment and a gas temperature high enough to promote growth. Using this technique, diamond can be synthesized in a variety of ways, with characteristics, e. g., purity, crystalline quality, etc., that depend on the method used to generate the reactive gas phase to ensure metastable conditions and growth conditions.

In addition, we can distinguish two broad categories of nanodiamond elaboration processes: **Top-Down** and **Bottom-Up approaches**. While the Top-Down approach involves starting with a large natural or synthetic diamond crystal and then reducing it to the desired nanoscale dimensions by milling, the bottom-up approach consists of growing nanodiamonds from simple chemicals such as CH_4 . These techniques have been reviewed by Shenderova et al.⁵¹ and are summarized in Figure 1.10.

1.2.2.1 Top-down approach

As the approach produces NDs from milling large diamond crystals, these are also called milled nanodiamonds (M-NDs). Although the top-down approach is a very commonly used technique to produce nanodiamonds, it suffers from several drawbacks. In fact, grinding and cutting introduce several impurities from abrasive materials, which require expensive chemical purification processes. Moreover, M-NDs are limited by the size and purity of the initial materials and suffer a severe strain that can restrict their final applications. The synthetic diamonds that are milled are produced from HPHT or CVD processes, which are described below.

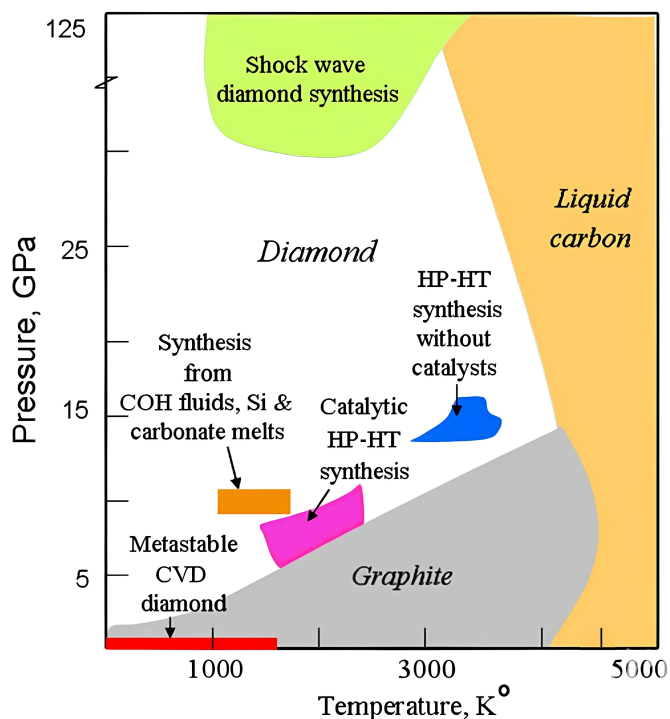


Figure 1.9: Carbon phase diagram including temperature and pressure zones for the main diamond synthesis methods⁵⁰

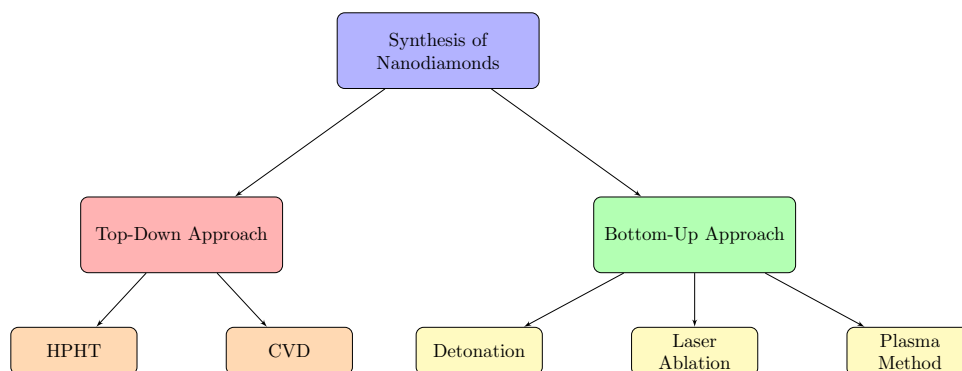


Figure 1.10: Synthesis techniques for nanodiamonds

High Pressure High Temperature

To synthesize a diamond crystal under thermodynamic equilibrium conditions, it is necessary to recreate extreme pressure and temperature conditions identical to those found in the mantle of the Earth, which allow the formation of natural diamond crystals⁵². In other words, temperature conditions of 3000 K and pressures exceeding 14 GPa are necessary, as shown in the blue region of the carbon phase diagram (see Figure 1.9). This technique, known as HPHT for High Pressure-High Temperature, was only commonly mastered in the 1950s when devices capable of withstanding such enormous pressures and temperatures were developed.

The synthesis of diamonds by HPHT is based on the allotropic transformation of graphite into a diamond. The temperature and pressure ranges used in this synthesis are typically 2000-4000 K and 5-15 GPa, respectively. Diamond synthesis can be performed under less extreme conditions

when a metallic solvent such as iron or nickel, capable of dissolving carbon, is used and the metal-carbon mixture is brought to conditions corresponding to the diamond stability domain using a hydraulic press (see zone 2 Figure 1.9).

The diagram also shows a purple region where the diamond is synthesized at a temperature of approximately 1600 K and a pressure of 6 GPa in the presence of a metal catalyst⁵³. These less extreme conditions enabled industrial-scale production of synthetic diamonds at a more reasonable cost. Generally, this process involves immersing a carbon source (graphite or microdiamond crystals) in a solvent made up of transition metals (iron, nickel, cobalt, and manganese). The system is then brought to high pressure and high temperature, establishing a temperature gradient within the cell. This gradient, of only about 20°C, is particularly critical and difficult to control. Crystallization occurs in a single-crystal seed, forming a diamond crystal of 3×3 to 5×5 mm² (see Figure 1.11(b)). Recently, crystals of almost 60 carats have been produced using this technique⁵⁴. The synthesis process is illustrated in Figure 1.11(a). The growth conditions that favor the appearance of one specific crystalline orientation are not disclosed and, therefore, remain the property of industrial manufacturers.

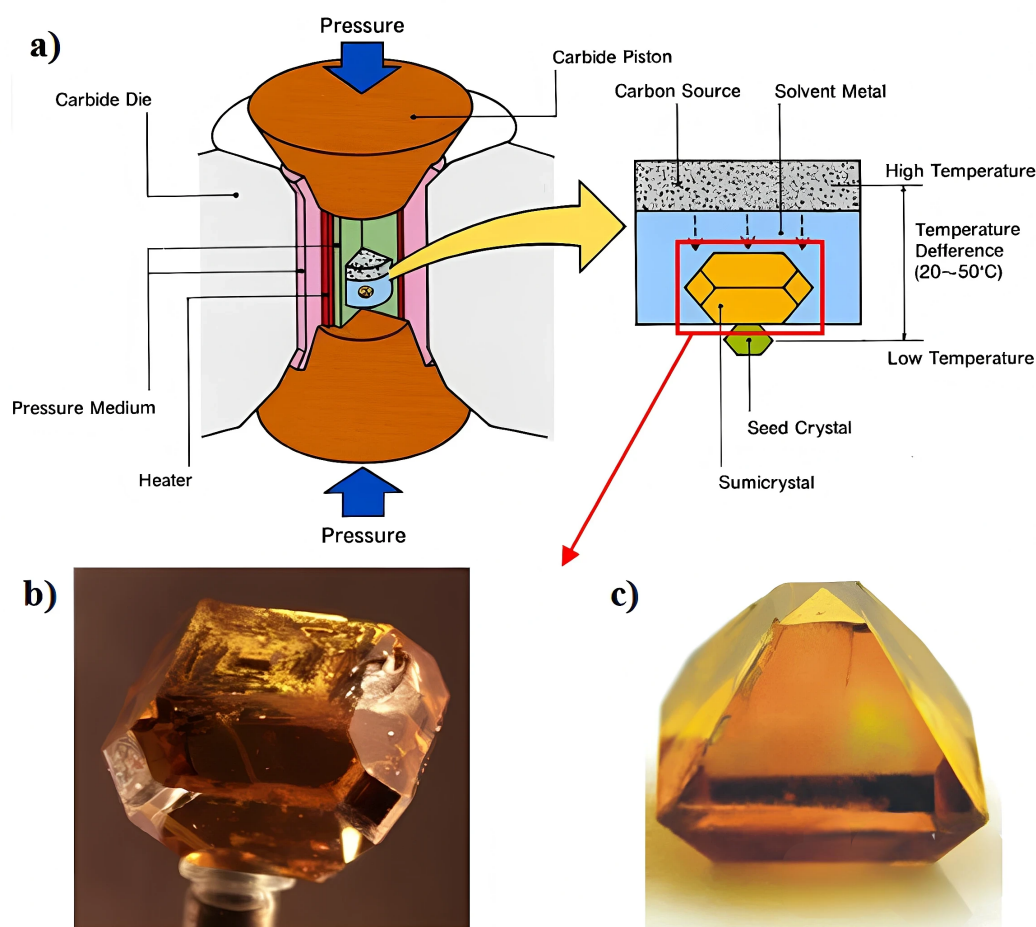


Figure 1.11: (a) Cross-section diagram of Sumitomo's high-pressure, high-temperature growth framework, (b) HPHT diamond single crystals obtained under conditions favoring the formation of oriented faces (100)⁵⁵, and (c) conditions favoring the formation of oriented faces (111)⁵⁶.

Crystals synthesized by this method are often contaminated by impurities during growth, although significant progress has recently been made in this area⁵⁷. Nevertheless, residual impurities from solvent metals (Ni, Co) are frequently found, particularly a concentration of nitrogen from the atmosphere and the catalytic solvent. Therefore, HPHT crystals are generally not directly usable for applications in the field of electronics.

The difference in nitrogen contamination levels in substrates results in the classification of diamond samples into two broad categories, "I" and "II." These are further subdivided into two classes: type "a" and type "b." Type I diamonds contain the largest amount of nitrogen (from 200 to 4000 ppm), while type II diamonds, which represent 1 to 2% of natural diamonds, contain less than 2 ppm⁵⁸. This latter type of diamond is obtained using solvents with a high affinity for nitrogen (iron or cobalt alloys)⁵⁹, and by incorporating nitrogen getters such as aluminum, titanium, or zirconium, which form stable nitrides at high temperatures and thus trap the nitrogen in the solution.

Type Ia diamonds contain aggregated nitrogen atoms, while type Ib diamonds have nitrogen atoms at substitutional sites in the diamond matrix. Type IIa diamonds are "pure" and electrically insulating. They do not contain defects visible in the infrared, whereas type IIb diamonds have a semiconductor nature due to their boron content (higher than nitrogen), which is found in substitution sites, around 1 ppm in natural diamonds⁶⁰.

Although the purity of HPHT diamond substrates is not satisfactory, their crystalline quality remains reasonable, allowing them to be used as substrates for CVD deposition techniques, where it is easier to control the environment in terms of residual impurities.

To obtain small-sized diamonds, the synthesized diamond substrates are generally milled into nanometric-sized debris for various uses.

Chemical Vapor Deposition Technique (CVD)

Unlike HPHT diamonds, CVD diamond synthesis is carried out outside its stability zone, at pressures below atmospheric pressure and at relatively low temperatures ($< 1000\text{ }^{\circ}\text{C}$)¹¹. This process relies on the generation of chemical species in the gas phase that interact with the growing diamond film, facilitating its growth under metastable conditions.

CVD process involves injecting a gas mixture containing a carbon source (e.g. methane, acetylene, ketones, and alcohols) and molecular hydrogen into a reactor and then activating it with an external energy source. There are several CVD methods depending on the energy source used, (i) thermal CVD and (ii) plasma-enhanced CVD (PECVD).

In PECVD systems, a plasma is generated by applying an electric or electromagnetic field. Three main types of plasma can be distinguished: (i) DC plasmas, where the gas is excited by a constant potential difference applied between two electrodes⁶¹; (ii) radio frequency plasmas, where the gas is excited by a radio frequency electric field⁶², typically at 13.56 MHz, applied between two electrodes; (iii) microwave plasmas, where the gas is subjected to a microwave electromagnetic field at 2.45 GHz or 915 MHz⁶³. However, the latter remains the most common method for transferring energy to the gas phase as far as diamond deposition is concerned.

1.2.2.2 Bottom-up Approach

The Bottom-Up approach enables the assemblage of individual atoms or molecules of carbon into larger molecules that eventually nucleate into nanodiamonds. The major techniques within this approach either adopt extreme conditions of temperature and pressure such as detonation and laser ablation, or softer conditions such as plasma-based methods. The latter relies on plasma to promote nucleation and further growth of nanodiamonds from carbonaceous gases, such as methane (CH_4) or ethanol. The Bottom-Up approach shows many advantages: better control over nanodiamond size, purity, and structure enables the production of particles with well-defined characteristics. In addition, detonation and laser ablation methods are often more energy efficient than top-down techniques. These processes also make it possible to manufacture nanodiamonds of very high purity, perfectly meeting the requirements of cutting-edge applications where high-quality materials are needed.

Detonation technique

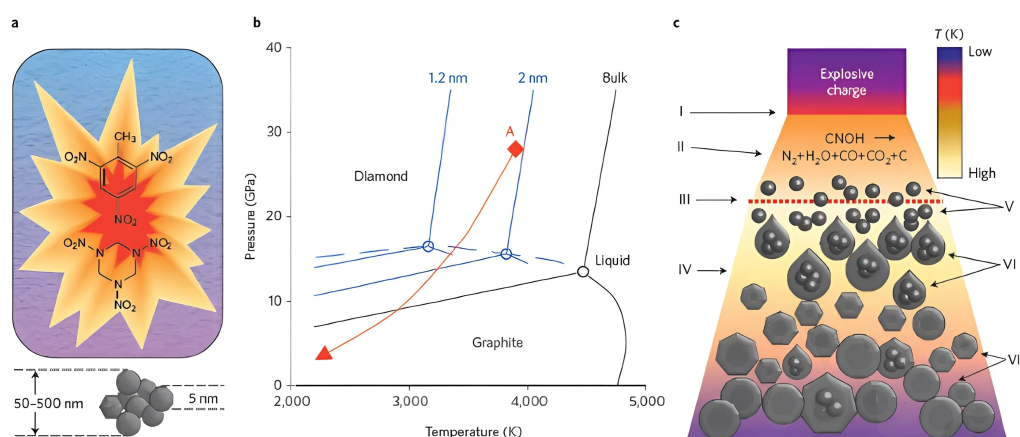


Figure 1.12: (a) Illustration of nanodiamond synthesis by detonation. (b) Carbon phase diagram. Immediately after detonation, the carbon atoms are at the Jouguet point (point A) and follow the pressure and temperature conditions shown in red during cooling. (c) Summary of the different stages of ND growth during detonation.³⁴

This method, invented in the Soviet Union in the 1960s^{34,51,64,65}, involves detonating a mixture of explosives and a carbon source in a tank (Figure 1.12 (a)). During the explosion, the pressure and temperature conditions (point A on the carbon phase diagram, Figure 1.12(b)), enable the formation of nanometric diamond clusters. The temperature and pressure drop rapidly after the explosion, which stops the crystallization of NDPs after a few microseconds. These NDs are known as detonation nanodiamonds (DNDs).

The final product collected on the walls of the detonation tank consists of several hundred nanometer agglomerates containing NDs with a very homogeneous primary size of around 5 nm. However, these NDs are coated with a thick layer of graphitic or amorphous carbon^{51,64}. Purification treatments are then required to remove nondiamond carbon and metallic impurities originating from the vessel walls and to deagglomerate the primary NDs. Purification is generally

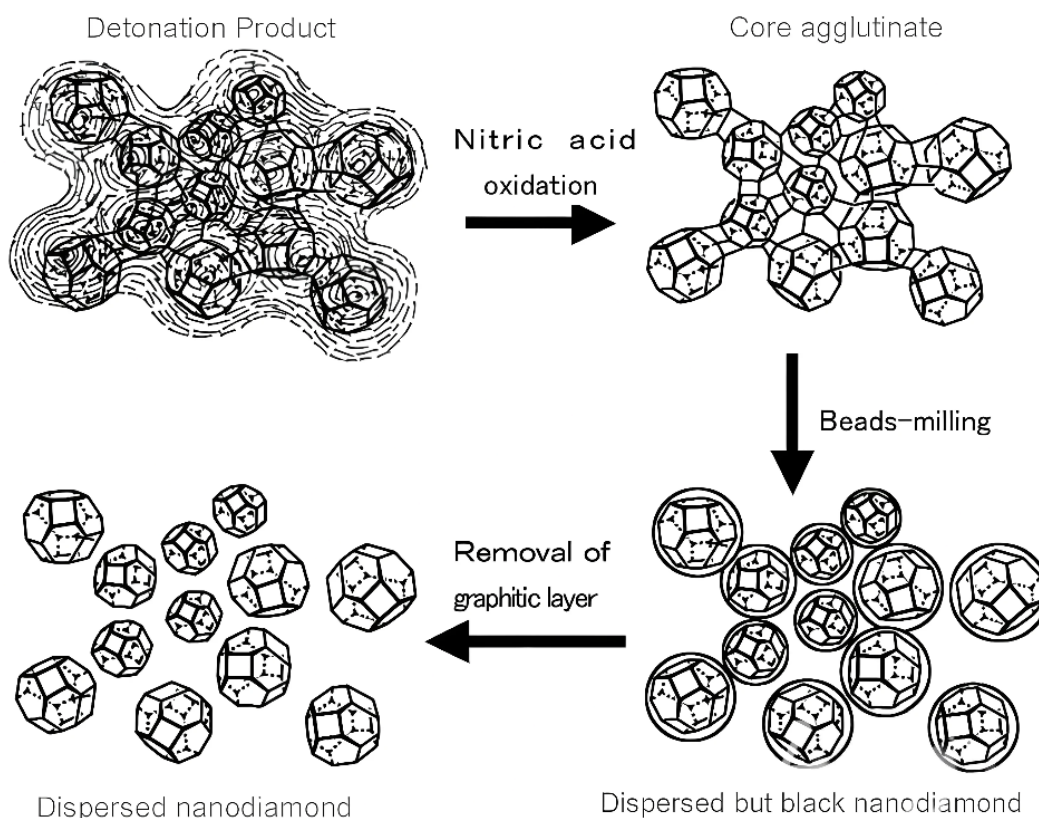


Figure 1.13: Procedure for purifying and deagglomerating detonation nanodiamonds.⁶⁶

achieved by acid bath treatment⁶⁴. Deagglomeration can be achieved by mechanical grinding, e.g. with zirconium beads^{66,67}. This can lead to the formation of graphitic carbon, which can be removed by further purification treatments. Thus, it is possible to obtain primary-sized NDs, which can then be dispersed in solution⁶⁸. The preparation process is summarized in Figure 1.13.

Laser Ablation

The development of the ruby laser paved the way for laser ablation processes. The Pulsed Laser Ablation in Liquid (PLAL) technique is a physicochemical method for the generation of nanomaterials, notably nanodiamonds, based on the interaction of high-energy laser and matter from a solid target immersed in a liquid^{70,71}.

During the PLAL technique, a high-energy pulsed laser is directed at a solid target, generally composed of a colloidal solution of microcrystalline graphite in a liquid such as water, ethanol, or other organic solvents (1.14). During ablation, the laser energy is absorbed by the target, causing rapid vaporization and ionization, forming a dense plasma at the surface of the target. This is possible when the power density on the target surface exceeds 10^8 W/cm^2 . The formed plasma then rapidly expands into the surrounding liquid, cooling quickly and leading to the nucleation and growth of crystalline nanodiamonds. A shock wave can also create favorable conditions for this production. The condensation of carbon vapor produces nanodiamond particles when high-

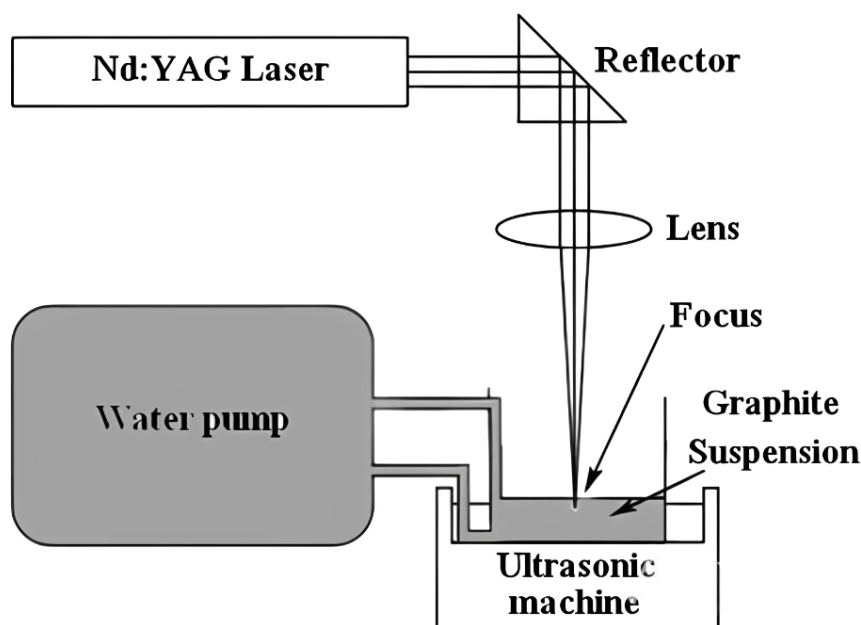


Figure 1.14: Schematic of the setup of ND synthesis by PLAL.⁶⁹

pressure and high-temperature conditions are met. The formed nanodiamonds are surrounded by several layers of graphite. Nanodiamonds of 3 to 6 nm are thermodynamically more stable than their graphitic counterparts at these size scales. The size of the nanodiamonds is limited by the pressure and temperature conditions, and the graphite layers prevent unlimited growth of the diamond particles. The characteristics of the nanodiamonds can also be influenced by the laser pulse and intensity, excitation wavelength, and the type of solvent used.

Plasma-nucleated nanodiamonds

Plasma-based processes offer mild nucleation and growth conditions that are necessary for production of doped DNPs using a bottom-up approach where a selective introduction of precursors permits incorporation of impurities into the lattice of the DNPs during the nucleation/early growth process leading to the formation of color-centers. Historically, most studies reporting nanodiamond formation have actually been dedicated to the growth of CVD diamond in a plasma. One of the first studies to report the formation of NDs was Frenklach et al.⁷² in a mixture of hydrogen and methane in a moderate-pressure MW-assisted plasma. Their findings pointed to the critical role of chemistry in diamond nucleation and concluded that NDs are formed in the gas phase. In this study, the deposits are collected from downstream of the reaction zone and submitted to wet oxidation to remove nondiamond phases. Different combinations of hydrocarbons diluted in gas mixtures such as argon, hydrogen, and oxygen have been tested⁷². In most cases, only non-diamond materials such as graphite and carbyne were obtained. However, homogeneous diamond nucleation was clearly observed in mixtures of dichloromethane and trichloroethylene with oxygen. The formed particles had predominantly hexagonal crystalline shapes, with sizes ranging from 50 nm to 0.2 μm . Optical, microscopic, and spectroscopic analyzes identified that these powders were composed of different diamond polytypes. As the

diamond community was much more interested in growing polycrystalline diamond coatings and monocrystalline substrates in CVD reactors, the interest in formation of NDs waned. However, the new potential applications of NDs found in the past decade have resulted in the reemergence of the interest in the production of NDs using plasma-based processes. Vandenbulcke et al.⁷³ investigated nanodiamond formation in a low-pressure, dusty MW plasma system, utilizing a carbon-hydrogen-oxygen (C-H-O) gas mixture. Their work demonstrated that nanodiamonds could form under relatively low pressure conditions (~ 30 mTorr), with the material characterization revealing the presence of a diamond phase among the amorphous and graphitic phases. In their experiments, careful control of plasma conditions and gas composition facilitated homogeneous nucleation of diamond nanoparticles. The generation of nanodiamond grains (15 to 100 nm in size) occurs under specific conditions of high methane content and low microwave power. These grains are primarily composed of diamond nanocrystals (2–10 nm in size), a size consistent with terrestrial and extraterrestrial nanodiamonds. Gas-phase nucleation led to the formation of diamond nanocrystals (2–10 nm) that later agglomerated into larger particles. For longer plasma durations, sp^2 -hybridized carbon structures formed, indicating a transition from diamond to graphitic phases due to changes in plasma conditions⁷⁴.

Kumar et al.⁷⁵ showed gas phase nucleation of nanodiamonds by using a microplasma reactor at atmospheric pressure to dissociate ethanol vapor. Their method stands out for its ease of use; the plasma was generated with a low-power (50 W) microplasma source, no hydrogen gas, just ethanol vapor for the carbon source. This process formed nanodiamond clusters in the gas phase, and hydrogen gas was added to etch nondiamond carbon and stabilize the diamond phase. The resulting nanodiamond particles, mostly 2–5 nm in diameter, formed by rapid quenching of carbon clusters and had crystal structures of cubic diamond, n-diamond and lonsdaleite, a hexagonal form of diamond⁷⁵. Iqbal et al.⁷⁶ also studied the effect of the flow rate of the carrier gas on nanodiamond formation via microplasma, they used argon as the carrier gas and showed the effect of argon on the size and distribution of the particles.

De Feudis et al.⁷⁷ described a surface-based method to produce highly emissive NDs by CVD. They focus on SiV-doped (silicon vacancy) and GeV-doped (germanium vacancy) nanodiamonds from solid sources, which have applications in quantum technologies and bioimaging as a result of their strong luminescence and photostability. The nanoparticles grow on a cold surface (molybdenum substrate), without seeds. This prevents the formation of a continuous polycrystalline film and allows bulk particle recovery. Although the authors claim that the nanodiamonds may have been collected as a result of the thermophoresis forces, there is no clarity as to the mechanism of formation of nanodiamonds itself.

Nikhar and Baryshev⁷⁸ have provided more evidence of nanodiamond nucleation in a microwave plasma-assisted chemical vapor deposition (MPCVD) setup. They used a gas mixture of methane and hydrogen, with microwave powers of 600–1000 W. They modified their MW CVD reactor to physically separate the plasma from the substrate using a molybdenum disk with a pinhole to selectively collect plasma-nucleated nanoparticles on the substrate. Raman and SEM analysis showed the presence of NDs, which is indicative of their gas-phase nucleation. They argue that the activation energy for nanodiamond nucleation in the gas phase is different from that of diamond growth, and that gas-phase nucleation may occur at much lower energies

(10 kcal/mol) because of different kinetic barriers for particle formation in the plasma. However, they did not suggest possible molecular growth or nucleation mechanisms for nanodiamond.

Plasma-based processes have been widely used to produce high-quality nanoparticles⁷⁹. These processes can be finely tuned to control the chemistry and, therefore, are useful in the synthesis of tailored nanoparticles (NPs). The thesis looks forward to exploiting the advantages of plasmas toward the production of high-quality nanodiamonds. In the next section, we intend to explore and clarify the essential properties and production techniques of non-equilibrium plasmas, with a special focus on those formed through microwave discharges induced by nucleation of carbon nanostructures in these plasmas.

1.3 Motivation and objectives of the thesis

Current methods for producing nanodiamonds, such as High-pressure High temperature (HPHT), detonation, laser ablation, and ultrasonic cavitation, are based on extreme temperature and pressure conditions that favor the stability of the diamond phase over the graphitic phase. However, these extreme conditions and the very short timescales involved offer limited control over the final products. The majority of commercial NDs are produced by detonation of an explosive hydrocarbon mixture, resulting in temperatures around 4000 K and pressures of 20-21 GPa, with reaction times of the order of microseconds. This process yields NDs with a wide size distribution, heterogeneous crystalline quality, and numerous impurities²⁰. In contrast, although the HPHT method allows the production of a high-quality single-crystal diamond (ranging from 100 nm to several micrometers), grinding these crystals down to nanometric sizes deteriorates their crystalline quality and introduces impurities due to the abrasives used¹⁸. The chemical purification of NDs, necessary to remove these impurities, is an expensive, energy-intensive, and environmentally unfriendly step¹⁷. Furthermore, the uneven distribution of impurities limits their use in critical technologies. For example, the creation of vacancy centers in these nanoparticles is not uniform because of the uneven distribution of dopant atoms as well as non-homogeneous sp^2 coverage over the shell, thus limiting the extended use of nanodiamond in biological and quantum applications.

From this perspective, the production of nanodiamonds from CVD processes can be interesting owing to the softer conditions that they offer. These conditions may be used to produce high-quality nanodiamond. Recent research has demonstrated the possibility of homogeneous nucleation of NDs in the gas phase using plasmas with various precursor gases of hydrocarbons, such as methane^{74,78}, ethanol^{75,76} and halogenated hydrocarbons^{72,80}. The carbon nanostructures resulting from these nucleation processes include hybrid aggregates of graphitic and amorphous carbon, as well as ND crystals ranging from 2 to 10 nm. This observation aligns with theoretical calculations showing that the formation of NDs is favorable for small particles (<10 nm), while sp^2 structures form for larger sizes.

Although the understanding of optimal conditions for the nucleation of NDs in the gas phase is still limited, the development of gas-based plasma nucleated nanodiamonds appears promising to meet the demands of critical technologies discussed above. Nanodiamonds were also produced in our group⁸¹ using an internal MW microplasma torch with a gas mixture

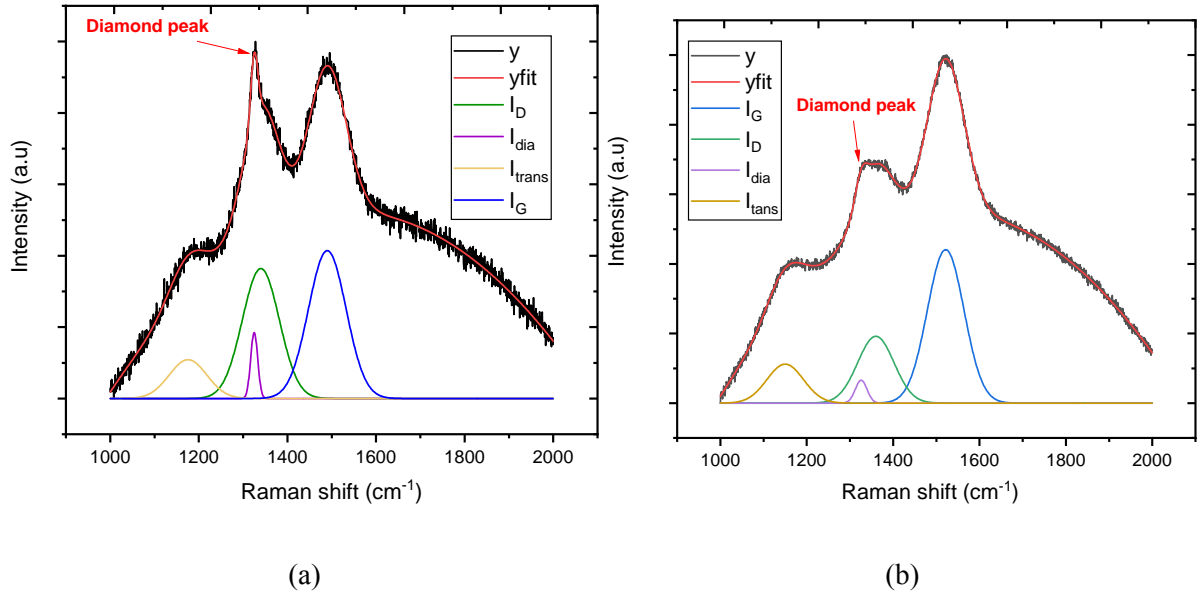


Figure 1.15: Raman spectra of carbon nanostructures produced using MW plasma torch at 100 mbar and $\text{CH}_4 = 3\%$, $\text{H}_2 = 97\%$ (a) 80 W and (b) 70 W.

composed of H_2 and CH_4 ⁸¹. The resulting carbon nanostructures include hybrid aggregates of graphitic, transpolyacetylene and amorphous carbon, as well as diamond crystals (ranging from 2 to 10 nm). As we can see in the figure 1.15, the diamond peak in Raman spectra at different operating conditions confirms the production of nanodiamonds. This background sets the motivation for my present thesis to extend the studies carried out during my master's thesis to address the following key questions:

- What conditions favor nucleation of nanodiamonds?
- What is the mechanism of nucleation of nanodiamonds?
- What could be the key intermediate species/radicals responsible for the nucleation of nanodiamonds?

The aim of the research work carried out in this thesis is to identify the operating regimes of the torch conducive to the formation of well-defined carbonaceous nanostructures with focus on sp^3 nanostructures of nanodiamond type.

1.4 Organization of the thesis

In order to address the key questions and achieve the objectives of the thesis, the research methodology involves combining characterization of plasma and carbon nanostructures by torch to identify the conditions favoring the formation of nanodiamonds. The research work was carried out with the following objectives:

- characterization of the local plasma conditions of the microplasma torch, and especially the evolution of their space-time distributions as function of the process parameters,
- identification of the types of nanostructures obtained as function of the local plasma conditions,

- (iii) and correlating the results of plasma and material characterization to identify the local plasma conditions that favour the formation of nanodiamonds.

This thesis is organized as follows.

- Chapter 2 provides the position of the thesis with respect to the state of the art on (i) MW assisted plasmas, (ii) CVD growth of diamond, (iii) heterogeneous nucleation of diamond on surfaces, and (iv) nucleation of carbon nanostructures and in particular nanodiamonds in gas phase.
- Chapter 3 describes the experimental setups for deposition and the different techniques used to characterize plasma and deposited materials.
- Chapter 4 focuses on the detailed characterization of the microwave plasma torch by presenting MW-plasma coupling and electrical characterization of the plasma. Optical emission spectroscopy experiments were carried out to determine the rotational temperatures of some plasma species using the Boltzmann plot approach and the electron density using Stark broadening of the Balmer series lines⁸². Actinometry measurements were also carried out to trace the relative density of atomic hydrogen⁸³. Eventually, laser-induced two-photon fluorescence measurements were carried out to monitor the space-distribution of the absolute density of atomic hydrogen, a key species in the nonequilibrium processes taking place in these plasmas. The last part of the chapter discusses the new method that was developed during the thesis to recover gas temperatures from ps-TALIF fluorescence signals.
- Chapter 5 presents the results of the nanodiamond synthesis using the H₂/CH₄ mixture. The characterization techniques used are Raman spectroscopy, X-ray photoelectron spectroscopy (XPS), scanning electron microscopy (SEM), transmission electron microscopy (TEM) and atomic force microscopy (AFM). The first two techniques were used to assess the quality of the nanodiamonds produced, by measuring the sp³/sp² ratio. The others were used to study the morphology and crystallinity of the deposited materials. We analyze the influence of methane on nanodiamond synthesis by presenting the results of material characterization and understanding the nucleation route. An extensive work was carried out to correlate the characteristics of the plasma characteristics and of the carbon nanostructures and deposits produced. The objective was to identify the discharge conditions that lead to nanostructures with a high sp³ fraction, and in particular nano-diamonds. Although optical diagnostics provide valuable information on plasma composition and physical characteristics, a significant part of the local conditions of these plasmas remains experimentally inaccessible. Therefore, using a 0D global model, discussion of the hydrocarbon chemistry of the primary radicals that contain 2 carbon atoms in the torch and the possible routes of ND nucleation are discussed.
- The last chapter provides the general conclusion of the thesis. Following this, perspectives on future process development have been provided. Finally, a potential application of using plasma-nucleated nanodiamonds as seeds for the growth of NCD or microdiamond films is evaluated.

Chapter 2

Review of related literature

Contents

2.1	Plasma assisted processes	20
2.1.1	MW plasmas	21
2.1.2	Growth of diamond in CVD reactors	26
2.1.3	Nucleation of diamond on non-diamond surfaces	28
2.1.4	Homogeneous Nucleation of carbon nanostructures	30
2.1.5	Gas-phase nucleation of nanodiamonds	34
2.2	Conclusion	36

This chapter outlines the stance of the thesis in relation to current advancements. The chapter delves into plasma-assisted hydrocarbon processes, concentrating on the formation of various diamond structures as well as other carbon nanostructures.

2.1 Plasma assisted processes

Plasma, the fourth state of matter⁸⁴ after solids, liquids, and gases, is a mixture of molecules, atoms, and free charged particles. It is globally neutral with equal densities of positively and negatively charged species. Approximately 99% of the visible universe consists of plasma, including stars and interstellar matter. Natural plasmas are less common on Earth, where they are found in natural phenomena such as lightning and the aurora borealis. Due to their high potential for various technological applications—such as pollutant abatement, sterilization, deposition, etching, propulsion and fusion, laboratory discharge plasmas were the subject of strongly growing interest in many economic sectors, e. g., health, energy, environment, transport, and materials processing.

Plasmas can be divided into two types: **thermal plasmas** in which electrons, ions, and neutral species are in local thermodynamic equilibrium, and **non-thermal plasmas**, partially ionized and out of thermodynamic equilibrium.

Nonthermal plasmas are thermodynamically out-of-equilibrium plasmas where $T_e > T_{vib} > T_{rot} \approx T_g \approx T_i$. T_e , T_{vib} , T_{rot} and T_g are the electron, vibrational, rotational, gas temperatures,

and ion temperature respectively. They exhibit an electron energy distribution function (EEDF) that is generally not Maxwellian. These distributions may show large populations of high-energy electrons that are capable of efficiently dissociating precursor molecules, particularly molecular gases, leading to the formation of reactive radical species^{85,86}. Nonequilibrium plasmas can be generated by different electrical excitations, such as DC/ RF or MW, and can be pulsed or stationary. Stationary non-equilibrium plasmas are governed by the balance between the rates of ionization and of recombination of charged species⁸⁷. This thesis focuses on the study of MW assisted non-thermal, or cold plasmas, which are a characteristic feature of our microplasma torch. The subsequent subsections are organized as follows.

1. brief overview on different MW applicators for sustaining plasmas
2. Growth of CVD diamond in MW reactors
3. Nucleation of diamond on non-diamond surfaces
4. Gas phase nucleation of different carbon nanostructures, including nanodiamond.

2.1.1 MW plasmas

MW plasma sources have been extensively used for the development of a wide range of carbon nanomaterials such as CVD diamond, graphene, and nanotubes. The major advantages of MW sources are the efficiency of energy transfer from the HF EM field to the plasma, the ability to achieve large power densities, and, in some situations, the electrodeless nature of the discharge. These peculiarities enable process intensification, generation of highly reactive media, and avoiding contamination issues usually encountered when using electrodes such as in capacitively coupled DC/AC or RF discharges.

In a MW assisted plasma reactor, the plasma is formed by the acceleration of free electrons under the effect of the high-frequency electric field and elastic collisions. The electrons transfer their energy to the gas molecules through inelastic collisions. Given the large mass ratio between the electrons and the feed gas species, electrons bounce off the heavy particles and transfer only a small fraction of their energy to the translational mode of the heavy species. The plasma is maintained when the electrons gain enough energy to sustain energy-intensive inelastic collisions such as vibrational and electronic excitation, dissociation, and ionization. These processes generate new species that undergo a new series of collisions, leading to chemical reactions and energy redistribution. The plasma thus contains electrons and heavy species, both neutral and charged. Transport phenomena bring these species to the plasma-substrate and reactor wall interfaces.

The set of microwave plasma sources described here includes: (i) a MW generator that through (ii) a power transmission line with (iii) a tuning system for impedance matching, (iv) transfers the MW power to an applicator which is the load (the plasma in our case), and (v) a circulator that directs the power reflected from the load (the plasma in our case) to a dummy load (generally water) in order to protect the MW source). The key point of microwave sources is the ignition of the discharge.

Traditionally, magnetron has been the major component of the MW generator. It is composed of a high voltage source with an emissive cathode that produces an electron swarm,(ii) a

magnetron system where the electrons emitted at the cathode experience a peculiar dynamic effect under the action of the high voltage field and a perpendicular magnetic field and end up trapped inside anodic cavities where they undergo a strong resonance effect leading to microwave emission. However, with advances in solid-state electronics, the magnetron can be replaced by a MW circuit that allows for generating signals at different frequencies and, when coupled to a power amplifier, can generate MW at the desired frequency and power output.

Mw can be transmitted through different types of waveguides, namely rectangular, coaxial, and microstrip-based (coplanar and stripline) waveguides. Rectangular waveguides are used for high loads of MW power such as KWs, coaxial waveguides can support MW up to 1KW, while microstrips are restricted to MW powers of few 10s of Ws. Naturally, a variety of plasma sources can be supported by different transmission lines. The impedance matching of the tuner is usually performed using a 3-stub unit or/and a plunger that effectively couples the load to the MW source and minimizes the reflected energy. A circulator is used to deflect the remaining reflected power into a heat sink and protect the MW source from damage.

With respect to the applicator, there have been several methodologies to couple the MW and the plasma. The key here is to ensure that the energy transmitted to the gas electrons must be sufficiently high to ignite and generate a plasma. This is commonly achieved by concentrating large MW electromagnetic energy in a small volume to ignite and sustain the plasma^{88–90}. The word "small" again is a misnomer as MW plasmas can be produced over several dimensions ranging from 10s of cm as in 915 MHz resonating cavity plasmas to few 100s of μm as in the case of microplasmas. Moreover, MW plasmas are known to exist over pressures ranging from few pascals as in electron cyclotron resonance plasma (ECR), to moderate pressures of 10s of mbar as in resonating cavities and even to atmospheric pressure microplasma jets generated in microstrip or coaxial feeds. The following paragraphs focus on the most common MW-plasma coupling techniques.

Surface discharges

A common technique to couple MW and plasma is to place a quartz tube across a waveguide. The feed gas flows in a quartz tube that crosses the wave guide and interacts with the microwave for the plasma to be generated, maintained, and then transported downstream in the quartz tube⁹¹. In these discharges, the HF field that maintains the plasma is mainly confined to the vicinity of the surface of the quartz tube, and the associated wave propagates along the axial coordinate of the tube, allowing the plasma to extend over relatively long distances. The most common applicator for this type of coupling is the surfatron guide⁹² where the quartz tube is inserted into the rectangular guide. There have been however several variations of this coupling system, for example: in a surfaguide⁹³, a coaxial waveguide with a quartz tube to produce MW plasma or a "striplastron"⁹⁴ that couples a stripline split-ring-based resonators and the plasma. The advantage of these applicators is that they have a long plasma along the length of the quartz tube. However, the propagation of the surface wave is the subject of several conditions, among which is a significant constraint on the tube diameter. In fact, the diameter of the quartz tube would limit the maximum pressure for plasma operation, with a few cms at low pressure to

a few millimeters at atmospheric pressure. In addition, the constraint on the thermal stability of the quartz would also limit the range of operation of these sources. Nevertheless, surface-wave discharges have been used for applications ranging from chemical analysis and chemical synthesis to the elaboration of carbon materials. For example, the surfatron guide has been used to produce graphene flakes^{95,96}.

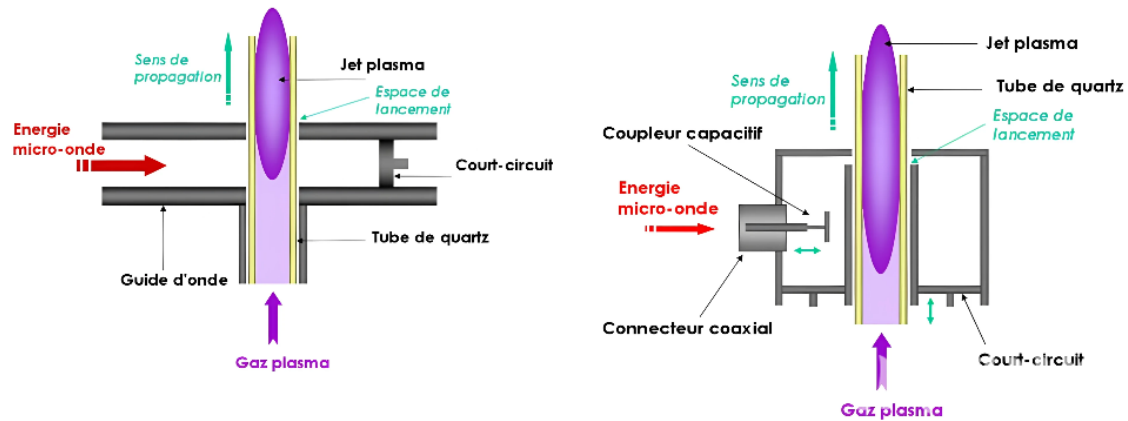


Figure 2.1: Schematic diagram of MPT. There are two types of applicator: surfaguide (left) and surfatron (right)⁹⁷.

Transmission line resonators

Transmission line resonators work on the principle of igniting the plasma zone by creating resonance. The length of the transmission line is designed in such a way that there is resonance at the zone where the plasma is intended. For example, coaxial transmission line resonators can be created that have a coaxial element of length $(2n - 1)\lambda/4$ so that the plasma can be sustained at the end of the plasma. Several examples of such a component are microplasmas based on coaxial transmission line resonators (CTLR), described by Choi et al.⁹⁸, Lee et al.⁹⁹ at frequencies of 915 MHz and 2.45 GHz at atmospheric pressure. Moreover, adding a stub control allows for a precise matching of the impedance. Several variations of the same can be found. For example, a nozzle-like configuration allows for a MW sustained plasma jet. However, placing a ceramic source at the end of the coaxial structure allows for creation of an antenna-type plasma source resembling a pencil that has been commercialized by Sairem as "Hi-Wave" that functions at pressures lower than 1 mbar. In "Aura-wave", commercially sold by Sairem, a magnet at the end of the plasma source allows for creating an ECR effect and functions at even lower pressure. The "Hi-wave" as well as the "Aura wave" have been extensively used at LSPM for various applications such as studied plasma surface interaction^{100,101}, and growth of nanocrystalline diamond^{102,103} to name a few.

The axial injection torch (AIT) developed by Moisan *et al.*¹⁰⁵ operates on the principle of a rectangular guide-coaxial line transition. The microwaves generated by the magnetron are guided via a circuit made of rectangular and coaxial guides, and the discharge is ignited at the

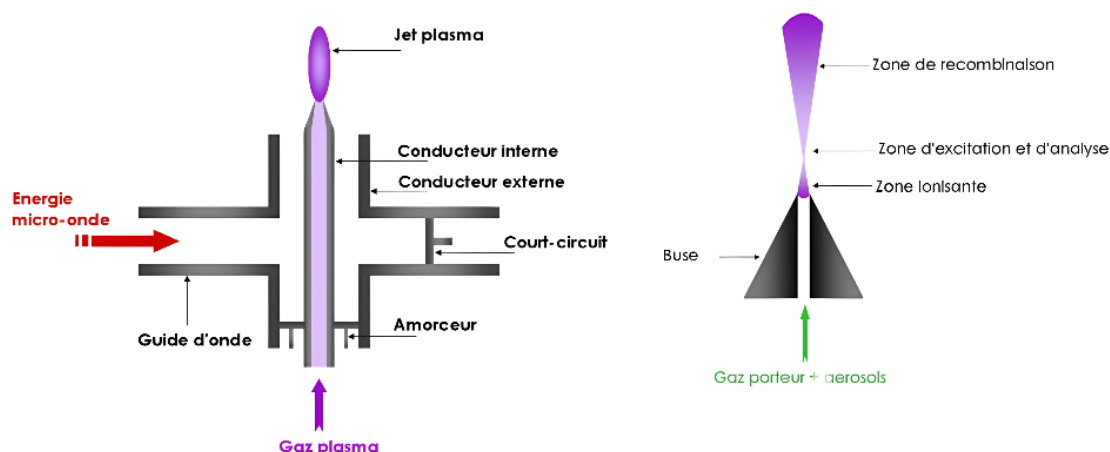


Figure 2.2: AIT schematic diagram (left) and the three different zones that can be distinguished in a plasma jet produced by the AIT (right)¹⁰⁴

nozzle at the end of the coaxial guide because of resonance. The rectangular waveguide is designed to propagate a single TE_{10} mode, i.e., Transverse Electric with zero field component in the direction of wave propagation, while the coaxial line is designed to propagate TEM mode, i.e., a transverse electric and magnetic mode where both electric and magnetic field components in the propagation direction are zero. The feed gas is injected into the inner conductor of the coax and exits through the nozzle (Figure 2.2 (left)). The plasma consists of a very intense cone and a less luminous plume (Figure 2.2 (right)). This limited number of modes prevents any energy loss as a result of the excitation of parasitic modes that do not participate in plasma ignition and maintenance. The short circuit and the igniter allow circuit tuning (optimizing the transition between the TE_{10} and TEM modes) and minimizing reflected power.

Another variation of the transmission line resonators is by using microstrip-based transmission lines as demonstrated by Kim and Terashima¹⁰⁶, Hopwood et al.¹⁰⁷. Different device configurations similar to rectangular and coaxial waveguide can be imagined. Plasma is initiated by creating resonating structures similar to CLTR^{106,108} or split ring resonators^{107,109}. The microstrip circuits depend on printing or micro-milling of substrates and therefore are subjected to error in tuning frequency. External plungers and stubs can also be used to match the impedance and minimize the reflected power¹⁰⁸. Normally, these types of devices operate at low power and have been adopted in applications such as chemical analysis and gas detection. In spite of their relative simplicity, these applicators are limited by the degradation of microstrip substrates affecting the continuous operations of these types of devices.

In fact, the microplasma torch used in this thesis is based on a CTLR similar to Kim et al.⁹⁸ and has been chosen because of its relative ease of fabrication and can be operated under a wide range of operating conditions. The characterization of this torch will be discussed in Chapter 4.

Resonating cavities

The limitations of the transmission line resonators and surface guides are the contact of the plasma with the surfaces. One of the major advantages of MW systems is that one could design resonating structures and create plasmas sufficiently far away from the electrodes. A resonant cavity uses the phenomenon of resonance to amplify the electromagnetic field. The design of the cavity is such that standing waves of resonating structures are present that can sustain a plasma. This energy allows for the initiation of the discharge. The resonance frequency of the cavity depends greatly on its geometric parameters, especially its radius in the case of a cylindrical cavity. It is therefore essential to adapt the cavity geometry to the frequency delivered by the microwave generator (2.45 GHz) to ensure plasma. The Beenakker cavity¹¹⁰ is the first resonant structure proposed to generate a microwave plasma.

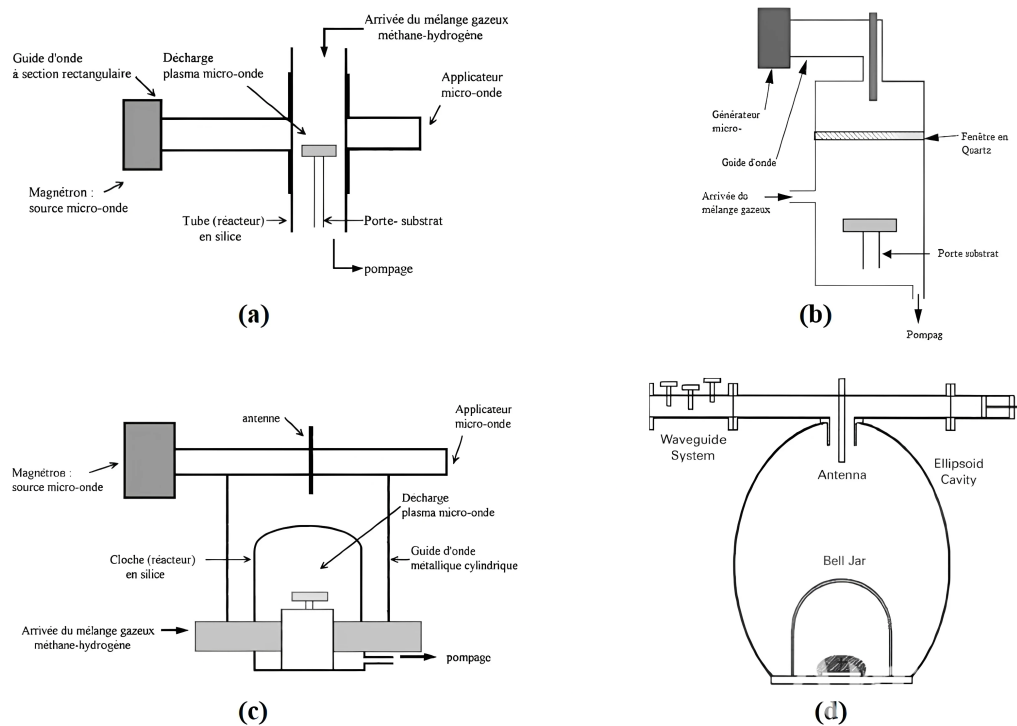


Figure 2.3: Schematic diagram of (a) Tubular¹¹¹, (b) ASTEX metal wall¹¹², (c) Bell jar¹¹³, and (d) ellipsoidal reactor¹¹⁴.

Currently, resonant cavities are employed in the mass production of both doped and undoped CVD diamonds. The energy from the plasma in the cavity dissociates the precursor gas' methane and hydrogen into reactive species, which then deposit as diamonds on the substrate. The capability of the cavity to sustain high energy density and uniform distribution of plasma impact the quality and the diamond growth rate.

Microwave plasmas are created in a reduced-pressure chamber inserted into a resonant cavity whose dimensions must be adapted to the excitation frequency used. The first MWEPCVD

reactor was developed at NIRIM by Kamo *et al.*,¹¹¹. This reactor consists of a quartz discharge tube passing through a rectangular waveguide (2.45 GHz) at the center of which a stable plasma is created. Given the proximity of the quartz walls, this device (see Figure 2.3(a)) does not allow the injection of powers greater than 2 kW, which limits the diamond growth rate to 2 or 3 $\mu\text{m/h}$. Furthermore, the diameter of the quartz reactor (50 to 60 mm) limits the deposition surface. Finally, the risks of film contamination by diamonds as a result of possible etching of the quartz walls are significant.

The more prominent configuration of the MWPECVD reactor is where the MW is injected into a cylindrical cavity through an antenna and the plasma is created in a reduced pressure chamber within the cylindrical cavity. The pressure chamber itself is made up of elements of quartz that transmit MW radiation. Some examples of the same are the Bell Jar type reactor developed by Bachmann *et al.*¹¹³ (Figure 2.3(c)) and the ellipsoidal reactor developed by Funer *et al.*¹¹⁴ (Figure 2.3(d)). For each of these reactors, the reduced-pressure chamber itself is a quartz bell jar. However, these reactors cannot sustain high-MW power because of the temperature limits of quartz. Further improvement of the bell jar reactor was made by replacing the glass bell jar with a metallic chamber with quartz windows, commercialized by ASTEX (see Figure 2.3(b)). In this type of reactor, the reduced-pressure chamber itself constitutes the resonant cavity. It is water-cooled, and the microwaves are coupled using an antenna. These configurations allow for the injection of high microwave power, which is necessary to increase the reactivity of the gas mixture, thereby enhancing the growth rate and the quality of the films for applications in the field of electronics.

A detailed understanding of the growth of diamond in plasma assisted CVD reactors will be provided in the next section.

2.1.2 Growth of diamond in CVD reactors

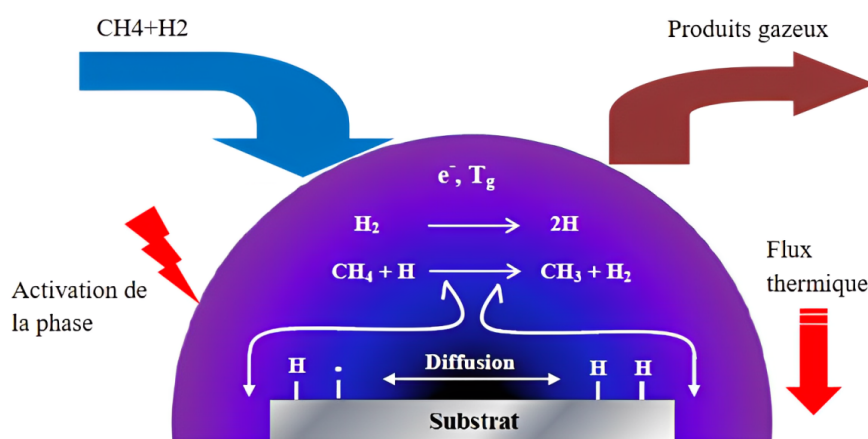


Figure 2.4: Simplified diagram of diamond growth using the MWPECVD process¹¹

As mentioned previously, to create the species necessary for diamond growth, CVD techniques require the activation of the gas phase through an external energy supply. We have classified CVD reactors according to the different forms of gas phase activation. Among these

reactors, we have DC-Plasma Arc Jet Reactor^{115–120}, Oxyacetylene Torch Reactor^{121–124}, Hot Filament Reactor¹²⁵ and Microwave Plasma-Enhanced Chemical Vapor Deposition (MWPECVD)^{9,113,114}. The most widely used technique is MWPECVD.

Figure 2.4 illustrates the MW process for diamond synthesis. The precursor gases, mainly CH₄ and H₂ with/without Ar, are injected into the reaction chamber and activated by a microwave field, creating an electron-rich plasma with high electron temperature (i.e., exceeds 1 eV). In particular, H₂ molecules dissociate into hydrogen atoms and CH₄ forms CH₃ radicals. The plasma region above the substrate contains hydrogenated carbon species (CH₃, C₂) that diffuse toward the substrate. When reaching the surface, these radicals undergo surface reactions that lead to the growth of diamond. Atomic hydrogen plays a critical role¹²⁶ by selectively etching non-diamond phases and saturating dangling bonds of carbon atoms on the growing film's surface, ensuring the sp³ hybridization necessary for diamond growth. The methyl radical (CH₃) incorporates carbon into the lattice. Achieving high densities of CH₃ requires significant hydrogen dissociation at high temperatures. Research at LSPM shows that this dissociation is effective at temperatures above 3000 K, while CH₃ production requires temperatures below 2200 K at moderate pressure^{11,14}. The CVD process must favor diamond phase growth and eliminate non-diamond phases. The gas mixture used should produce species that influence growth kinetics, preferentially eliminating nondiamond contributions. In the H₂/CH₄ mixture, hydrogen preferentially etches graphitic phases, promoting the growth of the diamond film^{127,128}. Atomic hydrogen reacts strongly with graphite, forming volatile compounds and thus supporting diamond growth by removing non-diamond phases from the film surface.

Diamond growth and nucleation via CVD depend on several thermodynamic parameters, such as substrate temperature, reactor pressure, and gas mixture composition. The nucleation of diamond on a substrate concerns the very first appearance of diamond crystals on the surface of any solid material, while growth refers to the continuous attachment of C-layers to existing diamond layers. Typically, the substrate temperature for optimal diamond growth ranges from 700°C to 1100°C^{126,129}. At lower temperatures, the available energy is insufficient to form sp³ bonds, which leads to the formation of amorphous carbon. In contrast, at higher temperatures, carbon radicals may desorb from the substrate surface before they can be incorporated into the diamond structure. Reactor pressure is another key parameter that influences the reactivity of carbon radicals and their interaction with the substrate. Pressures between 20 and 100 Torr are generally considered ideal for the growth of high-quality diamond films^{127,129}.

Traditionally, argon is added for the synthesis of nanocrystalline and polycrystalline chemical vapor deposition (CVD) diamonds and is known to directly influence their growth and quality^{130,131}. Studies show that argon, in combination with other gases such as hydrogen and methane, enables better management of the deposition conditions, leading to more uniform and high-quality diamond films^{130–132}. More importantly, they also show that argon-rich atmospheres favor the formation of UNCD films, characterized by extremely fine grains and a dense structure, in contrast to hydrogen-rich atmospheres which tend to produce films with larger grains over time^{130,131}. Argon promotes frequent secondary nucleation, preventing excessive crystalline growth and reducing the diamond grain size, resulting in films with smoother surfaces and improved mechanical and electronic properties. Diamond films synthesized under argon-rich

conditions often exhibit enhanced electrical conductivity due to an increase in sp^2 carbon content, which is particularly useful for electrochemical applications^{130,132}.

Of course, these conditions are not acceptable for the growth of monocrystalline diamond and the methane/hydrogen balance should be chosen so that there is no secondary nucleation of diamond and only growth takes place through successive addition of CH_3 radicals and etching by H-atoms. The composition of the gas mixture, particularly the ratio between methane (CH_4) and hydrogen (H_2), is crucial for the growth of CVD. A methane/ H_2 ratio between 1 and 5% in volume is often used to produce high-quality diamond films. If the partial pressure of methane is too high, nucleation on the surface can accelerate, and the risk of graphite formation increases; conversely, insufficient methane limits the growth rate¹³³. So, optimal values of the C/H ratio can promote more selective growth and higher diamond quality. The other effect of increasing methane is the formation of dust particles in the gas phase¹³⁴, which not only affects the coupling of the MW-plasma but also the quality of the diamond grown. This aspect will be discussed later. The quality of the grown diamond can be further controlled by adding O-containing species such as CO_2 , where the O atom and OH are also known to etch the sp^2 phase^{103,135,136}.

2.1.3 Nucleation of diamond on non-diamond surfaces

Although secondary nucleation of diamond on carbon (diamond) is easier, the same cannot be true for nucleation of diamond phase on other substrates. Due to the inherently high surface energy of diamond on a non-diamond substrate, spontaneous nucleation on these substrates is very challenging^{80,125,127}. Therefore, we need to use specific nucleation techniques to increase the density of diamond nuclei on nondiamond substrates to promote the growth and secondary nucleation of continuous nanocrystalline diamond films. Over the years, many methods have been developed to overcome this nucleation barrier, each with its own advantages depending on the substrate and application.

The most common approach is to coat the substrate with a layer of nanodiamond seeds. Once exposed to CVD conditions, these seeds act as nucleation points from which diamond films grow. The growth follows the Volmer-Weber mechanism, where individual crystal islands form, grow, and coalesce. As mentioned by Mandal¹³⁷, the density of seeds can be controlled by tuning the size and concentration of nanodiamond particles. Other studies, such as those of Arnault et al.¹³⁸ have explored other ways to increase seeding density by modifying the electrostatic properties of the substrate or by introducing functional groups to attract NDs. These methods have shown a significant improvement in the rate of nucleation leading to more uniform growth of the diamond film on various substrates.

The simplest seeding technique is mechanical abrasion that involves polishing the substrate with diamond grit and, therefore, embedding small diamond particles on the surface, which then serve as nucleation sites during subsequent CVD growth¹³⁷. Although this method is relatively straightforward and effective, especially for ceramic substrates, it struggles to achieve uniform seeding or high nucleation densities. Electrostatic seeding is another common technique to increase nucleation density, especially when growing NCD on non-diamond substrates. In this process, the substrate is dipped in colloidal solution containing nanodiamonds to deposit a

monolayer of diamond seeds¹³⁷. The result depends on the properties of the colloidal suspension and, more particularly, on its zeta potential with the substrate surface. The zeta potential defines the surface charge of the substrate / liquid interface and therefore determines the electrostatic interactions of the substrate with liquid droplets laden with diamond particles. A zeta potential outside the range of -30-30 mV maintains colloidal stability and favors effective seeding¹³⁹. Other factors influencing colloidal stability include the size and concentration of nanodiamonds, and these parameters need to be optimized to avoid particle agglomeration¹⁴⁰. In fact, particle agglomeration reduces seeding efficiency, especially in suspensions that contain detonation nanodiamonds (DND), as reported in several experiments¹⁴¹, and the colloidal suspension of nanodiamonds is usually ultrasonicated to have uniform nanodiamond deposition on the substrate¹⁴¹. Plasma treatments are also commonly used for substrate surface conditioning, enhancing the zeta potential, and improving electrostatic interactions with nanodiamond colloids¹⁴². The seeding process can be improved through various techniques, such as spin-coating, electrospraying, and mechanical abrasion. For example, electrospraying can force charged nanodiamond particles toward the substrate, which could yield higher seed densities¹³⁷. However, a completely uniform monolayer is still difficult to obtain, and further improvements in colloid preparation and surface conditioning are important for highly qualified films.

Bias-enhanced nucleation (BEN) is another widely used method, especially for epitaxial growth on conductive substrates. This involves applying a negative DC bias to the substrate during the initial stages of CVD growth, increasing the ion bombardment energy at the surface and promoting diamond nucleation¹⁴³. The mechanism behind BEN relies on the implantation of carbon atoms in the substrate, fostering the formation of sp^3 bonded carbon clusters. Ion bombardment preferentially etches away sp^2 -bonded carbon, leaving stable diamond nuclei behind¹⁴⁴. This technique has been successfully applied to substrates such as silicon, iridium, and silicon carbide, illustrating its versatility. BEN can produce very high nucleation densities, up to 10^{10} cm^{-2} ^{143,145} and is very effective for dense diamond films. Recent studies have shown that the combination of BEN with a predeposited carbon layer leads to higher nucleation densities and better film uniformity¹³⁷. However, it is limited to conductive materials as the biasing process depends on the electrical conductivity of the substrate.

Further refinements in the seeding technique have introduced hybrid approaches, in which substrates are pretreated with a carbon interlayer to improve adhesion and nucleation^{146,147}. A more recent approach to diamond nucleation is the use of diamondoid molecules as seeding agents. Diamondoids, such as adamantane, are cage-shaped hydrocarbons that have the diamond lattice structure¹⁴⁸. These molecules can act as molecular precursors during CVD and provide a template for diamond nucleation. The coating of the substrate with adamantane before CVD has been shown to improve the nucleation density even at low temperatures¹⁴⁹. In theory these small molecules could allow for seeding densities as high as 10^{13} cm^{-2} but in practice colloidal stability and surface interactions reduce the achievable density. Despite the drawbacks, diamondoid-based chemical nucleation is a promising method, especially for ultrathin diamond films. Diamondoids, especially adamantane and diamantane, have become increasingly important in recent years for diamond nucleation in CVD processes. With their sp^3 hybridized carbon framework close to the diamond lattice, diamondoids are excellent molecular precursors for diamond growth and

provide nucleation sites that mimic the atomic structure of diamond¹⁵⁰.

2.1.4 Homogeneous Nucleation of carbon nanostructures

Classical theory of homogeneous nucleation based on thermodynamics predicts nucleation by minimizing the Gibbs free energy. Assuming that the atoms aggregate to form a liquid spherical droplet, the total Gibbs free energy is the sum of two terms: the first term is the change in the Gibbs free energy due to phase change and is proportional to the volume of the sphere, while the second term is the change due to surface energy that binds the sphere and is proportional to the area. The Gibbs free energy of the phase change depends on the temperature and vapor pressure of the atoms outside the droplet. Under saturated or super saturated conditions with abundant supply of individual atoms pushes the equilibrium towards the liquid phase, i.e., the atoms are bound to aggregate and condense into the liquid phase. The Gibbs free energy of the phase change under such conditions would be negative, indicating conditions favoring condensation/nucleation. However, nucleation has to overcome an energy barrier because of the positive surface energy. As a result, one can establish a critical radius where the total Gibbs energy is the maximum. For droplets of sizes below the critical radius, the surface energy is too high for a droplet to be stable and, therefore, does not support condensation. However, a radius larger than the critical radius promotes condensation and growth of the droplet. With respect to carbon, carbon atoms can arrange themselves into either sp^2 hybridized graphitic structures or sp^3 hybridized diamond phase based on the lower Gibbs free energy at given temperatures and pressures, as seen in the carbon phase diagram. No wonder processes like laser ablation and detonation achieve high pressure and temperature conditions where carbon atoms can nucleate into diamond phase²⁰.

In a microwave, radio frequency (RF) or discharge plasma, carbonaceous precursors (usually hydrocarbons such as methane or acetylene) are introduced into the reactor. These precursors are then dissociated by electronic impact or thermally into reactive species, such as radicals, carbon atoms, hydrocarbon ions ($C_2H_2^+$, C_2H^- , etc.), and other molecular fragments (e.g. CH_3 radicals, C_2H , etc.). The classical nucleation theory is no longer valid for the plasma conditions discussed above, especially in an environment containing several radicals, such as H-atom. Whether nucleated nps belong to the sp^3 or sp^2 phase is secondary, as the first aspect of nucleation in reactive plasmas is the molecular growth of stable molecules and their eventual nucleation.

Firstly, let us try to understand the different processes that could occur in a dusty hydrocarbon plasma. Plasma conditions, such as electron density, electron temperature, and gas mixture composition, strongly influence particle nucleation and growth rates. The molecular growth and homogeneous nucleation process of carbon nanoparticles is depicted in Figure 2.5.

Radical chemistry can initiate the growth of larger hydrocarbon molecules, which, when sufficiently large, would nucleate to form NPs^{151,152}. The molecular growth process of carbon clusters in plasma can be described as a series of chemical and physical reactions due to frequent collisions between the clusters and the reactive species present in the plasma. The initial nucleation of the particles is followed by a growth phase, during which hydrocarbon molecules or radicals stick to the NPs. NPs can also grow through the coagulation of two different NPs.

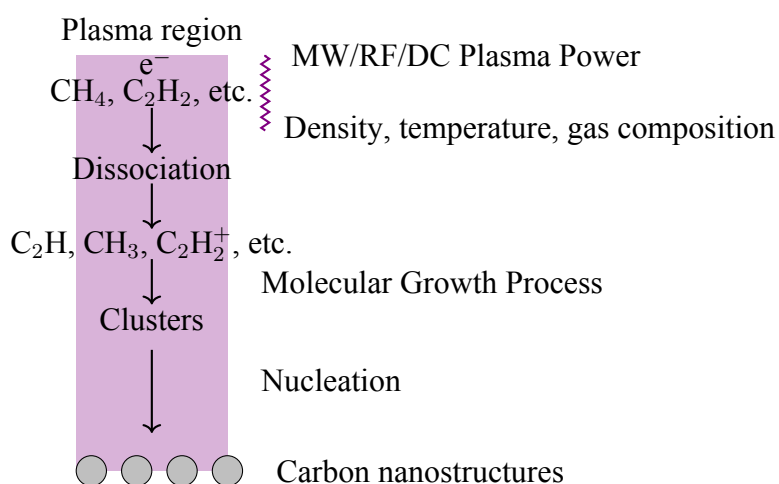


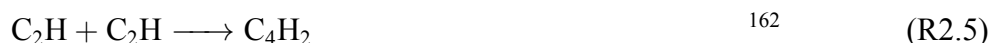
Figure 2.5: Gas phase nucleation process

NPs are charged because of their interaction with ions and electrons in the plasma. Moreover, stochastic particle charging is associated with heating as a result of continuous bombardment of ions and electrons. The energy injected into the NPs could also cause a phase change, which is particularly important for small particles < 10 nm. Several studies looked at gas phase nucleation of carbon nanostructures. In both interstellar clouds and plasma reactors, ion-neutral and radical-driven reactions allow carbon cluster nucleation, which can grow into larger nanostructures. Herbst and Leung¹⁵³ showed how complex hydrocarbons and carbon-based structures can form in the gas phase environment, especially in dense interstellar clouds. The model developed by Herbst and Leung¹⁵³ made use of the pseudo-time-dependent approach to simulate the chemistry of the gas phase in interstellar clouds, where reactions between neutral molecules and molecular ions produce complex hydrocarbon species. Although the work deals with astrochemical environments, basic similarities still exist with plasma-assisted processes in nanocarbon synthesis, especially in the role that radicals and ions play in driving nucleation. Their pseudo-time-dependent gas-phase model showed how hydrocarbons such as C_9H_2 and related cyanopolynes can form under low-temperature and high-density conditions. Although the work mentioned by these authors pertains to interstellar conditions, the basic chemical processes they describe, such as the role of molecular ions and neutral-neutral reactions, can also explain how such complex carbon structures can arise in plasma environments, including those applied to nanodiamond synthesis. Herbst and Leung's model¹⁵³ highlights the role of molecular ions such as CH_3^+ and $C_2H_2^+$ in driving the formation of complex hydrocarbons. This chemistry is analogous to the gas-phase processes occurring in plasma-assisted CVD systems used for the synthesis of carbon nanostructures.

Two main classes of intermediate species leading to nucleation of carbon nanoparticles are polyaromatic hydrocarbons (PAHs) and unsaturated linear chains such as polyynes and trans-polyacetylene. These intermediaries are primarily driven by acetylene chemistry. PAHs are organic compounds composed of multiple aromatic rings and are precursors to soot. PAHs have received a lot of attention as a result of their formation in acetylene-rich plasma environments. Polyynes are linear carbon chains with alternating single and triple bonds (like polyynes) termi-

nated by acetylenic groups. They are prevalent in Ar-acetylene plasmas excited by RF^{154–156} and MW¹⁵⁷. Trans-polyacetylene is a linear chain that contains alternate double and single bonds and has been reported under H-rich conditions, such as during the synthesis of nanocrystalline diamond^{158,159}.

Radicals such as C, CH₃ and C₂H_x radicals (ethynyl, C₂H and vinyl, C₂H₃) play a key role in the formation of larger radicals C₃ and C₄.



Then Diels-Alder reactions involving C₂ and C₄ radicals lead to the first aromatic ring C₆ such as benzene. For example,



In a plasma environment, PAH growth may also be supported by ions. Calcote et al.¹⁶³ identified C₃H₃⁺ as the primary precursor ion and the discharge conditions of diamond growth, C₃H₃⁺ are mainly formed due to



Once C₃H₃⁺ is formed, it undergoes linearization processes in which the addition of acetylene (C₂H₂) leads to the formation of larger ions such as C₅H₃⁺ and C₄H₃⁺. Subsequent addition of acetylene leads to spontaneous cyclization and formation of aromatic ions, as shown in Figure 2.6.

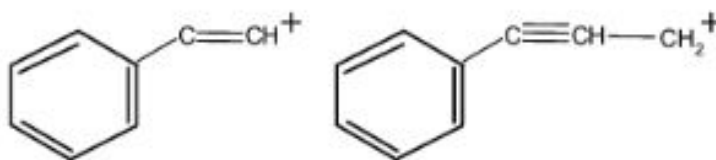


Figure 2.6: Chemical structure of the smallest aromatic ions predicted by Calcote mechanism¹³⁴

Once the first aromatics are formed, the further addition of carbon radicals leads to polycyclization leading to the formation of PAHs and soot. They are different mechanisms that have been proposed, such as the Hydrogen-abstraction Carbon(C₂)-addition (HACA), Hydrogen-abstraction-vinyl radical addition (HAVA), methyl-addition cyclization (MAC), phenyl-addition

cyclization (PAC), and resonance-stabilized radical chain reactions (RSR). HACA mechanism is the most prominent and is prevalent at temperatures above 1300 K as observed in combustion applications. This mechanism is well studied in combustion environments and is responsible for the formation of polycyclic aromatic hydrocarbons (PAHs) that nucleate to form soot^{162,164–167}. HACA process involves the successive addition of acetylene molecules (C_2H_2) onto free radicals, forming complex aromatic structures¹⁶⁷ as shown in Figure 2.7. The addition of acetylene to aromatic radicals generates stable products such as pyrene, enabling this mechanism to overcome thermodynamic barriers that would otherwise slow the growth of PAHs¹⁶⁵. In addition, Frenklach et al.¹⁶⁴ highlighted the importance of temperature limits in the HACA mechanism, showing that this mechanism remains relevant even at relatively low temperatures of 1000 K, with possible competition with other mechanisms such as CAHM (Carbon Addition Hydrogen Migration). An

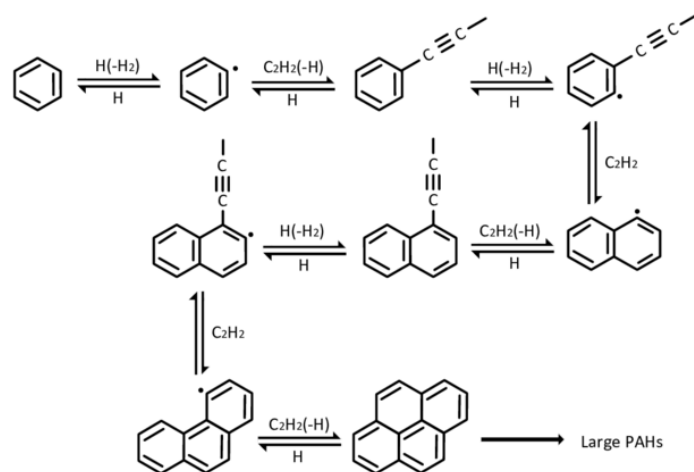


Figure 2.7: PAH formation through HACA mechanism¹⁶⁸

outcome of PAH formation is the possibility of nucleation of graphene flakes^{96,169}. Introducing a carbon-containing precursor, such as ethanol, into a surface wave microwave plasma generated by argon plasma leads to breaking the precursor into reactive fragments such as C, C_2 , and C_2H_2 . These grow through the formation of aromatic rings and under the right conditions nucleate into 2D graphene flakes in the plasma afterglow. The growth of these layers is controlled by the continuous supply of carbon fragments that attach to the edges of the growing graphene sheet and allow for lateral growth.

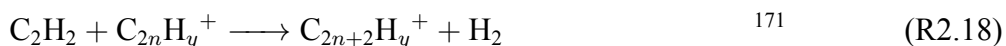
However, at low temperatures < 1000 K, carbon growth occurs predominantly through aliphatic linear chains. Such structures precede larger carbon clusters in plasmas, especially in acetylene-based environments, and play a leading role in nanoparticle growth. Deschenaux et al.¹⁵⁵ demonstrated the importance of acetylenic compounds (C_2H_x) in the growth of carbon nanoparticles in dusty RF plasmas using FTIR absorption spectroscopy and mass spectrometry. They suggested that ion-neutral reactions, particularly those involving high-mass carbon anions, play a crucial role in nanoparticle formation¹⁵⁵. Tetard's work¹⁵⁴ further expands our understanding of carbon cluster formation by highlighting how RF discharges in acetylene-based plasmas promote the growth of carbon clusters through interactions with ions such as $C_{2n}H_y^+$. In fact, the strong electronegative nature of the argon/acetylene discharge results in a slower ambipolar diffusion transport and a longer residence time of the positive ions in the RF discharge. As a

result, these ions experience an enhanced molecular growth leading to an enhanced nucleation¹⁵⁶. Similar ion-driven molecular growth has also been reported by Ouaras et al.¹⁵⁷ in a low pressure MW Ar-C₂H₂ plasmas. These mechanisms are known to be prevalent at low temperature (<1000 K)¹⁵⁶.

The presence of large amounts of C₄ radicals can also lead to the formation of linear chains¹⁶².



In addition, the molecular growth of linear chains can follow neutral, positive, or negative ions as described in the following reactions.



2.1.5 Gas-phase nucleation of nanodiamonds

Nanodiamonds represent a special case of gas-phase nucleation, where sp³-hybridized carbon structures are favored over sp² graphitic phases. Although several experimental studies^{72,75–78,80} have shown a gas-phase nucleation of diamonds, there is very little understanding of the possible mechanisms that lead to nucleation of nanodiamonds. Although the carbon phase diagram is valid for bulk materials, the stability of the phases could change at nanoscales based on their surrounding environment. Concerning the stability of NDs, theoretical studies show that nanodiamonds can be stable for sizes less than 10 nm under the conditions encountered in CVD processes^{172–174}. Gamarnik¹⁷² was one of the first to study the size-related stabilization of nanodiamonds with respect to graphite. By computing the free energies of formation of diamond and graphite of different sizes as a function of the pressure and temperature prevalent in a CVD reactor, it was concluded that diamond of a size less than 10 nm is more stable than a graphite phase. However, the stability of the diamond phase itself decreases as temperature increases, for example: the critical radius of the diamond reduces from 10 nm at room temperature to approximately 5 nm at 1000 °C. Hwang et al.¹⁷³ proposed a charged cluster model and indicated that the presence of charged clusters and particles in a plasma could make the diamond phase more stable than the graphitic phase at the nanoscale. Their hypothesis is that the surface energy of diamond reduces with charging when compared to that of graphite. Diamond being a dielectric, it exhibits a much greater decrease in surface energy when compared to conductive graphite. Barnard et al.¹⁷⁴ have studied the relative stability of carbon nanoparticles, focusing on NDs and fullerenes using density functional theory (DFT). They show that the stability of the different carbon phases depends on the particle size. The results indicate that the NDs are stable in a size window between around 1.9 and 5.2 nm. Below 1.9 nm, fullerenes are more stable than NDs, while above 5.2 nm, graphite becomes the most stable phase. These findings help to

explain the experimentally observed transformations of NDs into 'carbon anions' (fullerene structures) at certain particle sizes and temperatures. One of their major conclusions is that H-terminated nanodiamonds are relatively more stable than an unterminated nanodiamond. The work thus offers a better understanding of the phase transitions of carbon nanoparticles and their stability as a function of size and is also indicative that, like CVD diamonds, the H-atom would indeed stabilize the nanodiamond. However, how nanodiamond itself can be formed

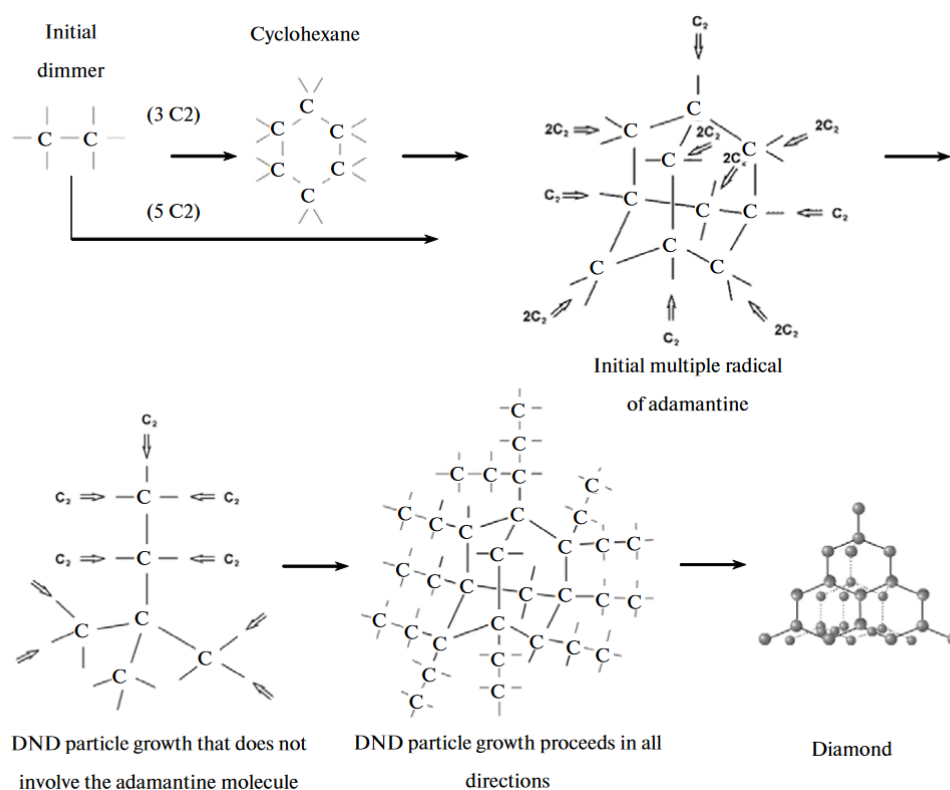


Figure 2.8: Mechanism of detonation nanodiamond proposed by Dolmatov et al.¹⁷⁵

from primary hydrocarbon molecules such as methane remains an enigma. The only known mechanism that explains the formation of a large sp^3 structure in the gas phase, known to us, comes from Dolmatov et al.^{20,175} for the detonation conditions as depicted in Figure 2.8. According to them, diamondoids are the key intermediary species that lead to the nucleation of NDs. Diamondoids are a class of organic molecules that are composed of multiple cages of adamantane ($C_{10}H_{16}$), the smallest unit cage structure of the diamond crystal lattice. They indicate that C_2 is the main radical under these conditions that quickly combine to form linear chains that undergo subsequent cyclization that results in the formation of cyclohexane. The further addition of C_2 radicals leads to the formation of adamantane. They also propose an alternative reaction mechanism that does not involve the formation of adamantane, but C_2 radical remains the key radical here as well. From the growth of CVD diamond, it is known that atomic hydrogen would be particularly important in this process, as it selectively etchs the sp^2 carbon, allowing the formation of sp^3 structures. It is also possible that the CH_3 radical is necessary for the growth of sp^3 molecules, leading to nucleation of NDs.

Studies have shown that CH_3 radicals can be attached to adamantane to form larger diamon-

doids^{150,176}. Stauss et al.¹⁵⁰ produced higher diamondoids in adamantane, methane, and argon microplasma reactors, operating under atmospheric pressure conditions. They show that higher hydrogen concentrations favor the formation of diamond growth. Through the analysis of the products by GC-MS, Ishii et al.¹⁷⁶ conclude that molecular growth to higher diamondoids occurs through the extraction of hydrogen from adamantane and the subsequent addition of CH_3 radicals. To the best of our knowledge, no further investigation of sp^3 molecular growth is available in the literature.

2.2 Conclusion

Based on this current knowledge of nucleation and growth of carbon nanostructures in plasma, the aim of this thesis is to build on the initial promising results obtained using the MW plasma torch towards the development of a process that favors the formation of sp^3 over other forms of carbon nanostructures and to obtain a high yield of high-quality nanodiamonds. The thesis will particularly focus on identifying the domains of local plasma conditions in terms of gas temperature, electron densities and temperature, H-atom and the primary reactive radicals CH_3 and C_2 that are likely to promote sp^3 molecular growth and nucleation of nanodiamonds.

Chapter 3

Experimental setups and instruments

Contents

3.1	Introduction	37
3.2	Description of the MW-torch	38
3.3	Deposition Experiments	38
3.3.1	Heating/biasing system	39
3.3.2	Substrate cooling system or cold finger	39
3.4	Plasma diagnostics	40
3.4.1	Optical emission spectroscopy (OES)	40
3.4.2	Two-photon Absorption Laser Induced Fluorescence (TALIF)	42
3.5	Material characterization technique	46
3.5.1	Raman spectroscopy	47
3.5.2	X-ray Photoelectron Spectroscopy	49
3.5.3	Atomic force microscopy	51
3.5.4	Scanning Electron Microscopy	52
3.5.5	Transmission Electron Microscopy	54

3.1 Introduction

As stated in the previous two chapters, the objective of this thesis is to develop an improved understanding of local plasma phenomena leading to homogeneous nucleation of sp^3 -type carbon nanoparticles, particularly nanodiamonds or diamond nanoparticles (DNPs). For this purpose, the research methodology follows an integrated approach that involves plasma characterization, material characterization, and numerical simulation. The aim of this chapter is to present the various experimental setups and techniques used to characterize the plasma and the deposited carbon nanostructures.

This chapter is structured as follows: the first part describes the MW torch and the various reactor chambers as well as the experimental set-up and the deposition process. Next, we describe the different instruments used to characterize the microplasma optically. Finally, we discuss material characterization techniques used to assess the size, quality, and morphology of carbon nanoparticles.

3.2 Description of the MW-torch

The home-made MW microplasma used for the synthesis of nanocarbons is based on coaxial transmission line resonator (CLTR) coupling techniques at 2.45 GHz⁹⁸. The design principle of this MW-torch relies on the creation of a resonance at the end of the coaxial transmission line that results in a strong concentration of electromagnetic field that sustains the plasma. The length of the present torch is approximately equal to $\frac{3}{4} \lambda$, which facilitates the electromagnetic resonance at one end of the torch. As a result, a high density plasma ($n_e \approx 10^{13} \text{ cm}^{-3}$) is created in a small 250 μm gap located at the end of the torch between a circular cap of 4 mm-diameter and a concentric steel pin of 3 mm-diameter as shown in Figure 3.1. The plasma volume created is very small $O(\text{mm}^{-3})$ resulting in MW power densities as high as $5 \times 10^9 \text{ W/m}^{-3}$, which is three orders of magnitude higher than in a conventional CVD reactor used for diamond growth¹⁷⁷. This provides a distinct advantage for producing highly nonequilibrium discharges with high electron densities and moderate gas temperatures which can produce a wide range of reactive environments with charged species, radicals, and photons over dimensions limited to a few millimeters. The torch is cooled using a double wall water cooling system connected to a chiller. This allows for the microplasma to operate under extremely high power density conditions. The feed gas is injected through the inlet port. The microwave is fed through a hermetically sealed MW n-type feed-through. The present torch can be operated under a wide range of pressure conditions (10 mbar–1 atm), with different gas mixtures such as argon, hydrogen, methane, acetylene, and ethanol. The next section describes the characterization of this torch. In the course of the research work described in this thesis, two identical MW torches were manufactured. The first was used for plasma characterization, while the second was used for deposition.

3.3 Deposition Experiments

The carbon nanostructures synthesized in the micro-plasmas generated in H_2/CH_4 and $\text{H}_2/\text{CH}_4/\text{Ar}$ mixtures were collected on a substrate positioned downstream of the flowing plasma. The present work used two different collection systems. This enabled changing the local conditions at the substrate surface by varying the electrical polarization, that is, the voltage of the substrate, with respect to the torch and the substrate temperature. This makes it possible to investigate the plasma surface interaction and/or collect dust particles produced in the plasma.

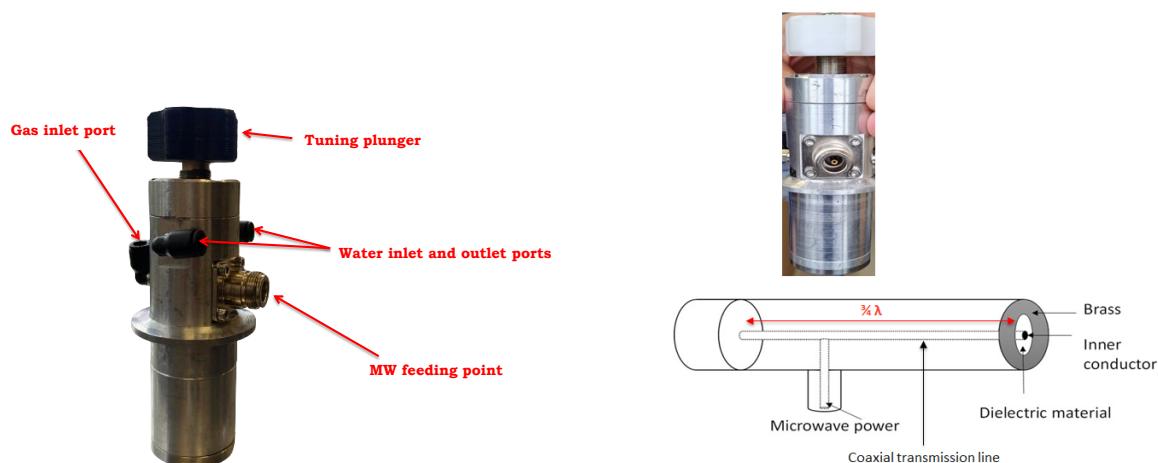


Figure 3.1: MW microplasma torch

3.3.1 Heating/biasing system

The first system allows polarizing or heating the substrate. The reactor is basically a six-way cross with five CF 100-flanges and one KF40-flange. The latter was used to connect the microplasma torch to the system. The collector holder was placed directly below the torch. It is composed of a sandwich of molybdenum disc, graphite heater, and an alumina cup. The temperature of the substrate was measured using a thermocouple located beneath the molybdenum disc. The ceramic cup was placed on a stainless steel tube. This design of the collector holder provided flexibility in the process by making it possible to heat and polarize the collector up to 500 °C and ± 1 kV, respectively. Moreover, the distance between the collector holder and the torch can be changed, which offers the possibility of investigating the evolution of the synthesized nanostructures as a function of the residence time in the reactive flow generated by the discharge. The collectors were made of silicon or fiberglass placed on a holder located downstream of the plasma torch. The plasma system is schematically illustrated in Figure 3.2. This shows the elements of the vacuum system (gauge, pump), the torch and a 200 W Sairem microwave generator at 2.45 GHz (GMP20). Unless otherwise specified, deposition experiments were performed using this reactor.

3.3.2 Substrate cooling system or cold finger

The second system allows cooling the substrate and studying lower temperature conditions that were not achievable with the first system. The reactor was basically a 6-way KF40 cross, one arm of which was dedicated to the microplasma torch. The particles are collected in a collector that is standing on a water-cooled holder, placed directly below the torch (Figure 3.3). The distance between the collector and the plasma torch is set to 1 cm in this configuration. The upper part of the collector holder is a conical nozzle that directs the gas discharge flow toward the substrate placed on the cold-copper-made heat exchanger. Cold water from a chiller flows into the heat exchanger, where it is introduced through liquid feed-through.

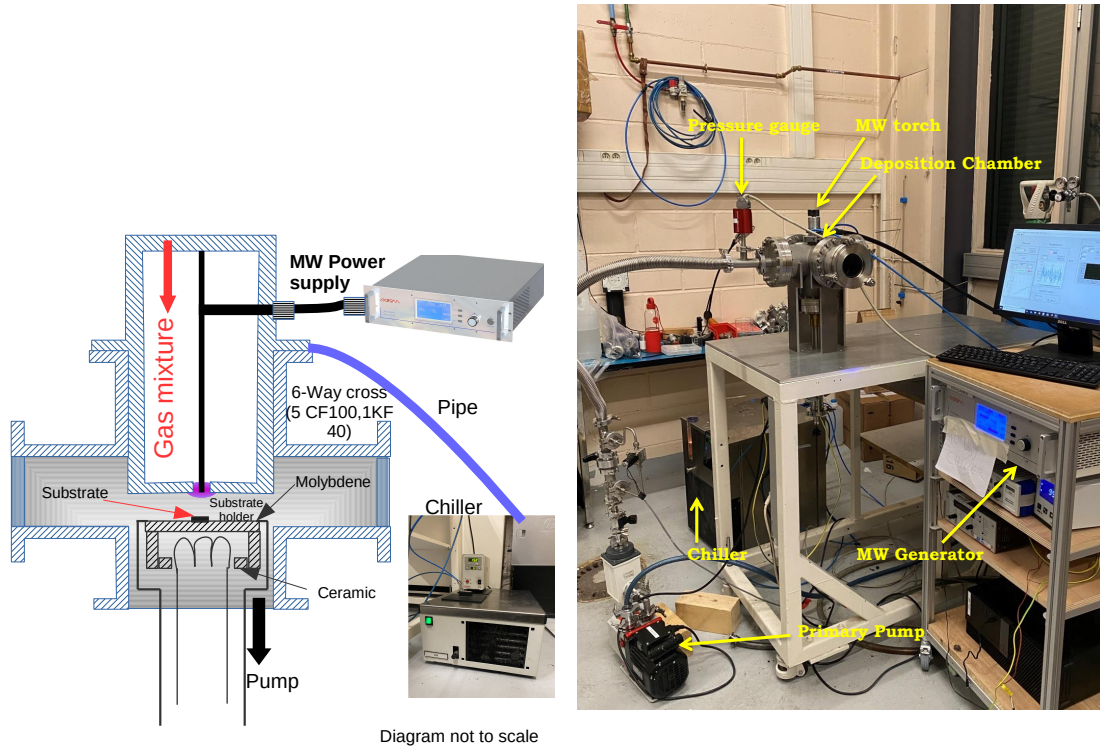


Figure 3.2: Experimental set-up for carbon particle deposition using the MW microplasma torch

3.4 Plasma diagnostics

Characterization of the plasma was conducted using optical emission spectrometry (OES) and TALIF (Two-Photon Absorption Laser Induced Fluorescence) diagnostics to determine different parameters as summarized in 3.1. The details of the instruments used are detailed below and the detailed methodology to determine the plasma parameters are described in Chapter 4.

Table 3.1: Parameters determined by OES and ps-TALIF

Measured Parameters	Method Used
T_g	OES: Rotational temperatures from G-Band and Fulcher α of H_2 ps-TALIF: Effective lifetime (τ_H) of two-photon laser-excited H-atom
n_e	Stark broadening of the H_β line
n_H	Actionmetry ps-TALIF

3.4.1 Optical emission spectroscopy (OES)

Optical Emission Spectroscopy (OES) is a widely used *in situ* diagnostic technique to characterize plasmas. It relies on studying the light emitted by different species in the plasma. The excited plasma states of atomic or molecular species undergo radiative deexcitation, generating a photon

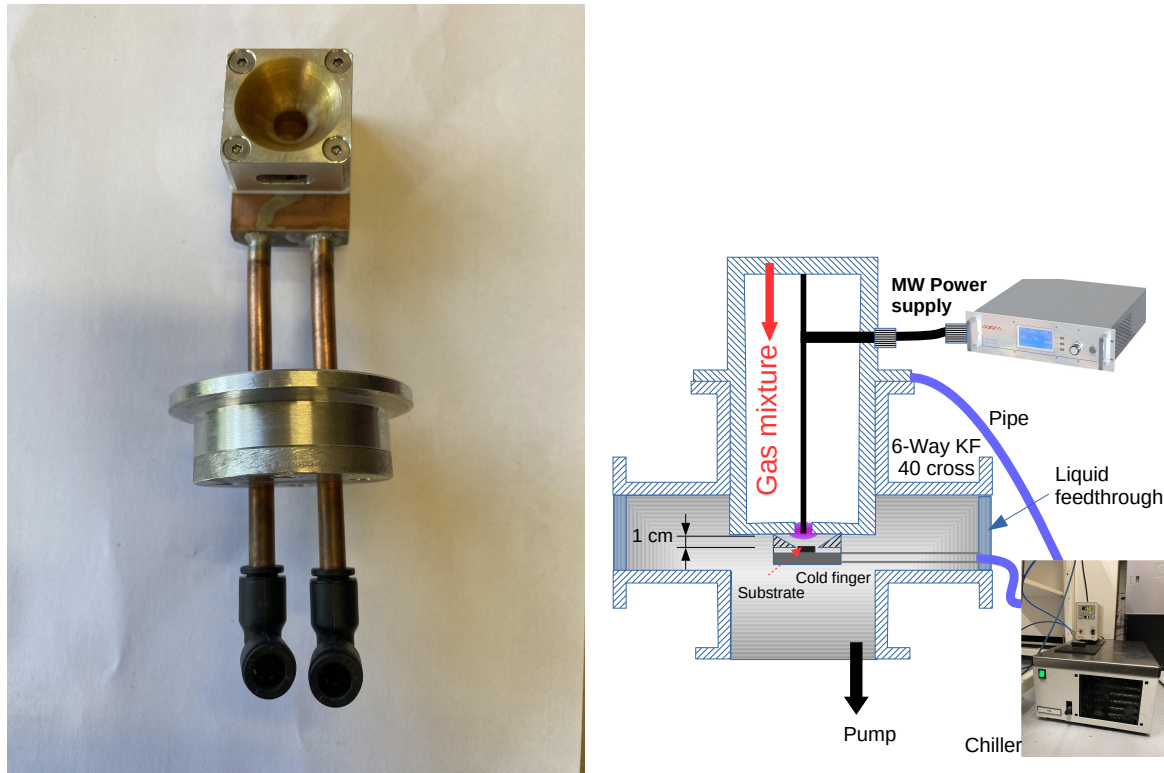


Figure 3.3: Experimental set-up of the deposition with substrate cooling system

with energy $h\nu$ (corresponding to a wavelength λ) according to the following process:



Correlating the emitted spectrum to the plasma parameters allows one to access the properties of the reactive medium¹⁷⁸.

The core of the OES is a monochromator or spectrometer coupled to a detector such as the photomultiplier tube (PMT) and charge-coupled device (CCD) camera. The light from the emitting source enters the spectrometer through an entrance slit and is guided through a system of collimating and focusing mirrors on to a dispersive element such as a prism or a grating. Holographic gratings are commonly used as the dispersive element, which is made up of closely spaced grooves. Each of these grooves diffracts light, creating an overall interference effect, and therefore disperses the incident light. The gratings are placed on a rotating stage that allows the detector to select the wavelength that exits the spectrometer and is recorded by the detector. The amount of light entering the spectrometer is controlled by the entrance slit. The spectral resolution of the spectrometer depends on the focal length of the focus mirrors, the angle of the blaze, the density of the gratings used, and the width of the slit. Spectral resolution increases with an increase in focal length and groove density and decreases with larger slit opening.

We used a 1m Jobin-Yvon THR 1000 spectrometer with a 1800 grooves per mm grating blazed at 250 nm and an angular dispersion of about 8 Å/mm. The spectral resolution of this spectrometer is around 0.03 nm using a 40 μm slit. This spectrometer is equipped with a Horiba DPM-HVH photomultiplier tube. This PMT shows high sensitivity over a large wavelength range, i.e., 190-800 nm. It is used with a high voltage power supply controlled by spectrAcq2

(data acquisition system). This provides a maximum voltage of 1.25 kV with a gain of about 10^5 that is suitable for detecting weak light signals.

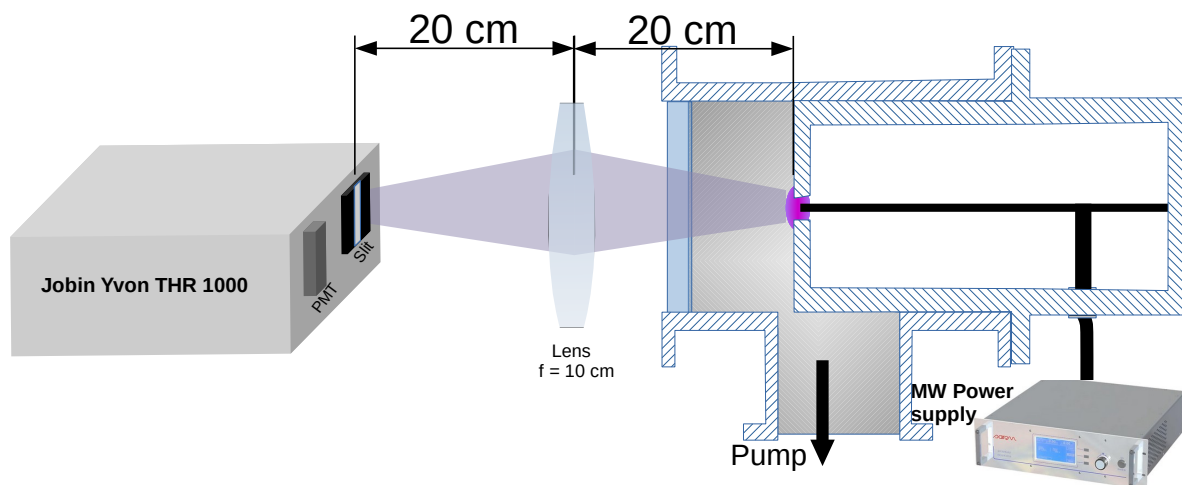


Figure 3.4: Schematic of the experimental setup for performing OES

The experimental setup used to perform the OES is depicted in Figure 3.4. The microplasma torch was placed on the longer arm of a KF-40 Tee with a borosilicate optical window on the opposite. The KF-40 tee was placed in an x-y linear stage so that the center of the microplasma was aligned with the vertical slit (1 cm high) of the spectrometer. 2f-arrangement was used to collect the emission signal, where a biconvex lens of 100 mm focal length biconvex lens was placed at an equal distance of 20 cm between the plasma and the slit of the spectrometer. This arrangement ensures that the emission from the entire radial section of the microplasma is captured by the spectrometer and the photomultiplier tube. As a result, the plasma quantities deduced from OES measurements correspond to radially averaged spectra and yield an overall characterization of the microplasma.

The spectral response of the spectrometer was determined using a tungsten lamp. The lamp was switched on and positioned to illuminate the spectrometer's detector uniformly. The resulting signal (shown in Figure 3.5) demonstrates the detector's sensitivity as a function of wavelength. We can see that the detector is sensitive from 350-850 nm. This range covers most of the emissions from the species analyzed in this thesis, and therefore guarantees high signal detection accuracy.

3.4.2 Two-photon Absorption Laser Induced Fluorescence (TALIF)

Details of the methodology are provided in Chapter 4 while the ps-laser and streak camera system are described here.

3.4.2.1 Principle

Two-photon absorption laser-induced fluorescence (TALIF) is an efficient method for measuring atomic densities in plasmas or flames. This technique is based on the excitation of a ground-state atom by absorption of two identical UV laser photons and the subsequent deexcitation of these

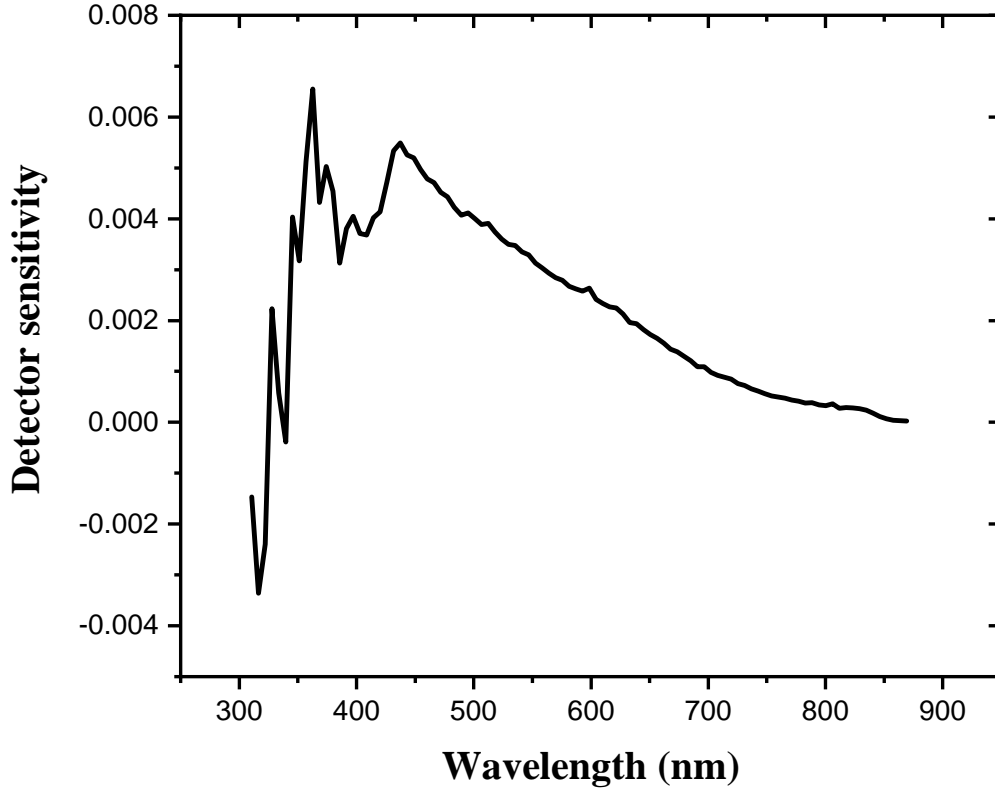


Figure 3.5: Spectral response of the 1-m spectrometer

laser-excited atoms, which results in a fluorescence signal that allows the measurement of ground-state atomic densities^{179,180}. Absolute density measurements for an atom are possible when using a calibration procedure in which TALIF measurements are carried out on a rare gas, such as krypton or xenon, with known densities. The scheme of TALIF with the H atom is shown in Figure 3.6. For atomic hydrogen, krypton (Kr) serves as a rare gas for calibration.

H-atoms TALIF scheme

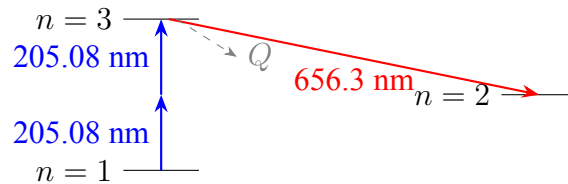


Figure 3.6: Scheme of H-atoms TALIF

Concerning the laser system, we used a ps-laser from EKSPLA®. It is composed of three distinct units that are : (i) a **Nd:YLF pump laser (PL3140)** that produces a fundamental laser beam at 1053 nm with a maximum output energy of 50 mJ and a pulse width of ≈ 10 ps, operating either in pulse train mode or at a fixed repetition rate of 5 Hz ; (ii) a **harmonic generator (APL2100)** designed to double (527 nm) and triple (351 nm) the fundamental frequency, with a

maximum output energy of 50 mJ and a pulse width of less than 15 ps ; (iii) and a **solid-state optical parametric generator (PG411)** that generates 10 ps-width laser pulses with a line-width of 17 pm (evaluated by the manufacturer) in the wavelength range 193-2300 nm. The maximum output energy of the pulse is 2 mJ and the repetition frequency is 5 Hz. As far as ps-TALIF on the H atom is concerned, the laser energy is 60 μJ /pulse for a wavelength around 205 nm (two-photon excitation wavelength of H).

The Nd:YLF pump laser (PL3140) serves as the primary light source for the entire system. This laser utilizes a YLF crystal as its active medium, which is doped with neodymium ions (Nd^{3+}). When this crystal is exposed to an energy source such as a flashlamp or laser diodes, the neodymium ions in the crystal get excited. The amplification process starts when these ions return to a lower-energy state, emitting photons. These photons then stimulate other excited neodymium ions to produce more photons in the same phase and direction. This process in turn increases the amount of light through stimulated emission. This results in a coherent laser beam at 1053 nm in the near-infrared range. This laser beam is directed to the **harmonic generator (APL2100)** unit to produce higher harmonic beams at 527 nm (second harmonic) and 351 nm (third harmonic). This device uses non-linear crystals, such as potassium dihydrogen phosphate (KDP) or beta barium borate (BBO) to convert the fundamental wavelength of 1053 nm into higher harmonics. The beam exiting the harmonic generator is diverted to the **solid-state optical parametric generator (PG411)** which combines the primary laser beam and its harmonics to produce a tunable output laser beam.

We used a streak camera (HAMAMATSU® C10910-05) as a detector to record the fluorescence signal. This camera has a high temporal resolution, enabling capturing both fast (nanosecond timescale) and ultrafast (ps timescale) events. The scanning camera is therefore particularly well suited to capturing the continuous temporal evolution of light signals with good temporal resolution (about 1 ps). Although efficient, it requires precise configuration and calibration to work properly. The operation process of the streak camera is illustrated in Figure 3.7. Light from the event enters through a slit before reaching a photocathode, which converts photons into electrons. These electrons are focused by lenses, accelerated and then deflected according to their emission time by scanning electrodes triggered by a signal. The result is a time-resolved image. The electrons are then amplified using a microchannel plate (MCP) and sent to a phosphorescent screen, generating a light signal that is captured and digitized by a CMOS camera (ORCA®-Flash4.0 V3 C13440-20CU). The final image shows light intensity as a function of time (x-axis) and space (y-axis).

3.4.2.2 Optical setup for TALIF

The experimental setup used in our TALIF experiments is shown in Figure 3.8, showing the ps-laser, the streak camera, and the reactor chamber housing the MW plasma source. At the two-photon excitation wavelength of the H-atom (205.08 nm), the ps laser system can generate pulses up to 60 μJ /pulse with a width of around 10 ps at a repetition frequency of 5 Hz. A fused-silica lens with a focal length of 500 mm was used to obtain a laser spot of 500 μm diameter in the center of the plasma chamber. The energy of the laser beam exiting the plasma chamber is

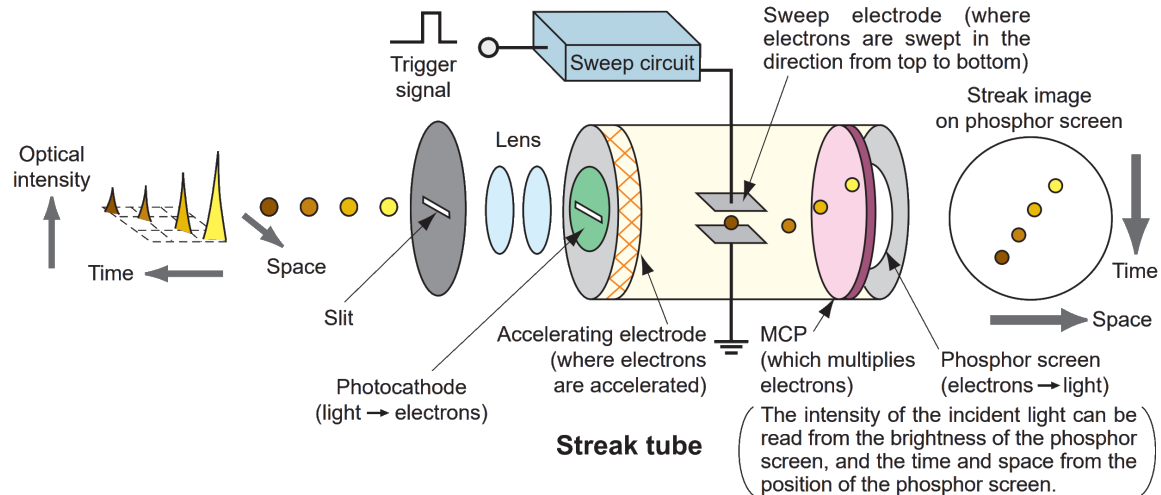


Figure 3.7: Diagram showing the path of a photon through the streak camera¹⁸¹

measured using a calorimeter (Coherent J-10MB-LE) connected to a digital oscilloscope. The energy of the laser was controlled using the internal amplification of the laser system and a combination of neutral-density filters. The fluorescence signal was collected in the perpendicular direction to the laser beam using an achromatic lens of 100 mm focal length and an appropriate bandpass filter mounted in front of the entrance slit of the streak camera.

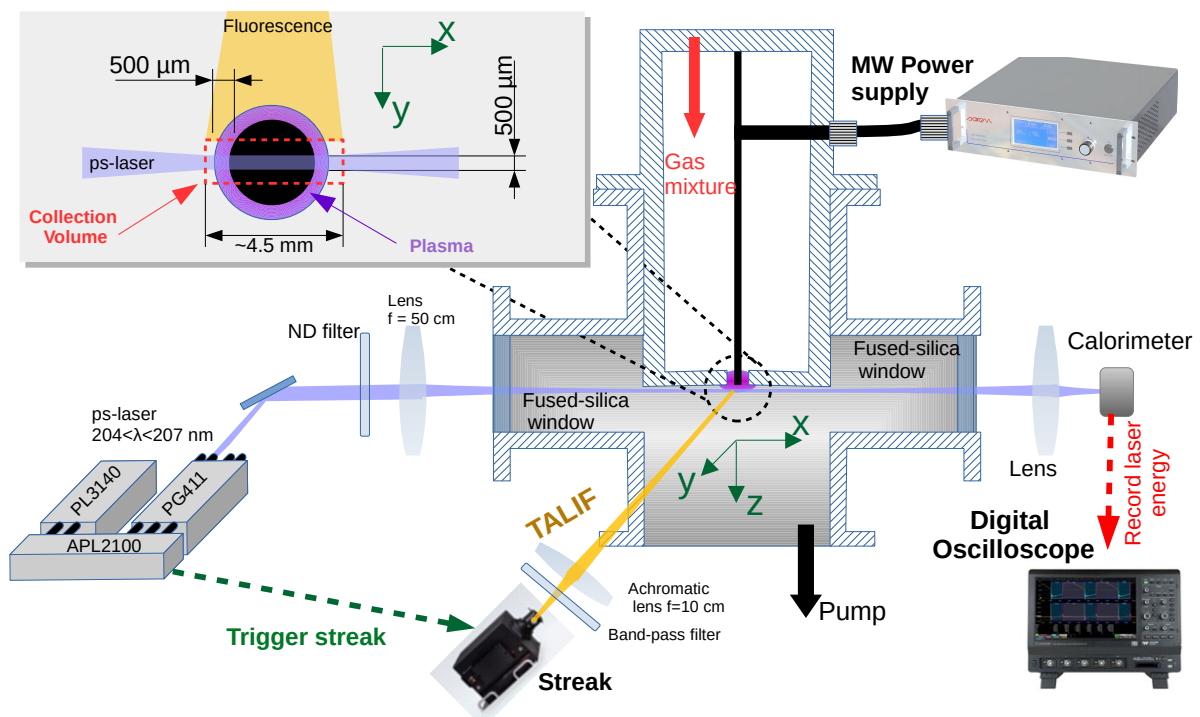


Figure 3.8: Schematic of the experimental setup showing the layout of MW plasma reactor, ps-laser and streak camera.

The microplasma torch was embedded into an octagonal vacuum chamber with three optical viewports dedicated to laser diagnostics. The UV-laser beam enters the chamber through a

first UV-transparent fused silica window, crosses the reactive flow generated by the plasma, where it induces two-photon excitation of the hydrogen atoms produced by dissociation, and then exits the chamber through the second fused silica window. The resulting fluorescence was collected through a borosilicate window. The reactor chamber was placed on a translation stage that allowed the plasma to be moved perpendicularly to the laser beam, cf. Figure 3.8, so as to investigate the radial variation of the atom density. The path of the laser was aligned with the x-axis of the reactor with focus close to the axis of the microplasma. Calibration of the z-axis was performed accurately using the laser calorimeter and the streak camera to identify the measurable region where the laser and the fluorescence signals are not affected by the torch wall. The plasma source was displaced with respect to the laser until the laser and the fluorescence signals remained constant on the calorimeter and the streak camera, respectively. This position was found to be 0.5 mm from the bottom surface of the torch and has been marked as the origin 0 for all future representations. The scope of this study is restricted to the following gas mixtures: pure H_2 , H_2/CH_4 and $H_2/CH_4/Ar$ system.

3.5 Material characterization technique

Given the wide range of carbon structures synthesized in this work, a thorough characterization is required to determine their composition, structure, and properties. Therefore, for the characterization of these materials, we made use of several complementary techniques, as summarized in Table 3.2 and will be described in the following sections.

Table 3.2: Types of information obtained from material characterization techniques.

Characterization Technique	Types of Information
Raman	Qualitative information on carbon nanoparticles produced (diamond, graphite and amorphous carbon), analysis of molecular structure, identification of chemical bonds (sp^2 and sp^3), identification of crystalline phases and detection of impurities.
XPS	Surface chemical composition, oxidation states of elements, and chemical bonding analysis in the near-surface region (approximately 5–10 nm).
AFM	Surface topography at nanometer scale, measurement of particle size distribution of synthesized nanocarbons, and detection of surface defects.
SEM	Observation of surface morphology of the particles.
TEM	Analysis of crystalline structure of nanoparticles, particle size distribution, and study of crystal defects.

3.5.1 Raman spectroscopy

3.5.1.1 Principle

One of the most commonly used techniques for characterizing materials in general, and carbonaceous materials in particular, is Raman scattering spectroscopy. This technique probes matter and reveals its structure on a molecular scale by analyzing the vibrational modes of different chemical bonds^{1,3}. The technique is based on the fact that when the analyzed material is excited by a monochromatic wave of frequency ν_0 , two types of scattering can occur: elastic scattering when the material re-emits photons with the same frequency ν_0 , known as Rayleigh scattering, and inelastic scattering when the material re-emits photons with a different frequency; this is Raman scattering. This energy transfer between the photon and the material can occur in both directions, since the material can either receive or lose energy during the inelastic scattering process. A Raman spectrum thus consists of two symmetric lines or bands with respect to the laser excitation frequency called Stokes and anti-Stokes scattering, depending on the direction of the exchange. Figure 3.9 illustrates these different scattering phenomena.

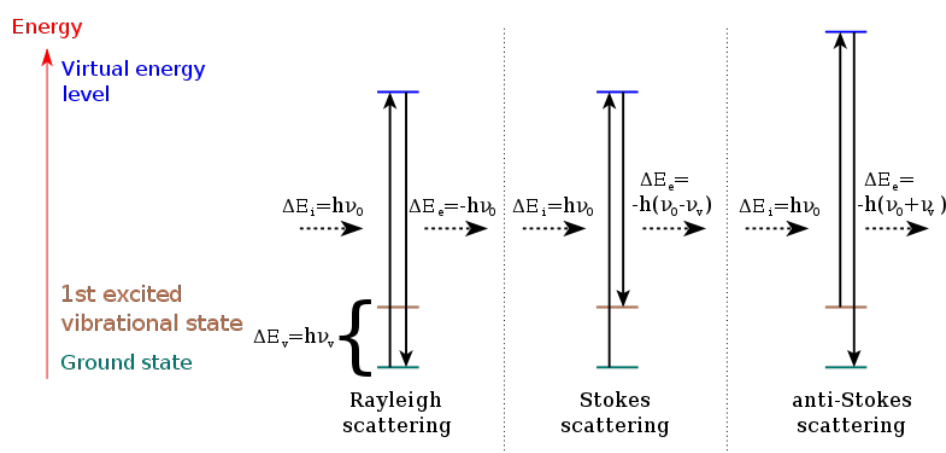


Figure 3.9: Representation of the different light scattering phenomena including Raman scattering¹⁸²

In a Raman spectrum, typically, Stokes lines dominate below and at room temperature because anti-Stokes transitions require populating higher excited states that need to be excited thermally. Spectra are established by indicating the Raman shift in wave numbers of the scattered photons compared to the photons from Rayleigh scattering, which have the same frequency as the excitation wavelength.

$$\nu(\text{cm}^{-1}) = \frac{1}{\lambda_{\text{Rayleigh}}} - \frac{1}{\lambda_{\text{Stokes}}} \quad (3.1)$$

3.5.1.2 Instrumentation

HR-800 Raman spectrometer commercialized by Jobin Yvon (Figure 3.10) has been used. It is equipped with a motorized X-Y stage for Raman imaging of an entire sample. The device has

a confocal system with an adjustable aperture slit. A multiobjective microanalysis apparatus (x10, x20, x40, x100 and x100 LWD (for "Long Working Distance")) combined with a CCD detector cooled by a Peltier device at -70°C allows high sensitivity and flexible use. Depending on the type of analysis performed, the dispersion of the scattered beam can be achieved by different gratings (300, 1800, and 2400 grooves/mm). To obtain the best spectral resolution ($\approx 1\text{ cm}^{-1}$), only the 2400 grooves/mm grating was used. The acquisition and processing of spectra is carried out using Labspec 5 software. Several sources at different wavelengths are available: a Helium/Neon laser emitting at 632.8 nm and a solid-state laser (Coboltblue™) providing a light beam at 473 nm. The intensity of Raman scattering is proportional to λ^{-4} of the excitation wavelength^{183,184}. Consequently, excitation at short wavelengths (e.g. visible or UV) generates strong Raman signals, while excitation at longer wavelengths (infrared) reduces the Raman signal by a factor of 15 or more¹⁸⁴. Hence, the choice of the visible blue laser (473 nm) for our analyses.

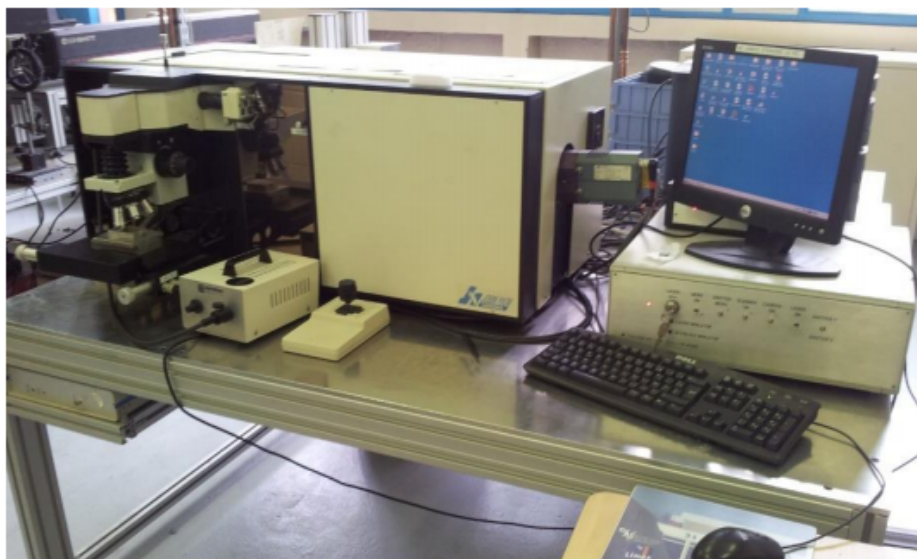
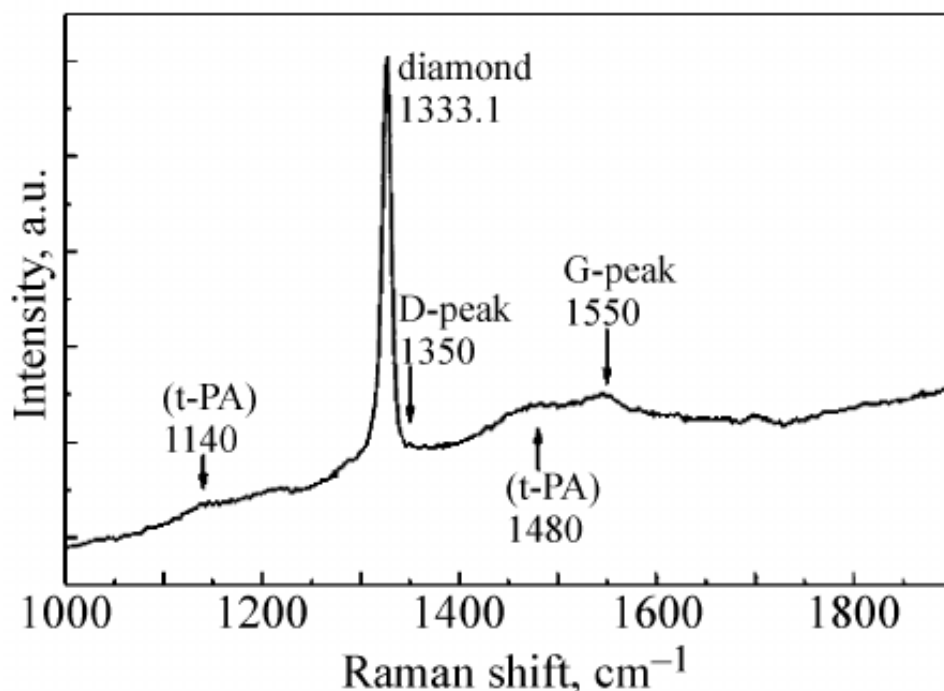


Figure 3.10: HR-800 spectrometer at LSPM was used for characterizing the carbon nanostructures

The Raman peaks illustrated in figure 3.11 are the most frequently observed and considered in this thesis. The peaks correspond to diamond, graphite, and transpolyacetylene (TPA), and contain further information on the composition and structural characteristics of the material. The characteristic peak at 1332 cm^{-1} ^{185–187} represents the diamond peak and indicates the presence of diamond crystallites in a sample. The presence of the graphite phase is associated with two characteristic peaks, the G band ranging $1540\text{--}1600\text{ cm}^{-1}$ and the D band (1350 cm^{-1})^{188–190}. The G band, indicative of sp^2 hybridized carbon atoms sp^2 typically in graphitic structures, arises from the E_{2g} vibration mode, associated with the stretching vibrations of sp^2 carbon pairs^{188–191}. Meanwhile, the D band, linked to structural defects and disorder, corresponds to the A_{1g} vibrational mode, involving phonons near the boundary of the Brillouin zone, with "D" symbolizing "Disordered"^{190–192}. In addition, TPA also refers to sp^2 phase and is identified by peaks at 1180 cm^{-1} and 1480 cm^{-1} , characteristic of its chain-like structure^{193–195}.

Figure 3.11: Typical Raman peaks considered¹⁹⁶

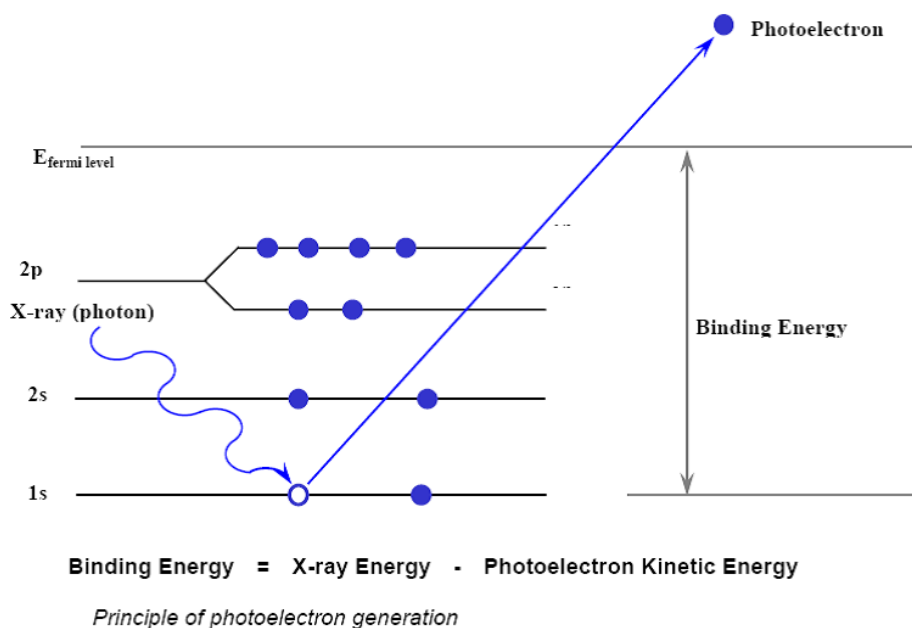
3.5.2 X-ray Photoelectron Spectroscopy

3.5.2.1 Principle

XPS is based on the interaction of a sample with a monochromatic X-ray beam. The sample is subjected to high-energy X-ray photons that strip the electrons from the inner layers (core) of the sample atoms on the surface, generating photoelectrons. The energy conservation during this interaction is expressed by the Einstein relation (Equation 3.2) and schematically illustrated in the energy diagram in Figure 3.12.

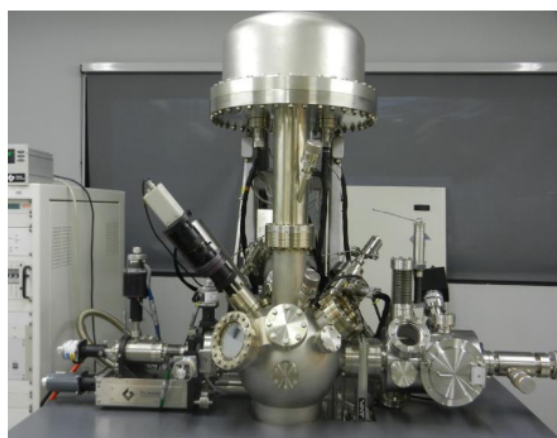
$$h\nu = E_{\text{kin}} + E_{\text{b}} \quad (3.2)$$

where ν is the frequency of the monochromatic X-ray beam, E_{kin} represents the energy (kinetic energy) of the emitted photoelectron while E_{b} is the energy of the initial (bound) state of the electron (binding energy). Measuring the kinetic energy of the emitted photoelectrons allows us to obtain information on the binding energy that is a characteristic physical quantity of the emitter atoms along with its chemical bonds with the surrounding atoms, i.e., chemical environment. The depth of the probed region of the sample depends on the mean free path of the photoelectrons in the material. It generally ranges between 1 and 12 nm. Therefore, XPS enables (i) identifying the nature of the surface atoms (except for H and He, which lack detectable core electrons in XPS), (ii) determining the chemical bonds where they are involved through the chemical shift (which reveals the nature of their neighbors), and (iii) evaluating their concentration, thus providing the surface chemical composition of the probed material.

Figure 3.12: Principle of photoelectron generation¹⁹⁷

3.5.2.2 Instrumentation

XPS measurements carried out in this thesis were performed in the ITODYS laboratory. The system used has an X-ray source (Al $K\alpha$, 1486.6 eV) with a double monochromator. The diameter of the X-ray source is variable from 120 to 650 μm (Figure 3.13). It also has a high-resolution hemispherical analyzer with a magnetic lens and a dual charge compensation system (slow electron gun and argon ions) to neutralize surface charging. Ion etching, performed using a monoatomic argon ion gun, allows access to subsurface layers for depth profiling. Data processing was performed using Advantage software.

Figure 3.13: High-resolution XPS analysis system at ITODYS laboratory¹⁹⁸

The concentrations, in atomic percentage of the different elements, in the probed region of the samples were inferred from the peak area using the equation 3.3. No spectral calibration was performed and the sensitivity factor values provided by the manufacturer were used.

$$\%A = \frac{\frac{I_A}{S_A}}{\sum_i \frac{I_i}{S_i}} \times 100\% \quad (3.3)$$

3.5.3 Atomic force microscopy

3.5.3.1 Principle

AFM is a local probe microscopy method for examining the surface topology. Using a scanning probe, AFM enables point-by-point surface analysis¹⁹⁹. The technique relies on an extremely fine tip at the end of a flexible micro-lever (cantilever). This type of microscopy works by evaluating the attractive or repulsive interaction between the atoms that make up the nanometric tip and the surface atoms of a sample. When the tip is close to a surface, the interaction forces between the tip and the sample deflect the lever according to Hooke's law. Using a laser to analyze the deflection of the lever, we can simultaneously identify the precise path of the tip and evaluate the interactions forces between the tip and the sample (Figure 3.14).

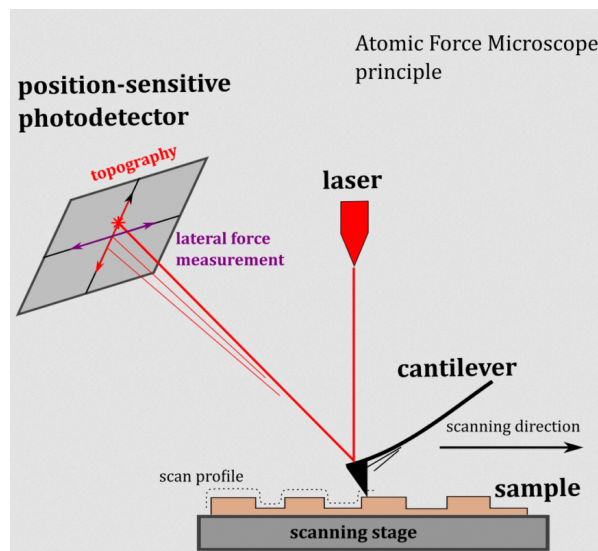


Figure 3.14: The main components of an atomic force microscope²⁰⁰

3.5.3.2 Instrumentation

In this study, samples were examined by a BRUKER AFM/STM apparatus working in semi-contact mode (see Figure 3.15). Acquisition parameters were chosen to ensure reliable data collection, that is, the feedback gain was set to 1.000 in order to identify surface changes, and magnification of 0.116 allowed for a reasonable field of view without compromising the resolution. The Set point was fixed at 10.000 to ensure optimal tip-sample interaction force, and the voltage used was 0 V to avoid electrical interference on the sample during scanning. The recorded deflection signal (DFL) was -0.28, which indicates the interaction between the tip and sample during the scan, and the lateral force (LF) was recorded -0.01, which indicates the deformation of the cantilever. The laser was set at 18.23 so that the cantilever deflection

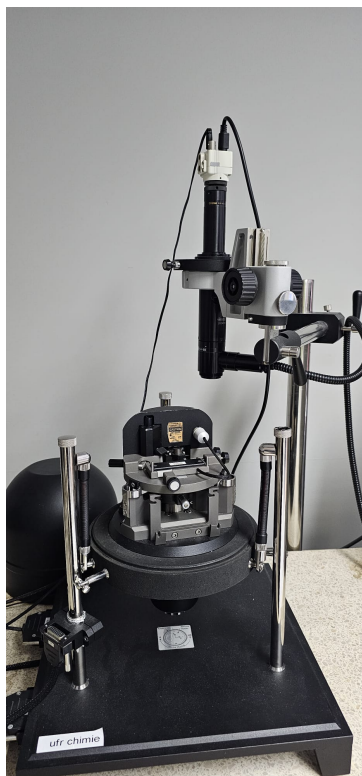


Figure 3.15: AFM instrument

could be accurately measured. Data were taken using Nova 1.1.0.1780 software, which made it possible to study surface features at the nanoscale.

3.5.4 Scanning Electron Microscopy

3.5.4.1 Principle

In a Scanning Electron Microscopy experiment an electron beam interacts with the surface of the sample. This interaction produces different types of emission (Figure 3.16) such as secondary electrons, backscattered electrons, and photons (X-rays)²⁰¹. Secondary electrons (SE) provide information on the topography of the sample, enabling an image of its surface to be obtained. Backscattered electrons provide chemical contrast on a flat surface and crystallographic information. The use of X-ray photons provides access to the chemical composition using Energy Dispersive Spectroscopy (EDS). In our study, we used only SEM imaging using secondary electrons.

3.5.4.2 Instrumentation

LSPM is equipped with a ZEISS SUPRA™ 40 SEM-FEG (cf. Figure 3.17), designed for the observation and analysis of materials. It uses a GEMINI® FESEM column to provide high-resolution images while reducing magnetic interference. The electron beam is generated from a Schottky-type tungsten tip with a ZrO coating, accelerating electrons at voltages between 0.1 and 30 kV, with a magnification range of 12X to 900,000X, allowing both low- and high-

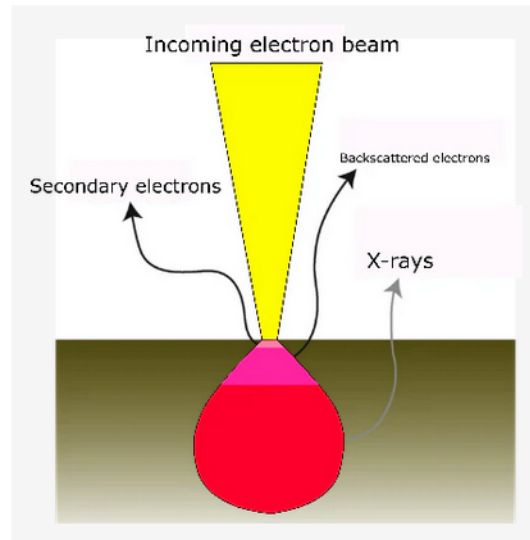


Figure 3.16: Different types of emissions produced by SEM²⁰²

magnification observations. The probe current can range from 4 pA to 10 nA. It also provides a flexible working distance from 1 to 50 mm depending on the operating conditions. The instrument also includes variable pressure mode (2–133 Pa) for nonconductive samples to neutralize surface charges and prevent damage while providing high-quality images of sensitive materials. This SEM uses a field-emission cathode to improve precision and avoid complications with fragile samples. The integrated X-Act system enables elemental composition analysis and elemental mapping. During our measurements, the nominal resolution reached 1.5 nm at 10 kV with a working distance of 2 mm.

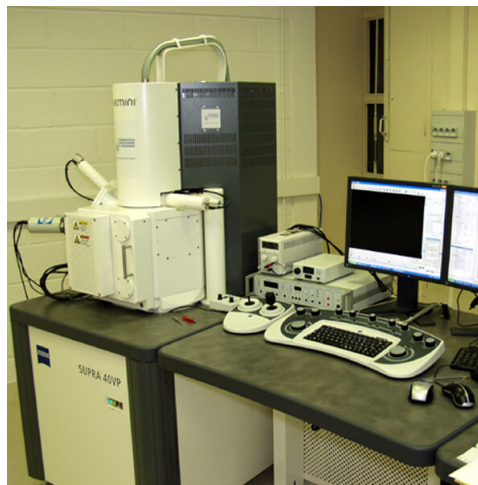


Figure 3.17: SEM instrument

3.5.5 Transmission Electron Microscopy

3.5.5.1 Principle

In TEM, the electron plays a similar role to that of the photon in an optical microscope, and the technique operates on the same basic principles (cf. Figure 3.18). An electron source (such as a tungsten filament or a lanthanum hexaboride crystal) is heated to emit electrons²⁰³. These electrons are then accelerated by a high voltage (from 200 to 1000 kV), giving them a very short wavelength, approximately one picometer. This short wavelength enables the TEM to achieve high resolution. However, the actual resolution of the TEM is ultimately limited to subnanometer scales because of aberrations in the magnetic lenses used to focus the electron beam. After setting up the secondary vacuum, we operate the electron beam that passes through a very thin sample, typically less than 20 nanometers thick. Magnetic lenses are then used to direct the electron beam onto a detection screen or photographic plate. Because of its ability to resolve distances on the scale of atomic spacings, TEM is ideally suited for analyzing the atomic structure, allowing observation of their internal crystalline structure and any defects present.

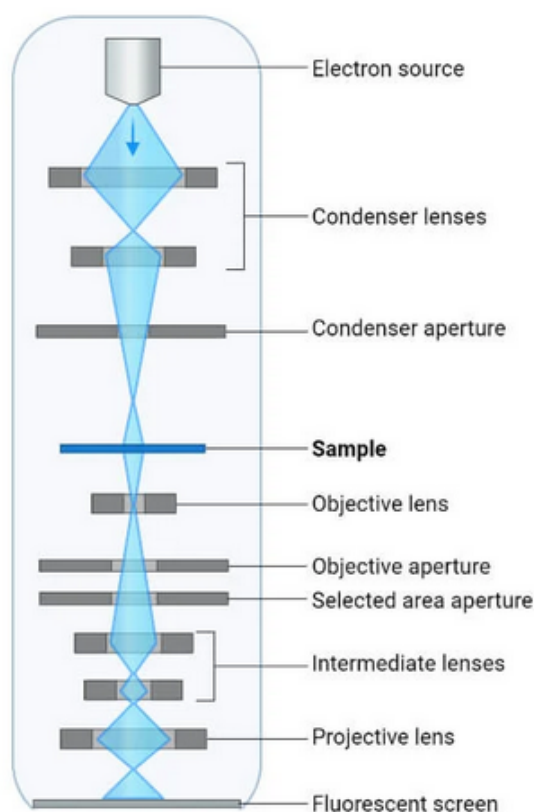


Figure 3.18: Schematic flow diagram of a transmission electron microscope²⁰⁴

3.5.5.2 Different operating modes

Transmission electron microscopy can be used in different ways: **in image mode**, **in diffraction mode** and **in high-resolution mode**^{203,205,206}.

- (i) **In image mode**, electrons move through the sample. Electron absorption varies according to the thickness, density, or local chemical nature of the sample. When the detector is placed in the image plane (photographic plate), a magnified image of the area exposed to the electron beam can be observed. In biology, it is used mainly to observe cells or other microorganisms.
- (ii) **In diffraction mode**, the wave-like nature of the electrons is utilized. According to De Broglie's theory proposed in 1924, all matter exhibits wave properties. Thus, electrons can behave like waves. When these electron waves interact with a crystalline sample, diffraction occurs: The waves are scattered and the directions of the diffracted waves depend on the atomic arrangement within the crystal. A diffraction pattern is obtained by collecting the diffracted beams on a detector placed at the focal plane, which provides information about the atomic organization and orientation of the crystals. This mode has been used to study the crystalline quality of synthesized nanodiamonds.
- (iii) **In high-resolution mode (HRTEM)**, the contrast is generated by the interaction between the electron beam and the atomic potentials of the sample, enabling us to see features at the atomic scale. An interference pattern is produced by the interaction of the transmitted electron beam (passing directly through the sample) with the diffracted beams. This pattern shows the arrangement of the atomic columns as white or black dots (or both) in the image. These dots aren't just a straightforward picture of the atoms but are the result of complex interference between electron waves, which hold information on the atomic structure. Once the image is processed, this mode provides information on the crystalline structure, grain boundaries, dislocations, and various defects.

3.5.5.3 Instrumentation

LSPM is equipped with a MET 200 kV JOEL JEM 2011, designed for high-resolution imaging and analysis (c.f. 3.19). It operates within an accelerating voltage range of 80-200 kV and achieves a resolution of 0.14 nm. The magnification ranges from 50x to 1,500,000x. The microscope is equipped with a Schottky-type field emission gun and includes systems for filtered imaging using a Gatan Imaging Filter (GIF) and beam scanning via Scanning Transmission Electron Microscopy (STEM). It features two digital cameras with 1000x1000 resolution: one placed at the wide-angle port for low-magnification observations and diffraction pattern indexing, and the other positioned at the GIF filter output for high-resolution imaging. Analytical capabilities include Energy Dispersive X-ray Spectroscopy (EDS) for elemental analysis at the nanometer scale. The instrument supports various specimen holders (e.g., single-tilt, rotation-tilt, heating) and sample preparation techniques such as electrochemical polishing (STRUERS TENUPOLE III) and ion thinning (GATAN PIPS).

In our study, two techniques were used to analyze the particles by TEM. The first involved sonicating the nanoparticles (deposited on the silicon substrate) in an isopropyl alcohol solution in an ultrasonification bath. The resulting colloidal solution was then drop-casted onto TEM grids for analysis. The second method consisted of depositing the nanoparticles directly onto the TEM grids (placed on the silicon substrate) during a 5-min deposition period. The deposition



Figure 3.19: TEM Instrument

took place in the chamber described in section 3.3.1. The TEM grids containing the nanoparticles were then analyzed without further processing.

Chapter 4

Characterization of MW torch

Contents

4.1	Introduction	57
4.2	Working principle of the MW torch	58
4.3	MW-plasma coupling and electrical characterization of plasma	61
4.4	Gas temperature (T_g) measurement from OES	65
4.4.1	Gas temperature from rotational distribution of molecule	65
4.4.2	Methodology used	67
4.4.3	Results	68
4.5	Measurement of electron density n_e	69
4.5.1	Principle	69
4.5.2	Plasma parameters	72
4.6	Measurement of atomic Hydrogen density	76
4.6.1	Measurement of atomic Hydrogen density by actinometry	76
4.6.2	Measurement of H-atom density using ps-TALIF	77
4.6.3	Data post-processing	78
4.6.4	Results	79
4.7	Gas temperature measurement from ps-TALIF	80
4.7.1	Analysis of propagation of errors	81
4.7.2	Validation of the novel proposed approach	83
4.7.3	Spatial distribution of T_g and n_H	84
4.8	Conclusion	86

4.1 Introduction

This chapter focuses on the characterization of the developed MW-microplasma torch. This characterization has been performed mainly in pure hydrogen at pressures between 50 and 125

mbar. The chapter is divided into different sections. We start the chapter by discussing the working principle of the MW torch as well as its electrical characterization and MW-plasma coupling. This is followed by optical diagnostics of the microplasma using OES and ps-TALIF, as summarized in Table 3.1. OES was used to determine the gas temperature, derived from the rotational temperature of electronically excited H_2 states; the electron density, determined from the Stark broadening of the H_β line; and the atomic hydrogen density, measured using actinometry. The next section is then devoted to the optical diagnostic using advanced ps-TALIF. This technique was used here to measure the absolute density of atomic hydrogen. To conclude this chapter, still using ps-TALIF, we developed a novel technique to retrieve gas temperatures from the effective lifetime τ_H of species excited by ps laser. Therefore, this advanced ps-TALIF diagnostic allows for simultaneous measurements of absolute atom densities and gas temperature in moderate-pressure reactive plasmas.

4.2 Working principle of the MW torch

The design principle of our MW-torch is based on the creation of resonance at the open end of the coaxial transmission line that results in an electromagnetic field that is strong enough to induce gas breakdown and to sustain a high-density microplasma⁹⁸. Before discussing the design of the torch, it is worth understanding the physics of MW plasma coupling. The electromagnetic coupling structure is basically a coaxial waveguide, where a transverse electric magnetic (TEM) MW mode is propagated. In this mode, the axial components, i.e., the component along the propagation direction, of the electric and magnetic fields are zero, i.e. $\mathbf{E}_z = \mathbf{H}_z = 0$. The boundary conditions at the metallic surfaces of the coaxial waveguide impose that the tangential component of the electric field and the normal component of the magnetic field vanish at the boundaries, i.e. $\mathbf{E}_\phi = 0$ and $\mathbf{H}_r = 0$ at the metallic wall boundary. Consequently, the high-frequency electric field is purely radial (\mathbf{E}_r), while the magnetic field is purely azimuthal (\mathbf{H}_ϕ). The Maxwell equations applied to the EM waves of the form $\mathbf{E}_r = E_r \exp[j(\omega t - kz)]$ propagating through the coaxial structures containing plasma can be written as follows:

$$\begin{aligned} \frac{\partial \mathbf{E}_r}{\partial z} &= j\mu_0\omega\mathbf{H}_\phi, \\ \frac{\partial \mathbf{H}_\phi}{\partial z} &= j\epsilon_0\omega\mathbf{E}_r + \mathbf{J}_r, \end{aligned} \quad (4.1)$$

where \mathbf{J}_r is the high frequency (HF) component of the current density in the plasma. This determines the coupling between the electromagnetic waves and the plasma. The high frequency electrical current of the plasma is ensured by the high mobility electrons that are able to follow the applied HF electromagnetic field. Therefore, \mathbf{J}_r is proportional to the HF component of the drift velocity of electrons $\mathbf{v}_{e,r}$ through $\mathbf{J}_r = q_en_e\mathbf{v}_{e,r}$, q_e and n_e being the electron charge and density. Electron oscillations under the action of the HF EM-field are, however, damped because of the frequent collisions it undergoes with the heavy species. As a result, the electron dynamics is determined by the balance between the electrostatic force and the collisional damping by using the following high-frequency momentum balance equation.

$$(j\omega + \nu_m) \mathbf{v}_{e,r} = -\frac{q_e}{m_e} \mathbf{E}_r, \quad (4.2)$$

where ν_m is the collision frequency of electron momentum transfer and m_e is the mass of the electron. ν_m depends on the collision cross section of momentum transfer, the electron energy distribution function of the electrons, and the density of the heavy species. From equation 4.2, one obtains the following expression for the current density of the HF as a function of the electric field of the HF :

$$\mathbf{J}_r = \frac{\epsilon_0 \omega_p^2}{\nu_m^2 + \omega^2} (\nu_m - j\omega) \mathbf{E}_r, \quad (4.3)$$

where $\omega_p = (q_e^2 n_e / \epsilon_0 m_e)^{1/2} = 56.400 \sqrt{n_e} (m^{-3})$ is the plasma frequency. Combining equations 4.1 and 4.3 and eliminating \mathbf{H}_ϕ , the propagation of EM in the coaxial structure containing plasma reduces to a Hemholtz equation for \mathbf{E}_r of the form

$$\frac{\partial^2 \mathbf{E}_r}{\partial z^2} + \epsilon_0 \mu_0 \omega^2 \epsilon_p \mathbf{E}_r = 0. \quad (4.4)$$

Equation 4.4 can be solved by imposing a short circuit ($E_r = 0$) at one end and plasma conditions at the other end. The relative dielectric permittivity of the plasma ϵ_p given by

$$\epsilon_p = \epsilon'_p - j\epsilon''_p = 1 - \frac{\omega_p^2}{\nu_m^2 + \omega^2} - j \frac{\nu_m}{\omega} \frac{\omega_p^2}{\nu_m^2 + \omega^2}, \quad (4.5)$$

with $\epsilon_p = 1$ throughout the length of the coaxial waveguide. The real part of the dielectric permittivity ϵ'_p of the plasma is related to the propagation of the MW and one can conclude that $\frac{\omega_p^2}{\nu_m^2 + \omega^2} < 1$ is a necessary condition for the propagation of the MW. In fact, plasma behaves like a high-pass filter. This means that when an electromagnetic wave of frequency ω is incident on a plasma medium such that $\omega < \omega_p$, the wave would be reflected. However, in the context of the micrometric size of the microplasma torch, the MW would penetrate the plasma up to the skin depth given by the following relation :

$$\delta = \frac{c}{\omega_p}. \quad (4.6)$$

The MW that penetrates the plasma causes heating of electrons, which themselves undergo inelastic collisions with heavy species leading to ionization, excitation, and dissociation and sustain the discharge. The MW power absorbed P_{abs} by the electrons is $|\mathbf{J} \cdot \mathbf{E}|$ and can be expressed in terms of the imaginary part of the permittivity ϵ''_p as follows

$$P_{abs} = \frac{1}{2} \omega \epsilon''_p |\mathbf{E}_r|^2 = \frac{1}{2} \frac{q_e^2 n_e}{\epsilon_0 m_e} \frac{\nu_m}{\nu_m^2 + \omega^2} |\mathbf{E}_r|^2. \quad (4.7)$$

The energy transfer from the EM waves to the plasma is maximum when $\nu_m = \omega$. Accounting for the inelastic collision between the heavy species and the electrons, one can also express the energy transfer from electrons to heavy species as follows

$$P_{abs} = n_e \sum_i K_i(T_e) n_i E_i, \quad (4.8)$$

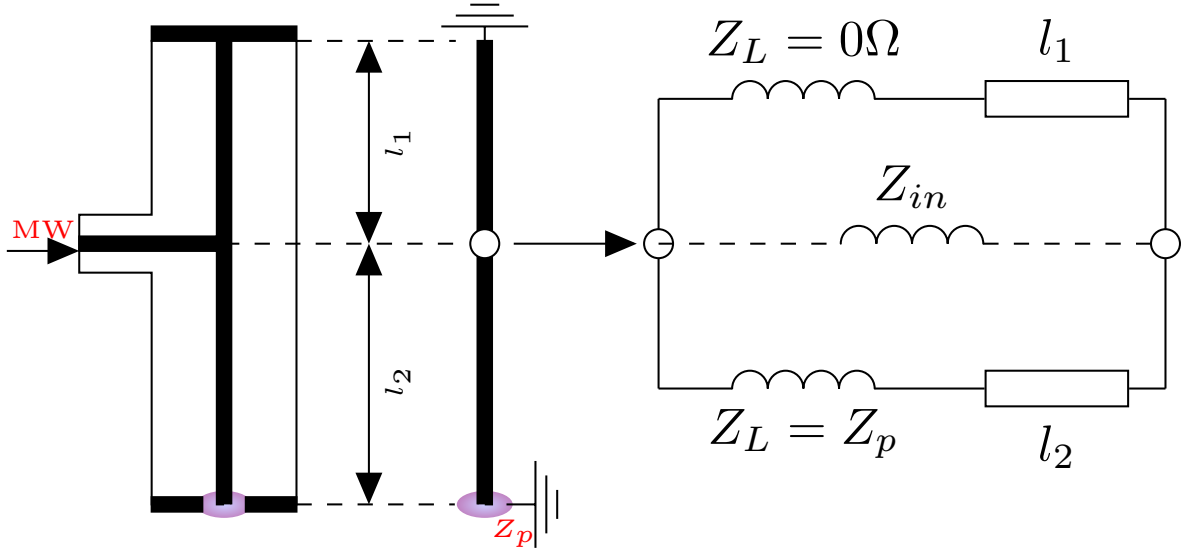


Figure 4.1: Design of MW-torch and its equivalent circuit

where K_i and E_i being the corresponding reaction rate and activation energy of the electron impact reaction with the heavy species of density n_i . Therefore, it is necessary to achieve sufficient EM energy in order to sustain ionization and hence the plasma. Consequently, the balance between the electron impact collisions, K_i as well as ν_m would influence the electron energy distribution function (eedf) and hence the electron temperature T_e .

The design of the torch itself relies on the propagation of the MW in the coaxial elements of the torch with the MW power dissipated at the open resonating end. To simplify the initial design, the plasma can be assumed to be homogeneous between the coaxial structure of the torch. This allows for the design of the coaxial circuit using a lossy transmission line approach. The schematic of the torch, along with its equivalent MW circuit, is shown in Figure 4.1. The amplification of the electric field at the open resonating end of the torch is ensured by maintaining a small gap distance of $500 \mu m$ between the grounded outer circular head and the central pin. The other end of the torch is a movable short-circuit stub that allows for fine-tuning the operation of the plasma torch. MW is injected into the torch with a N-type connector at a distance l_1 and l_2 from the short-circuit end and the open-circuit end of the coaxial waveguide, respectively. From an operational point of view, the position of the MW feeding is critical in order to achieve optimal coupling between the MW and the plasma.

The equivalent MW circuit consists of two parallel impedances, represented by the two arms of length l_1 and l_2 with impedances of Z_{l_1} and Z_{l_2} respectively. It is clear from the diagram that the loads at the end of the two transmission lines are 0 i.e., short circuit and plasma load Z_p , respectively. From transmission line theory, the impedance of a transmission line of length l having a load Z_L at its end is given by²⁰⁷

$$Z_l = Z_0 \frac{Z_L + Z_0 j \tan kl}{Z_0 + Z_L j \tan kl}. \quad (4.9)$$

Z_0 being the characteristic impedance of the transmission line, which is 50Ω in the present case.

Therefore, the input impedance of the device Z_{in} is

$$Z_{in} = \left\{ \frac{1}{Z_{l_1}} + \frac{1}{Z_{l_2}} \right\}^{-1} = Z_0 \left\{ \frac{1}{\tanh(jkl_1)} + \frac{Z_0 + Z_p \tan(jk(l - l_1))}{Z_p + Z_0 \tan(jk(l - l_1))} \right\}^{-1}, \quad (4.10)$$

where k is the wave number and Z_p is the wave impedance at the open end of the torch. The first major design criterion is to have a resonance at the open end of the torch to ignite the plasma. The other major criterion requires the input impedance at the feeding position of MW $Z_{in} = Z_0 = 50 \, \Omega$ under no plasma conditions to minimize the reflection of the injected MW. This means that the input impedance can be controlled by controlling l_1 and in the present case is achieved by the movable short-circuit stub. In the absence of plasma, the open end acts like a resistor with infinite impedance, i.e. $Z_p = \infty$. Substituting the same in equation 4.10, one obtains

$$\tan\left(\frac{2\pi}{\lambda}l_1\right) \tan\left(\frac{2\pi}{\lambda}l_2\right) = 1. \quad (4.11)$$

To meet these conditions, the total length of the torch $l = l_1 + l_2$, i.e. the distance between the open and short-circuited ends, has to be odd multiples of quarter wavelength

$$l = l_1 + l_2 = (2n - 1) \frac{\lambda}{4}. \quad (4.12)$$

Thus, the length l of the present torch has been fixed at $\frac{3}{4} \lambda$ i.e. $\sim 92 \, mm$ to have resonance at excitation frequency around $f=2.45 \, GHz$. Under this condition, constructive interferences between incident and reflected waves in the coaxial waveguide take place, which leads to a resonance effect at the open end of the coaxial torch.

4.3 MW-plasma coupling and electrical characterization of plasma

In this section, we discuss the electrical characterization of the MW plasma through measurement of reflected and absorbed power, as well as discharge images, to describe the evolution of the microplasma space-distribution as a function of operating conditions. Figure 4.2 shows the evolution of the diameter of the microplasma as a function of the absorbed power at a pressure of 50 mbar for pure hydrogen plasma.

The different regimes of plasma operation are depicted in Figure 4.2. At low power (10-30 W), the plasma is a small arc whose size increases with power. This is the **first regime** denoted **partial annular regime**. This growth continues until the plasma forms a complete circle at 40 W, at which point the **second regime** begins called the **full-circle regime**. In this regime (40-50W), plasma growth is more pronounced and emission is more intense and stable as power increases. Then, at 60W, the plasma returns to the partial circle: this is the secondary plasma phase due to the formation of secondary plasma inside the torch. This is the **third regime** ($\geq 60 \, W$) where the MW power is shared between the primary and secondary plasmas, and the volume and emission of the primary plasma decrease. This phenomenon was further confirmed by direct observation on the pin, where the secondary plasma was always located at a distance

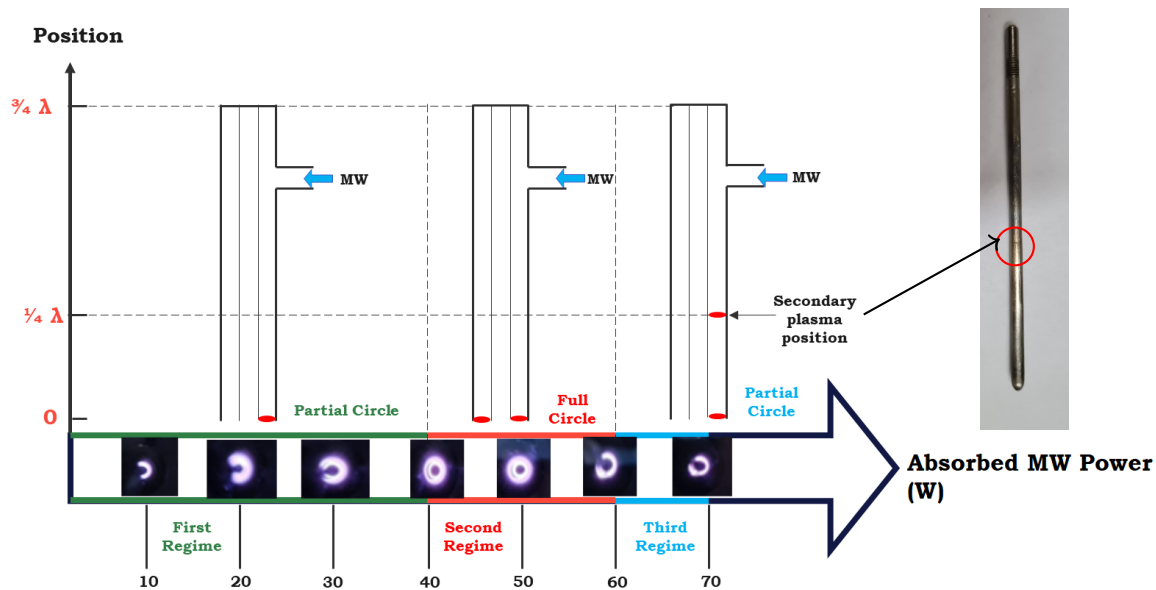


Figure 4.2: Evolution of microplasma as a function of absorbed power at 50 mbar. Inset (top right): Spots of the plasmas formed.

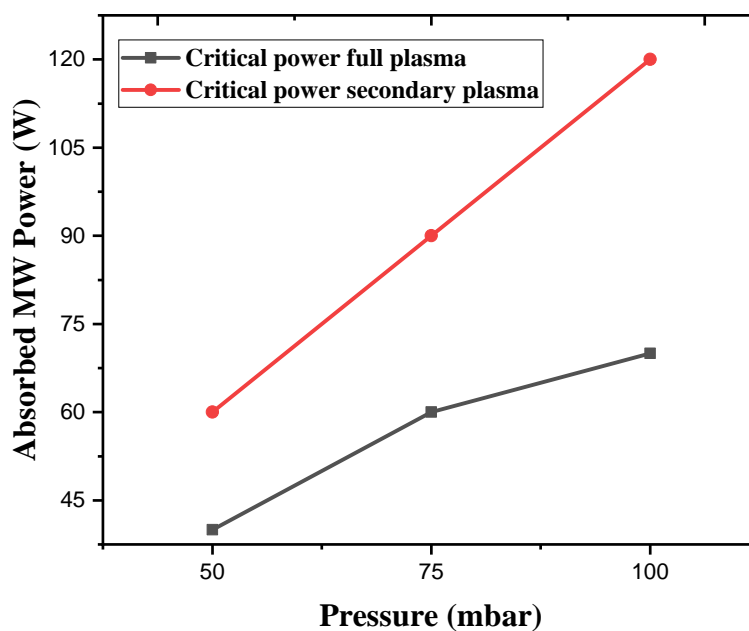


Figure 4.3: Representation of critical power as a function of pressure

of $\frac{1}{4} \lambda \sim 3 \text{ cm}$ from the main plasma, corresponding to the position of the secondary resonance, as shown in Figure 4.2. The critical power values for sustaining a full plasma and the onset of instability (secondary plasma) increase linearly with pressure, as shown in Figure 4.3. The full plasma appears at 40 W at 50 mbar, 60 W at 75 mbar, and 70 W at 100 mbar. However, the secondary plasma appears at 60 W at 50 mbar, 90 W at 75 mbar, and 120 W at 100 mbar.

Assuming that the power dissipation in the coaxial structures is negligible, the MW power absorbed by the torch is the difference between the injected and the reflected MW powers. Figure 4.4 illustrates how the reflected power varies with the absorbed power at different pressures. The reflected power increases with the absorbed power at a given pressure. Distinctively, the curves reveal an abrupt jump in reflected power that corresponds to the formation of the secondary plasma inside the torch. The abrupt jump can be explained by the poor matching of the MW-plasma system due to the secondary plasma.

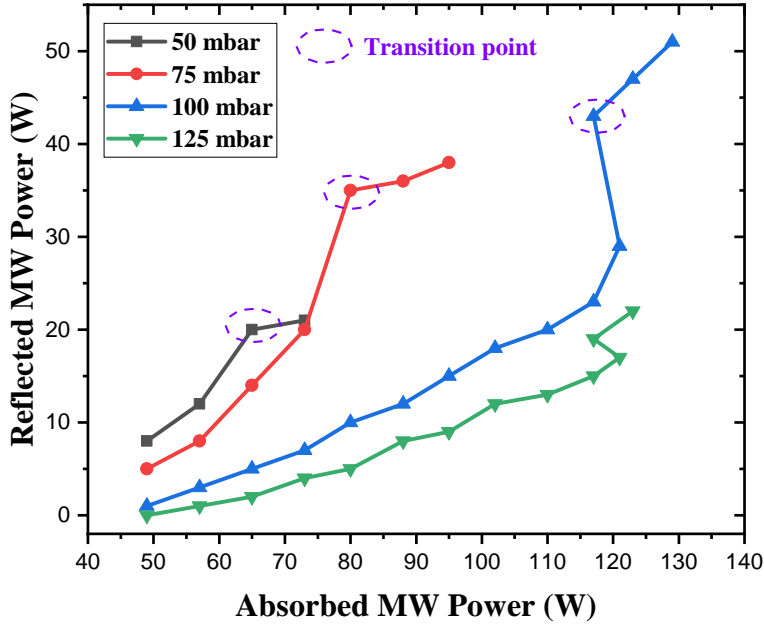


Figure 4.4: Representation of reflected power as a function of absorbed power for different pressures

The measurements of MW reflected power permit us to estimate the reflection coefficient of the plasma, S_{11} , as follows.

$$S_{11} = \sqrt{\frac{P_{ref}}{P_{inj}}} = \frac{Z_{in} - Z_0}{Z_{in} + Z_0} = \frac{1 - \left(\frac{1}{\tanh(jkl_1)} + \frac{Z_0 + Z_p \tan(jkl_2)}{Z_p + Z_0 \tan(jkl_2)} \right)}{1 + \left(\frac{1}{\tanh(jkl_1)} + \frac{Z_0 + Z_p \tan(jkl_2)}{Z_p + Z_0 \tan(jkl_2)} \right)}. \quad (4.13)$$

Furthermore, as the plasma is small compared to the length of the coaxial structures, the plasma end of the torch can be modelled by the lumped elements. In such a case, the impedance at the plasma end of the coaxial structure can be written as

$$Z_p = \sqrt{\frac{j\omega L}{G + j\omega C}}, \quad (4.14)$$

where L , G and C are the inductance, conductance, and capacitance of the coaxial waveguide. The resistance of the coaxial has been assumed to be negligible owing to the good conductance of the central rod. However, the presence of plasma introduces a finite conductance G due to

the presence of plasma currents between the central rod and the grounded outer annular head at the open end. By introducing the expressions of L, G and C for a coaxial waveguide²⁰⁷, Z_p can be expressed as

$$Z_p = \sqrt{\frac{\mu_0}{\epsilon_0}} \frac{\ln b/a}{2\pi} \frac{1}{\sqrt{\epsilon' - j\epsilon''}} = \frac{Z_0}{\bar{n}_{p,eff}}, \quad (4.15)$$

where $\epsilon_{p,eff} = \epsilon'_p - j\epsilon''_p$ and $\bar{n}_{p,eff} = n + i\kappa$ are the effective dielectric permittivity given by equation 4.5 and effective complex refractive index of the plasma structure at the open-end respectively. This allows for retrieving the effective refractive index and relative dielectric constant of the plasma medium from measurements of S_{11} and further directly estimate the plasma parameters n_e and T_e from Equation 4.5

$$\omega_p^2(n_e) = 56.4n_e = \left| (1 - \epsilon'_p) \left(1 + \left[\frac{\epsilon''_p}{1 - \epsilon'_p} \right]^2 \right) \omega^2 \right|, \quad (4.16)$$

$$\nu_m(T_e) = \frac{\epsilon''_p}{1 - \epsilon'_p} \omega. \quad (4.17)$$

It should be noted that the above equations assume that the plasma is homogeneously annular, which is only true for full regime of plasma operation. Figure 4.5a shows that an increase in the reflection coefficient leads to a decrease in resistance (real part) and an increase in inductance (imaginary part). The decrease in resistance indicates reduced energy dissipation within the plasma, which translates into an increase in the reflection coefficient, as much of the energy injected is reflected rather than absorbed. The estimated values of n_e from the measured plasma inductance are $O(10^{13} \text{ cm}^{-3})$ as seen in Figure 4.5b. Moreover, the plasma frequency is much higher than the MW frequency consistently under all conditions. For electron density values of $O(10^{13}) \text{ cm}^{-3}$, the skin depth would be on the order of 1 mm, which makes the penetration of the MW into the plasma significant. This penetration allows the MW field to penetrate the plasma, sustaining the plasma, causing an increase in the effective resistance as the absorbed power rises.

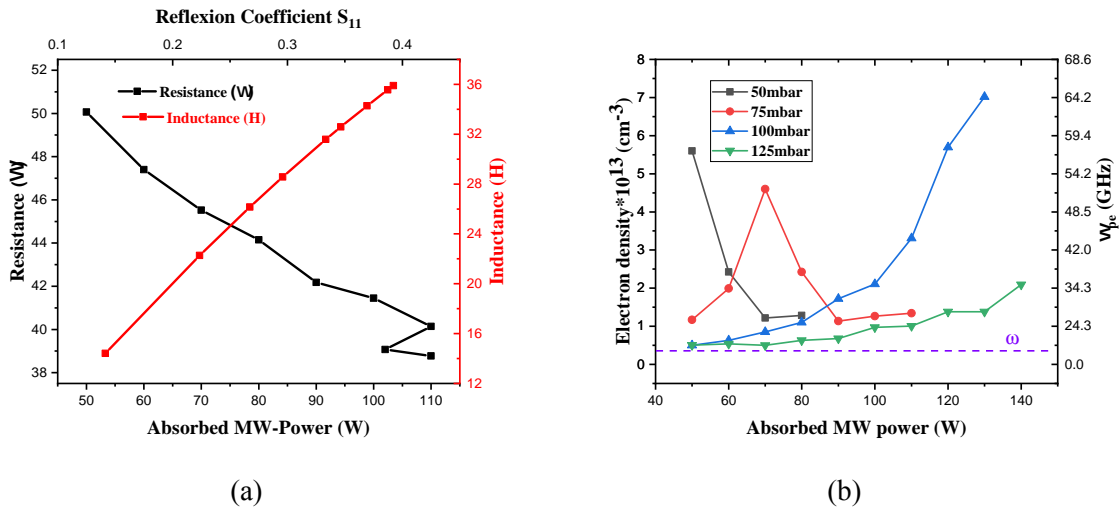


Figure 4.5: (a) Resistance and Inductance as a function of power and coefficient reflection at 100 mbar and (b) Evolution of n_e as a function of absorbed power at different pressures

The above analysis, though very qualitative and approximate, provides ample insight into the coupling of the MW and the plasma. In the following sections, we will measure the plasma parameters more accurately using optical diagnostics.

4.4 Gas temperature (T_g) measurement from OES

The gas temperature is a key plasma parameter as it has a significant influence on plasma chemistry, which is at the root of most plasma applications. In nonequilibrium plasmas like that of the MW microplasma torch, the electrons are preferentially heated, which results in a nonequilibrium condition among the different degrees of freedom within molecules, such as excitation, vibration, rotation, and translation. Consequently, the temperatures associated with these degrees of freedom follow a specific hierarchy, typically characterized by the inequality $T_e > T_{ex} > T_{vib} > T_{rot} > T_{trans}$, where T_e is the electron temperature, T_{ex} is the excitation temperature, T_{vib} is the vibrational temperature, T_{rot} is the rotational temperature, and T_{trans} is the translational temperature. Several methods are available to determine the gas temperature²⁰⁸ such as: **rotational distribution of molecules** (often and mostly diatomic molecules), **line profiles of atomic species** and **Thermal probes** that measure temperature directly by contacting the gas, etc. Here, we will focus on the description of gas temperature measurement from the rotational structures of molecular bands using optical emission spectroscopy.

4.4.1 Gas temperature from rotational distribution of molecule

Numerous works^{208–211} have clearly established that the temperature of gases in nonequilibrium plasmas can be assessed using optical emission spectroscopy. This method is based on the spectroscopic analysis of the rotational distribution of diatomic molecules (H_2 , N_2 , OH) in their excited states, which can be detected because these molecules emit in the visible and near-ultraviolet region.

The gas temperature is usually inferred from the rotational temperature, assuming a rotational-translational equilibrium. The validity of this assumption requires a very fast energy transfer between rotation and translation. Typically, equilibration of the rotational and translational modes for molecules in their electronic ground state requires few collisions²¹² and the assumption of rotational-translational thermal equilibrium is usually fulfilled for ground state species for the pressure conditions of interest in this work. The situation is more complex for excited-state species that are actually probed by OES. The rotational distributions of molecules in their ground and electronically excited states can differ significantly. The excited-state molecules and more specifically the radiative states probed by OES show a relatively short lifetime and do not necessarily experience enough collisions to achieve a rotational-translational equilibrium.

In nonequilibrium plasmas, radiative excited states are often produced by electron impact processes on electronically ground states and under go radiative and collisional de-excitation. The rotational distribution of these excited states depends on the time required for thermalization of the rotational levels ($\tau_{thermal}$) relative to the effective lifetime of the excited state (τ_{eff}). As

such, one may distinguish two limiting cases as far as rotational distributions of these states are concerned :

- In the highly collisional regime, i.e. at high pressure, before a photon is emitted, the excited state may undergo collisions before radiative de-excitation, which results in a thermal equilibrium between the translational and rotation modes for this state. The rotational modes of the electronically excited and ground states are also in thermal equilibrium. In this situation, the rotational temperature of the excited state may be inferred from the rotational structure of a ro-vibrational band of the emission spectrum using a Boltzmann plot with the rotational constant of the excited state.
- In the noncollisional regime (during the lifetime of the excited state), i.e. at low pressure. The electronic and nuclear dynamics are fully decoupled during the excitation process (Frank-Condon principle), and the rotational distribution does not change during the excitation process. As a result, the rotational distributions of the excited and ground states are exactly the same. The rotational temperature of the ground state can be determined from the rotational structure of a ro-vibrational band of the emission spectrum using a Boltzmann plot with the rotational constant of the ground state.

In intermediate situations, when the radiative de-excitation frequency of the excited state is comparable with the collision frequency, the rotational distribution of the excited state is neither identical to the ground-state rotational distribution nor in thermal equilibrium with the translational mode. In this case, the gas temperature can no longer be inferred from the rotational distribution of excited species.

For an equilibrium rotation mode, the rotational temperature can be calculated from a Boltzmann plot²⁰⁸. In the case where the rotational lines are fully resolved, the rotational spectra can be analyzed by plotting the logarithm of intensity (corrected by the Höln-London factor and level degeneracy) versus rotational energy levels (equation 4.18).

$$\ln\left(\frac{I_{\rightarrow''}}{S_{K'} g} \lambda^4\right) = \frac{-h C}{k_B T_{rot}} E_{J'}. \quad (4.18)$$

In this equation, $I_{\rightarrow''}$ represents the intensity of the line, g is the spin degeneracy, λ the wavelength of the rotational lines, and $E_{J'}$ the rotational energy of the appropriate level. This level may be either the upper or lower energy levels depending on the collisional regime. In high-collision regimes, the distribution might favor the upper levels, while in low-collision regimes, the ground states may be more suitable for an accurate determination of the rotational temperature. k_B the Boltzmann's constant. $S_{K'}$ denotes the Höln-London (HL) factors²¹³. These factors are coefficients used to account for the quantum selection rules that govern rotational transitions in molecules, along with molecular properties like the symmetry and parity of the rotational states that are involved in the transition.

For molecular hydrogen, $g = 1$ for even and $g = 3$ for odd values of the rotational quantum number K ²¹⁴. The Höln-London factors are expressed in the following relationships²¹⁵:

$$S_{K'} = \begin{cases} \frac{K' + 1}{2} & R - Branch, \\ \frac{K'^2 + 1}{2} & Q - Branch. \end{cases} \quad (4.19)$$

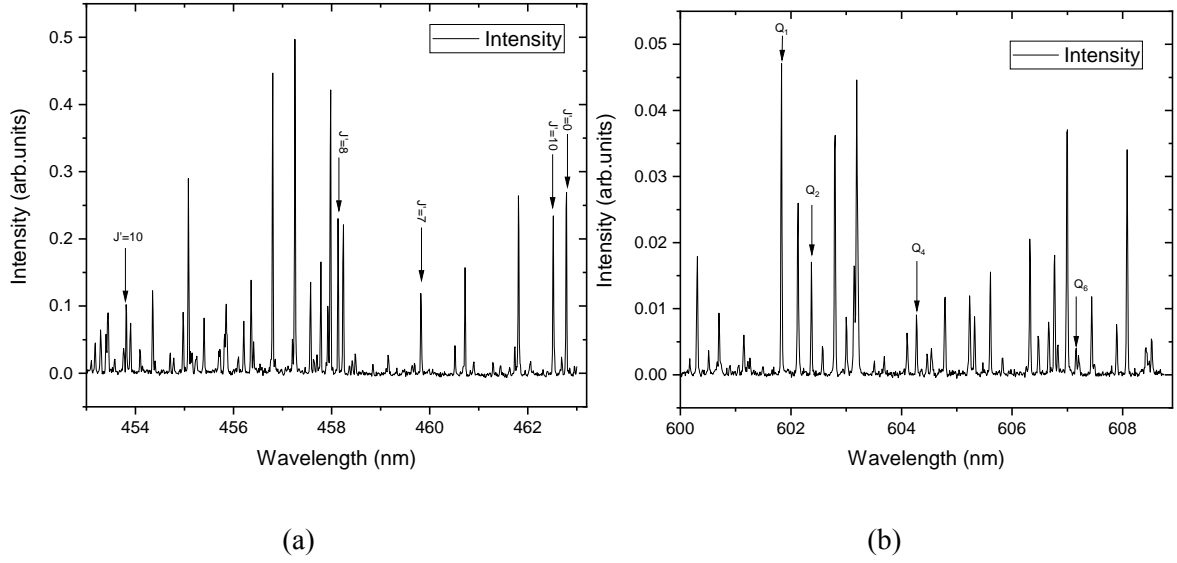


Figure 4.6: Spectra of the (a) first R-branch lines of the transition $G^1 \Sigma_g^+, \nu' = 0 \rightarrow B^1 \Sigma_u^+, \nu'' = 0$ and (b) the transition $d^3 \Pi_u^+ \rightarrow a^3 \Sigma_g^+ (0,0)$ at 50 mbar operating pressure

By plotting $\ln\left(\frac{I \lambda^4}{S_{K'g}}\right)$ as a function of the energy of the appropriate levels we obtain a line which slope is $\frac{-h \times C}{k \times T_{rot}}$. The rotational temperature can be therefore deduced from the slope of Boltzmann plot.

As we mentioned above, we can use the rotational band structures of different molecules such as H_2 , N_2 , OH , etc. to determine the gas temperature. Because our microplasma is rich in hydrogen, we decided to use different bands of this molecule because these bands give a reliable rotational temperature according to several studies. The most commonly used rotational bands are (i) the R branch of the transition $G^1 \Sigma_g^+, \nu' = 0 \rightarrow B^1 \Sigma_u^+, \nu'' = 0$ ^{83,208,216–219} and (ii) the Q-Branch $d^3 \Pi_u^+, \nu' = 0 \rightarrow a^3 \Sigma_g^+, \nu'' = 0$ of the Fulcher- α band^{220,221}. A typical spectrum of the R-Branch of $G^1 \Sigma_g^+, \nu' = 0 \rightarrow B^1 \Sigma_u^+, \nu'' = 0$ and the Fulcher Q-branch obtained with THR 1000 is shown in Figure 4.6.

4.4.2 Methodology used

The H_2 Fulcher- α rotational band has several branches, but the Q-Branch is the most used because it is free of perturbations²²⁰. The spectrum of Fulcher- α band extends from a wavelength of 600 to 610 nm (cf. Figure 4.6b). The Q_3 , Q_5 , Q_7 and Q_{10} transitions of the (0-0) band overlap the transitions from other bands of the H_2 spectrum²²⁰. Therefore, using these transitions in the Boltzmann plot results in erroneous values for the H_2 rotational temperature. The emission line Q_9 cannot be separated from high-intensity neighboring transitions with the spectrometer²²². Therefore, only the transitions Q_1 , Q_2 , Q_4 and Q_6 were used in determining the rotation temperatures from the Q branch of the (0-0) Fulcher- α band in this work.

With respect to $d^3 \Pi_u^-$ of the Fulcher band in the current experimental conditions, the collisional quenching time (~ 50 ns at 1000 K and 100 mbar) is of the same order of magnitude as that of its radiative decay (60 ns)²²⁰. Therefore, $d^3 \Pi_u^-$ undergoes collisions, and the rotational distribution of the excited state would not represent the ground state. However, the number of

collisions is not large enough to equilibrate the $d^3 \Pi_u^-$ rotational mode²²⁰. Therefore, the kinetic temperature of the gas would be between the rotational temperature values determined from Boltzmann plots using the rotational constants of the upper state $d^3 \Pi_u^-$ and the ground state $X^1 \Sigma_g^+$, respectively and are referred to as $T_{rot}(d)$ and $T_{rot}(X)$, respectively.

The spectrum of the R-Branch of $G^1 \Sigma_g^+$, $\nu' = 0 \rightarrow B^1 \Sigma_u^+$, $\nu'' = 0$ extends from a wavelength of 452 to 463 nm (c.f. Figure 4.6a). Regarding the G-Band, the lower level, $B^1 \Sigma_u^+$ is well described by the Hund b-case approximation. This approximation considers that the angular momentum of the electrons is partially decoupled from the internuclear axis of the molecule. Its radiative lifetime is 1.0 ± 0.2 ns. However, the upper level, $G^1 \Sigma_g^+$ is not as straightforward and lies between Hund's cases (b) and (d)²²³. In Hund's case (d), the electronic angular momentum is fully decoupled from the internuclear axis, complicating the definition of quantum number Λ (which represents the projection of the electronic angular momentum along the internuclear axis). Consequently, the rotational energy is no longer a simple linear function of $K(K+1)$. Additionally, the $G^1 \Sigma_g^+$ level is strongly perturbed by the vibrational sublevels of $K^1 \Sigma_g^+$, and the high vibrational levels of $EF^1 \Sigma_g^+$, causing deviations from the simpler Hund case (b). Assuming that $G^1 \Sigma_g^+$ follows case (b) of Hund, $S_{K'}$ of the rotational lines are described by the Höln-London formula (equation 4.19).

The radiative lifetime of the excited state $G^1 \Sigma_g^+$ is about 33 ns, while the characteristic collision time for thermalization is around 0.4 ns (at 1000 K and 100 mbar). This suggests that collisional thermalization is faster than radiative decay, allowing the excited state to reach thermal equilibrium with the gas before radiative de-excitation. Consequently, the rotational temperature of $G^1 \Sigma_g^+$ under moderate pressure (greater than 20 mbar) may reflect the temperature of the gas^{216,217,224,225}.

Only ten emission lines R_0 - R_{10} were identified. The R_1 and R_4 lines are not resolved and were not used in the Boltzmann plot. The R_6 and R_9 lines show a large deviation from the Boltzmann plot obtained with the ten first lines²²⁴. Fig. 4.7 shows the Boltzmann plot obtained from $\ln(\frac{I \lambda^4}{S_{K'g}})$ vs. $E_{K'+1}$.

4.4.3 Results

With an error of up to 5 % in the determination of the line intensity, the uncertainty in the gas temperature, depending on the different conditions and methods, varies from 32 to 130 K. Using both methods, an error of up to 9 % on T_g was achieved. Fig.4.8 shows the gas temperature measured as a function of pressure and MW power. The gas temperatures generally increased with MW power and varied between 1000 and 1400 K for G-Band ($T_{rot}(G)$) and between 500 and 800 K for $T_{rot}(X)$ of Fulcher- α . The gas temperature estimated with $T_{rot}(X)$ of the Fulcher- α band is lower than that of G-Band. This can be explained by the fact that $H_2(d^3 \Pi_u)$ does not thermalize under the present conditions due to the very short lifetime of $H_2(d^3 \Pi_u)$ state²²⁶.

We observe the presence of a temperature drop that is consistent with the increase of the reflected power shown in Figure 4.4, which takes place at the transition between a single and a double plasma volumes for pressure values below 125 mbar.

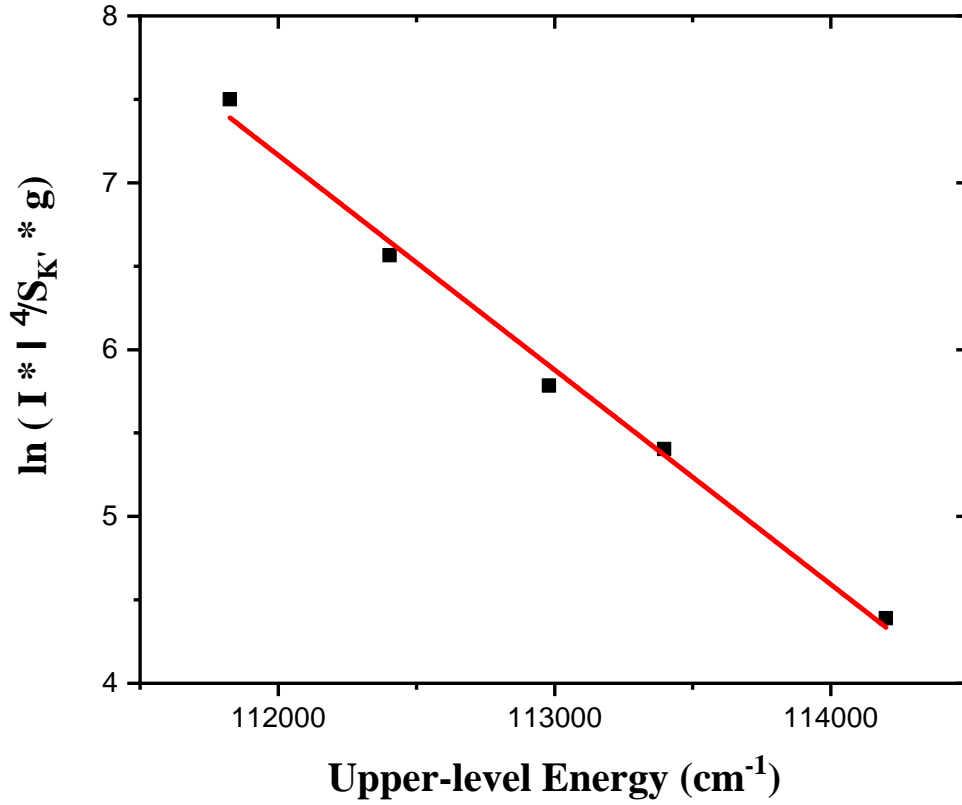


Figure 4.7: Boltzmann diagram for the determination of rotational temperature from R branch of $G^1 \sum_g^+, \nu' = 0 \rightarrow B^1 \sum_u^+, \nu'' = 0$ (THR100, 80W 100 sccm H₂, 100 mbar)

4.5 Measurement of electron density n_e

4.5.1 Principle

Electrons play a crucial role in initiating and sustaining microwave discharges, as they absorb energy from the electromagnetic wave and transfer it to atoms/molecules through inelastic collisions. To estimate the electron density (n_e), we opt for a well-established spectroscopic method based on Stark's broadening of the Balmer series lines of the H-atom^{82,219,227–229}. The profile of an emission line, i.e. its intensity distribution around a central wavelength λ_0 , can be affected by several broadening mechanisms. These mechanisms include Doppler broadening, van der Waals broadening, and Stark broadening. The line profile is also affected by the characteristics of the optical and spectroscopic equipment that introduce instrumental broadening of the emission lines. Each of these broadening effects contributes to the overall profile of the emission line and can be characterized by its full width at half-maximum (FWHM). Line profiles of atoms serve as a probe in which the deconvolution of different contributions may provide access to plasma parameters such as gas temperature T_{gas} and electron density n_e . Stark broadening results from the interaction between the emitting atoms and the surrounding charged particles (electrons and ions). It dominates other broadening mechanisms (Doppler, natural, etc.) under conditions where the electron density is high. In such a case, the Stark broadening can be used to measure the electron density n_e .

H _{β} (486.1 nm) emission line is known to be sensitive to Stark broadening and is used

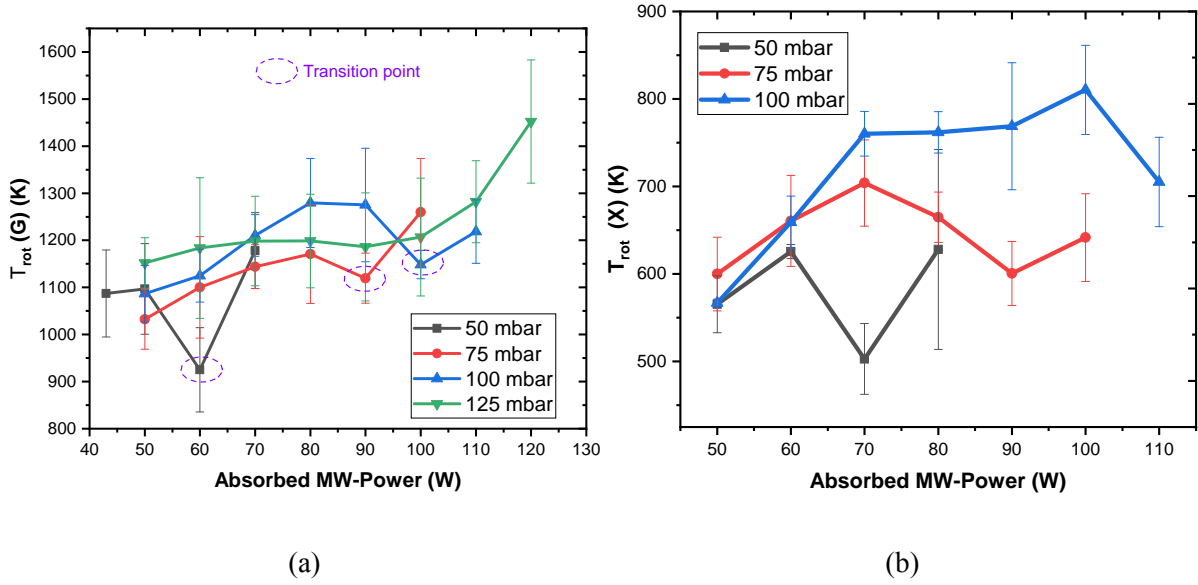


Figure 4.8: Representation of $T_{rot} (G)$ (a) and $T_{rot} (X)$ of Fulcher- α (b) as a function of absorbed power and pressure

frequently to measure the electron density. Under our experimental conditions, we considered two Gaussian broadenings (instrumental and Doppler) and two Lorentzian broadenings (Stark and van der Waals), which combine to form the observed line profile that can be approximated by a voigt function. The different broadening mechanisms are briefly explained in the following.

Instrumental broadening $\Delta\lambda_{app}$ depends on the resolving power of the spectrometer, i.e. slit aperture, grating size, focal length, etc. Also known as the instrument function, this component is induced solely by the measuring instrument. It is representative of the wavelength resolution of the set-up, so it varies with the width of the input slit. If the width of the input slit is changed, the device function must be measured. To measure the device function, emission lines must be used, where only instrumental broadening broadens the line. In other words, the finest possible line is sought: Rotational line of nitrogen, ideally ionic lines and Hg lines 579 nm in the second order, emitted by the fluorescent tubes in the room. Instrumental broadening was determined from the Hg line at 579 nm. For a slit opening of 40 μm , the instrumental broadening was found to be 0.0235 nm.

Doppler broadening ($\Delta\lambda_D$) is due to thermal agitation of the emitting atoms. If we consider that their energy distribution function is Maxwell-Boltzmann with a temperature T_g , this effect generates a Gaussian profile whose FWHM linewidth $\Delta\lambda_D$ that depends on T_g following the relation^{228,230}:

$$\Delta\lambda_D = 7.16 \times 10^{-7} \lambda \sqrt{\frac{T_g}{M}}, \quad (4.20)$$

Where T_g is in kelvin, λ is the wavelength in nanometers and M is the atomic mass of the emitting atom in atomic mass units. For example, at a gas temperature of $T_g = 1000$ K, the Doppler line width of the H_β line is approximately $\Delta\lambda_D = 0.011$ nm.

Van der Waals broadening ($\Delta\lambda_{vdW}$) occurs during a dipolar interaction between the emitter atom and the dipole it induces on a neutral atom in the ground state, called the perturber. For the

H_β line, line-width $\Delta\lambda_{vdW}$ is defined by²²⁸:

$$\Delta\lambda_{vdW} = 5.95 \times 10^{-3} \frac{P}{T_g^{0.7}}, \quad (4.21)$$

where P is the pressure in mbar. For example, at a pressure of $P = 100$ mbar and a gas temperature $T_g = 1000$ K, the van der Waals line width for the H_β line is approximately $\Delta\lambda_{vdW} = 0.0047$ nm.

The stark broadening ($\Delta\lambda_S$) is caused by the electric fields of charged particles (ions and electrons) in plasma. The difference between the slow motion of ions and the fast motion of electrons causes fluctuations in the microelectric field experienced by the emitting atoms. The interaction between the emitter atom and the time-varying local electric field results in a broadening of the spectral line. This broadening occurs even in the absence of direct collisions. The Stark broadening of the H_β line is particularly significant because its theoretical basis is well-established, and analytical expressions that relate the electron density to the line broadening are available. According to Kepple and Griem theory²³¹, valid for electron densities between 10^{13} cm^{-3} and 10^{19} cm^{-3} , the line-width of the Stark broadened H_β line $\Delta\lambda_S$ is given by⁸²:

$$\Delta\lambda_S = 2.5 \times 10^{-10} \alpha(n_e, T_e) n_e^{\frac{2}{3}}, \quad (4.22)$$

where $\alpha(n_e, T_e)$ is the reduced width of the Stark profile, and n_e is the electron density in cm^{-3} . For the conditions encountered in our microplasmas, this method provides a reliable and sensitive measure of electron density, with a typical detection limit of 10^{13} cm^{-3} ^{82,231,232}.

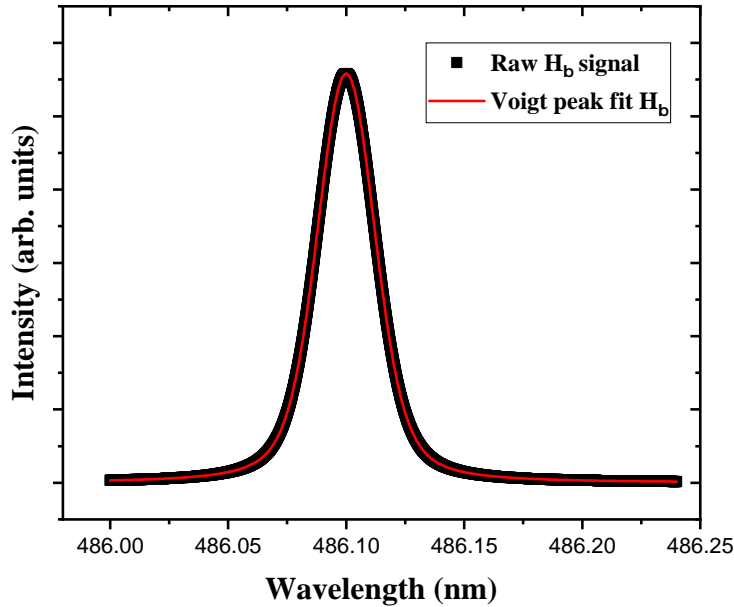


Figure 4.9: H_β line profile

A typical line spectra of H_β fitted with a voigt profile captured under our conditions is shown in Figure 4.9. It is characterized by its line-width $\Delta\lambda_V$, which can be deconvoluted as follows²³³:

$$\Delta\lambda_V \approx \left[\left(\frac{\Delta\lambda_L}{2} \right)^2 + (\Delta\lambda_G)^2 \right]^{\frac{1}{2}}, \quad (4.23)$$

where the Gaussian line-width $\Delta\lambda_G$ consists of Doppler $\Delta\lambda_D$ and instrument broadening $\Delta\lambda_{app}$ i.e. $\Delta\lambda_G = \sqrt{\Delta\lambda_D^2 + \Delta\lambda_{app}^2}$ and Lorentzian line-width is composed of van Der Waals $\Delta\lambda_{vdW}$ and Stark broadening $\Delta\lambda_S$ i.e. $\Delta\lambda_L = \Delta\lambda_{vdW} + \Delta\lambda_S$.

However, since both Doppler and Stark broadening were found to be significant under our plasma conditions, simultaneous estimation of these line widths by fitting the profile with the Voigt function leads to higher uncertainty²³⁴. Therefore, in order to improve the robustness of the fitting, the rotational temperature $T_{rot}(G)$ has been used to estimate the Doppler and van der Waals broadenings. This allows one to estimate the Stark linewidth $\Delta\lambda_S = \Delta\lambda_L - \Delta\lambda_{vdW}$ and therefore estimate the electron density. The procedure is summarized in Figure 4.10.

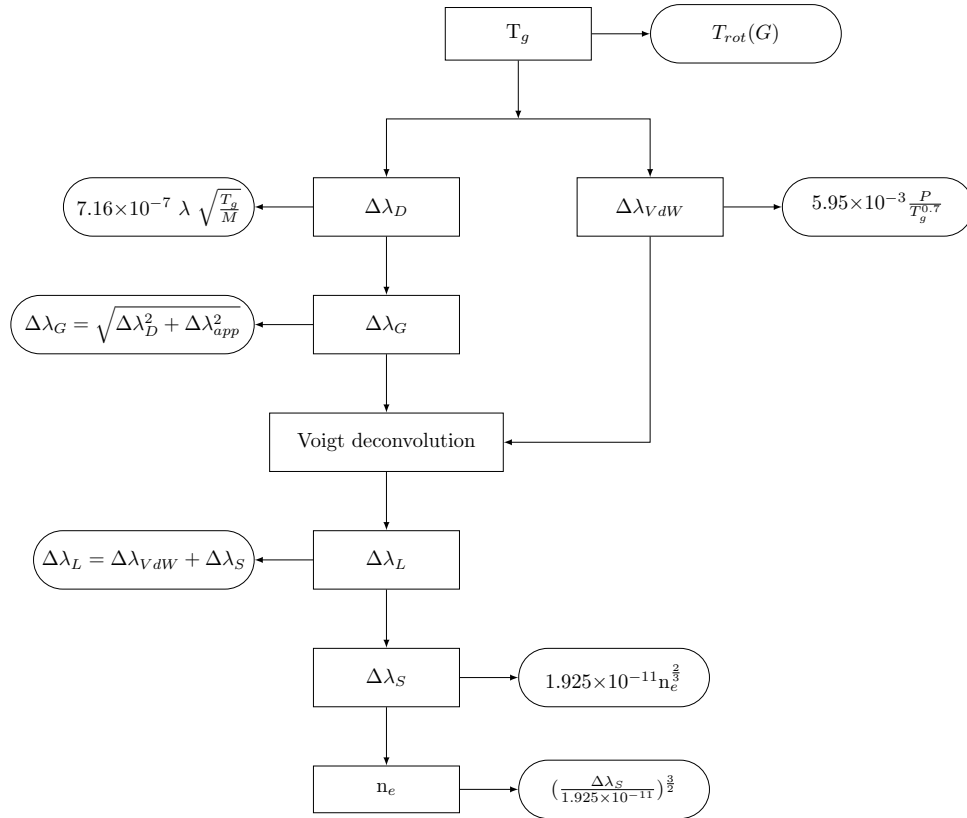


Figure 4.10: Method for determination of electron density

4.5.2 Plasma parameters

Under the conditions we examined, the Stark linewidth varies between 0.013 and 0.017 nm. Electron densities (cf. Figure 4.11) were found to increase slightly with pressure. Consequently, n_e appears to be independent of operating conditions with values around $2 \times 10^{13} \text{ cm}^{-3}$. These values are similar orders of magnitude as that estimated from the measurement of S_{11} (c.f. Figure 4.5b). This is indicative of the fact that plasma volume increases with injected power (as observed in Figure 4.2), so that the MW power densities and electron densities keep values in general similar to the investigated discharge conditions.

Equation 4.8, shows that the plasma parameters n_e , T_e , absorbed microwave power density ($PMWD$) along with plasma volume are coupled. Unfortunately, deducing the other parameters

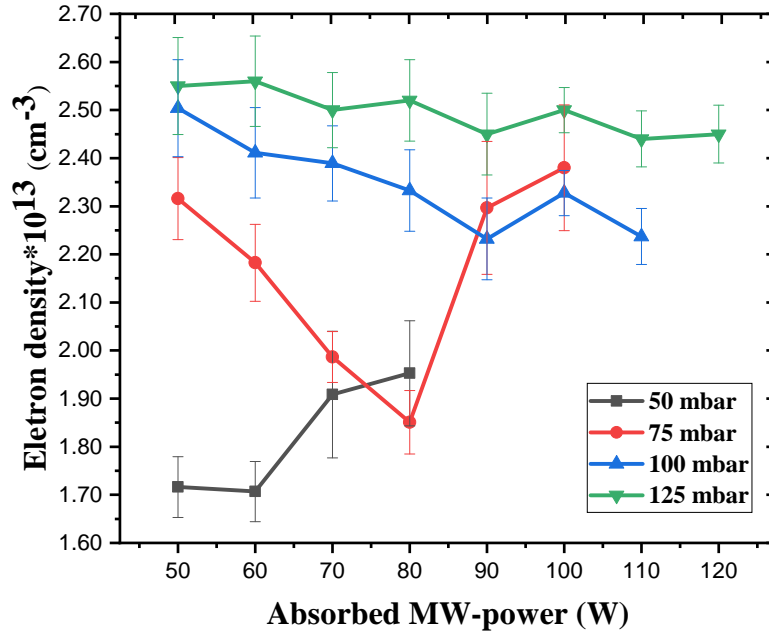


Figure 4.11: Representation of electron density as a function of absorbed power

apart from n_e is not straightforward. The estimated skin depth is around 1.5-2 mm with a plasma volume estimated to be $1.5 \times 10^{-8} \text{ m}^3$. The corresponding PMWD is $6 \times 10^9 \text{ Wm}^{-3}$ and is about 3 orders of magnitude higher than the larger MW plasmas at similar pressures²³⁵. This possibly explains the higher degree of ionization of the present microplasma torch system.

Under conditions where the electronic states of atoms are mainly excited by direct electron-impact processes on the corresponding ground state, it is possible to estimate the electron temperature from the ratio of line intensities of two electronic states of the atom. For example, the electron temperature can be determined from the intensity ratio of the H_α (656.3 nm) and H_β (486.1 nm) lines^{235,236} when the corresponding excited states, H (n=3) for H_α and H (n=4) for H_β , are mainly populated by direct electron impact from the ground state of the H atom. In this case, the electron excitation temperature of the H atom can be considered as indicative of the electron temperature. The intensity ratio of the emission lines H_α and H_β is given by the equation 4.24.

$$\frac{I_{H_\alpha}}{I_{H_\beta}} = \frac{k_e^{H_\alpha}(T_e)}{k_e^{H_\beta}(T_e)} \cdot \frac{\nu_{H_\alpha}}{\nu_{H_\beta}} \cdot \frac{A_{32}}{A_{42}} \cdot Q_{T_H} \cdot \frac{F(\lambda_{H_\alpha})}{F(\lambda_{H_\beta})}, \quad (4.24)$$

where $k_e^{H_\alpha}$ and $k_e^{H_\beta}$ are the rate constants for electron impact excitation to the H (n=3) and H (n=4) levels, respectively, ν_{H_α} and ν_{H_β} are the radiation frequencies of the H_α and H_β lines, A_{32} and A_{42} are the spontaneous transition probabilities, $F(\lambda_{H_\alpha})$ and $F(\lambda_{H_\beta})$ are the optical spectral responses at 656.3 nm and 486.1 nm respectively, and Q_{T_H} accounts for additional radiative and quenching processes.

The spectral response of our 1 m spectrometer was determined using a reference tungsten lamp of 300 nm to 900 nm. The values of $F(\lambda_{H_\alpha})$ are around 0.0016 and $F(\lambda_{H_\beta})$ is 0.0042.

As the plasma is composed of H et H₂ species the term Q_{TH} is given by this relation :

$$Q_{TH} = \frac{k'_r + n_{H_2}k_{Q_{H\beta}/H_2} + n_Hk_{Q_{H\beta}/H}}{k_r + n_{H_2}k_{Q_{H\alpha}/H_2} + n_Hk_{Q_{H\alpha}/H}}, \quad (4.25)$$

where k_r and k'_r are the total radiative probability constants for the levels H (n=3) and H (n=4) respectively and $k_{Q_{H\alpha}/H_2}$, $k_{Q_{H\beta}/H_2}$, $k_{Q_{H\alpha}/H}$, and $k_{Q_{H\beta}/H}$ are the quenching constants for the excited hydrogen levels due to collisions with H₂ and H. The evaluation of term Q_{TH} requires knowledge of the density of the H atom and the temperature of the gas. For the initial calculation, the degree of dissociation was assumed to be small and collisional quenching occurs mainly due to molecular H₂. The electron temperature thus estimated was around 4000 K in the pressure range of 50 to 125 mbar for the power conditions studied. However, the estimated electron temperature is significantly lower than the values found for similar MW plasmas. This discrepancy could be attributed to quenching effects, where the high collision frequency in the plasma leads to an underestimation of the true electron temperature. In such a collisional regime, the measured temperature may represent an average value between the electron temperature (T_e) and the gas temperature (T_g), reflecting the complex interplay of ionization, excitation, and collisional de-excitation processes.

In view of the above, the electron temperature was alternatively estimated from equation 4.8. All important electron impact reactions with atomic hydrogen and molecular hydrogen, i.e. excitation (translational, vibrational, and electronic), ionization, and dissociation, have been taken into account²³⁷. The reaction coefficients (K_x) are influenced by the electron temperature, which has an effect on the energy distribution in the plasma.



As a general rule, as the electron temperature rises, the reaction rates increase and the probability of ionization and excitation processes increases. It is worth mentioning that the vibrational temperature (T_{vib}) and the translational temperature (T_{trans}) are also important, since T_{vib} increases the population of molecules in the excited vibrational state, favoring certain reactions, while T_{trans} increases the energy of the motion of the particles, affecting collision rates. The electron temperature values estimated under stable plasma conditions for 90 W absorbed power in the pressure range 50-125 mbar as a function of the value assumed for the plasma length are shown in figure 4.12 (full circle). The corresponding electron temperature would be in the range of 1.6 to 2.3 eV. The thus estimated electron temperature was found to be around 1.9 eV which looks more reasonable for the discharge conditions.

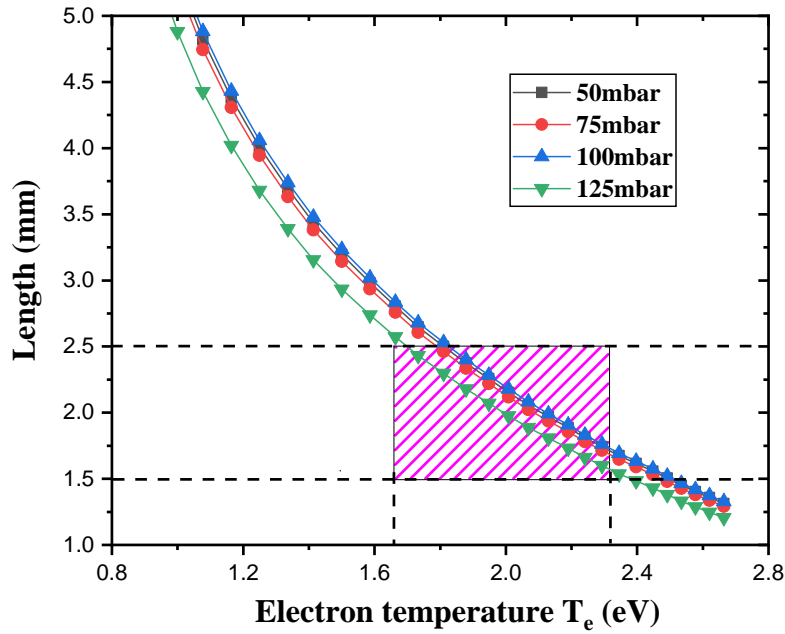


Figure 4.12: Representation of plasma length as a function of absorbed power at different operating pressures and at 90W

Finally, MW power densities and volumes have been evaluated for fixed electron temperature at 1.9 eV, as shown in Figure 4.13. One can clearly observe that, as n_e , the PMWD of the plasma torch has the same trend. It increases slightly with pressure. However, the plasma volume decreases with the pressure and increases almost linearly with injected MW power at a given pressure. These observations are consistent with those for the MW plasmas.

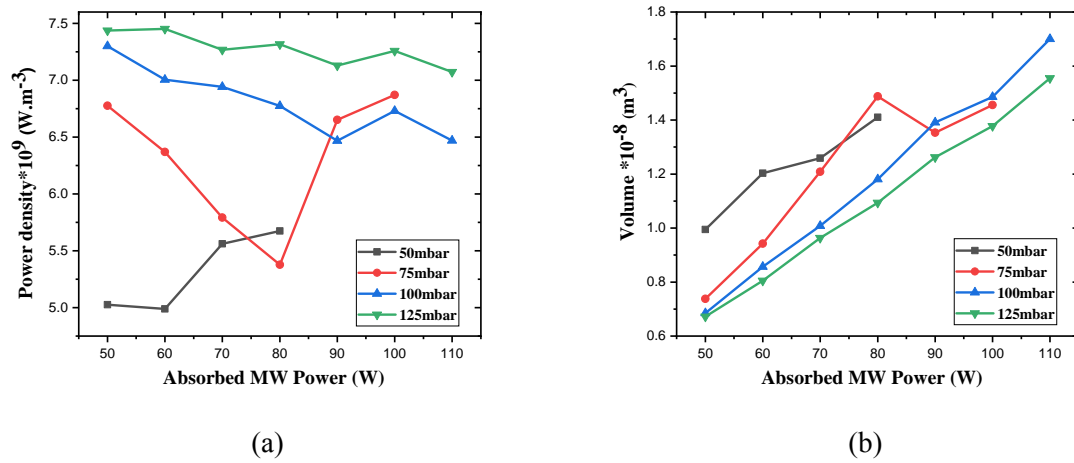


Figure 4.13: Representation of PMWD (a) and plasma volume (b) as a function of absorbed power at different pressures

4.6 Measurement of atomic Hydrogen density

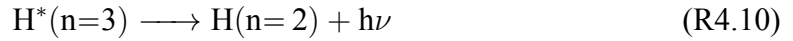
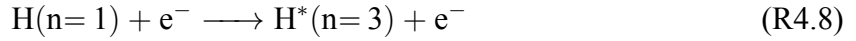
4.6.1 Measurement of atomic Hydrogen density by actinometry

It is possible to estimate the concentration of atomic hydrogen $[H]$ by optical emission spectroscopy using a method called actinometry. This method consists of measuring the relative concentration of a reactive species by comparing its optical emission with that of an inert gas, called an actinometer or tracer, deliberately introduced in very small quantities ($\sim 1\%$) into the discharge. This comparison is based on the assumption that the reactive species and the actinometer are at the same temperature and that their excitation processes are similar²³⁸.

The principle of this method has been described by many authors⁸³ and is based on the following assumptions:

- (i) The actinometer must be introduced into the plasma in small and constant quantities. This quantity must not interfere with the reaction mechanisms of the plasma ;
- (ii) The production of the excited states (X^* and A^*) is due to a direct electron-impact excitation of the corresponding ground states (reactive species X and actinometer A);
- (iii) The de-excitation of the two species (X -species and actinometer A) is mainly radiative and not collisional ;
- (iv) The excitation cross-sections must have a similar shape and the same threshold energies;
- (v) All other excitation or de-excitation mechanisms can be neglected.

The reduced scheme for the excitation and de-excitation processes is the following :



Thus, a simple relationship exists between the intensities of the emission lines of the excited species $I(X^*)$, and the density of these species in the ground state $[X]$, which allows the relative densities to be determined:

$$[X] = K \frac{I(X^*)}{I(A^*)} [A], \quad (4.26)$$

Where $[X]$ and $[A]$ are the concentrations of electronic ground states of X and actinometer species, respectively. K is a constant, and $\frac{I(X^*)}{I(A^*)}$ is the ratio of emission intensities of the excited X species and the excited actinometer species A . In this work, the reference gas used is argon (Ar line at 750 nm), which serves as an actinometer for hydrogen, and the hydrogen line considered is H_α . A small percentage of argon (about 1%) is added to the hydrogen plasma. By comparing the intensity of the de-excitation lines of atomic hydrogen and argon, we can evaluate the relative density of hydrogen atoms in the ground state.

Equation 4.26 is taken from equation 4.27 in the case of hydrogen.

$$\frac{I_{H_\alpha}}{I_{Ar750}} = \frac{k_e^{H_\alpha}(T_e)}{k_e^{Ar750}(T_e)} \cdot \frac{\nu_{H_\alpha}}{\nu_{Ar750}} \cdot \frac{A_{H_\alpha}}{A_{Ar750}} \cdot Q_{T_H} \cdot \frac{F(\lambda_{H_\alpha})}{F(\lambda_{Ar750})} \cdot \frac{n_{H_\alpha}}{n_{Ar750}}. \quad (4.27)$$

The constant K therefore is expressed as follows:

$$K = \frac{k_e^H(T_e)}{k_e^{Ar750}(T_e)} \cdot \frac{\nu_H}{\nu_{Ar750}} \cdot \frac{A_H}{A_{Ar}} \cdot Q_{T_H} \cdot \frac{F(\lambda_H)}{F(\lambda_{Ar750})}. \quad (4.28)$$

The different terms of these equations have already been defined in Section 4.5.2 (Equation 4.24) with $F(\lambda_{Ar750}) = 5.6 \times 10^{-4}$.

4.6.2 Measurement of H-atom density using ps-TALIF

As mentioned in Chapter 3, TALIF is a diagnostic technique used mainly to measure the density of atomic species present in plasmas or flames. In this technique, a laser is used to excite species of interest that absorb simultaneously two photons, which then results in fluorescence. The fluorescence intensity can be related to the absolute density of the probed species. Equation 4.29 gives the absolute density of a probed atomic species i using TALIF.

$$n_i = n_C \frac{\int_t \int_\lambda S_{F_i} \frac{\eta_C}{\eta_i} \frac{T_C}{T_i} \frac{\sigma_C}{\sigma_i} \frac{A_C}{A_i} \frac{\tau_C}{\tau_i} \frac{E_C^2}{E_i^2} \frac{\lambda_C^2}{\lambda_i^2}, \quad (4.29)$$

with subscripts i and C referring to the probed and calibrated atomic species, respectively. $\int_t \int_\lambda S_{F_i}$ is the temporally and spectrally integrated fluorescence signal. n_i/n_C , η_i/η_C , T_i/T_C , σ_i/σ_C , A_i/A_C , τ_i/τ_C , E_i/E_C and λ_i/λ_C , are the densities, the quantum efficiencies of the detector, the transmissions of the optics at the fluorescence wavelengths, the two-photon excitation cross-sections, the Einstein coefficients of the radiative decay of the laser excited states, the experimentally measured fluorescence decay times of the laser-excited states, the energies, and the wavelengths of the lasers used for performing the TALIF measurements for the probed (i) and the calibrating (C) atomic species, respectively. For ps-TALIF on the H atom, the ground state of the H atom is excited to H ($n = 3$) by absorption of two photons at an excitation wavelength of 205.08 nm and the resulting fluorescence is collected from the Balmer α line ($H_{n=3} \rightarrow H_{n=2}$) at 656.3 nm.

For the plasmas considered in this study, due to collisional quenching (induced by the moderate pressure conditions), the effective lifetime of the probed species may vary between a few tens of picoseconds and a few nanoseconds, depending on the pressure and temperature. This requires the use of a laser system capable of providing two-photon excitation within time periods much shorter than the fluorescence decay time. Additionally, the laser pulses must be short enough to prevent a significant overlapping between the excitation and the fluorescence phase to ensure an accurate determination of the fluorescence decay. TALIF experiments also require an acquisition system with a temporal resolution enabling one to capture the very fast fluorescence decay processes. To meet all these requirements, we used a ps-laser for two-photon excitation of H_α , coupled with a streak camera to capture the fluorescence signal with picosecond time-scale resolution (both tools are explained in Chapter 3).

In general, streak cameras are distinguished by their ability to receive light signals within a specific time interval, known as the sweep time, which ranges from 100 ps to 1 ms. In line with the work of Invernizzi et al.¹⁸⁰, the time window of the line image was ideally set at 5 ns to accurately extract τ_H over the range of experimental conditions considered in this work.

This enables reproducing the full decay phase of the fluorescence signal, which is essential to ensure an accurate determination of the fluorescence lifetime τ_H over the range of experimental conditions explored in this work.

4.6.3 Data post-processing

The equation 4.29 requires the signal to be integrated temporally and spectrally. In other words, it is necessary to measure the full spectral profile of the excitation line and, therefore, to have a series of TALIF measurements at several wavelengths (in general, ten or fifteen wavelengths are necessary to describe this profile properly). Even if the measurements are carried out automatically, it is possible that between the first acquisition and the last: i) the plasma is not exactly the same (fluctuation of the pressure, background, the temperature, etc.) and ii) the laser energy changes. Furthermore, if the plasma has to be operated for a short time for general stability reasons, e.g. gas scarcity or stability of the optical transmittance (for example, a plasma with methane will blacken the windows, so the transmittance of the windows will fall), then it is preferable to reduce the TALIF experiment time. To shorten the TALIF experiment, especially when plasma conditions are not stable over time, it is good to get a full spectral profile under stable conditions to get the FWHM of the fluorescence line. For subsequent measurements, instead of measuring the full profile again, just record the maximum intensity at the resonance wavelength. Using the previously measured FWHM, we can then mathematically reconstruct the full profile. This method, known as the peak method, enables faster data acquisition while preserving the accuracy of the profile¹⁰¹. This assumption is valid when experimental conditions (such as stable plasma temperature and pressure) ensure that the width of the fluorescence line does not vary. The TALIF equation of H-atom corresponding to the peak method is as follows:

$$n_i = n_C \frac{\int_t S_{Fi}}{\int_t S_{FC}} \frac{\eta_C}{\eta_i} \frac{T_C}{T_i} \frac{\sigma_C}{\sigma_i} \frac{A_C}{A_i} \frac{\tau_C}{\tau_i} \frac{E_C^2}{E_i^2} \frac{\lambda_C^2}{\lambda_i^2} \frac{g_{\nu(\text{peak})C}}{g_{\nu(\text{peak})i}}, \quad (4.30)$$

Where $\int_t S_{Fi}$ is the time-integrated fluorescence signal of i and $g_{\nu(\text{peak})i}$ is the two-photon absorption profile of the species i and it is obtained for a Gaussian (when the laser broadening is dominant) this value corresponds to $\frac{\sqrt{\frac{4 \ln(2)}{\pi}}}{FWMH_i}$.

The raw TALIF signal captured using a streak camera is a 2D image where the x-axis (673 pixels) and the y-axis (508 pixels) are indicative of the spatial (i.e. x-axis of the reactor) and temporal coordinate, respectively. The slit of the streak camera is horizontal (that is, along the x-axis) and captures a fluorescence zone of approximately 4.5 ± 2 mm centered around the plasma torch axis as shown in Figure 4.14. The large focal length of the laser focus lens (500 mm) ensures that the laser cross section ($\sim 500 \mu\text{m}$) remains constant throughout the fluorescence zone. The height of the plasma with respect to the laser beam (i.e. in the z direction) was varied in order to construct the 2D fields of H-atom density and other associated quantities in the x - z plane.

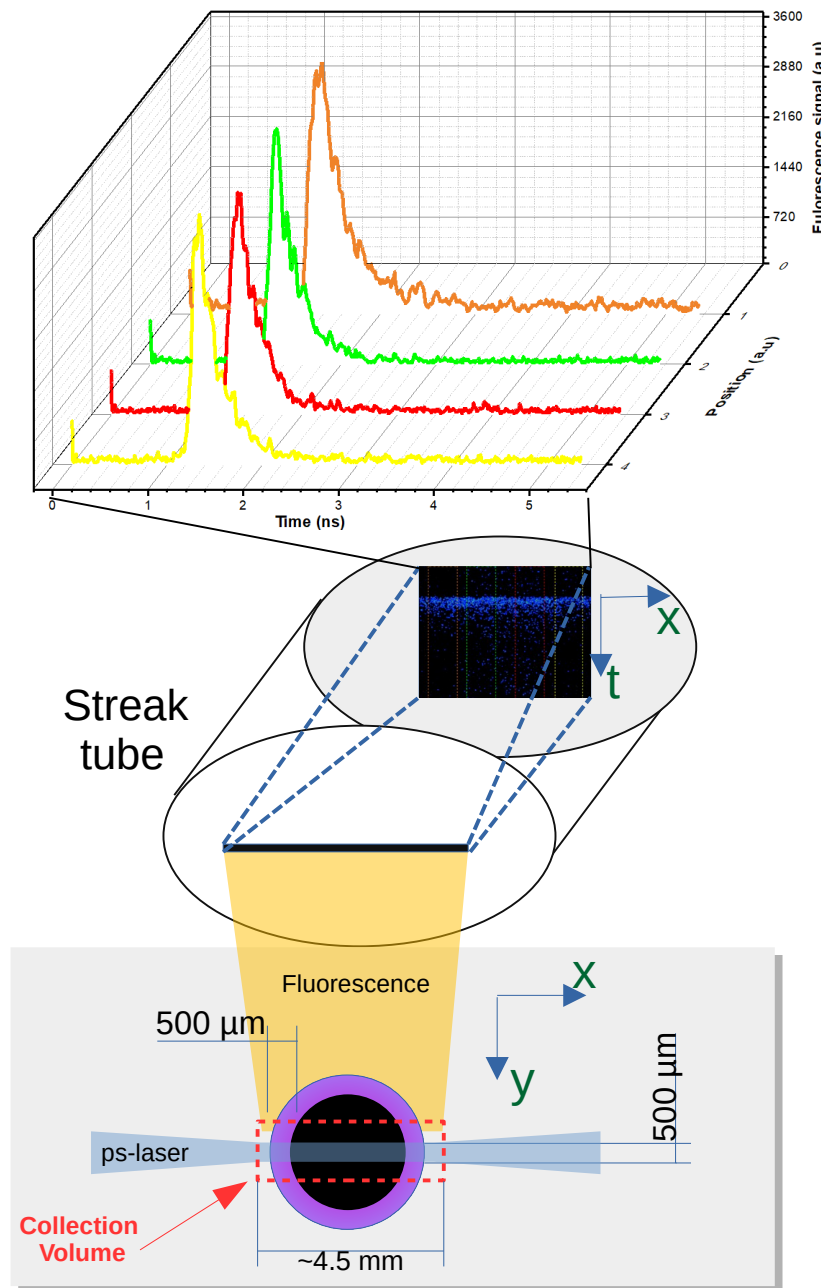


Figure 4.14: Illustration of the fluorescence captured by the streak camera.

4.6.4 Results

Measurements of atom densities were performed using actinometry and ps-TALIF. The quadratic dependence of the fluorescence intensity with respect to the laser energy (as required by Equation 4.29) was verified for different operating conditions (cf. Figure 4.15a). To achieve absolute density measurements, H-atom density calibration was initially performed using krypton²³⁹. For this calibration, ps-TALIF measurements were performed in pure krypton within a quartz cuvette at 200 Pa. However, following the measurement campaign, it was realized that the optical properties such as transmittance of the cuvette and the plasma reactor chamber differed significantly. This discrepancy required an additional calibration. Consequently, actinometry

was chosen as the reference for determining relative densities. The ratio of H-atom densities, obtained by ps-TALIF and actinometry, was measured under reference conditions (100 mbar, 90 W power) and was found to be 0.78. This ratio was subsequently applied to all measurements as correction for optical properties.

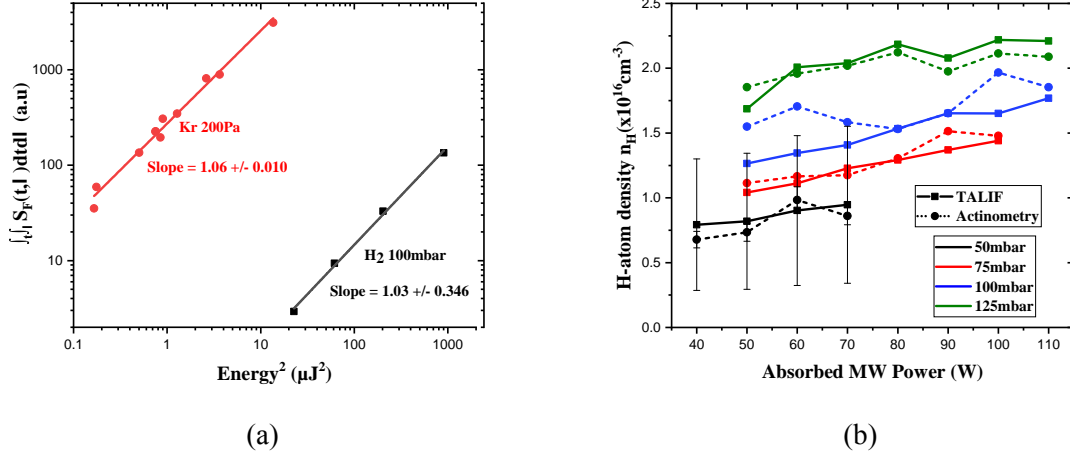


Figure 4.15: (a) Variations of S_{F_i} as a function of laser energy for H and Kr and (b) H-atom densities measured using actinometry and ps-TALIF as a function of pressure and power.

Figure 4.15b compares the H-atom densities measured using ps-TALIF and actinometry. The two measurements are in relative agreement with each other in the pressure and power ranges studied, which validates the absolute calibration approach used in our study. It is observed that n_H increases with pressure and varies between 7×10^{15} and $2 \times 10^{16} \text{cm}^{-3}$, leading to a stronger dissociation of H₂. For this pressure range, dissociation of up to 10% is achieved. In particular, for a given pressure, the density of atomic hydrogen does not vary significantly with power. This is probably due to the fact that the main effect of a power increase is an increase of the plasma volume, the local power density that determine the electron density, and therefore the kinetics of electron-impact processes, i.e., ionization and dissociation, kinetics and thermal heating of the plasma being almost constant.

4.7 Gas temperature measurement from ps-TALIF

This section explores a novel straightforward and direct approach to determine the gas temperature in collisional plasmas from ps-TALIF. The effective lifetimes τ_X measured during ps-TALIF serve as a probe of local plasma conditions, as it depends on all the radiative and collisional quenching processes^{240,241}. The effective lifetime τ_i characterizes the collisional and radiative decay processes of the excited species following the laser excitation. It can be written as:

$$\frac{1}{\tau_i} = A_i + Q_i = A_i + \frac{P}{k_B T_g} \sum_j^{\text{quenchants}} k_{Q_{i/j}} x_j, \quad (4.31)$$

Where Q_i and A_i are the quenching rate and the total Einstein coefficient of radiative decay of the excited state. P is the local pressure, T_g is the gas temperature, k_B is the Boltzmann

constant, and x_j is the molar fraction of the quencher j . $k_{Q_{i/j}}$ is the rate coefficient of quenching of excited species i by quencher j and can be expressed as :

$$k_{Q_{i/j}} = \sigma_{Q_{i/j}} \nu_{i/j} = \sigma_{Q_{i/j}} \sqrt{\frac{8k_B T_g}{\pi \mu_{i/j}}}, \quad (4.32)$$

where $\sigma_{Q_{i/j}}$ is the collisional quenching cross-section, $\nu_{i/j}$ and $\mu_{i/j}$ are the mean thermal velocity and the reduced mass of the collision pair i/j .

The measurement of τ_i and the use of Equation 4.31 allow one to determine the radiative decay rate $1/A_i$ and the collisional quenching cross section $\sigma_{Q_{i/j}}$. This can be achieved using the Stern-Volmer plot of $\frac{1}{\tau_i}$ as a function of the pressures²⁴¹. In general, Stern-Volmer plots distinguish three distinct regimes:

- Radiation dominated regime at extremely low pressures i.e. $A_i \gg Q_i$,
- Collision dominated regime at high pressures where $A_i \ll Q_i$,
- Mixed radiative-collisional regime at intermediate pressures i.e. $A_i \sim Q_i$.

Similarly, knowing radiative and collisional decay constants, it is possible to deduce the gas temperature T_g by rewriting equation 4.31 as :

$$T_g = \frac{8}{\pi k_B} \left(\frac{P \tau_i}{1 - \tau_i A_i} \sum_j \frac{x_j \sigma_{Q_{i/j}}}{\sqrt{\mu_{i/j}}} \right)^2. \quad (4.33)$$

To ensure the accuracy of T_g estimation from τ_i , the collisionality parameter $\gamma_i = 1 - \tau_i A_i$, which appears in the denominator of equation 4.33, must be considered. It is easy to notice that γ_i varies between 0 and 1 where the lower asymptotic limit $\gamma_i \rightarrow 0$ is indicative of a radiation-dominated decay process while the opposite $\gamma_i \rightarrow 1$ is indicative of a collision-dominated regime. It is obvious that temperature recovery is not applicable for radiative-dominated decay regimes (mathematically $\gamma_i \rightarrow 0$, $T_g \rightarrow \infty$).

4.7.1 Analysis of propagation of errors

The determination of τ_H with good accuracy is absolutely necessary for the reliable retrieval of T_g . Moving point averaging with a window size of 200 pixels (which covers approximately 1.5 mm) was performed to suppress the noise in the raw images and to obtain the average spatial variation of the space-distributions for H-atom density and gas temperatures. The uncertainty in τ_i would naturally depend on the density of the probed atomic species. Lower atom densities would indicate lower TALIF signal intensity as well as increased noise, making it difficult to accurately extract τ_i from the raw TALIF data, therefore including a larger uncertainty. The uncertainty in τ_H was estimated within 5 % in our conditions, which makes the measurements of T_g by the approach discussed here fairly reasonable.

The uncertainty of the gas temperature measurements ΔT_g is determined from the partial uncertainties of all the independent variables as follows:

$$\Delta T_g = \sqrt{\left(\frac{\partial T_g}{\partial P} \Delta P \right)^2 + \left(\frac{\partial T_g}{\partial A_i} \Delta A_i \right)^2 + \left(\frac{\partial T_g}{\partial \tau_i} \Delta \tau_i \right)^2 + \sum_j \left\{ \left(\frac{\partial T_g}{\partial \sigma_j} \Delta \sigma_j \right)^2 + \left(\frac{\partial T_g}{\partial x_j} \Delta x_j \right)^2 \right\}}, \quad (4.34)$$

where the partial derivative of T_g with respect to the different independent variables are given by

$$\begin{aligned} \frac{\partial T_g}{\partial P} &= T_g \frac{2}{P} & \frac{\partial T_g}{\partial A_i} &= T_g \frac{2\tau_i}{\gamma_i} & \frac{\partial T_g}{\partial \tau_i} &= T_g \frac{2}{\gamma_i \tau_i} \\ \frac{\partial T_g}{\partial \sigma_j} &= \frac{16\sigma_j}{\pi k_B} \left(\frac{P\tau_i}{\gamma_i} \frac{x_j}{\sqrt{\mu_j}} \right)^2 & \frac{\partial T_g}{\partial x_j} &= \frac{16x_j}{\pi k_B} \left(\frac{P\tau_i}{\gamma_i} \frac{\sigma_j}{\sqrt{\mu_j}} \right)^2 \end{aligned} \quad (4.35)$$

In conditions where the degree of dissociation is small, and only one quencher species j is dominant (as seen in our experimental conditions), the uncertainty ΔT_g depends only on the relative uncertainty of individual variables as given below

$$\frac{\Delta T_g}{T_g} \approx 2 \sqrt{\left(\frac{\Delta P}{P} \right)^2 + \left(\frac{\Delta A_i \tau_i}{\gamma_i} \right)^2 + \left(\frac{\Delta \tau_i}{\gamma_i \tau_i} \right)^2 + \left(\frac{\Delta \sigma_j}{\sigma_j} \right)^2 + \left(\frac{\Delta x_j}{x_j} \right)^2} \quad (4.36)$$

The contribution of Δx_j is negligible owing to low degree of dissociation. Furthermore, the impact of ΔA_i and $\Delta \tau_i$ on the uncertainty of T_g is minimal when $\gamma_i \rightarrow 1$. In fact, the contribution of ΔA_i is negligible and only three terms play a role in uncertainty, ie P , τ_i , and σ_j .

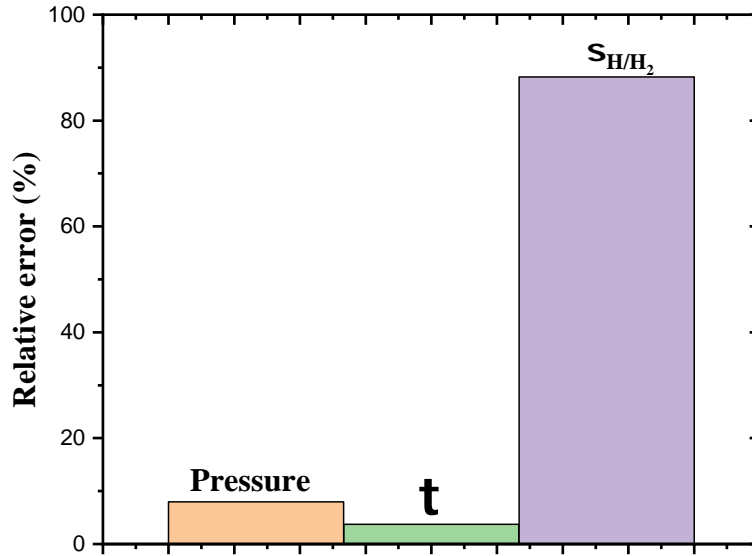


Figure 4.16: Relative errors for the different terms of the gas temperature equation at 100 mbar and 100W.

Analysis of propagation of errors (as inferred from Equation 4.34), indicates that the major contribution comes from the uncertainty of the collisional quenching cross section σ_{H/H_2} for all the conditions studied, as shown in Figure 4.16. Due to low dissociation ($< 5\%$) and weak quenching by H-atoms ($\sigma_{H/H} \ll \sigma_{H/H_2}$), H-atom density does not play a major role in temperature measurements. For our experiments, the pressure was well controlled within ± 1 mbar or

$\pm 2\%$ and therefore does not affect the overall uncertainty to a large extent. Therefore, the only experimentally measured parameter that affects temperature measurement is τ_H . Nevertheless, its contribution towards the total uncertainty is low for most conditions with a maximum of 30% far away from the plasma zone, where the temperature is much lower and close to ambient. However, due to the high uncertainty on σ_{H/H_2} of 10%, the minimum uncertainty of T_g translates to about 20% and marks the limitation of the present methodology. Therefore, an appropriate choice of collisional cross sections is necessary for an accurate measurement of gas temperature. Moreover, the uncertainty analysis indicates that the propagation of errors is minimum when $\gamma \rightarrow 1$. For example, errors emerging from different components can be amplified up to two times when $\gamma_i = 0.5$ (see Equation 4.36). Such collisional conditions would ensure the thermal equilibrium of heavy species²⁴², which is key to the validity of equation 4.33.

4.7.2 Validation of the novel proposed approach

For the pressure and power conditions examined, the plasma is highly collisional with τ_H ranging between 100 and 450 ps while $\gamma_H > 0.95$ (calculated using $A_{H(n=3)} = 4.41 \times 10^7 \text{ s}^{-1}$ for Balmer α line²⁴³) as shown in Figure 4.17. τ_H decreases with increasing pressure, indicating an increase in collisionality. Therefore, in principle, one single fluorescence signal should be sufficient to measure simultaneously the H-atom density and the gas temperature.

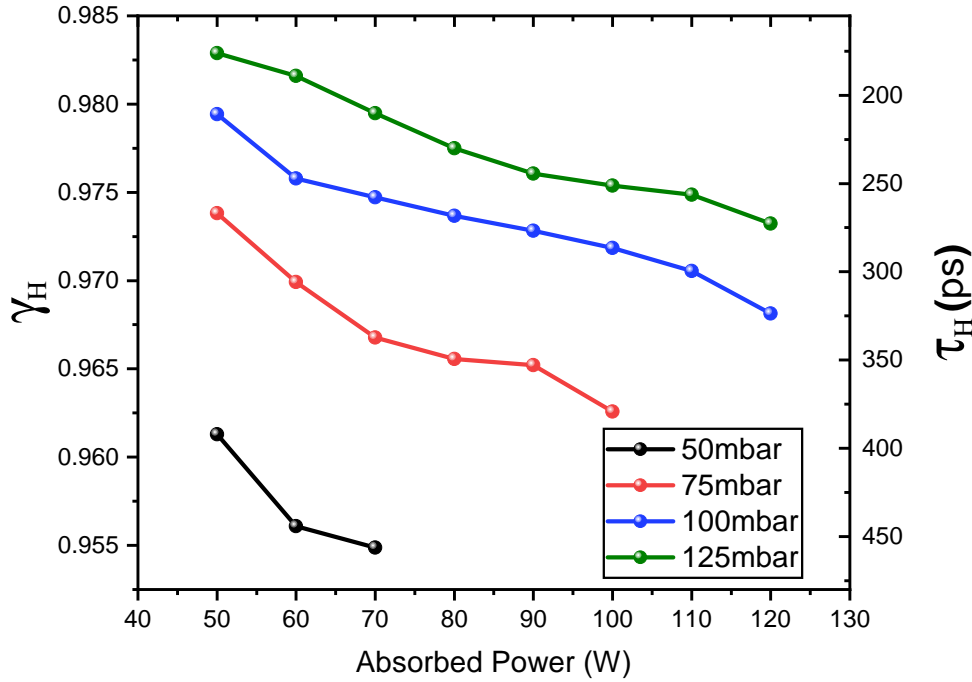


Figure 4.17: Variation of τ_H extracted from ps-TALIF signals and corresponding γ_H as a function of pressure and power for the experimental conditions considered

The high collisionality would mean that complex radiative processes that are associated with the $H(n=3)$ level have little influence, and collisional processes dictate the values of τ_H . Therefore, as evident in equation 4.33, knowledge of all collision quenchers and the corresponding composition and cross section is necessary. H_2 is the main quencher with $\sigma_{H/H_2} = 98 \pm 10 \text{ \AA}^2$ ²⁴¹ while the H-atom is a weak quencher with a much smaller $\sigma_{H/H}$ of 3.8 \AA^2 ²⁴⁴.

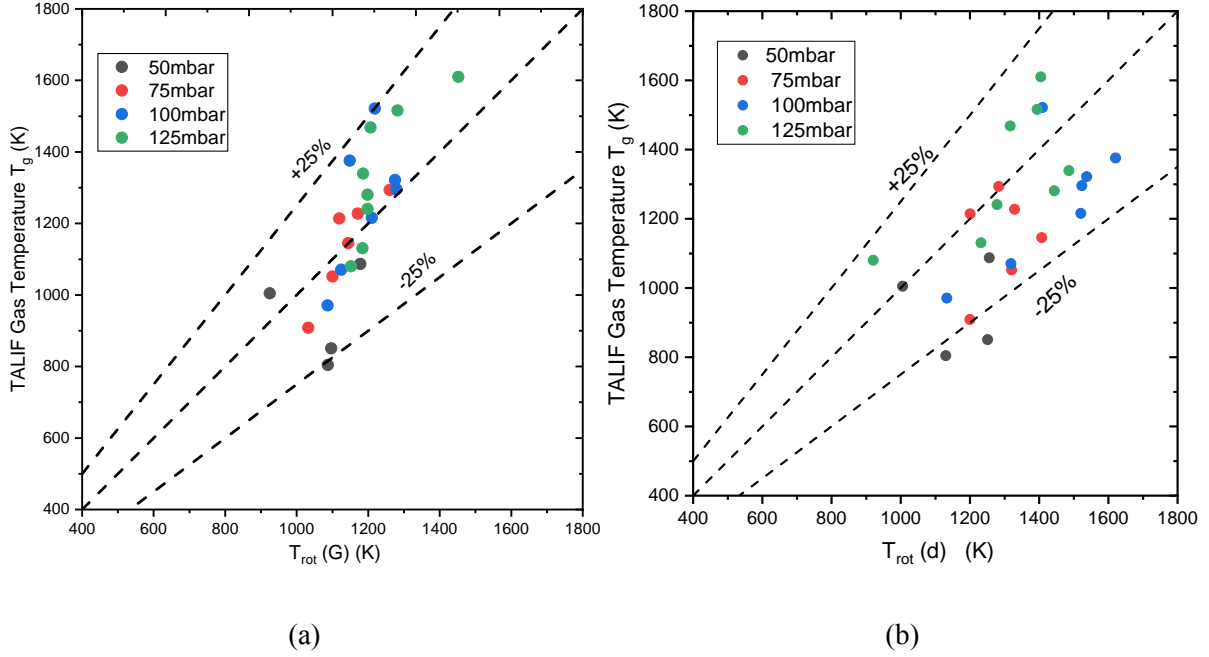


Figure 4.18: Parity plot comparing gas temperature measurement from ps-TALIF using $\sigma_{H/H_2} = 98 \text{ \AA}^2$ with rotational temperatures (a) $T_{rot}(G)$ and (b) $T_{rot}(d)$.

The gas temperature values obtained from τ_H representing the emissive region of the plasma are compared to the rotational temperature determined from the emission spectra of $T_{rot}(G)$ and the upper and lower rotational temperature limits ($T_{rot}(d)$ and $T_{rot}(X)$) of the Fulcher- α band. The gas temperature of τ_H compares well with $T_{rot}(G)$ and is about 300 K lower than $T_{rot}(d)$ at 100 mbar. $T_{rot}(G)$ and T_g from τ_H compare well within the margin $\pm 25\%$ for the entire range of pressure and power studied, as shown in Figure 4.18(a). Likewise, the relative difference between the values of $T_{rot}(d)$ and the T_g inferred from τ_H is within $\pm 25\%$, although with greater scatter than in the former case, as seen in Figure 4.18(b). In addition, we used Pearson's correlation coefficient, which is a measure of the linear relationship between two variables, ranging from -1 (perfect negative correlation) to +1 (perfect positive correlation). The Pearson correlation coefficient between $T_{rot}(G)$ and T_g is much better (~ 0.80) than between $T_{rot}(d)$ and T_g (~ 0.60). This is also indicative of the fact that $T_{rot}(G)$ is a better representative of T_g than $T_{rot}(d)$ in the pressure and power ranges considered in this study.

The differences between the measurements of gas temperature from the τ_H and rotational temperatures from the G-band are partly due to the spatial variation of the gas temperatures which is actually captured in the raw fluorescence images, while the emission spectra capture the entire emissive volume.

4.7.3 Spatial distribution of T_g and n_H

The major advantage of the proposed new method of gas temperature measurement is that gas temperature is accessed directly, as against methods that require equilibrium between rotational and translational modes. Furthermore, the method allows for the simultaneous determination of the spatial distributions of the H-atom and the gas temperature. Figure 4.19 shows the 2D

contour plots of the density of the H-atom and the temperature of the gas under different pressure conditions. The x-axis is represented in pixels as axial calibration was not performed, while the y-axis refers to the z-direction with 0 corresponding to the first possible laser measurement, approximately 0.5 mm from the base of the torch.

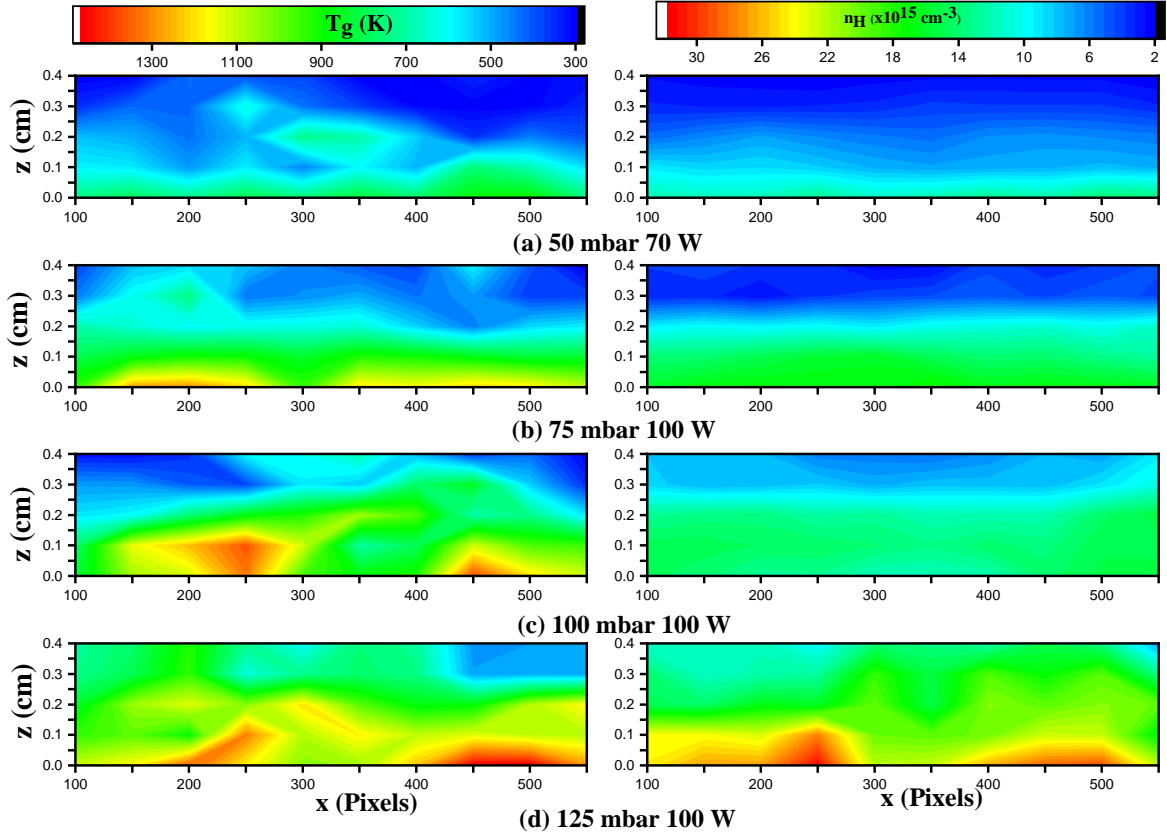


Figure 4.19: Constructed 2D contour plots of H-atom density and T_g for different pressures. The x-axis is in pixels, and the y-axis refers to z with 0 referring to the first possible laser measurement about 0.5 mm from the base of the torch.

Both H-atom and T_g are much more homogeneous axially at lower pressures such as 50 and 75 mbar. However, as pressure increases, it can be clearly recognized that two local hot zones are separated by a cold zone close to the $z = 0$ plane, indicative of the annular shape of the microplasma. One can clearly observe that there is a strong hydrogen dissociation locally in these hot zones at 125 mbar, which is absent at lower pressures. This is representative of the plasma-MW coupling, where the volume plasma decreases and the MW power density increases with pressure as shown in figure 4.13. These spatial variations of both the H-atom and T_g could not be visually deciphered from the raw fluorescence signals and could only be deduced from the post-treatment of these signals. More importantly, the method was able to capture the strong temperature gradients within the microplasma. The temperature differences between the hot zones and the surrounding regions were as high as 600 K. Also, there is a sharp decrease in temperature and H-atom density away from the plasma discharge, which are homogeneous within 3 mm from the plasma region. T_g becomes closer to the ambient temperature within about 5 mm of the discharge zone. However, there is still a substantial amount of H-atom (around $1 \times 10^{15} \text{ cm}^{-3}$) at such low temperatures, which indicates an enhanced chemical nonequilibrium effect

that may be interesting for applications involving the treatment of thermosensitive materials or the formation of carbon nanostructures, such as in our nanodiamond deposition process.

4.8 Conclusion

In this chapter, we characterized the MW-microplasma torch operating in pure hydrogen gas at pressures ranging from 50 to 125 mbar. Using OES and ps-TALIF, we determined key plasma parameters such as gas temperature, electron density, and atomic hydrogen density. We observed that plasma evolution follows several regimes, marked by initial plasma expansion, its development into a stable circular shape, and then the appearance of a secondary plasma at critical power values. The results showed that G-Band gives a reliable gas temperature that increases with MW power and pressure in the range 1000 K-1400 K. On the other hand, the electron density ($2 \times 10^{13} \text{ cm}^{-3}$) is nearly constant overall under operating conditions, while the atomic hydrogen density is almost constant with power and increases with pressure. The highest values of electron and H-atom densities are reached in the stable and full plasma regime. These are the conditions at which the deposition of carbon nanostructures will be performed. The formation of carbon nanostructures under such H-atom-rich conditions will be studied in the next chapter.

Chapter 5

Carbon nps in H-rich CH₄ plasmas

Contents

5.1	Introduction	87
5.2	Characterization of carbon nanostructures	88
5.2.1	Morphological and structural analysis of carbon nanostructures . . .	88
5.2.2	Evaluation of the abundance of sp ³ phase	90
5.3	Carbon NPs produced in H ₂ /CH ₄ plasmas	92
5.3.1	Characterization of H ₂ /CH ₄ plasmas	93
5.3.2	Effect of MW power on carbon NPs	95
5.3.3	Effect of pressure and methane on carbon NPs	96
5.3.4	Influence of Argon on nanodiamond yield	99
5.4	Investigation of NDs nucleation mechanisms	102
5.4.1	Consistency Across Substrates	104
5.4.2	Effect of substrate temperature	105
5.4.3	Application of substrate bias	106
5.4.4	Time-Dependent Deposition Studies	107
5.4.5	Carbon nanostructures collection in different deposition zones . . .	108
5.4.6	Transfer of nanodiamonds to solution	110
5.5	Discussion on nucleation of nanodiamonds	110
5.6	Conclusions	115

5.1 Introduction

This chapter discusses the quality, morphology and yield of carbon nanostructures, particularly nanodiamonds, synthesized using the MW plasma torch with CH₄ as a hydrocarbon precursor and with and without argon. The first part of the chapter is dedicated to the characterization of carbon

nanostructures through morphological and structural analysis. We also discuss the abundance of sp³ carbon, i.e. the diamond phase. In the second part, we present a parametric study of the synthesis of carbon nanoparticles synthesis in H₂/CH₄ mixture (\pm Ar). We correlate the material characteristics with the plasma local parameters as inferred from optical diagnostic. The objective is to find the best conditions for the formation of nanodiamonds. We also investigated whether the formation of diamond nanoparticles is affected by the characteristics of the substrate. Subsequently, the possible nucleation pathways of nanodiamonds are discussed with the aid of a 0D global model.

5.2 Characterization of carbon nanostructures

5.2.1 Morphological and structural analysis of carbon nanostructures

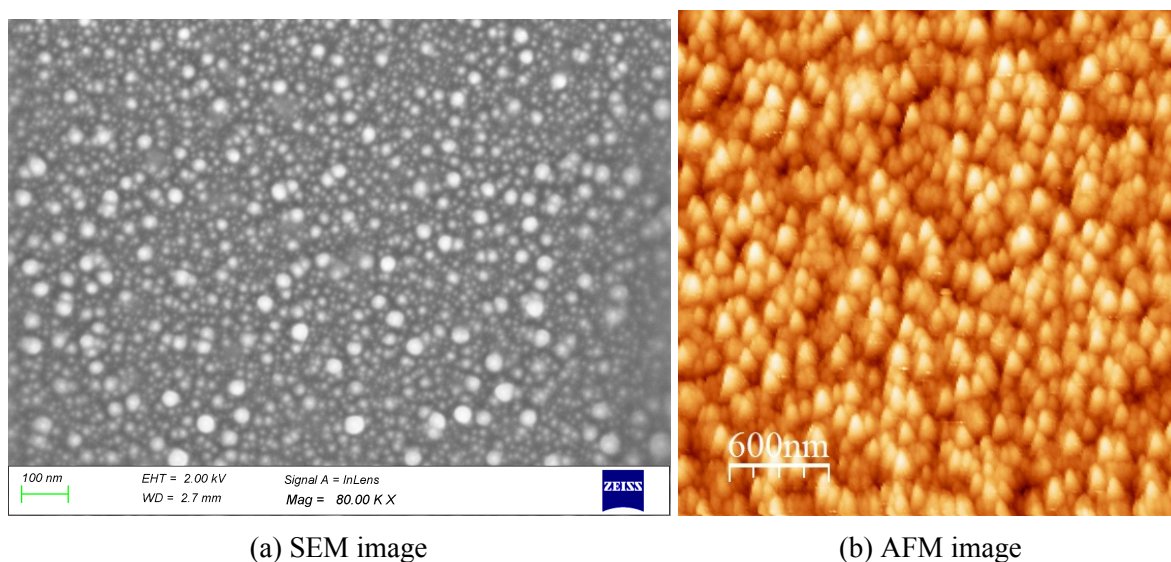


Figure 5.1: Experimental conditions: Gas composition 96:4 H₂/CH₄, Pressure = 100 mbar, MW power = 90 W.

Carbon nanostructures could be collected on the substrate and visually observed for most of the working conditions of the plasma and collection system. All carbon nanostructures characterized in this chapter were collected in the heating/biasing collection chamber (Figure 3.2) on a substrate placed 1 cm below the plasma torch for one hour of operation where neither the substrate was heated nor bias was applied. Energy-dispersive X-ray spectroscopy (EDX) revealed that the observed nanostructures are mainly composed of carbon (C), with minor traces of oxygen (O) and silicon (Si). These impurities are probably due to contamination by the silicon substrate during material characterization experiments and oxidation by the ambient atmosphere when the sample is extracted from the plasma reactor for characterization purposes. The AFM, SEM, and TEM characterizations clearly showed the deposition of agglomerated nanostructures with an approximate particle size of 10 nm. Figure 5.1 reveals the morphology of carbon nanostructures, collected at 100 mbar and 90 W MW power for a gas composition of 96:4 H₂/CH₄ characterized, using SEM and AFM imaging techniques. At 80,000x magnification, the

SEM image (Figure 5.1a) shows a dense and uniform distribution of particles on the substrate surface. The particles appear as white spheres on a gray background, indicating a relatively homogeneous size with a slight variation in diameter. The 100 nm scale bar is used as a reference to estimate the dimensions of the observed particles. Carbon nanoparticles appear as fine and well-dispersed grains, typical of high-purity materials^{34,137}. Figure 5.1b shows an AFM image of carbon nanostructures taken at a scale of 600 nm, which reveals a densely packed and uniform distribution of the nanostructures.

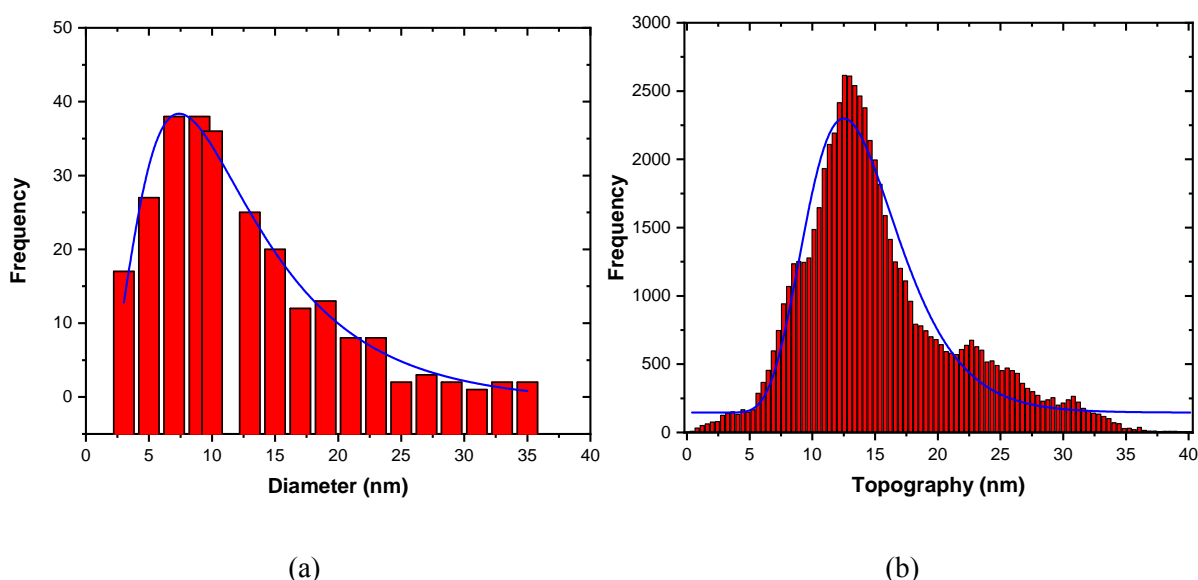


Figure 5.2: Particle size distribution using (a) SEM and (b) AFM

Figure 5.2 shows the size distribution of DNPs obtained from the SEM and AFM images depicted in Figure 5.1. The particle size distribution was measured from SEM images using ImageJ software. This is a histogram with a superimposed lognormal distribution curve. The x-axis represents the particle diameter in nanometers, and the y-axis represents the frequency of each size interval. The particle distribution is asymmetrical, with a long tail for larger sizes and a maximum frequency between 8 and 10 nm. The log-normal distribution of the particle populations revealed by the SEM image a mean diameter $d_c = 10.86$ nm and a standard deviation $w = 0.62$ while that of the AFM data fits a log-normal distribution with a mean diameter $d_c = 13.63$ nm and a standard deviation $w = 0.294$.

TEM images and SAED patterns confirmed the crystalline nature of the nanostructures, while EELS spectra demonstrated the presence of hybridized carbons of sp^2 and sp^3 (cf. Figure 5.3). Figure 5.3a presents the TEM image of carbon nanostructures collected with a power of 90 W. The image reveals hybrid nanostructures composed of both graphitic carbon and diamond. The observed d-spacings of 0.21 nm and 0.35 nm correspond to the planes (111) of diamond and planes (002) of graphite, respectively. Figure 5.3b shows the selected area electron diffraction pattern corresponding to the TEM image. The crystalline nature of the collected carbon nanostructures is confirmed by the observation of concentric rings in the electron diffraction patterns, strongly indicating the presence of the diamond plan (111), (220) and (311). The electron energy loss spectroscopy (EELS) spectra of the carbon nanostructures

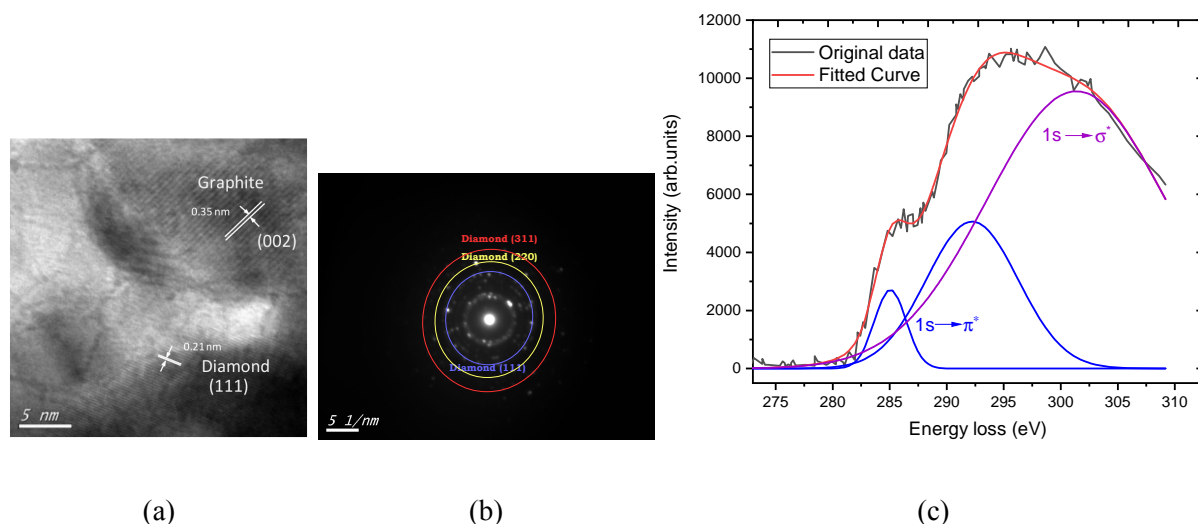


Figure 5.3: (a) TEM image of carbon nanoparticles at a resolution of 1.8 Å, its corresponding (b) selected area electron diffraction with blue circle refers to the (111) plane and red circle to the (311) plane of diamond phase and (c) EELS spectra of carbon nanoparticles. Experimental conditions: CH₄ = 4 sccm, H₂ = 96 sccm, pressure of reactor = 100 mbar, MW power = 90 W.

are presented in Figure 5.3c. Two important peaks are observed in the spectrum: the peak π^* at about 285 eV, corresponding to the carbon hybridized sp^2 , and the peak σ^* at about 290 eV, corresponding to the carbon hybridized sp^3 ²⁰.

5.2.2 Evaluation of the abundance of sp^3 phase

The quality of nanodiamonds in the collected carbon nanostructures can be described by the sp^3/sp^2 hybridization ratio. A high proportion of sp^3 bonds is characterized by a high ratio, which indicates a diamond-rich nanostructure. However, a low ratio indicates the presence of a high proportion of sp^2 bonds, characteristic of the graphite phase. Quantitatively, this quantity can be obtained from Raman and XPS analysis.

Figure 5.4a shows an example of typical Raman spectra found in the collected carbon nanostructures containing nanodiamonds. The different individual Raman bands are also indicated that were obtained using a deconvolution procedure. The structures corresponding to these bands are discussed in Table 5.1. Deconvolution of the Raman spectra of carbon nanostructures, as produced in the torch, is challenging, because of the broadened overlapping bands. Moreover, the signal-to-noise ratio of the Raman signals from our samples turned out to be quite low because of the low deposit quantity. As a consequence, the interpretation of the Raman data is not straightforward, and special attention needs to be paid to fit the raw Raman data with the different peaks. In particular, isolating diamond bands is difficult due to the proximity of the broadened D band and the Diamond peak^{247,248}. Furthermore, there can be appreciable shifts and broadening of the different bands. For example, nanodiamonds display a broadening of Diamond band as large as 40 cm^{-1} ^{247,248}. Various methods have been suggested to deconvolute the different peaks. However, there is no clear consensus on the profile of the Raman bands. Some studies recommend the use of Gaussian profiles^{253–255}, while other equally significant studies suggested

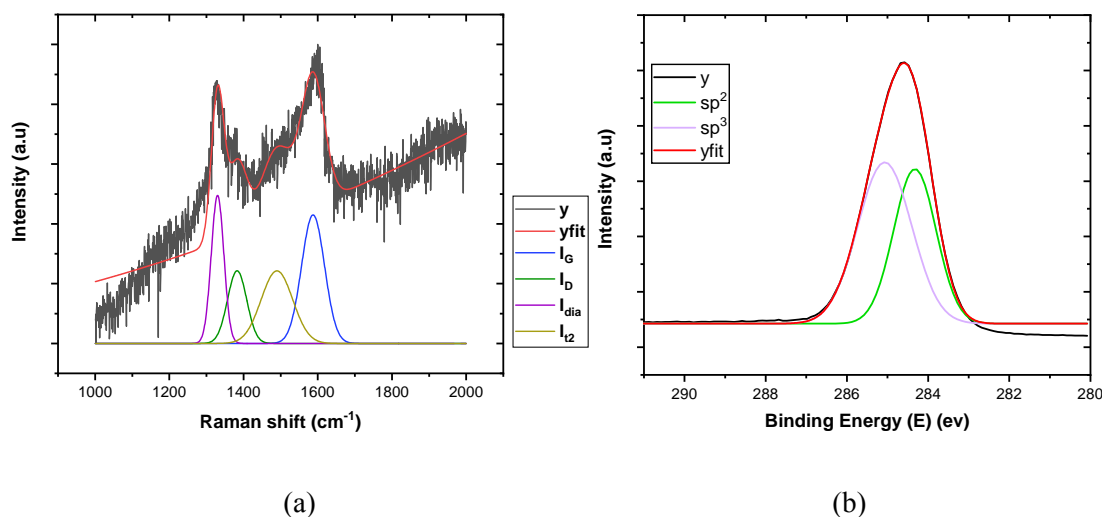


Figure 5.4: An example of (a) Raman spectra and (b) XPS C1s line observed for carbon nanostructures produced in the torch. Also shown are the deconvolution of the raw spectra to identify individual Raman bands and deconvolution of XPS C1s line to sp^3/sp^2 configuration.

Table 5.1: Key spectral features of interest in the Raman spectra of carbon nanostructures.

Spectra	$\nu \text{ cm}^{-1}$	Characteristics	Symbol
D-Band	1350	Indicative of disordered sp^2 carbon structures, commonly associated with defects and disorder in the graphite lattice ^{190,191} .	I_D
G-Band	1550	Represents the E_{2g} phonon of sp^2 carbon domains, signifying the presence of graphitic carbon.	I_G
Diamond	1332	This peak is typically sharp in high-quality bulk diamonds. Asymmetrically broadened and blue-shifted to 1329 cm^{-1} due to phonon confinement effects in nanometer-sized diamond grains ^{245,246} . The presence of small nanodiamond particles leads to broadening and overlapping of peaks in the Raman spectra ^{246–248} .	I_{dia}
Transpolyacetylene (TPA) μ_1 mode	1480	Associated with the transpolyacetylene chains (C=C stretch), related to the μ_1 vibrational mode ^{249–251} .	I_{t2}
Transpolyacetylene (μ_3 mode)	1130	Associated with the transpolyacetylene chains (C-H in plane bending), related to the μ_3 vibrational mode ^{192,249,252} .	I_{t1}

the use of Lorentzian profiles^{256,257}. Voigt profiles, Gaussian-Lorentzian combinations, have also been used^{191,258,259}. In general, the Gaussian profile is associated with non-homogeneous peak broadening in amorphous materials, while a Lorentzian profile assumption is used when homogeneous broadening dominates, as in bulk crystalline materials²⁶⁰. The Raman band of the synthesized nanostructures could be fitted by both Lorentzian and Gaussian, which would indicate that the nanostructures contain a high degree of disordered materials. This behavior has already been observed in the case of nanodiamonds with a size less than 20 nm. Therefore, to simplify the analysis, we adopted a deconvolution procedure that assumes Gaussian profiles

for the different bands and uses a least-square fitting procedure with constraints on the peak position and FWHM. A Python code was developed to automate the deconvolution process and was employed throughout the thesis.

The quantity ratio of the phases of sp³ to sp² (cf. equation 5.1), is determined from the intensity ratio of the diamond peak (I_{dia}) to all non-diamond peaks, ie, the G and D band of the graphite and trans-polyacetylene bands.

$$sp^3/sp^2 = \frac{I_{dia}}{I_G + I_D + I_{t1} + I_{t2}} \quad (5.1)$$

The sp³ fraction, can be evaluated using^{102,103}.

$$sp^3(\%) = 100 \cdot \left(\frac{60 \cdot I_{dia}}{60 \cdot I_{dia} + \sum I_{non-diamond}} \right) \quad (5.2)$$

where I_{dia} is the Raman diamond peak, which represents the sp³ phase, and $\sum I_{non-diamond}$ is the sum of the Raman non-diamond peaks. Therefore, $\sum I_{non-diamond} = I_G + I_D + I_{t1} + I_{t2}$. The factor 60 contained in the equation represents the Raman signal efficiency factor between the non-diamond and sp³ phases, estimated for the excitation wavelength of 473 nm^{102,103,261}. The degree of defect or disorder can also be assessed by Raman spectroscopy using either the intensity ratio of the D-band to the G-band of graphite (I_D/I_G) or the intensity ratio of the μ_1 -TPA-band to the G-band (I_{t2}/I_G).

XPS analysis of the deposits was used to measure the sp³/sp² mass-ratio. Figure 5.4b shows the fit of the C1s peak with the sp³ and sp² components. A Voigt function was used to separate the contributions of sp² and sp³^{262–264}. The carbon peak of sp² is around 284.5 eV while the carbon peak of sp³ is 285.4 eV. The peaks between 286 and 289 eV are C1s emissions linked to carbon-oxygen bonds, in particular C-O and C=O²⁶³ bonds. The intensities and positions of these peaks can be used to identify the type of oxygen functionalities on the surface. As the XPS sensitivity factor is not affected by the chemical state of the atoms²⁶³, the relative fraction of each carbon component (sp² and sp³) was calculated on the basis of the integrated area under the corresponding peaks.

Figure 5.5 shows the variation of the sp³/sp² ratio as a function of CH₄ concentration (% CH₄) at 100 mbar and the 90W power deduced from Raman spectroscopy and XPS measurements. Given the good agreement between the two, Raman spectroscopy was used extensively to evaluate the sp³/sp² mass-ratio in the remainder of the thesis, due to easy access to the Raman spectrometer in our laboratory. It is clear from Figure 5.5 that the concentration of methane has a significant effect on the nature of the deposit, i.e. sp³/sp² mass-ratio. The effect of the plasma conditions on the characteristics of the carbon nanostructures is discussed in the next section.

5.3 Carbon NPs produced in H₂/CH₄ plasmas

A variety of carbon nanostructures have been collected for different precursor feed gas compositions (hydrogen and methane), working pressure, and injected MW power.

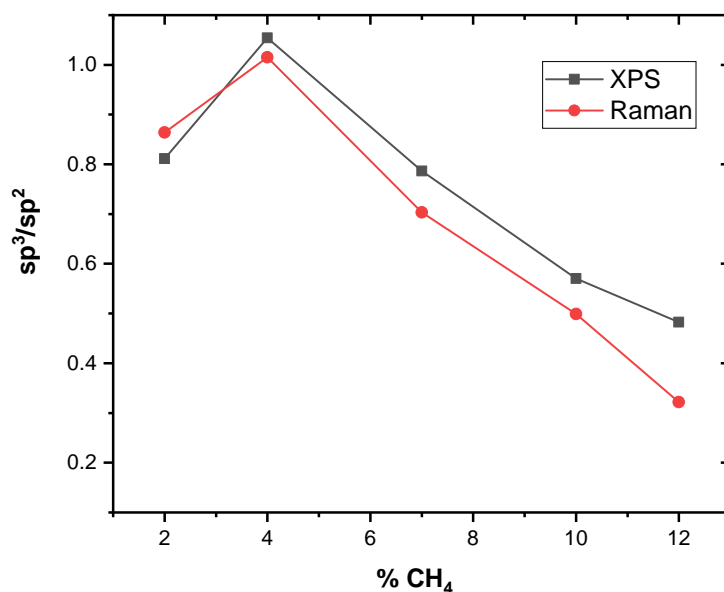


Figure 5.5: Variation of the sp^3/sp^2 ratio as a function of methane concentration measured by XPS (black) and Raman (red). Experimental conditions: Total flow-rate = 100 sccm with mixture H_2 and CH_4 , Pressure = 100 mbar, substrate = silicon, distance plasma-substrate = 1 cm and deposition time = 1 h.

5.3.1 Characterization of H_2/CH_4 plasmas

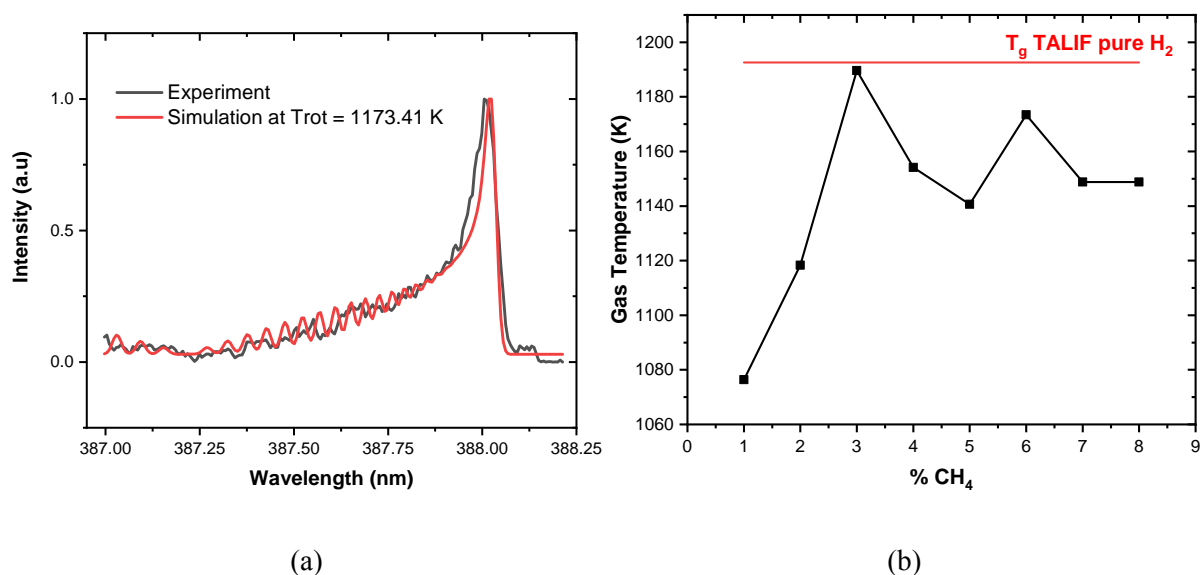


Figure 5.6: (a) Example of CN profile obtained with the conditions : $CH_4 = 6\%$, $H_2 = 94\%$, Pressure = 100 mbar and Power = 90 W and (b) Variation of gas temperature with methane concentration in the CH_4/H_2 mixture. Experimental conditions : $CH_4 + H_2 = 100$ sccm, Pressure = 100 mbar, Power = 90 W.

It is important to state here that the H_2 rich conditions, i.e., the concentration of methane $< 20\%$, used in the present study do not alter the operation regimes of the present torch. The transition from the “full circle” regime to unstable conditions occurs at the same power as that of pure H_2 plasma. This would mean that plasma properties such as electron density and

temperature and volume would be of similar orders of magnitude as those reported in Chapter 4. Efforts were made to access the influence of methane on the gas temperature and the density of H atoms. Unlike the case of pure hydrogen plasma discussed in section 4.4, it was not possible to use the G-band to determine the rotational temperature with the CH₄/H₂ mixture due to the strong overlap of the lines from the C₂ Swann band. Consequently, it was also not possible to use bands of C₂ Swann, CH(A-X) and CH(B-X) as there were strong overlaps with other systems. A small amount of N₂ gas was added to the plasma and the rotational temperature (T_{rot}) of the CN violet band $B^2\Sigma^+-X^2\Sigma^+$ (0, 0) located around 387.5 nm^{265–267} was used to study the variation of the gas temperature. The addition of 1% N₂ ensures sufficient CN formation for the measurements without significantly altering the thermal dynamics of the mixture. Although the system overlapped with the CH (B-X) system, the CN spectrum was relatively strong and therefore was used to estimate the influence of CH₄ on the rotational temperature and thus the gas temperature. Measurement of rotational temperature using the violet CN system in a plasma involves minimizing the difference between the observed and simulated emission spectrum of the CN ($B^2\Sigma^+-X^2\Sigma^+$ (0, 0)) transition as illustrated in Figure 5.6a. The mismatch between the two spectra is due to the overlap of the CH band. However, this band has been used to access the influence of methane on the gas temperature. Figure 5.6b shows the variation in the gas temperature as a function of the methane concentration in the mixture at a pressure of 100 mbar and a power of 90 W. The gas temperature is observed to vary very little with the concentration of methane with 1143.7 ± 32.3 K for the range of methane concentrations considered in this work. Therefore, one can conclude that the gas temperatures of hydrogen rich hydrocarbon plasmas are similar to the temperatures of a pure hydrogen plasma discussed in sections 4.4.3 and 4.7.2.

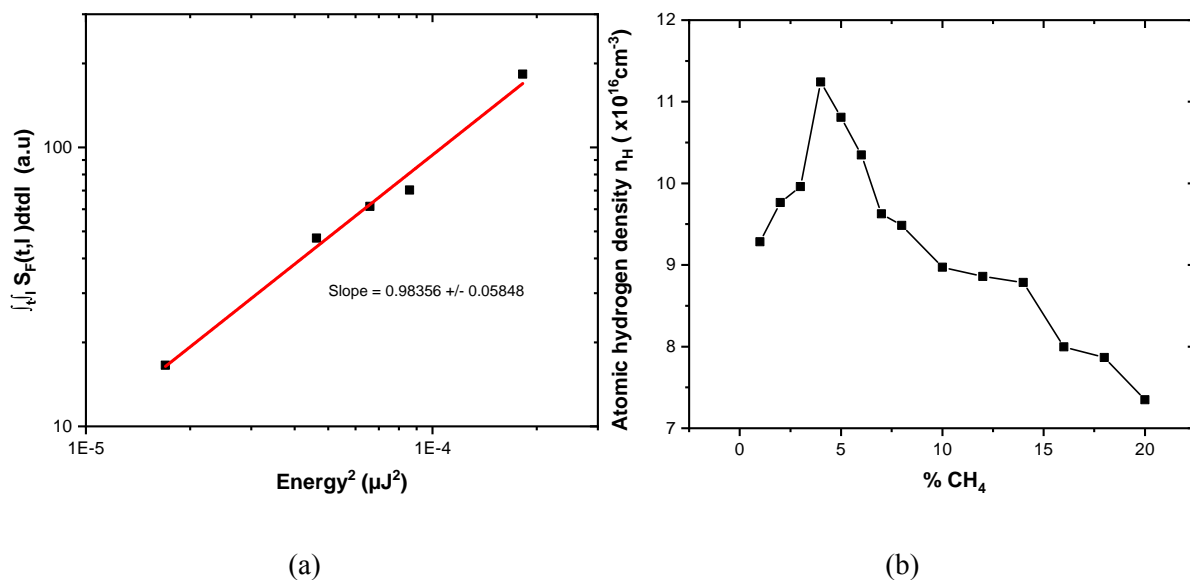


Figure 5.7: (a) Variations of SFi as a function of laser energy for H. Experimental conditions: CH₄ = 7% and H₂ = 93% , (b) n_H as a function of CH₄ concentration at 100 mbar and 90W from ps-TALIF.

However, the situation is different for the concentration of H atoms, as the hydrocarbon chemistry is dictated by the H atoms and the H₂ molecules. The H-atom density has been

measured using ps-TALIF. Performing ps-TALIF experiments in hydrocarbon plasma was much more challenging, as compared to the same measurements in H_2 -plasma. First, the high intensity of the ps laser can dissociate hydrocarbon species such as CH_4 , CH_3 , etc. to produce an H-atom. The laser-induced production of H-atoms will render the H-atom measurements erroneous. Therefore, efforts were made to make sure that the laser energy was sufficiently small to avoid such auxiliary laser-based processes. The quadratic regime for methane (as required by Equation 4.29) was verified for different conditions, and an example is shown in Figure 5.7a. The other major issue in performing laser-based experiments in a hydrocarbon plasma was the deposition of carbon nanostructures on the optical windows of the chamber. Therefore, to reduce carbon deposits and ensure data reliability, the optical windows were cleaned every hour. In addition, the transmissivity of the windows was measured at regular intervals. These measured transmissivities were taken into account when calculating the H-atom density. Independently, each data acquisition was repeated three times to account for repeatability. Gas temperature measurement from the TALIF fluorescence signal was also not pursued owing to the uncertainty of the quenchers and their quenching cross-section data and all the measurements reported for hydrocarbon plasmas are restricted to the zero point, just below the torch.

Figure 5.7b shows that the density of H atoms shows an almost 20 %-increase when the concentration of methane in the feed gas increases from 0 to 4%. The density of H-atoms reaches its maximum value for this last concentration of methane and then decreases significantly when methane is introduced further in the discharge. This behavior of the density of H atoms as a function of % CH_4 is observed for other pressure conditions. The significant increase in the concentration of H atoms at low methane concentration, i.e. $CH_4\% < 5$, is probably due to enhanced H atom production through electron impact dissociation of methane and increased electron density when methane is introduced into the plasma. However, because the main source of H atoms is the electron impact dissociation of molecular hydrogen, the decrease in the densities of H atoms for higher concentrations of methane is simply due to lower injected densities of molecular hydrogen. Secondly, the increased methane densities would increase the consumption of H-atoms through the H-shift reactions explained above and therefore further decrease the H-atom densities. In some way, the decrease in the density of H atoms with the concentration of methane could also explain the decrease in sp^3 content at higher concentrations of methane as observed earlier in Figure 5.5.

5.3.2 Effect of MW power on carbon NPs

The Raman spectra presented in Figure 5.8a show the influence of MW power on the characteristics of the carbonaceous materials formed. It can be seen that increasing the MW power leads to a variation in the graphite D- and G-band peaks, indicating a change in the sp^2 content. In particular, the diamond peak becomes more prominent at higher MW powers, indicating greater formation of sp^3 carbon structures. For MW powers above 70 W, a diamond peak emerges around 1332 cm^{-1} . The ratio of the peak at 1480 cm^{-1} to the G peak also increases with the power of MW, indicating a higher fraction of transpolyacetylene or related structures in the carbon network. Figure 5.8b presents the evolution of the sp^3/sp^2 ratio and the I_D/I_G ratio as

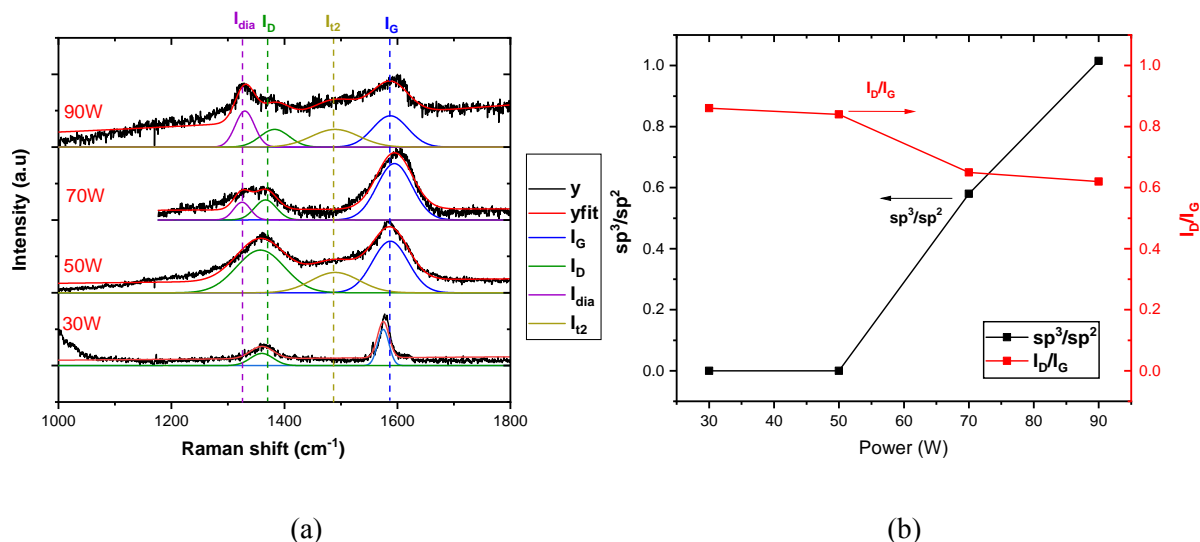


Figure 5.8: (a) The Raman spectra of the samples and (b) its corresponding sp^3/sp^2 (left) and I_D/I_G (right) ratio as a function of input power. Experimental conditions: CH₄ = 4 sccm, H₂ = 96 sccm, Pressure = 100 mbar, substrate = silicon, distance plasma-substrate = 1 cm and deposition time = 1 h.

functions of the MW power at these conditions. While the sp^3/sp^2 ratio (black line) increases with the MW power, the I_D/I_G ratio (red line) decreases. This inverse relationship suggests that as the sp^3 content increases and the amorphous content reduces. In Chapter 4, the gas temperature increased with MW power and the operating regime is a 'full circle' only above 80 W at a pressure of 100 mbar. However, the H-atom density did not change significantly with power. Note that the H-atom density produced by the torch is fairly high compared to the conventional resonating MW reactor used for CVD growth of diamond. This higher density of H-atoms would result in an enhanced stabilization of the diamond phase. The preferential formation of the diamond phase also depends on the amount of key primary hydrocarbon radicals, such as CH₃, available in the plasma. Because hydrocarbon chemistry is sensitive to both gas temperature and H-atom density, the observations suggest that the production of key radicals leading to the formation of a diamond phase in the carbon nanostructures should increase with these conditions.

5.3.3 Effect of pressure and methane on carbon NPs

Although several types of deposit have been collected, only conditions showing substantial amounts of nanodiamonds are reported here. Figure 5.9 shows the evolution of the carbon nanostructures inferred from their respective Raman spectra, as a function of pressure at a fixed power of 90 W and for a methane concentration varying between 1 and 12%. The MW power of 90 W ensured that the plasma was in the "full-circle" regime without the formation of secondary plasma for all the considered pressures. The quality of the diamond phase has been accessed through the ratio of sp^3 (I_{dia})/ I_G , amorphous-disordered (I_D) and transpolyacetylene (I_{trans}) with respect to the G-band as well as the % sp^3 content. The highest I_{dia}/I_G ratio associated with the large sp^3 fraction (around 86%), indicating the best diamond quality, is observed at 4%

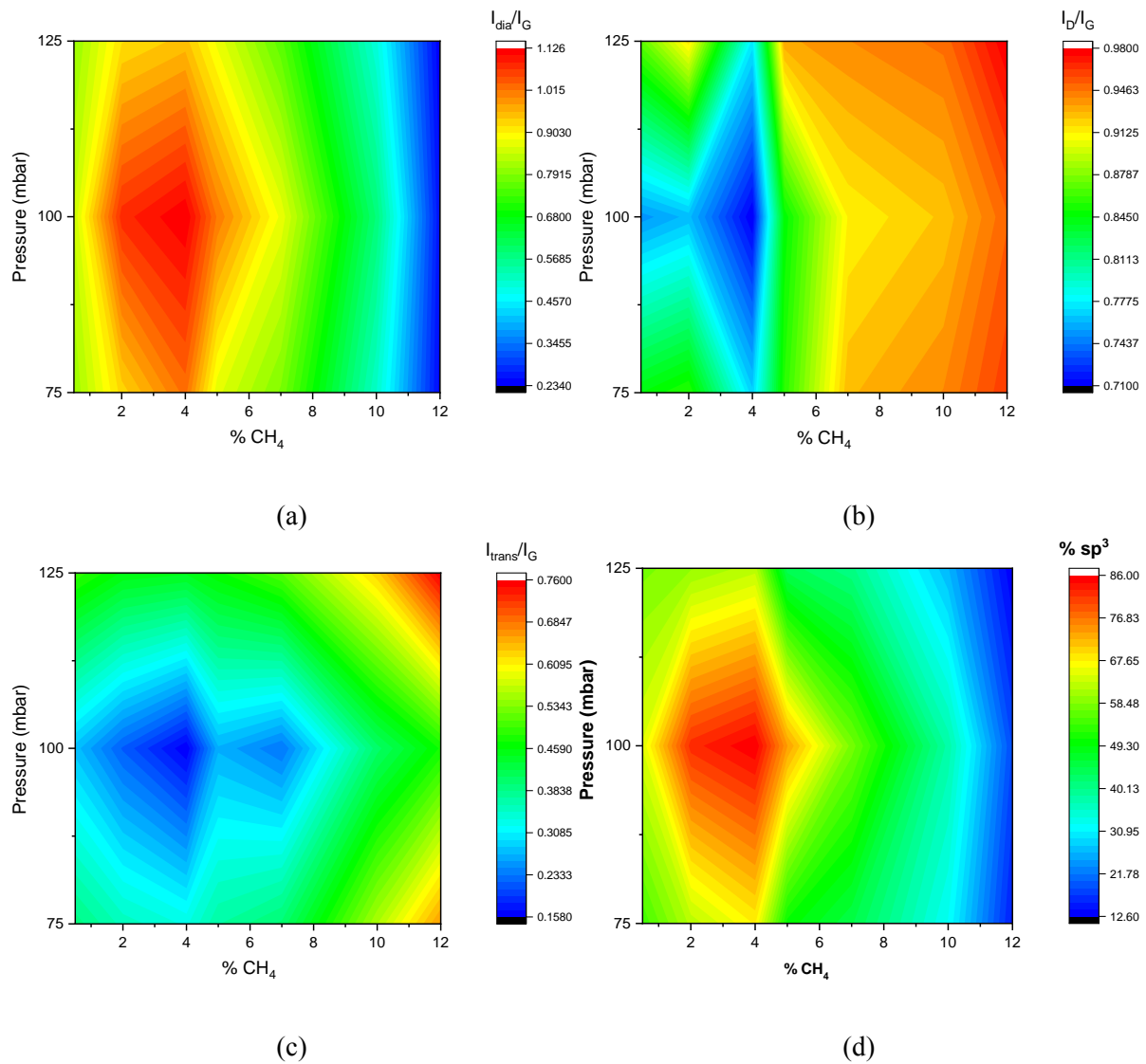


Figure 5.9: Distribution of (a) I_{dia}/I_G ratio, (b) I_D/I_G ratio, (c) I_{trans}/I_G and (d) sp³ fraction as a function of pressure and methane concentration.

methane concentration and a pressure of 100 mbar. This region is marked by the red color in the Figure 5.9a. This optimal point is also marked by the lowest I_D/I_G ratio as well as I_{trans}/I_G (represented by the blue area in Figures 5.9b and 5.9c). As a result, this condition corresponds to the maximum yield of the diamond phase, as evident in Figure 5.9d. In fact, for all investigated pressure conditions, the 4% of methane represents a maximum diamond phase, the other carbon phases having minimum values. Further, the I_{dia}/I_G ratio as well as sp³ fraction, also tend to decrease away from the optimal condition of 100 mbar and 4% methane concentration.

The amount of carbon nanostructures produced increases with methane concentration. This increase is due to the fact that there are more carbon atoms available, leading to the formation of various carbons (graphite, amorphous carbon, and diamond). Small concentrations of methane (< 2%) produced hardly any carbon nanostructures with predominantly sp² phase carbon. This could probably be explained by the lower concentrations of CH₃ (or other radical) necessary for the formation and growth of the diamond phase, while the formation of amorphous sp² carbon is

predominant. As methane concentration increases beyond 6%, the I_{dia}/I_G ratio as well as sp^3 fraction decreases. Unfortunately, an increase in the amount of methane seems to promote the formation of undesirable nanostructures, reducing the quality of synthesized nanodiamonds. This can be confirmed by the I_D/I_G and I_{trans}/I_G ratios which increase substantially with an increase in CH₄ concentration. The optimal condition of 4% should be indicative of a perfect balance between methane dissociation, the availability of carbon radicals needed to form sp^3 bonds, and the availability of H-atoms that ensure optimal metastability conditions, thus favoring the formation of nanodiamonds. When conditions deviate from this optimal zone, either by too high or too low pressure, or by inadequate H-atom density with respect to hydrocarbon concentration, the formation of sp^2 bonds becomes predominant, thus decreasing the quality of nanodiamond.

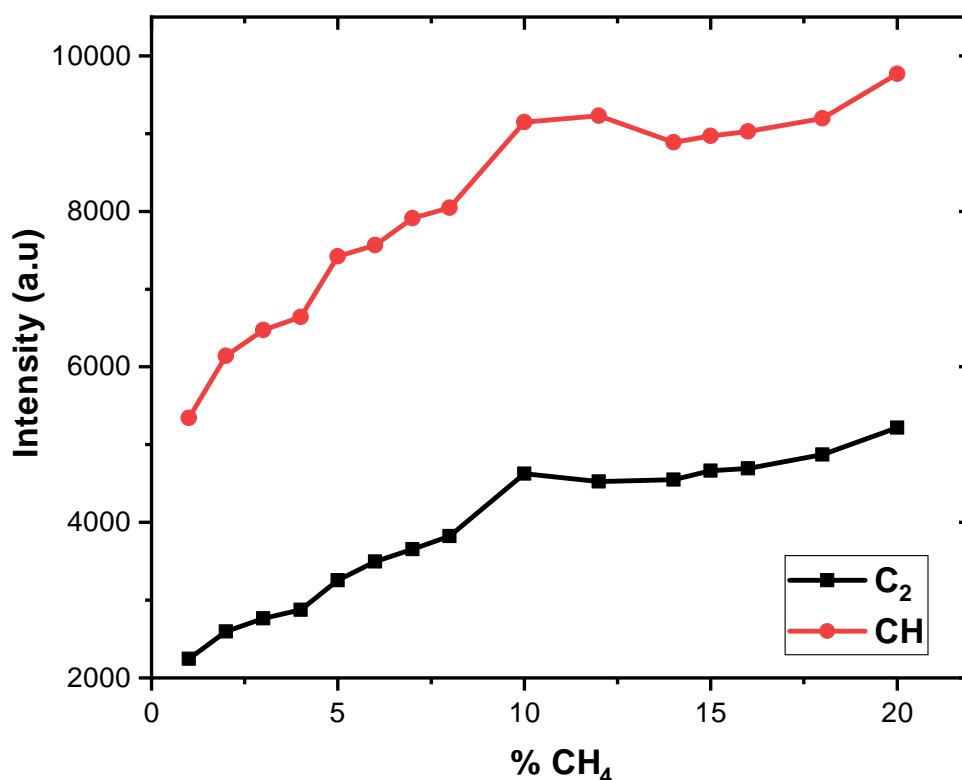


Figure 5.10: Evolution of C₂ and CH as a function of methane concentration at 100 mbar and 90W by OES as a function of methane concentration. Experimental conditions : Pressure = 100 mbar, Power = 90W and the total flowrate CH₄+H₂ = 100 sccm.

Efforts were made during the present thesis to make quantitative/qualitative measurements of carbon radicals C₂ and CH using laser induced fluorescence (LIF)²⁶⁸. This was motivated by the fact that the relative densities of CH and C₂ could be indicative of the CH₃ radical. In our study, we used an ns laser to excite the carbon radicals and record their fluorescence. Unfortunately, because of several technical limitations and a lack of time, these measurements could not be realized, and the experimental campaign was abandoned. However, since these two species are strongly emissive under the present conditions, OES was used to qualitatively monitor their evolutions as a function of methane concentration. The most prominent bands observed in our plasma correspond to the C₂ Swann ((0, 0) ($d^3\Pi_g \rightarrow a^3\Pi_u$)) at 516 nm and CH ($A^2\Delta \rightarrow X^2\Pi$ (0, 0)) at 431 nm. As methane concentration does not significantly affect

the plasma parameters in the investigated range of feed gas composition, the evolution trends of the emission intensities corresponding to these carbon radicals should be indicative of the density-variation-trends of the corresponding radicals in their electronic ground state. Figure 5.10 shows the evolution of the intensities of the C_2 and CH species as a function of the methane concentration measured at 100 mbar and 90 W. The graph reveals two regimes in the behavior of these species. In the first regime, when the methane concentration is below 10%, both C_2 and CH intensities increase linearly with increasing methane, indicative of the increase in the densities of methyl radicals. In the second regime that takes place beyond the 10% concentration of methane in the feed gas, the densities of these radicals remain constant. The difference in the emission trends between the two regimes for both C_2 and CH would indicate that the hydrocarbon chemistry in these two regimes is quite different. Clearly, to correlating the results of plasma and material characterization, small concentrations of methane are used to favor the formation of the diamond phase among other phases of carbon. This conclusion is not surprising, as it is seen in other reactive hydrocarbon systems such as conventional CVD diamond reactors or even flames²⁶⁹.

5.3.4 Influence of Argon on nanodiamond yield

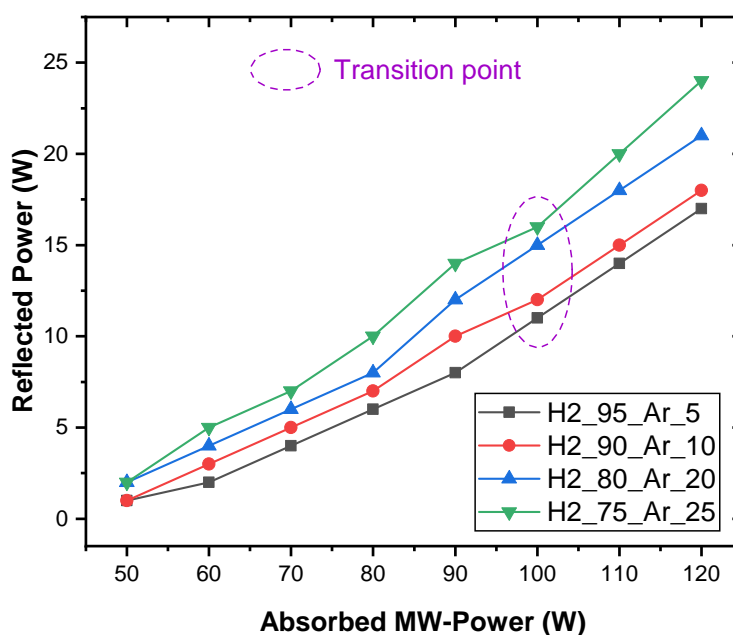


Figure 5.11: Representation of reflected power as a function of absorbed power at 100 mbar with different Ar/ H_2 mixture. The total flowrate Ar+ H_2 = 100 sccm.

This section discusses the effect of small amounts of argon on the quality and quantity of nanodiamonds. In order to evaluate the effect of Argon on nanodiamond formation, the working pressure and power were set to the value yielding the best yield of nanodiamonds in Argon-less plasmas i.e. 100 mbar and 90 W. Analysis of plasma stability at 100 mbar for different Ar/ H_2

mixture shows that the plasma becomes unstable at 100 W (cf. Figure 5.11). Here, the instability occurs at a lower power value compared to the pure hydrogen plasma, where the instability occurs at 120 W for a pressure of 100 mba. Therefore, the total flow rate of H₂ and CH₄ was set at 100 sccm and the argon flow rate was varied in the range 0-25 sccm, in which the plasma is stable without secondary plasma formation inside the torch upstream the open end. Even though the electron density has not been measured particularly for argon-laden plasmas, the increased reflection suggests that the addition of argon should increase the real part of the dielectric constant of the plasma (cf. Section 4.3) and therefore the electron density.

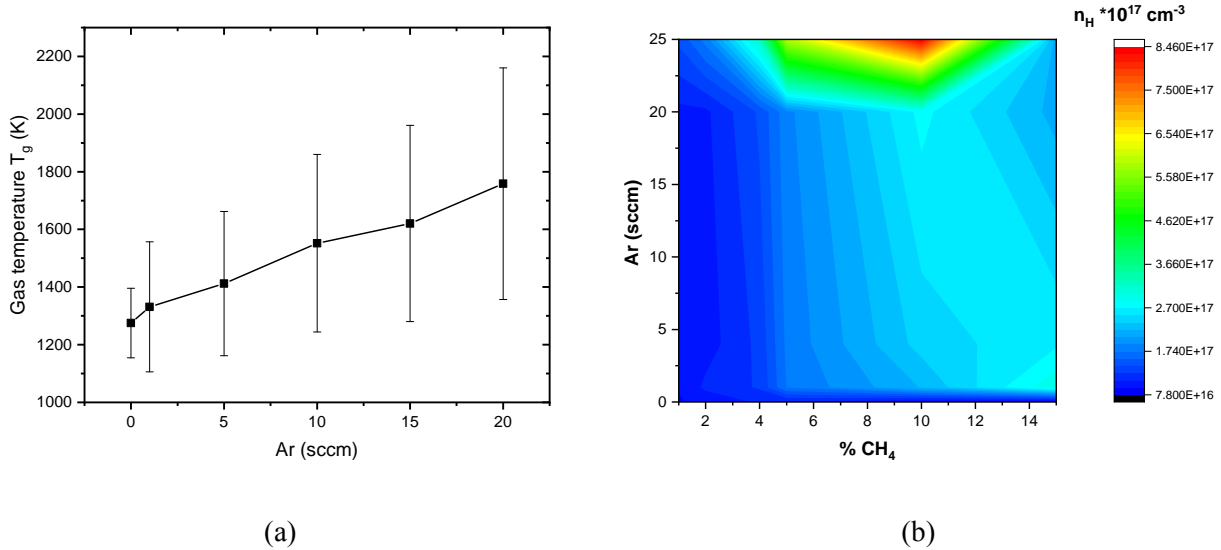


Figure 5.12: (a) Variation of T_g as a function of Ar flow rate and (b) n_H as a function of CH₄ concentration and argon flowrate (sccm) at 100 mbar and 90 W.

In the case of Argon, the gas temperature was estimated using the G-Band of hydrogen emission as highlighted in Chapter 3. As shown earlier for the case of H₂/CH₄ plasmas, one can assume that the influence of methane on gas temperature would remain negligible even for argon plasmas. However, the apparent change in the MW coupling when argon is introduced in the feed gas could have an impact on the gas temperatures. Therefore, the gas temperature has been evaluated from the rotational temperature of G-band in Ar-H₂ plasmas. Figure 5.12a shows the evolution of this temperature as a function of the argon flow rate in an Ar + H₂ plasma, the H₂ flow rate, pressure, and power being kept constant at 100 sccm, 100 mbar and 90 W, respectively. The consequence of the addition of argon was to increase the gas temperature from 1275 K to about 1750 K. This increase is likely due to an enhanced electron process along with a lower thermal diffusivity of the gas mixture. The H atom density was measured using ps-TALIF and steps were taken to ensure that acquisition was performed in the quadratic regime. The evolution of H-atom density as a function of methane concentration (% CH₄), and argon flow rate (in sccm) is presented in Figure 5.12b. The density of H-atoms is seen to increase by an order of magnitude when 20 sccm argon is introduced into the feed gas. The increased dissociation of H₂ could be due to the increase in gas temperature, the enhanced dissociation by electron impact processes and the reactive quenching of argon metastables by molecular hydrogen²⁷⁰. The variation of H-atom density with methane concentration follows trends similar

to those seen in the case of pure hydrogen plasmas with a maximum shift towards around 9% CH_4 concentration.

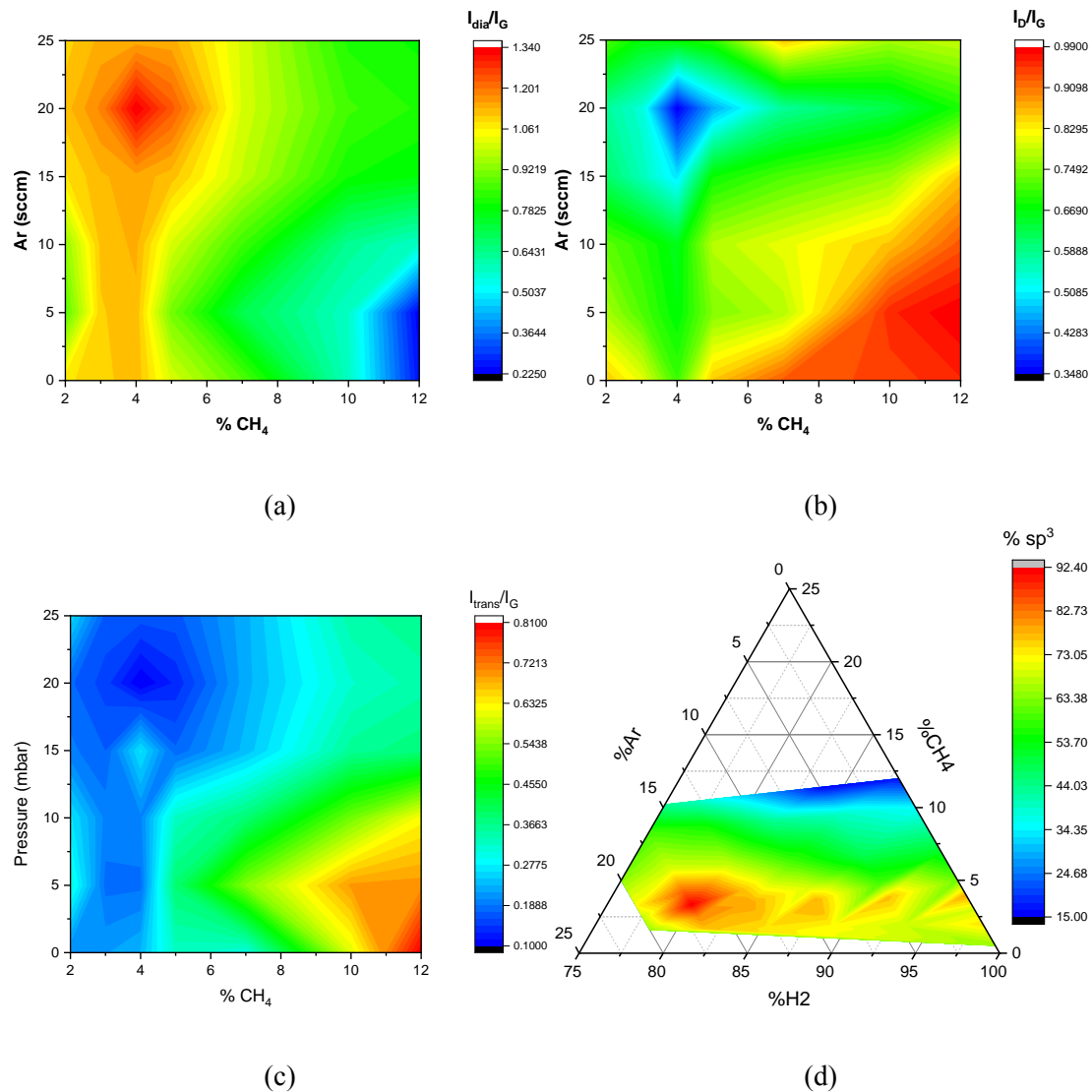


Figure 5.13: Distribution of (a) I_{dia}/I_G ratio, (b) I_D/I_G ratio, (c) I_{trans}/I_G as a function of Ar and methane concentration and (d) Ternary contour of mixture $H_2 + CH_4 + Ar$. Experimental conditions: Pressure = 100 mbar, Power = 90 W and the total flowrate $CH_4/H_2 = 100$ sccm.

The enhanced densities of H-atoms and gas temperatures affect the chemistry of hydrocarbons and the nature of the resulting carbon nanostructures. Firstly, argon-laden plasmas produce much more carbon nanostructures than argon-less plasmas. The optimal quality of nanodiamonds was obtained at 4% methane in the feed gas for all the investigated values of argon concentration. However, the quality of nanodiamonds is also sensitive to the absolute value of argon flow, and an optimal quality is obtained at 20 sccm. This behavior is represented by the red region in Figures 5.13a, where the minimum value of I_D/I_G and I_{trans}/I_G (Figures 5.13b and 5.13c with argon correspond to the optimal quality of the material. The addition of argon appears to improve the quality of nanodiamonds with sp^3 fraction reaching around 92%. The ternary

diagram shown in Figure 5.13d summarizes the diamond production zone by merging the results of H₄/CH₄ and H₂/CH₄/Ar mixture.

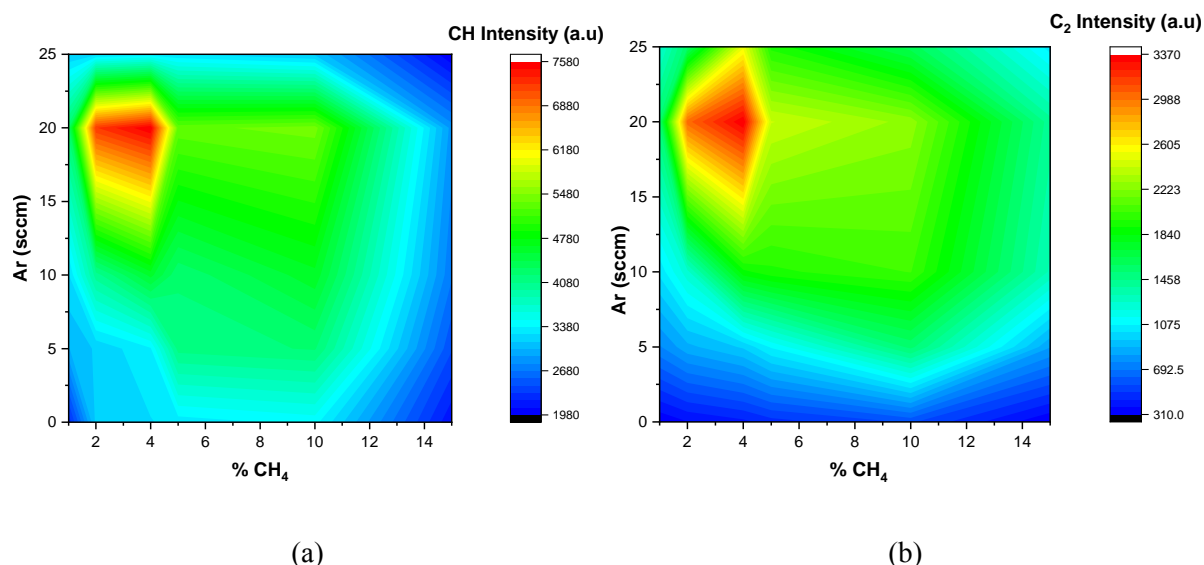


Figure 5.14: 2D Contour plot showing the evolution of (a) CH and (b) C₂ species as a function of methane concentration and argon flowrate. Experimental conditions : Pressure = 100 mbar, Power = 90W and flowrate of CH₄+H₂ = 100 sccm.

We investigated how the concentrations of some carbon-containing plasma species correlate with the characteristics of the produced carbon nanostructures. Figures 5.14a and 5.14b 2D contour plot of C₂ and CH radicals as a function of methane concentration and argon flow rate. The maximum emission intensities for both radicals can clearly be observed at 4% methane and 20 sccm Ar and this corresponds to the maximum quality of sp³ fraction in carbon nanostructures as shown in Figure 5.13. It is quite clear that these radicals should be important with respect to the diamond formation process. As CH is related to the CH₃ radical, increased amounts of CH would also indicate elevated amounts of CH₃. In correlation of the results of plasma diagnostics and material characterization, it can be concluded that elevated densities of H atoms in the presence of radicals CH₃ and C₂ are critical for nanodiamond formation.

5.4 Investigation of NDs nucleation mechanisms

Nucleation is the critical step in nanostructure formation, which influences the morphology and final properties of the materials. Recalling from Chapter 2, the nucleation of carbon nanostructures could occur due to either gas phase processes (cf. Figure 5.15) or surface processes (cf. Figure 2.4). This section is devoted to understanding the nucleation route that occurs during synthesis using the microplasma torch. The surface reactions leading to heterogeneous growth depend on the characteristics, composition, local plasma conditions at the substrate surface, and especially the substrate temperature and the availability of key radicals and sites on the surface⁷³. The relatively high energy of the interface between diamonds and other materials makes it difficult to induce diamond nucleation on non-diamond surfaces¹³⁷. In the present

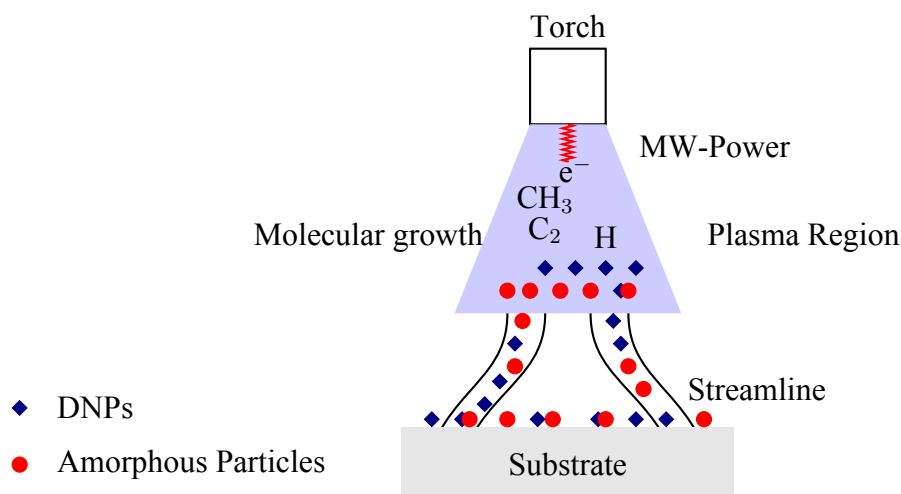


Figure 5.15: Schematic of gas-phase processes: molecular growth and nucleation and subsequent collection of NPs on the substrate

experiments, the major surfaces that come into contact with the reactive gas are the surfaces of the torch (central pin and surface) and the substrate located downstream the plasma where carbon nanostructures are collected. All of the experiments reported in the preceding section were performed on pristine substrates (Si) without any pretreatment or seeding and without heating. Normally, substrates are heated to very high temperatures (>800 C) in order to induce nucleation¹³⁷ which was not the case in the present condition. Even the outer surface of the torch was cooled to room temperature. However, the pin itself was not cooled and could have high temperatures that could potentially support nucleation sites for carbon, especially diamond. Moreover, being in the vicinity of the torch provides it with concentrations of key radicals and H-atoms. However, there was no visible deposition of carbon nanostructures on the surface of the pin around the optimal conditions supporting nanodiamond formation, and there were no signs of nanodiamonds in the Raman spectra of the pin as well. In fact, there is deposition on the pin only for very high concentrations of methane ($>10\%$) where nanodiamonds were not formed. In a way, the formation of these carbons at a high concentration of methane impedes the continuous running of the torch and thus has been mostly avoided.

For the present experimental configuration, gas-phase processes cannot be ruled out. Although the literature has shown evidence for gas-phase nucleation of nanodiamonds, the nucleation mechanism itself has not been identified. If all particles nucleated in the gas phase, the particles are transported by inertial drag and are collected on the substrate downstream due to impact. The collection efficiency would be poor as most of the particles formed in the gas phase may not stick to the substrate surface^{271,272}. The efficiency of particle collection can be influenced by several factors such as manipulating the forces acting on these particles. For example, the particles in the plasma are generally negatively charged as a result of the low mobility of electrons, and applying a positive bias can possibly attract these nanoparticles. However, creating steep temperature gradients helps to effectively collect nanoparticles due to thermophoresis forces. Further, even if the carbon nanostructures could not nucleate in the gas phase, growth of larger hydrocarbon molecules can occur in gas phase that may deposit on

the silicon substrate placed downstream, and therefore act as active sites to support growth and nucleation of nanodiamonds in the presence of CH₃ radical and H-atoms.

Therefore, in order to obtain a clear understanding of the role of the different competing/complementing processes, a systematic study was performed to identify the likely route (surface or gas phase) of nucleation of diamond nanoparticles. For this study, we have fixed the optimal plasma conditions, i.e. 4% CH₄ at 100 mbar and 90 W of injected MW power where the maximum yield of DNPs was obtained. In the following sections, we will look at the specific conditions that favor one of these mechanisms and the consequences of these processes on the characteristics of the resulting carbon nanostructures.

5.4.1 Consistency Across Substrates

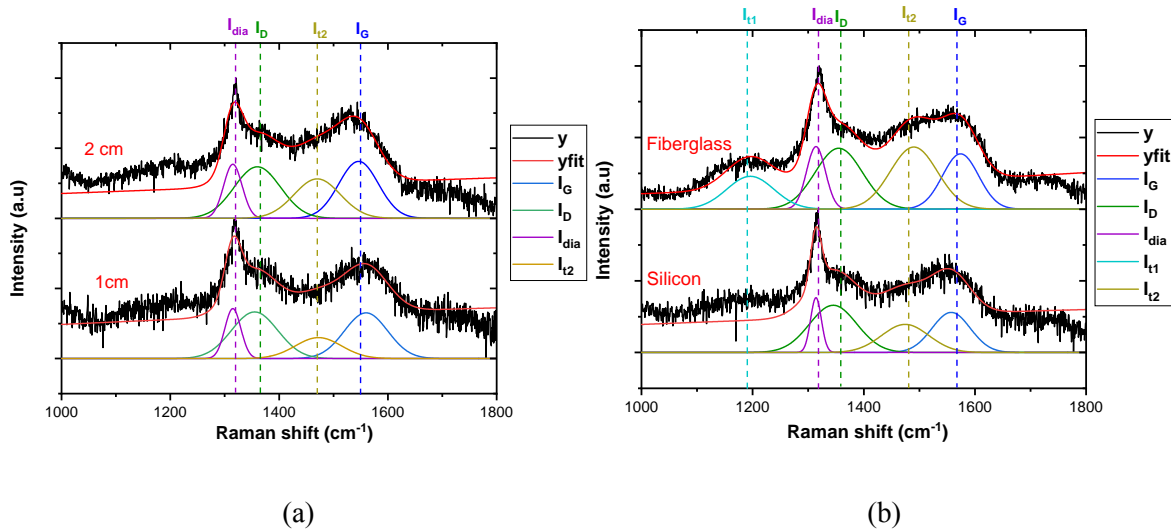


Figure 5.16: Raman spectra for (a) different plasma-substrate distances and (b) different type of substrate. Experimental conditions: CH₄ = 4 sccm, H₂ = 96 sccm, Pressure = 100 mbar, power = 90W and deposition time : 1h

Experiments were carried out where the distance between the substrate and the plasma source was varied within a range of 1 to 2 cm. The density of NPs on the surface decreased with distance, which is consistent with the hydrodynamics of the stagnation flow. In fact, a stagnation line flow is subject to radial convective losses that result in a decrease in the axial fluxes of the plasma components (active chemical species and solid particles)²⁷³. As such, the flux of chemical species and carbonaceous particles at the substrate surface would decrease with the distance between the source and the substrate. The Raman spectra of these carbon nanostructures (cf. Figure 5.16a) do not show any change with the distance between the substrate and the plasma source and are very similar. This suggests that proximity of the substrate to the plasma did not significantly alter the characteristics of the carbon nanostructures formed.

A second set of experiments were conducted with two different substrates: silicon and fiberglass placed 1 cm away from the plasma. The Raman spectra (Figure 5.16b) of the carbonaceous materials collected on these two substrates were identical. This indicates that neither the type of substrate nor the distance between the plasma and the substrate have an influence on the growth

process of carbon nanostructures. Moreover, the likelihood of radicals such as CH_3 to have a long lifetime are relatively low and may not reach distances of 2 cm. Therefore, we conclude that the substrate has no role in the nucleation of a nanodiamond.

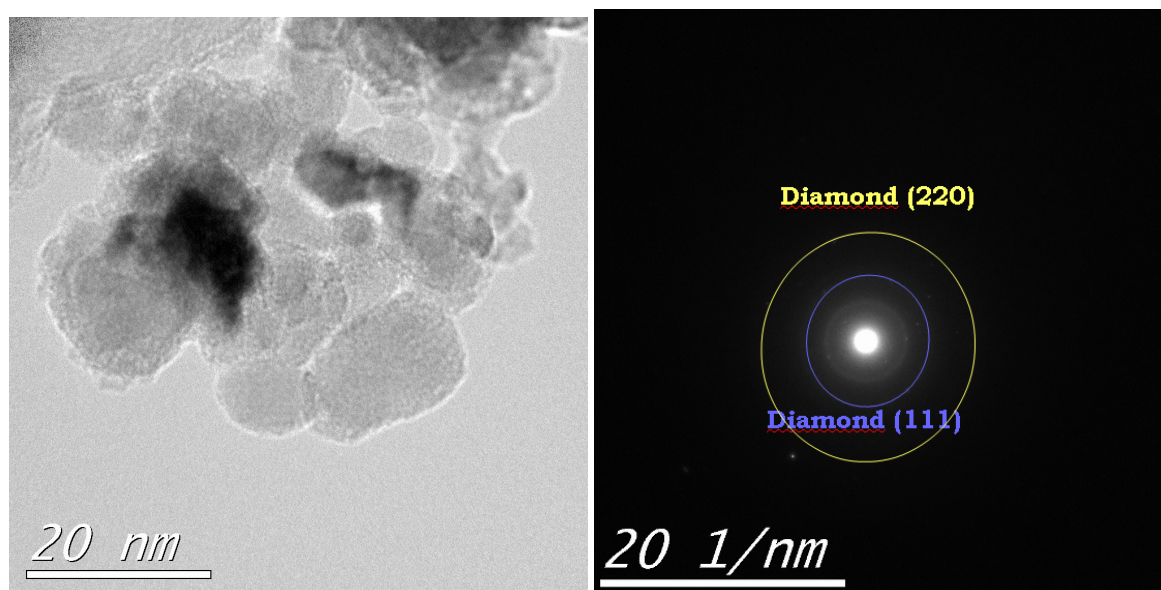


Figure 5.17: TEM image of carbon nanoparticles (left) and its corresponding selected area electron diffraction (right) for 5 min of deposition in the cold finger (experimental conditions: $\text{CH}_4 = 4$ sccm, $\text{H}_2 = 96$ sccm, pressure of reactor = 100 mbar, injected power = 90 W)

It was also possible to detect the diamond phase in carbon nanostructures collected directly on a carbon TEM grid placed on the cold finger for about 5 minutes. TEM images and electron diffraction of this deposit are shown in Figure 5.17. The TEM image shows aggregates of carbonaceous nanostructures. The particle size is of the order of a few nanometers, as indicated by the 20 nm scale. The associated electron diffraction image shows a characteristic diffraction pattern with concentric rings. This pattern indicates the presence of nanocrystals within the amorphous matrix. The diffraction rings suggest the presence of a crystalline diamond with orientations (111) and (220).

5.4.2 Effect of substrate temperature

The substrate temperatures investigated here are much lower than the high temperatures (>800 C) normally used to induce the nucleation of the diamond phase¹³⁷. This clearly indicates that nucleation of nanodiamonds cannot be supported by surface reaction of the substrate. If the nps are nucleated in the gas phase, the temperature gradient close to the substrate can influence the collection of these NPs. Therefore, we investigated the influence of substrate temperature on nanoparticle collection. The results presented here explore how variations in substrate temperature affect the quantity and quality of the nanoparticles collected.

The nanoparticles were collected for 1 hour on a substrate located at a distance of 1 cm from the plasma torch. The substrate was heated and five temperature values were investigated: 15, 30, 50, 70, and 100 °C. Note that the experiment with the substrate at 15 °C was performed using

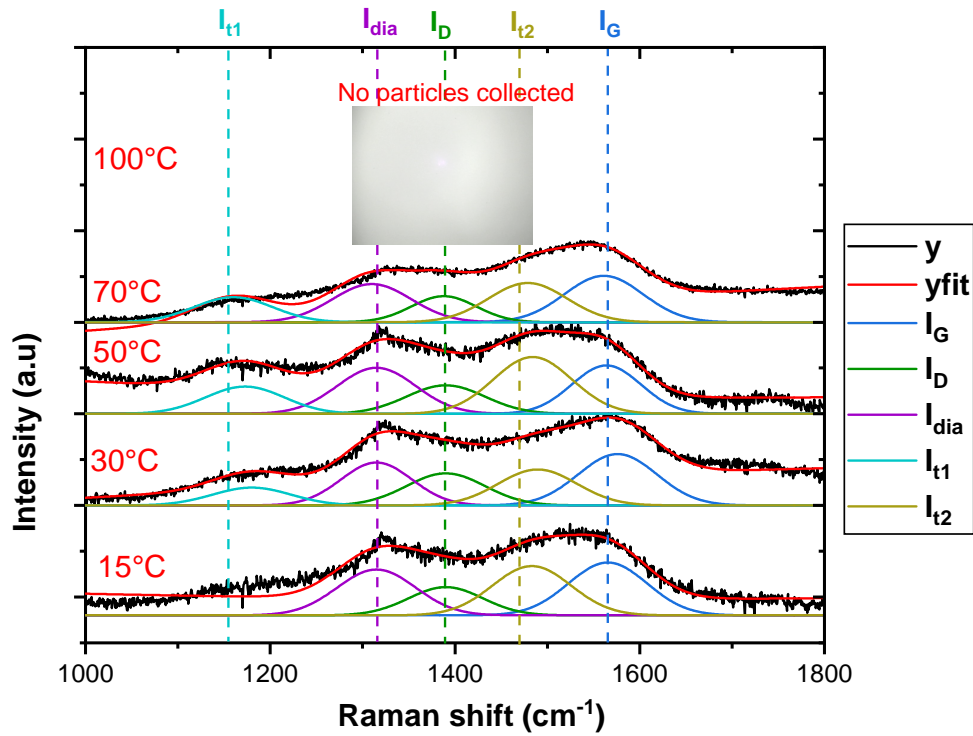


Figure 5.18: Raman spectra for different substrate temperature . Experimental conditions: CH_4 = 4 sccm, H_2 = 96 sccm, Pressure = 100 mbar, power = 90W and deposition time : 1h

the cold-finger system. The Raman spectra of the carbonaceous material obtained are shown in Figure 5.18. At 15 and 30 °C, the Raman spectra show significant peaks for the diamond and graphite phases. In fact, the high peak intensity in the Raman spectra would indicate that the material collected at 15 °C is very dense. As the substrate temperature rises to 50°C, there is a reduction in overall peak intensities due to the lower density of deposited nps. However, the quality of the deposit remains almost the same. At 70°C, the trend towards decreasing peak intensity continues. Diamond and graphite peaks are still present, but their intensity is greatly reduced. This reduction is consistent with the observation that the amount of nanoparticles collected decreases with increasing substrate temperature. When the substrate temperatures were increased to 100°C, there were no particles collected on the silicon substrate as can be seen in Figure 5.18.

The thermophoretic forces at high temperature push the nanoparticles away from the hot substrate, therefore reducing the chances of deposition. The higher the temperature, the more pronounced the effect, hence the decrease in nanoparticle collection when the temperature increases from 15 to 50 °C and then to 70 °C, along with the absence of particles at 100 °C. Therefore, we can conclude that the substrate plays little or no role in the deposition process and that the nucleation of nanodiamonds occurs in the gas phase.

5.4.3 Application of substrate bias

The nanoparticles formed in a plasma are usually charged, and the collection efficiency of the particles may be further improved by polarizing the substrate. However, from our spatial analysis

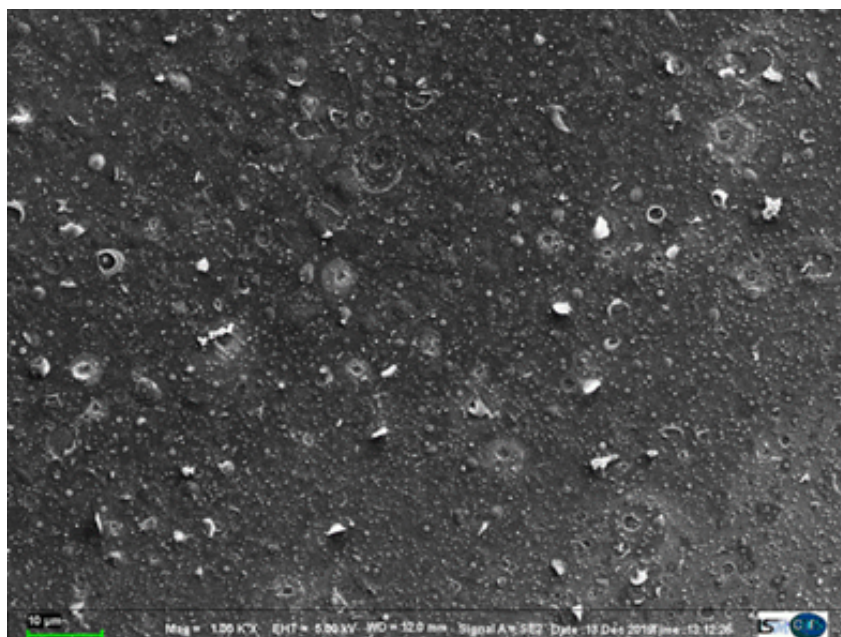


Figure 5.19: SEM image of carbon deposit obtained on a substrate with bias of 200 V.

of temperature and H-atom density, the plasma extent is no greater than 0.5 mm from the torch surface, and most particles beyond this range are likely to be neutral. Therefore, a polarized substrate needs to be placed very close to the torch. We therefore carried out experiments with the substrate placed 1 cm downstream the plasma torch and polarized either positively or negatively up to 250 V. We observed a drastic change in the nature of the deposit when applying a bias regardless of the voltage value for all of the discharge conditions investigated. The deposit evolved from nanoparticles to film morphology (cf. Figure 5.19), with no signs of a diamond phase in the Raman spectra. This could be due to the fact that polarization increases the flow of ions toward the substrate, which could initiate bias-enhanced nucleation of carbon nanostructures on the silicon surface. In fact, bias-enhanced nucleation is a common technique for initiating the nucleation of diamond on substrates¹³⁷. However, the absence of diamond phase is indicative of the fact that the chemistry of nucleation and subsequent growth is significantly altered when bias is applied. We can conclude that the use of polarization is not the best way to achieve the objective of collecting isolated diamond particles, since surface reactions result in the creation of an undesirable amorphous film.

5.4.4 Time-Dependent Deposition Studies

Figure 5.20(a) illustrates the Raman spectra of carbon nanostructures collected over different deposition durations ranging from 5 to 60 minutes. The similarity in the Raman spectral signatures of diamond, D-Band, G-Band and Transpolyacetylene peaks, consistency of sp^3/sp^2 and I_D/I_G ratios (Figure 5.20(b)) across these time intervals indicates that the fundamental characteristics of the carbon nanostructures were established early in the deposition process and did not evolve significantly with longer deposition times. Moreover, the SEM images indicated nucleation and limited growth of the nanoparticles without any film formation even after 1 hour

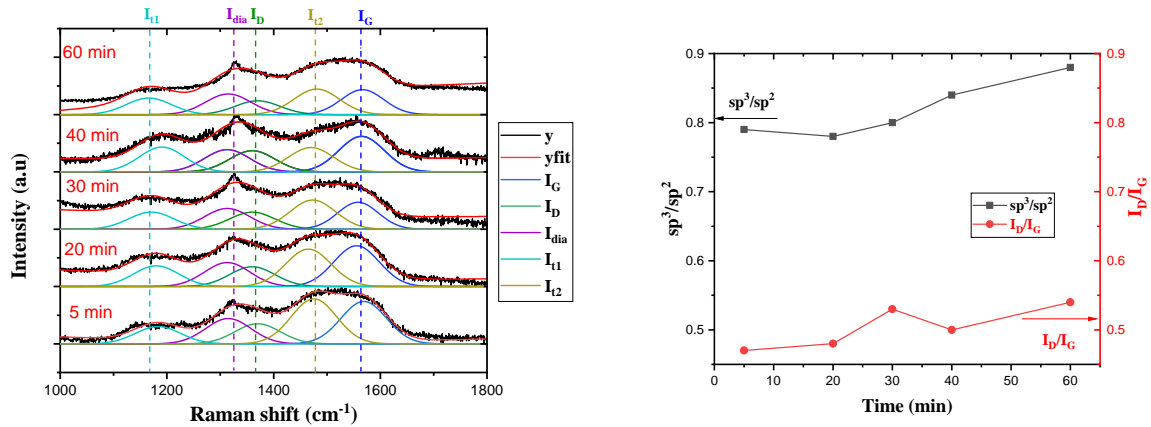


Figure 5.20: (a) Raman spectra and (b) its corresponding sp^3/sp^2 (left) and I_D/I_G (right) ratio for different deposition time. Experimental conditions: CH₄ = 4 sccm, H₂ = 96 sccm, Pressure = 100 mbar, power = 90W, distance plasma-substrate = 1 cm

of deposition. Further, the minimal subsequent evolution on the substrate is indicative that the surface mechanisms for subsequent growth of carbon nanostructures do not significantly modify the Raman signature of the carbon nanostructures. This supports the conclusion that initial nucleation in the gas phase establishes the primary structural characteristics. The temporal consistency in the Raman spectra suggests that the critical phase of nanostructure formation occurs rapidly, and the subsequent deposition time primarily increases the quantity rather than changing the quality of the nanostructures. This is indicative of the surface deposition and/or growth of carbonaceous NPs that play a minor role under these conditions. In other words, the nanoparticles are formed elsewhere between the torch and the substrate and are transported to the substrate where they are collected.

This can be further confirmed by the evolution of the average size and density of the synthesized particles as functions of the deposition time, as shown in Figure 5.21. The increase in particle density over time reflects the dynamics of the CVD process, where initial nucleation is followed by rapid growth and densification of carbon nanostructures. However, the average particle size hovers around 10 nm and does not change much with time, indicating that the growth processes are not dominant under these conditions. This is consistent with the results obtained from Raman analysis that show that the quality of the nanostructures remains constant over time within the first hour.

5.4.5 Carbon nanostructures collection in different deposition zones

Figure 5.22 presents Raman spectra of carbon nanostructures obtained after one hour of plasma synthesis with 96% H₂ and 4% CH₄ at a pressure of 100 mbar and a power of 90 W without external heating and polarization. Under these conditions, two distinct regions of deposits are observed, depending on their proximity to the plasma torch. The region closer to the plasma can be visibly identified by the dark zone on the silicon substrate and is marked as **Inner region** and has been the region focussed so far. However, there was a second region of deposition, referred

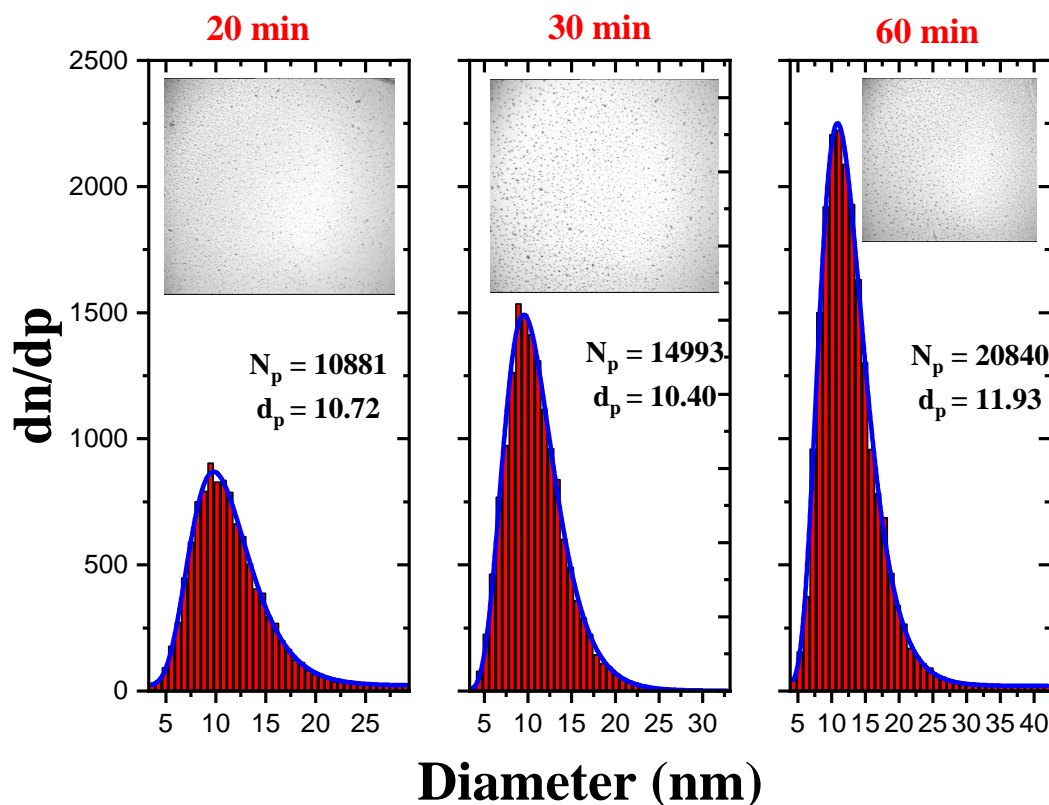


Figure 5.21: Particle size distribution for different deposition time. Insets of the respective images are shown. (b) Experimental conditions: $\text{CH}_4 = 4$ sccm, $\text{H}_2 = 96$ sccm, Pressure = 100 mbar, power = 90W, distance plasma-substrate = 1 cm

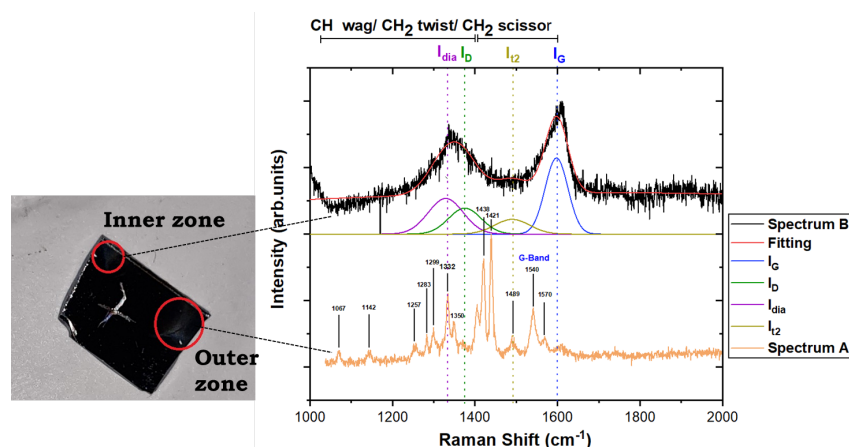


Figure 5.22: Raman spectra at different zones of deposition

to as **outer region**, located much farther away from the influence of the plasma and that can be visible by gray coloration (light zone on the silicon substrate). This region had well-dispersed nanostructures that should have been collected on the substrate because of the hydrodynamic drag. The Raman spectrum corresponding to this region shows several fine peaks associated with CH wag, CH_2 twist, and CH_2 scissor vibrational modes. These features suggest the presence of nascent molecular structures composed of CH_2 groups associated with sp^3 hybridized carbon as well as CH terminations associated with linear sp^2 chains such as poly-acetylene. However,

subsequent studies have been limited by the small amount of material collected. The presence of these molecular bands shows strong credence to the possible growth chemistry of large molecules in the gas phase and subsequent nucleation.

5.4.6 Transfer of nanodiamonds to solution

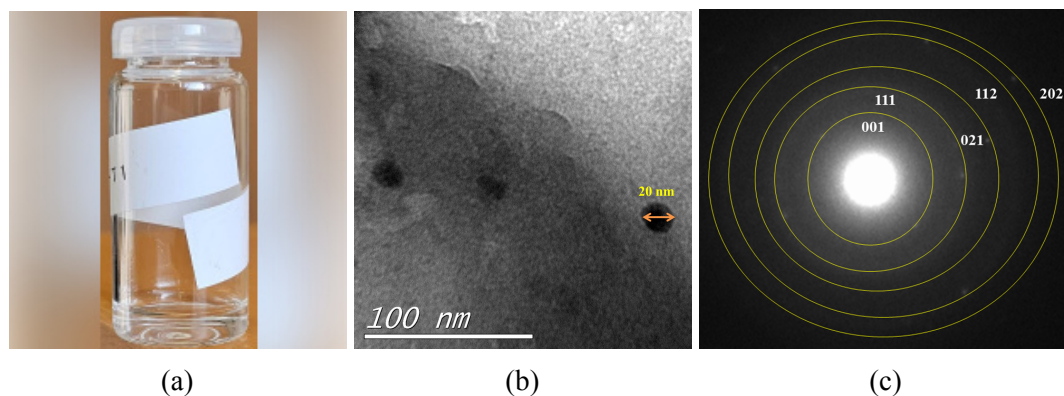


Figure 5.23: (a) Solution of iso-propanol containing NDs, and their (b) HR-TEM image and corresponding (c) SAED pattern. Experimental conditions: $\text{CH}_4 = 4$ sccm, $\text{H}_2 = 96$ sccm, Pressure = 100 mbar, power = 90W and deposition time : 1h

After depositing the carbon nanostructures on a silicon substrate placed 1 cm away from the plasma for one hour, the wafer was placed in a beaker containing 10 ml of 2-propanol and then sonicated for 30 min in an ultrasonication bath. This ensured that all of the collected carbon nanostructures were transferred from the silicon substrate to the isopropyl alcohol solution. The sonication resulted in a fair degree of deagglomeration of the nanoparticles, despite the fact that it did not use complex disaggregating mechanisms. The high resolution transmission electron microscopy (HR-TEM) image (Figure 5.23b) of the drop-casted nanodiamond solution on the TEM grid shows well isolated particles of a size of around 15-20 nm and its SAED pattern (Figure 5.23c) confirms that they are nanodiamonds. This is indicative of the carbon nanostructures not adhering strongly to the silicon substrate and that there exists no strong chemical bond between the carbon nanostructures and the silicon substrate.

5.5 Discussion on nucleation of nanodiamonds

From the previous section, the gas phase nucleation of nanodiamonds looks very likely. The homogeneous nucleation of NPs (Figure 5.15) in plasma is driven by local plasma parameters such as H-atom density, gas temperature and electron density and temperature, as well as the availability of different carbon radicals. These govern the thermal and electron-induced chemistry that determines the nature of the primary reactive radicals generated in the discharge. Once the nuclei resulting from the molecular growth initiated by these primary radicals are sufficiently stable, they can continue to grow by attaching carbon radicals. In fact, sp^2 is much more stable than sp^3 phase at low temperature and pressure typical of the conditions seen in this thesis and the nucleation of the sp^3 phase leading to nanodiamonds is observed only under high pressure and

The diagram illustrates the reaction network for the $\text{CH}_4\text{-C}_2\text{H}_2$ system. It shows the following species and their interconversions:

- Species:** CH_4 , CH_3 , CH_2 , CH_2^* , CH , C , C_2H_5 , C_2H_5^+ , C_2H_4 , CH_5^+ , C_2H_3^+ , C_2H_3 , C_2H_2 , C_2H_2^+ , C_2H , and C_2 .
- Reactions:**
 - $\text{CH}_4 \rightleftharpoons \text{CH}_3 + \text{H}$ (forward: H_2 , reverse: $\text{H} + \text{M}$)
 - $\text{CH}_3 \rightleftharpoons \text{CH}_2 + \text{H}$ (forward: H_2 , reverse: $\text{H} + \text{M}$)
 - $\text{CH}_3 \rightleftharpoons \text{CH}_2^* + \text{H}$ (forward: H_2 , reverse: $\text{H} + \text{M}$)
 - $\text{CH}_2 \rightleftharpoons \text{CH} + \text{H}$ (forward: H_2 , reverse: $\text{H} + \text{M}$)
 - $\text{CH} \rightleftharpoons \text{C} + \text{H}$ (forward: H_2 , reverse: $\text{H} + \text{M}$)
 - $\text{CH}_3 \rightleftharpoons \text{C}_2\text{H}_5$ (forward: CH_3 , reverse: H)
 - $\text{CH}_3 \rightleftharpoons \text{C}_2\text{H}_4$ (forward: H , reverse: $\text{H} + \text{M}$)
 - $\text{CH}_3 \rightleftharpoons \text{C}_2\text{H}_2$ (forward: H , reverse: $\text{H} + \text{M}$)
 - $\text{CH}_3 \rightleftharpoons \text{C}_2\text{H}$ (forward: CH , reverse: H)
 - $\text{CH}_3 \rightleftharpoons \text{C}_2$ (forward: H , reverse: $\text{H} + \text{M}$)
 - $\text{CH}_2 \rightleftharpoons \text{C}_2\text{H}_3$ (forward: H , reverse: $\text{H} + \text{M}$)
 - $\text{CH}_2 \rightleftharpoons \text{C}_2\text{H}_2$ (forward: H , reverse: $\text{H} + \text{M}$)
 - $\text{CH}_2 \rightleftharpoons \text{C}_2\text{H}$ (forward: H , reverse: $\text{H} + \text{M}$)
 - $\text{CH}_2 \rightleftharpoons \text{C}_2$ (forward: H , reverse: $\text{H} + \text{M}$)
 - $\text{CH}_2^* \rightleftharpoons \text{CH}_2$ (forward: H_2 , reverse: $\text{H} + \text{M}$)
 - $\text{CH}_2^* \rightleftharpoons \text{CH}$ (forward: H_2 , reverse: $\text{H} + \text{M}$)
 - $\text{CH}_2^* \rightleftharpoons \text{C}_2\text{H}_2$ (forward: H_2 , reverse: $\text{H} + \text{M}$)
 - $\text{CH}_2^* \rightleftharpoons \text{C}_2\text{H}$ (forward: H_2 , reverse: $\text{H} + \text{M}$)
 - $\text{CH}_2^* \rightleftharpoons \text{C}_2$ (forward: H_2 , reverse: $\text{H} + \text{M}$)
 - $\text{C}_2\text{H}_5 \rightleftharpoons \text{C}_2\text{H}_4$ (forward: $\text{H} + \text{M}$, reverse: H)
 - $\text{C}_2\text{H}_4 \rightleftharpoons \text{C}_2\text{H}_3$ (forward: H , reverse: $\text{H} + \text{M}$)
 - $\text{C}_2\text{H}_4 \rightleftharpoons \text{C}_2\text{H}_2$ (forward: H_2 , reverse: $\text{H} + \text{M}$)
 - $\text{C}_2\text{H}_4 \rightleftharpoons \text{C}_2\text{H}$ (forward: H , reverse: $\text{H} + \text{M}$)
 - $\text{C}_2\text{H}_4 \rightleftharpoons \text{C}_2$ (forward: H , reverse: $\text{H} + \text{M}$)
 - $\text{C}_2\text{H}_3 \rightleftharpoons \text{C}_2\text{H}_2$ (forward: H_2 , reverse: $\text{H} + \text{M}$)
 - $\text{C}_2\text{H}_3 \rightleftharpoons \text{C}_2\text{H}$ (forward: H , reverse: $\text{H} + \text{M}$)
 - $\text{C}_2\text{H}_3 \rightleftharpoons \text{C}_2$ (forward: H , reverse: $\text{H} + \text{M}$)
 - $\text{C}_2\text{H}_2 \rightleftharpoons \text{C}_2\text{H}$ (forward: H_2 , reverse: $\text{H} + \text{M}$)
 - $\text{C}_2\text{H}_2 \rightleftharpoons \text{C}_2$ (forward: H , reverse: $\text{H} + \text{M}$)
 - $\text{C}_2\text{H} \rightleftharpoons \text{C}_2$ (forward: H_2 , reverse: H)

This suggests that plasma chemistry involves a molecular growth effect that ends with sp^3 nucleation. In fact, the hydrocarbon chemistry encountered in non-equilibrium plasmas is quite complex, and small variations in local plasma conditions can yield a variety of carbon nanostructures including graphene, amorphous carbon, polyacetylene, polyyne, and nanodiamonds. In addition to the electron impact reactions that are responsible for the high degree of H_2 dissociation observed in the microplasma torch, the important pathways of hydrocarbons up to 2 carbon atoms are shown in Figure 5.24. The abundance of H-atom densities reduces methane toward lower hydrocarbon radicals such as CH_3 , CH_2 , CH , and finally C through H-shift reactions.

These successive stages of hydrogen loss are kinetically driven through collisions with hydrogen atoms. In a way, these reactions are key to the formation of the methyl radical, which is known to be critical for the growth of CVD diamond. Similarly, the formation of acetylene from methane is a thermodynamically driven process that involves multiple channels through the CH₃, CH and C₂ radicals. For example, two CH₃ radicals combine to form ethane C₂H₆ which subsequently reduces to C₂H₄ and then acetylene through a series of H-shift reactions similar to CH₃. Different hydrocarbon radicals such as C₂H, CH₃ can further undergo surface-based reactions or contribute to molecular growth and nucleation in the gas phase, leading to the formation of different carbon nanostructures that are collected downstream the torch. Furthermore, the concentration of H-atom density is key in stabilizing the sp³ phase wherever it is formed. It should be emphasized that the recombination of H-atom is a fairly slow process and a substantial amount of H-atom still exists downstream of the torch, which may affect the recombination chemistry in the post-discharge and influence the nature of the deposit.

To further gain insight into the hydrocarbon chemistry occurring in the plasma, a 0D two-temperature transient global model for H₂/CH₄ plasma was used²⁷⁴. In summary, this model assumes a homogeneous zone of plasma which is sustained by MW power with electrons and heavy species at electron and gas temperatures, respectively. Plasma-surface interaction is modeled by a linear diffusion through a boundary layer and recombination reaction with prescribed probabilities. The boundary layer thickness may be inferred from experiment or transport correlations²⁷⁴. The 0D model equation-set consists of a total energy equation, electron energy equation, and continuity equations for all the chemical species except electron whose density is determined from the electrical neutrality equation. Simulations are performed for given microwave power density, pressure, surface-to-volume ratio, and thermal and diffusion boundary layer thicknesses. The chemical model used to describe the hydrogen-methane plasma involves 28 species undergoing 140 reactions that account for different electron-impact processes such as ionization, dissociation, excitation, recombination, and neutral reactions between the different hydrogen and hydrocarbon species. Since our main purpose is to identify the main primary radicals and to investigate the evolution of their densities with discharge conditions, the chemical model used in this work is limited to two carbon atoms^{275,276}, as summarized in Figure 5.24. Of course, the present chemistry scheme does not include both the molecular growth of hydrocarbon molecules and the surface chemistry, which are important for the present conditions. Only recombination and adsorption processes of radicals and ions are taken into account in the balance of the gas phase species.

All simulations are restricted to the "full circle" regime of the torch, where the geometry is annular. The volume-to-surface ratio is calculated assuming a plasma of 3 mm length. MW power density obtained in Chapter 4 was used for the simulations. The thicknesses of the thermal and diffusion boundary layers could not be estimated or measured experimentally for the annular configuration considered here. We therefore adjusted these thicknesses to obtain the same values for the simulated and measured gas temperatures and H-atom densities. Of course, such an approach can only yield approximate values and evolution trends of the plasma characteristics, species densities, and electron temperature, and one would require a detailed 1D, or even 2D, models for more predictive simulations. In any case, the present approach makes it possible to

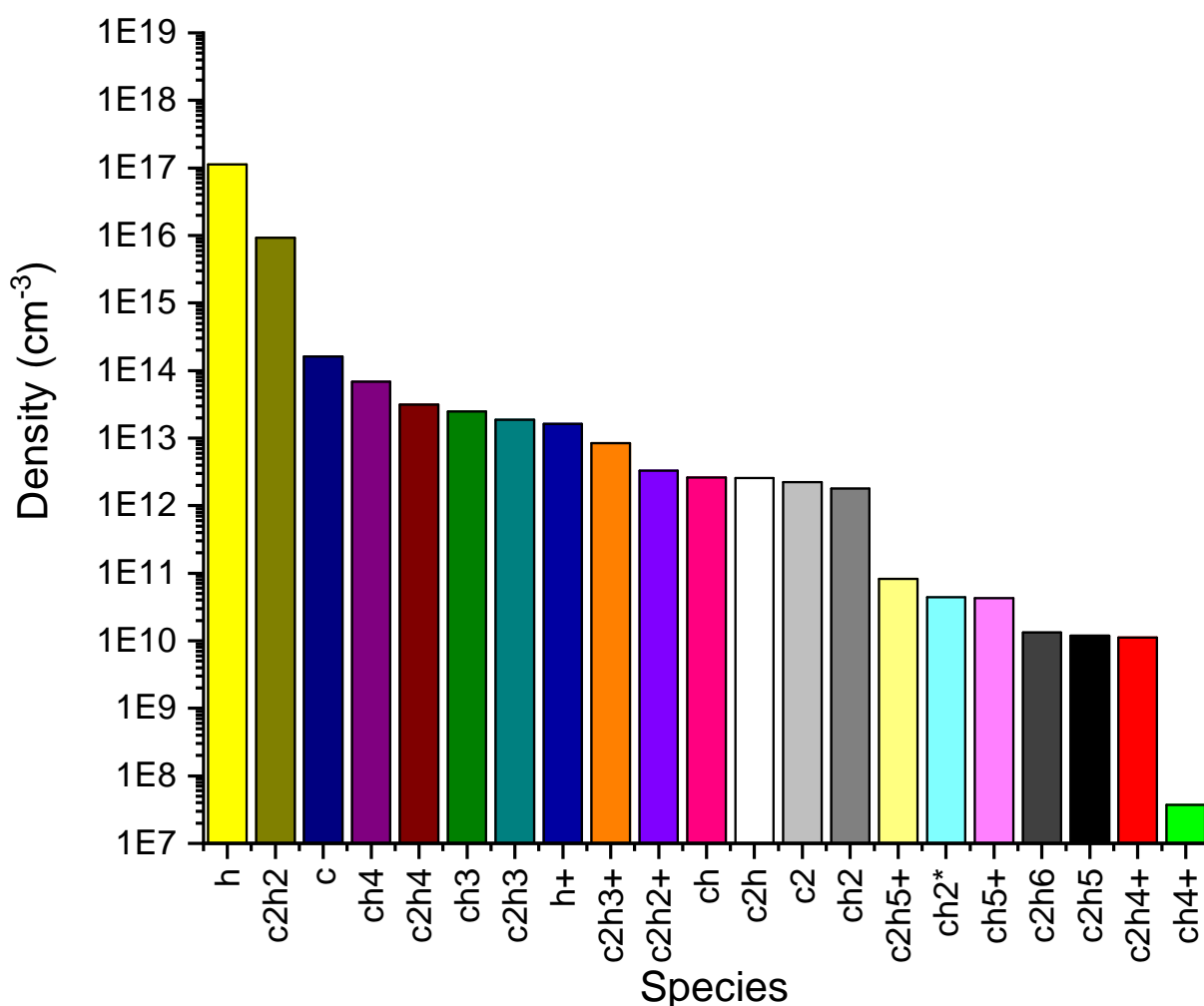


Figure 5.25: Density of main species produced in CH₄/H₂ mixture with 4% of CH₄ for a total flowrate of 100 sccm at 100 mbar pressure and 90 W power.

shed light on the primary radicals that may be important for diamond nucleation. The plasma simulations carried out here yield the variation of the plasma temperatures and composition as a function of the residence time in the discharge region.

Figure 5.25 shows the densities of different species that exit the plasma zone at 100 mbar. It is quite clear that almost all the methane has been transformed into acetylene under the conditions considered. In terms of ions, the high concentration of the H atom results in abundant H⁺ ions along with C₂H₃⁺ and C₂H₂⁺ coming from acetylene. The high concentration of C₂H₂ coupled with suitable gas temperatures is the driver of sp² growth. The growth of amorphous sp² carbon usually takes place involving C₂H₂, C, C₂H and vinyl C₂H₃ radicals (Section 2.1.4). Figure 5.26 summarizes these important radicals (C₂H, C and C₂H₃) promoting sp² growth at the exit of the torch as a function of the concentration of methane and the pressure at the exit of the torch. Clearly, one observes that the above-mentioned radicals increase with pressure. The range of temperatures observed in the plasma are in the lower limits compared to the conditions that support nucleation of soot through the HACA mechanism and are represented by the D and G bands found in the Raman spectrum. However, the downstream gas cools down very

quickly and may quickly quench these growth processes. At these conditions, the formation of linear aliphatic chains would be favored, as indicated by the presence of transpolyacetylene in the Raman spectrum. As a result, the combination of the stated radicals would cause enhanced growth and nucleation of the sp^2 carbon nanostructures, soot, and transpolyacetylene.

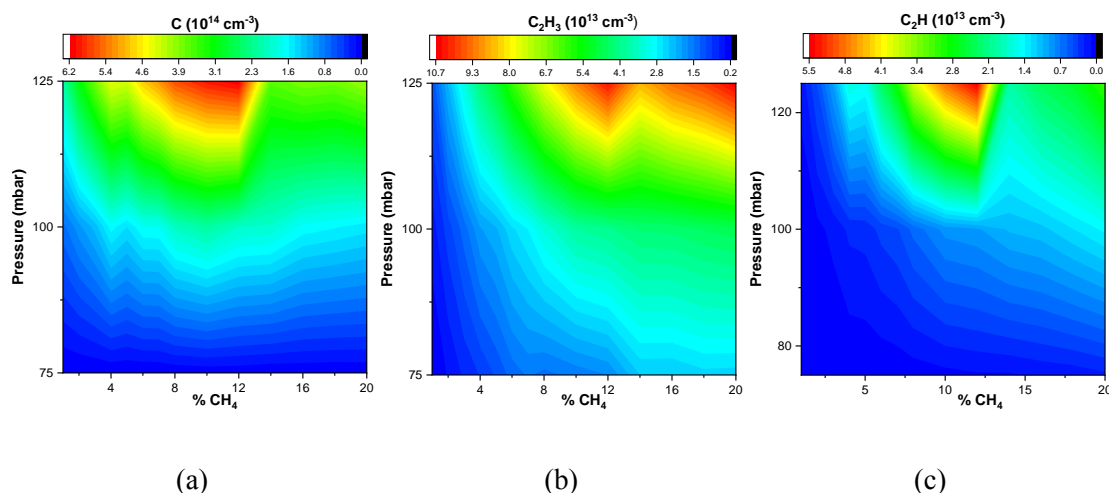


Figure 5.26: 2D contour plot showing the evolution of (a) C, (b) C_2H_3 and (c) C_2H as a function of methane concentration and pressure using the 0D model. Experimental conditions : Power = 90W and flowrate of $\text{CH}_4 + \text{H}_2 = 100$ sccm.

If the diamond is nucleated in the gas phase, the question remains how? The only known chemical scheme is provided by Dolmotov et al.¹⁷⁵ where C_2 radicals and hydrogen combine to form cyclohexane which, later, by addition of C_2 and CH_3 radicals, grows to form the first diamondoid, adamantane. Subsequent reactions occur by adding the methyl radical to form higher diamondoids¹⁷⁶. At present, there is no direct proof that this reaction occurs under the conditions of the torch. The positive correlation between the high emission of the C_2 Swann and

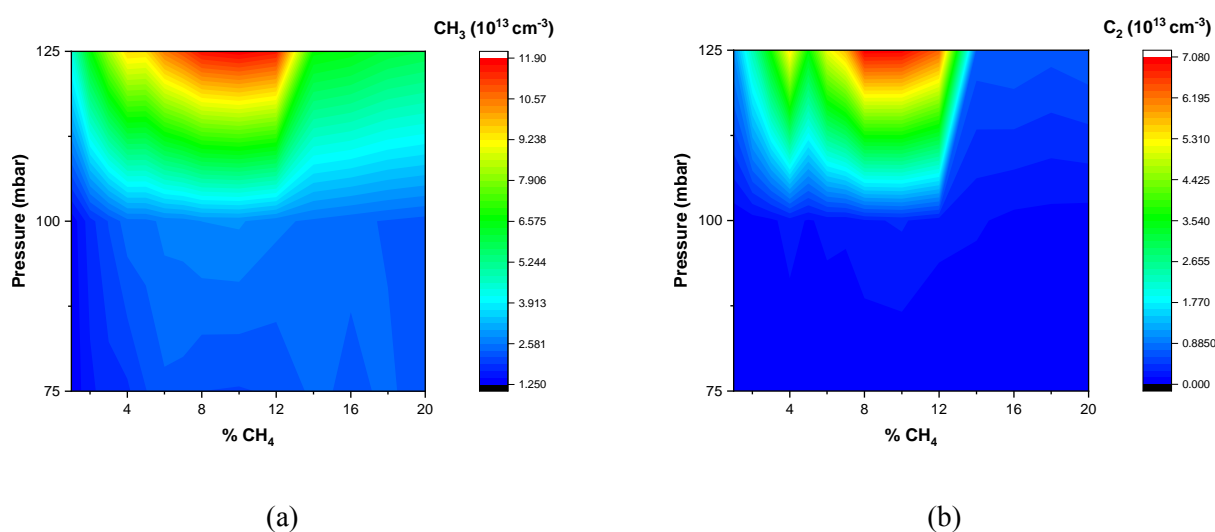


Figure 5.27: 2D contour plot showing the evolution of (a) CH_3 and (b) C_2 species as a function of methane concentration and pressure using the 0D model. Experimental conditions : Power = 90W and flowrate of $\text{CH}_4 + \text{H}_2 = 100$ sccm.

CH bands and the formation of diamonds (Figure 5.14b) certainly supports the belief that C_2 and CH_3 are important radicals for sp^3 growth. Figure 5.26 show the evolution of the density of these radicals C_2 and CH_3 at the exit of the torch as functions of methane concentration and pressure. Clearly, there is a lack of these radicals at a low pressure of 75 mbar. This possibly explains the low yield of nanodiamonds under these conditions, as key intermediate sp^3 molecules may not have formed. However, the high concentrations of these radicals at 125 mbar did not translate to a high nucleation of nanodiamonds. The relatively high temperature that characterize these discharge conditions tends to favours sp^2 over sp^3 phases as compared to 100 and 75 mbar case. As a result, an enhanced sp^2 growth channel would take place and largely dominate the sp^3 growth channel. It appears therefore, that carbon nucleation is thermodynamically driven at such relatively high temperature (~ 1500 K).

The above analysis does not take into account the further molecular growth that would occur downstream of the plasma, and the focus of future studies should be on understanding this post-discharge region. The thesis started with a clear set of goals to identify the local plasma conditions that favor nucleation of NDs. Correlation between optical plasma diagnostics and characterization of the carbon nanostructures produced points to the conclusion that CH_3/C_2 along with the H atom are likely to play an important role in nanodiamond nucleation, stabilization and growth. However, key questions remain to be addressed regarding the nucleation of NDs, particularly the growth pathway and key larger intermediate species.

5.6 Conclusions

This chapter examined the formation and properties of carbon nanostructures obtained from a CH_4/H_2 ($\pm Ar$) mixtures. The microwave torch can clearly establish high concentrations of hydrocarbon radicals, which, in conjunction with a high H-atom concentration and moderate temperature, produces conditions that support the formation of diamond nanoparticles. In summary, the major conclusions of this chapter are as follows:

1. Firstly, it is seen that the concentration of 4% methane emerges as the magic concentration that has the highest diamond phase yield among the carbon nanostructures. In conclusion, we can say that the gas temperature, the density of the H atom, as well as the radicals associated with C_2 and CH (say CH_3) seem to play an important role in the mechanism of nanodiamond production.
2. In correlating the plasma and material characterization, the importance of the H-atom density for the formation of the nanodiamonds emerges. Even when the gas temperatures are relatively high (as far as diamond versus graphite phase stability is concerned), as in the case of argon-laden plasmas, the increased H-atom density seems to stabilize the diamond phase as opposed to rapid graphitization.
3. More importantly, it is crucial to limit the sp^2 growth chemistry propelled by high densities of acetylene to have enhanced diamond phase yield. This means that it is necessary to clearly limit the density ratio of hydrocarbon species to H-atom in order to achieve favorable conditions for the growth of the sp^3 phase.

4. Nevertheless, it is also important to have substantial densities of hydrocarbon radicals necessary for the growth of the diamond phase. A positive correlation between increased intensities of C_2 and CH radicals indicates that these reactions would play a critical role in the formation of nanodiamond. The radicals CH_3 and C_2 seem to be key to the formation of intermediate sp^3 molecules and the nucleation of nanodiamonds.

Chapter 6

Conclusion and perspectives

6.1 General conclusions

This thesis highlights the characterization and application of a microwave plasma torch based on a coaxial transmission line (CTRL) operating in the mbar pressure range. It is intended for the synthesis of carbonaceous materials, in particular nanodiamonds. Through a series of experiments and analyzes, we have demonstrated the feasibility of using this torch to produce nanodiamonds under different pressure conditions (50-125 mbar) and gas composition with H_2/CH_4 (\pm Ar).

To understand how the plasma torch works, the first step was to estimate the plasma parameters using optical diagnostic tools such as OES and ps-TALIF in a hydrogen plasma. These diagnostic tools were used to measure, among other things, the electron density, the atomic hydrogen density, and the gas temperature. The plasma is of partial circle at low MW powers whose perimeter increases to attain "full circle" regime. The operation regime of the torch is marked by the upper critical power where the appearance of a secondary plasma occurs at the second resonance point. The critical powers of transition increased with pressure. The gas temperature was measured by OES using two rotational bands of H_2 , namely the G-band (453-462 nm) and Fulcher- α (600-610 nm). The results showed that the G-Band gives reliable gas temperature values over the pressure and power range studied, with values in the range of around 1000-1400 K. The electron density was estimated from the Stark broadening of the H_β transition. The Voigt fitting was performed with a Gaussian component fixed with Doppler width estimated from the gas temperature of the G-band. The microplasma torch produces plasmas with a high electron density ($2 \times 10^{13} \text{ cm}^{-3}$), which makes it possible to dissociate a large number of H_2 in the gas. This electron density is virtually almost constant over the pressure and power range studied. The estimated electron temperature is on the order of 1.9 eV. The estimated microwave power density was extremely high (10^9 W m^{-3}) and follows the same trend as n_e . Plasma volume ($\sim 1.3 \times 10^{-8} \text{ m}^{-3}$) decreases with pressure and increases with power. The density of atomic hydrogen was measured by actinometry and ps-TALIF and it was found to be $\text{O}(10^{16}) \text{ cm}^{-3}$, which makes the torch an efficient source of H-atoms. One of the major contributions of this thesis is the development of a new method for estimating the gas temperature using ps-TALIF. The approach is based on directly retrieving the translational temperature from

the fluorescence decay τ_H of ps-TALIF of pure H_2 plasmas. The temperatures measured by this technique were in good agreement with those estimated by the rotational structure of the G-Band of H_2 . Finally, a 2D map of the temperature and density of atomic hydrogen in the downstream region of the plasma was obtained. Both the gas temperature and atom densities were more localized at high pressures, indicating a smaller plasma volume compared to that of the lower pressure. In addition, the gas efflux cooled to $500^\circ C$ with substantial amounts of H atom (10^{15} cm^{-3}) within 5 mm downstream of the plasma.

Depositions were carried out using H_2/CH_4 (\pm Ar) mixtures in two chambers, one with a heating and bias system and the other with a cooling system. Morphological and structural characterization of the synthesized carbon nanostructures using SEM and AFM showed a particle size distribution of around 10 nm. Analysis of TEM images and SAED patterns confirmed the crystalline nature of the nanostructures, with the presence of hybrid nanostructures composed of graphite (sp^2) with plane 002 and diamond (sp^3) with plane 111. The quality of the collected carbon nanostructures was analyzed using the sp^3/sp^2 ratio measured by Raman and XPS. The study of the influence of power showed that diamond production is observed at 70 W with a peak at 90 W and 100 mbar. Experiments have shown that the substrate placed downstream the torch does not play any role in the formation of a nanodiamond. In particular, the insensitivity of the nanostructures with respect to the nature of the collection system, distance, and type of the substrate as well as with the duration of the collection are indicative that gas-phase processes are key to the formation of carbon nanostructures. The study of the influence of the pressure and the concentration of methane showed an optimum of diamond quality at 4% of methane and 100 mbar. By adding small amounts of argon (up to 25 sccm) to the H_2/CH_4 mixture, it was observed that a large quantity of nanostructures is produced with the maximum yield at 4% methane and 20 sccm argon. One major conclusion is that the best conditions for nanodiamonds coincide with the minimum yield of amorphous carbon such as soot and transpolyacetylene. From 0D simulations, it was seen that C_2H_2 is the major hydrocarbon molecule at the exit of the plasma. A high concentration of acetylene (C_2H_2) and temperature in the range 1500 K could lead to the formation of amorphous carbons through the HACA mechanism (hydrogen abstraction / carbon addition) or the linear chains of transpolyacetylene. Clearly, high concentration of methane leads to larger concentrations of acetylene and sp^2 radicals, and therefore promoting the growth of sp^2 phase over sp^3 phase. Nevertheless, it is important to have substantial densities of hydrocarbon radicals required for diamond phase growth. Although the primary radical responsible for nanodiamond growth has not yet been explicitly identified, a positive correlation between the increase in the emission intensities of the C_2 and CH radicals indicates that these species would play a critical role in nanodiamond formation. In fact, these species have a strong correlation with methane H-shift reactions and could indicate that the CH_3 radical should be important. On the other hand, atomic hydrogen should stabilize the diamond structure by saturating the dangling bonds on the nanodiamond surface, thus preventing the appearance of graphite (sp^2 bonds).

6.2 Perspectives on optimization of plasma-nucleation process

Future studies should focus on developing a plasma process that selectively promote the sp^3 chemistry along with rich densities of H-atom and CH_3/C_2 to form the "unidentified" intermediate precursors that nucleate to form nanodiamonds while minimizing acetylene-based chemistry that promotes amorphous carbon. This will require a consistent effort to understand the molecular growth processes through measurements and modeling. Although the 0D model has provided valuable insights, spatially resolved models (e.g., 1D or 2D models) are necessary to offer insights into the spatial evolution of species and the influence of transport phenomena, which are not captured in 0D. Future work should focus on improving the numerical model to incorporate more detailed and accurate chemical kinetics, especially for the Ar/ CH_4 /H₂ plasma system. Including additional chemical reactions and species, such as more detailed pathways for the formation and destruction of hydrocarbon species, will help providing a more comprehensive understanding of the plasma chemistry. The focus should be on the downstream flow, where neutral molecular growth chemistry will play an important role. Although the pathways for growth of sp^3 chemistry are not known, the models can be effectively used to identify and then avoid the conditions that support the growth of amorphous carbon through PAHs or linear chains.

Another major improvement that could be made is to measure carbon radicals as well as the larger molecules formed in the gas phase. Although efforts were made to measure radicals C_2 and CH using LIF during the course of this thesis, technical difficulties and time restrictions prevented these measurements. Further, the study of molecular growth processes through molecular beam mass spectrometry, Raman spectroscopy, or Fourier transform infrared spectroscopy would enhance the understanding of these processes by identifying the important intermediates formed in the plasma that nucleate to solid carbon materials such as nanodiamonds. In fact, effort was made to set up a fiber-enhanced Raman spectroscopy (FERS) during the course of this thesis to study the evolution of carbon species. Optical fibers are used to enhance the Raman signal from the gas molecules, enabling their detection. This technique is particularly useful for identifying and quantifying various hydrocarbons and intermediate species (such as C_2H_2 , C_2H_4 , C_2H_6 , etc.), providing a more comprehensive picture of plasma chemistry and helping to understand how intermediate species are formed. Furthermore, the MBMS available in the group has already been adapted for moderate pressure conditions studied in this thesis and should enable the identification of larger hydrocarbon molecules and clusters. Detailed mass spectrometry data will provide insight into molecular growth pathways and the influence of plasma conditions on these pathways.

The integration of these techniques and their use in combination with models will not only allow us to understand the chemical processes accompanying the nucleation of carbon nanostructures, but also help optimizing the process. Although the torch proved to be a tool for producing high H-atom densities that allowed nucleation of nanodiamonds, the design of the torch could be further improved in terms of achieving wider local plasma conditions such as residence time, electron and gas temperatures, electron density, etc. The process itself could

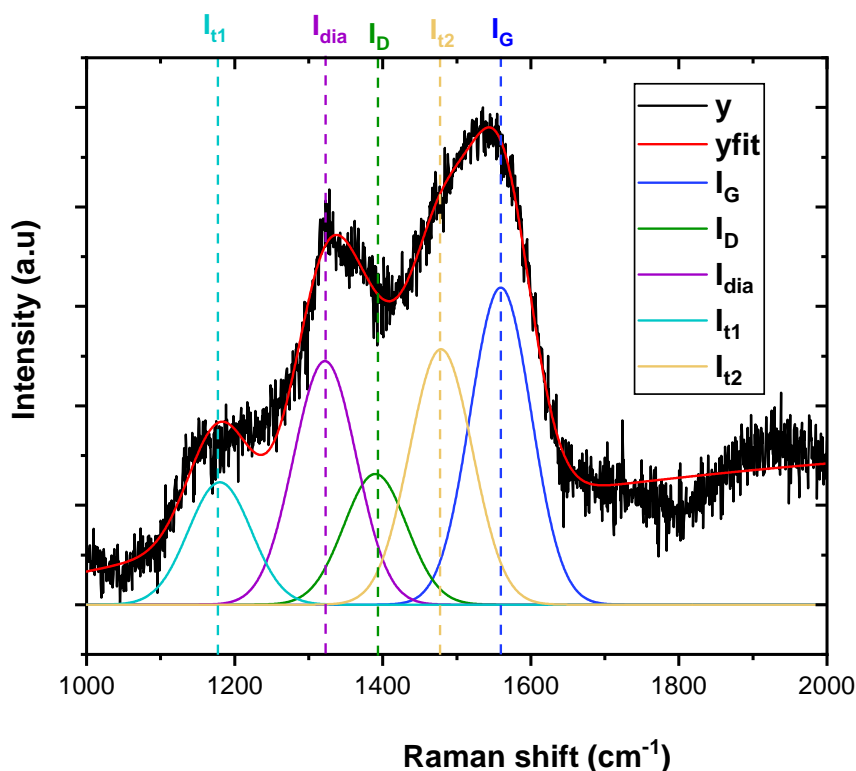


Figure 6.1: Raman spectrum with presence of ethanol. Conditions: Pressure = 100 mbar , Power = 90W, H_2 = 96sccm and 500 mg/L of ethanol

incorporate techniques to restrict acetylene formation and enhance the densities of CH_3 , C_2 and other benign radicals for sp^3 growth. For example, plasma pulsing can help in reducing the gas temperatures while maintaining similar orders of H-atom densities. This step could limit the transformation of methane to acetylene. The addition of oxygen-containing precursors can also be interesting, as O atoms are known to etch the sp^2 phase. In fact, nanodiamonds were observed to form when ethanol was used instead of methane (cf. Fig 6.1) in the present torch. Another possibility could be to add precursors, such as diamondoids, that can accelerate the nucleation of sp^3 phase carbon. Few researchers have already demonstrated this to produce higher diamondoids. Lastly, the process could itself be reimagined consisting of multiple stages with a combination of multiple plasma sources, each stage dedicated to particular chemical processes.

Bibliography

- [1] Nesrine Hellala. *Synthèse et caractérisation chimique de cristaux et films de diamant par dépôt chimique en phase vapeur assisté par plasma micro-ondes*. PhD thesis, Institut National Polytechnique de Lorraine, 2006.
- [2] Claude Cohen-Tannoudji, Bernard Diu, and Franck Laloë. *Mécanique quantique*. Hermann, 1973.
- [3] Caroline Chouquet. *Élaboration et caractérisation de revêtements type "Diamond-Like Carbon" déposés par un procédé chimique en phase vapeur assisté par un plasma basse fréquence*. PhD thesis, Institut National Polytechnique de Lorraine, 2008.
- [4] Zaabar Foudil. Les propriétés optiques des nanostructures du carbone et spectroscopie raman des suies. Master's thesis, Université A. MIRA de Béjaïa, 2013.
- [5] Yee Wen Yap, Norsuria Mahmed, Mohd Natashah Norizan, Shayfull Zamree Abd Rahim, Midhat Nabil Ahmad Salimi, Kamrosni Abdul Razak, Ili Salwani Mohamad, Mohd Mustafa Al-Bakri Abdullah, and Mohd Yusry Mohamad Yunus. Recent advances in synthesis of graphite from agricultural bio-waste material: A review. *Materials*, 16(9): 3601, 2023.
- [6] Harold W Kroto, James R Heath, Sean C O'Brien, Robert F Curl, and Richard E Smalley. C60: Buckminsterfullerene. *nature*, 318(6042):162–163, 1985.
- [7] Wolfgang Krätschmer, Lowell D Lamb, KHDR Fostiropoulos, and Donald R Huffman. Solid c60: a new form of carbon. *Nature*, 347(6291):354–358, 1990.
- [8] Filippo Giubileo, Antonio Di Bartolomeo, Laura Iemmo, Giuseppe Luongo, and Francesca Urban. Field emission from carbon nanostructures. *Applied Sciences*, 8(4):526, 2018.
- [9] Huimin Liu and David S. Dandy. *Diamond Chemical Vapor Deposition: Nucleation and Early Growth Stages*. Elsevier, 1996.
- [10] Thomas R. Anthony. Metastable synthesis of diamond. *Vacuum*, 41(4-6):1356–1359, 1990.
- [11] Amine Boussadi. *Optimisation d'un procédé de dépôt plasma micro-onde pour l'élaboration de substrats de diamant fortement dopés au bore*. PhD thesis, Université Sorbonne Paris Nord, 2016.

- [12] JH Eggert, DG Hicks, PM Celliers, DK Bradley, RS McWilliams, R Jeanloz, JE Miller, TR Boehly, and GW Collins. Melting temperature of diamond at ultrahigh pressure. *Nature Physics*, 6(1):40–43, 2010.
- [13] Vincent Pichot, Marc Comet, Éric Fousson, and Denis Spitzer. Les nanodiamants élaborés par détonation. *L'actualité chimique*, Avril(329):8, 2009.
- [14] Benoit Baudrillart. *Étude du procédé de croissance de films de diamant nanocristallin par dépôt chimique en phase vapeur assisté par plasma micro-onde distribué, à basse température et basse pression*. PhD thesis, Université Sorbonne Paris Nord, 2017.
- [15] Aiswarya Thekkedath and Karthiyayini Sridharan. Nanodiamonds and its applications. In *Applications and Use of Diamond*. IntechOpen, 2022.
- [16] Rohit R. Bhosale, Riyaz Ali Osmani, Prasanna P. Ghodake, Bhargav R. Harkare, Sabir M. Shaikh, and Sarika R. Chavan. Nanodiamonds: a new-fangled drug delivery system. *J Pharm Res*, 3(12):1395–1403, 2013.
- [17] Olga A. Shenderova, Alexander I. Shames, Nicholas A. Nunn, Marco D. Torelli, Igor Vlasov, and Alexander Zaitsev. Synthesis, properties, and applications of fluorescent diamond particles. *Journal of Vacuum Science & Technology B*, 37(3), 2019.
- [18] Sandeep Kumar, Monika Nehra, Deepak Kedia, Neeraj Dilbaghi, K. Tankeshwar, and Ki-Hyun Kim. Nanodiamonds: Emerging face of future nanotechnology. *Carbon*, 143: 678–699, 2019.
- [19] Nicholas Nunn, Marco Torelli, Gary McGuire, and Olga Shenderova. Nanodiamond: A high impact nanomaterial. *Current Opinion in Solid State and Materials Science*, 21(1): 1–9, 2017.
- [20] Valery Yu Dolmatov, Alexander N Ozerin, Inna I Kulakova, Oleksandr O Bochechka, Natalia M Lapchuk, Vesa Myllymäki, and Asko Vehanen. Detonation nanodiamonds: New aspects in the theory and practice of synthesis, properties and applications. *Russian Chemical Reviews*, 89(12):1428, 2020.
- [21] O Shenderova, V Grichko, S Hens, and J Walch. Detonation nanodiamonds as uv radiation filter. *Diamond and related materials*, 16(12):2003–2008, 2007.
- [22] Fedor Jelezko and Jörg Wrachtrup. Single defect centres in diamond: A review. *physica status solidi (a)*, 203(13):3207–3225, 2006.
- [23] Sciencee étonnante. Wave-corpuscle duality. <https://scienceetonnante.com/2021/01/15/1a-dualite-onde-corpuscule/>.
- [24] Christian Kurtsiefer, Sonja Mayer, Patrick Zarda, and Harald Weinfurter. Stable solid-state source of single photons. *Physical Review Letters*, 85(2):290, 2000.

- [25] Geraldine Dantelle, Abdallah Slablab, Loïc Rondin, F. Lainé, Frederick Carrel, Ph. Bergonzo, Sandrine Perruchas, Thierry Gacoin, François Treussart, and J.-F. Roch. Efficient production of nv colour centres in nanodiamonds using high-energy electron irradiation. *Journal of Luminescence*, 130(9):1655–1658, 2010.
- [26] Yi-Ren Chang, Hsu-Yang Lee, Kowa Chen, Chun-Chieh Chang, Dung-Sheng Tsai, Chi-Cheng Fu, Tsong-Shin Lim, Yan-Kai Tzeng, Chia-Yi Fang, and et al. Chau-Chung Han. Mass production and dynamic imaging of fluorescent nanodiamonds. *Nature Nanotechnology*, 3(5):284–288, 2008.
- [27] Jui-I Chao, Elena Perevedentseva, Pei-Hua Chung, Kuang-Kai Liu, Chih-Yuan Cheng, Chia-Ching Chang, and Chia-Liang Cheng. Nanometer-sized diamond particle as a probe for biolabeling. *Biophysical Journal*, 93(6):2199–2208, 2007.
- [28] Chi-Cheng Fu, Hsu-Yang Lee, Kowa Chen, Tsong-Shin Lim, Hsiao-Yun Wu, Po-Keng Lin, Pei-Kuen Wei, Pei-Hsi Tsao, Huan-Cheng Chang, and Wunshain Fann. Characterization and application of single fluorescent nanodiamonds as cellular biomarkers. *Proceedings of the National Academy of Sciences*, 104(3):727–732, 2007.
- [29] Amanda S. Barnard. Diamond standard in diagnostics: nanodiamond biolabels make their mark. *Analyst*, 134(9):1751–1764, 2009.
- [30] Vladimíra Petráková, Andrew Taylor, Irena Kratochvílová, František Fendrych, Jiří Vacík, Jan Kučka, Jan Štursa, Petr Cígler, Miroslav Ledvina, and et al. Anna Fišerová. Luminescence of nanodiamond driven by atomic functionalization: towards novel detection principles. *Advanced Functional Materials*, 22(4):812–819, 2012.
- [31] C. Bradac, T. Gaebel, N. Naidoo, M. J. Sellars, J. Twamley, L. J. Brown, A. S. Barnard, T. Plakhotnik, A. V. Zvyagin, and J. R. Rabeau. Observation and control of blinking nitrogen-vacancy centres in discrete nanodiamonds. *Nature Nanotechnology*, 5(5):345–349, 2010.
- [32] Liam P. McGuinness, Yuling Yan, Alastair Stacey, David A. Simpson, Liam T. Hall, Dougal Maclaurin, Steven Prawer, P. Mulvaney, J. Wrachtrup, and et al. F. Caruso. Quantum measurement and orientation tracking of fluorescent nanodiamonds inside living cells. *Nature Nanotechnology*, 6(6):358–363, 2011.
- [33] Roshanak Namdar and Shohreh Nafisi. Nanodiamond applications in skin preparations. *Drug Discovery Today*, 23(5):1152–1158, 2018.
- [34] Vadym Mochalin, Olga Shenderova, Dean Ho, and Yury Gogotsi. *The properties and applications of nanodiamonds*, pages 313–350. Jenny Stanford Publishing, 2020.
- [35] P. N. Volpe, N. Tranchant, J. C. Arnault, S. Saada, F. Jomard, and P. Bergonzo. Ultra-sharp boron interfaces for delta doped diamond structures. *physica status solidi (RRL)–Rapid Research Letters*, 6(2):59–61, 2012.

- [36] Yu V. Pleskov. Electrochemistry of diamond: A review. *Russian Journal of Electrochemistry*, 38:1275–1291, 2002.
- [37] Rocco Carcione, Silvia Battistoni, Elena Palmieri, Silvia Orlanducci, and Emanuela Tamburri. Pretreatment strategies of titanium substrates to modulate the electrochemical properties of cvd-grown ti-doped diamond electrodes for dopamine detection. *Surface and Coatings Technology*, 467:129662, 2023.
- [38] Gopalakrishnan Balasubramanian, I. Y. Chan, Roman Kolesov, Mohannad Al-Hmoud, Julia Tisler, Chang Shin, Changdong Kim, Aleksander Wojcik, Philip R. Hemmer, and et al. Anke Krueger. Nanoscale imaging magnetometry with diamond spins under ambient conditions. *Nature*, 455(7213):648–651, 2008.
- [39] Jeronimo R. Maze, Paul L. Stanwix, James S. Hodges, Seungpyo Hong, Jacob M. Taylor, Paola Cappellaro, Liang Jiang, M. V. Gurudev Dutt, Emre Togan, and et al. A. S. Zibrov. Nanoscale magnetic sensing with an individual electronic spin in diamond. *Nature*, 455(7213):644–647, 2008.
- [40] Florian Dolde, Helmut Fedder, Marcus W. Doherty, Tobias Nöbauer, Florian Rempp, Gopalakrishnan Balasubramanian, Thomas Wolf, Friedemann Reinhard, Lloyd C. L. Hollenberg, and et al. Fedor Jelezko. Electric-field sensing using single diamond spins. *Nature Physics*, 7(6):459–463, 2011.
- [41] Nobuteru Tsubouchi, M. Ogura, N. Mizuochi, and H. Watanabe. Electrical properties of a b doped layer in diamond formed by hot b implantation and high-temperature annealing. *Diamond and Related Materials*, 18(2-3):128–131, 2009.
- [42] Lu Wei and Gleb Yushin. Nanostructured activated carbons from natural precursors for electrical double layer capacitors. *Nano Energy*, 1(4):552–565, 2012.
- [43] Elena Palmieri, Francesca Pescosolido, Luca Montaina, Rocco Carcione, Greta Petrella, Daniel Oscar Cicero, Emanuela Tamburri, Silvia Battistoni, and Silvia Orlanducci. A sustainable hydroxypropyl cellulose-nanodiamond composite for flexible electronic applications. *Gels*, 8(12):783, 2022.
- [44] Amit Banerjee, Daniel Bernoulli, Hongti Zhang, Muk-Fung Yuen, Jiabin Liu, Jichen Dong, Feng Ding, Jian Lu, Ming Dao, and et al. Wenjun Zhang. Ultralarge elastic deformation of nanoscale diamond. *Science*, 360(6386):300–302, 2018.
- [45] M. G. Ivanov, S. V. Pavlyshko, D. M. Ivanov, I. Petrov, and O. Shenderova. Synergistic compositions of colloidal nanodiamond as lubricant-additive. *Journal of Vacuum Science & Technology B*, 28(4):869–877, 2010.
- [46] Vadym N. Mochalin, Ioannis Neitzel, Bastian J. M. Etzold, Amy Peterson, Giuseppe Palmese, and Yury Gogotsi. Covalent incorporation of aminated nanodiamond into an epoxy polymer network. *ACS Nano*, 5(9):7494–7502, 2011.

- [47] Ioannis Neitzel, Vadym Mochalin, Jason A. Bares, Robert W. Carpick, Ali Erdemir, and Y. Gogotsi. Tribological properties of nanodiamond-epoxy composites. *Tribology Letters*, 47:195–202, 2012.
- [48] Qingwei Zhang, Vadym N. Mochalin, Ioannis Neitzel, Isabel Y. Knoke, Jingjia Han, Christopher A. Klug, Jack G. Zhou, Peter I. Lelkes, and Yury Gogotsi. Fluorescent plla-nanodiamond composites for bone tissue engineering. *Biomaterials*, 32(1):87–94, 2011.
- [49] F. P. Bundy, H. Tracy Hall, H. M. Strong, and R. H. Wentorf Jr. Man-made diamonds. *Nature*, 176(4471):51–55, 1955.
- [50] Larissa F. Dobrzhinetskaya. Microdiamonds—frontier of ultrahigh-pressure metamorphism: a review. *Gondwana Research*, 21(1):207–223, 2012.
- [51] O. A. Shenderova, V. V. Zhirnov, and D. W. Brenner. Carbon nanostructures. *Critical Reviews in Solid State and Material Sciences*, 27(3-4):227–356, 2002.
- [52] John Edwin Field. *The properties of natural and synthetic diamond*. Academic Press, 1992.
- [53] W. Q. Liu, H. A. Ma, X. L. Li, Z. Z. Liang, R. Li, and X. Jia. Effects of additive al on the hpht diamond synthesis in an fe–mn–c system. *Diamond and Related Materials*, 16(8): 1486–1489, 2007.
- [54] Branko Deljanin, Matthias Alessandri, Adolf Peretti, and Mikko Åström. Ndt breaking the 10 carat barrier: World record faceted and gem-quality synthetic diamonds investigated. *Contributions to Gemology*, 15(1), 2015.
- [55] ITODYS. Wtacd-hpht. httpS://www.wtacd.be/en/Fundamental/Fundamental_research.html, .
- [56] Alexander F. Khokhryakov, Yuri N. Palyanov, Igor N. Kupriyanov, Yuri M. Borzdov, Alexander G. Sokol, Jürgen Härtwig, and Fabio Masiello. Crystal growth and perfection of large octahedral synthetic diamonds. *Journal of Crystal Growth*, 317(1):32–38, 2011.
- [57] Hitoshi Sumiya, Katsuko Harano, and Kenji Tamasaku. Hpht synthesis and crystalline quality of large high-quality (001) and (111) diamond crystals. *Diamond and Related Materials*, 58:221–225, 2015.
- [58] G. S. Woods. *The “type” terminology for diamond*. INSPEC, 1995.
- [59] R. C. Burns, A. I. Chumakov, S. H. Connell, D. Dube, H. P. Godfried, J. O. Hansen, J. Härtwig, J. Hoszowska, F. Masiello, and et al. L. Mkhonza. Hpht growth and x-ray characterization of high-quality type iia diamond. *Journal of Physics: Condensed Matter*, 21(36):364224, 2009.

- [60] M. Henini. Properties and growth of diamond: Gordon davies (ed.), inspec, institution of electrical engineers, london, uk, 1994. *MRS Bulletin*, 30(12):899–901, 1995.
- [61] Michael A Lieberman and Allan J Lichtenberg. Principles of plasma discharges and materials processing. *MRS Bulletin*, 30(12):899–901, 1994.
- [62] Jianjun Wang, Mingyao Zhu, Ron A. Outlaw, Xin Zhao, Dennis M. Manos, and Brian C. Holloway. Synthesis of carbon nanosheets by inductively coupled radio-frequency plasma enhanced chemical vapor deposition. *Carbon*, 42(14):2867–2872, 2004.
- [63] Lenka Zajíčková, Ondrej Jašek, Marek Eliáš, Petr Synek, Lukáš Lazar, Oldřich Schneeweiss, and Renáta Hanzlíková. Synthesis of carbon nanotubes by plasma-enhanced chemical vapor deposition in an atmospheric-pressure microwave torch. *Pure and Applied Chemistry*, 82(6):1259–1272, 2010.
- [64] Valerii Yu Dolmatov. Detonation-synthesis nanodiamonds: synthesis, structure, properties and applications. *Russian Chemical Reviews*, 76(4):339, 2007.
- [65] Viacheslav Vasilyovich Danilenko. On the history of the discovery of nanodiamond synthesis. *Physics of the Solid State*, 46:595–599, 2004.
- [66] Eiji Osawa. Monodisperse single nanodiamond particulates. *Pure and Applied Chemistry*, 80(7):1365–1379, 2008.
- [67] Anke Krüger, Fumiaki Kataoka, M. A. A. Ozawa, T. Fujino, Y. Suzuki, Aleksandr E. Aleksenskii, A. Ya Vul, and Eiji Osawa. Unusually tight aggregation in detonation nanodiamond: identification and disintegration. *Carbon*, 43(8):1722–1730, 2005.
- [68] Masaki Ozawa, Masayasu Inaguma, Makoto Takahashi, Fumiaki Kataoka, Anke Krueger, and E. Osawa. Preparation and behavior of brownish, clear nanodiamond colloids. *Advanced Materials*, 19(9):1201–1206, 2007.
- [69] F. Tian, J. Sun, S. L. Hu, and X. W. Du. Growth dynamics of nanodiamonds synthesized by pulsed-laser ablation. *Journal of Applied Physics*, 104(9), 2008.
- [70] Fei Tian, Hong Yang, Yong Guang Zhao, and Hong Mei Cao. Size effect on the transformation from graphite to nanodiamonds. In *Materials Science Forum*, volume 787, pages 412–418. Trans Tech Publ, 2014.
- [71] Gaurav Kumar Yogesh, Shivam Shukla, D. Sastikumar, and Pankaj Koinkar. Progress in pulsed laser ablation in liquid (plal) technique for the synthesis of carbon nanomaterials: a review. *Applied Physics A*, 127:1–40, 2021.
- [72] Michael Frenklach, R. Kematick, D. O. Huang, W. O. Howard, K. E. Spear, A. O. W. Phelps, and R. Koba. Homogeneous nucleation of diamond powder in the gas phase. *Journal of Applied Physics*, 66(1):395–399, 1989.

- [73] L. Vandenbulcke, T. Gries, and J. N. Rouzaud. Nanodiamonds in dusty low-pressure plasmas. *Applied Physics Letters*, 94(4), 2009.
- [74] T. Gries, L. Vandenbulcke, J. N. Rouzaud, and S. De Persis. Diagnostics in dusty c–h–o plasmas with diamond and graphitic nanoparticle generation. *Plasma Sources Science and Technology*, 19(2):025015, 2010.
- [75] Ajay Kumar, Pin Ann Lin, Albert Xue, Boyi Hao, Yoke Khin Yap, and R. Mohan Sankaran. Formation of nanodiamonds at near-ambient conditions via microplasma dissociation of ethanol vapour. *Nature Communications*, 4(1):2618, 2013.
- [76] Saman Iqbal, Muhammad Shahid Rafique, Muhammad Zahid, Shazia Bashir, Muhammad Ashfaq Ahmad, and Rabia Ahmad. Impact of carrier gas flow rate on the synthesis of nanodiamonds via microplasma technique. *Materials Science in Semiconductor Processing*, 74:31–41, 2018.
- [77] Mary De Feudis, Alexandre Tallaire, Louis Nicolas, Ovidiu Brinza, Philippe Goldner, Gabriel Hétet, Fabien Bénédic, and Jocelyn Achard. Large-scale fabrication of highly emissive nanodiamonds by chemical vapor deposition with controlled doping by siv and gev centers from a solid source. *Advanced Materials Interfaces*, 7(2):1901408, 2020.
- [78] Tanvi Nikhar and Sergey V. Baryshev. Evidence of gas phase nucleation of nanodiamond in microwave plasma assisted chemical vapor deposition. *AIP Advances*, 14(4), 2024.
- [79] Dorothée Szabó and Sabine Schlabach. Microwave plasma synthesis of materials—from physics and chemistry to nanoparticles: A materials scientist’s viewpoint. *Inorganics*, 2(3):468–507, 2014. ISSN 2304-6740. doi: 10.3390/inorganics2030468. URL <http://www.mdpi.com/2304-6740/2/3/468/>.
- [80] Michael Frenklach and Hai Wang. Detailed surface and gas-phase chemical kinetics of diamond deposition. *Physical Review B*, 43(2):1520, 1991.
- [81] Abdoulaye Constant Siby. Caractérisation d’une torche micro-plasma micro-onde pour l’élaboration de matériaux à base de carbone. Master’s thesis, Université Sorbonne Paris Nord, 2021.
- [82] A. Yu Nikiforov, Ch. Leys, M. A. Gonzalez, and J. L. Walsh. Electron density measurement in atmospheric pressure plasma jets: Stark broadening of hydrogenated and non-hydrogenated lines. *Plasma Sources Science and Technology*, 24(3):034001, 2015.
- [83] A. Gicquel, M. Chenevier, Kh. Hassouni, A. Tserepi, and M. Dubus. Validation of actinometry for estimating relative hydrogen atom densities and electron energy evolution in plasma assisted diamond deposition reactors. *Journal of Applied Physics*, 83(12): 7504–7521, 1998.
- [84] Jean-Loup Delcroix and Abraham Bers. *Physique des plasmas (Vol. II)*. EDP Sciences, 1994.

- [85] Alexander Fridman. *Plasma chemistry*. Cambridge University Press, 2008.
- [86] Th. Von Woedtke, Stephan Reuter, K. Masur, and K.-D. Weltmann. Plasmas for medicine. *Physics Reports*, 530(4):291–320, 2013.
- [87] Y. Kabouzi, M. D. Calzada, M. Moisan, K. C. Tran, and C. Trassy. Radial contraction of microwave-sustained columns at atmospheric pressure. *Journal of Applied Physics*, 91(3):1008–1019, 2002.
- [88] H. Matusiewicz. A novel microwave plasma cavity assembly for atomic emission spectrometry. *Spectrochimica Acta*, 47B(10):1221–1227, 1992.
- [89] Y. Okamoto, M. Yasuda, and S. Murayama. High-power microwave-induced plasma source for trace element analysis. *Japanese Journal of Applied Physics*, 29(4):670–672, 1990.
- [90] K. M. Green, M. C. Borrás, P. P. Woskov, G. J. Flores, K. Hadidi, and P. Thomas. Electronic excitation temperature profiles in an air microwave plasma torch. *IEEE Transactions on Plasma Science*, 29(2):399–406, 2001.
- [91] P. P. Woskov and K. Hadidi. Large electrodeless plasmas at atmospheric pressure sustained by a microwave waveguide. *IEEE Transactions on Plasma Science*, 30(1):156–157, 2002.
- [92] E. A. H. Timmermans, J. Jonkers, I. A. J. Thomas, A. Rodero, M. C. Quintero, A. Sola, A. Gamero, and J. A. M. Van Der Mullen. The behavior of molecules in microwave-induced plasmas studied by optical emission spectroscopy: 1. plasmas at atmospheric pressure. *Spectrochimica Acta Part B*, 53(11):1553–1566, 1998.
- [93] P. Leprince. Le plasma : milieu chimiquement actif pour le traitement de surface. In *Les plasmas froids dans l'industrie*, Lyon, 2003.
- [94] Olivier Leroy. The striplastron: A new circular stripline microwave launcher for plasma generation in capillary tubes. *Review of Scientific Instruments*, 93(7), 2022.
- [95] Albert Dato and Michael Frenklach. Substrate-free microwave synthesis of graphene: experimental conditions and hydrocarbon precursors. *New Journal of Physics*, 12(12):125013, 2010.
- [96] Albert Dato. Graphene synthesized in atmospheric plasmas—a review. *Journal of Materials Research*, 34(1):214–230, 2019.
- [97] Claire Tendero. *Torche plasma micro-onde à la pression atmosphérique: application au traitement de surfaces métalliques*. PhD thesis, Limoges, 2005.
- [98] J. Choi, F. Iza, H. J. Do, J. K. Lee, and M. H. Cho. Microwave-excited atmospheric-pressure microplasmas based on a coaxial transmission line resonator. *Plasma Sources Science and Technology*, 18(2):025029, 2009.

- [99] Jimo Lee and Gunsu S. Yun. Tunable microwave plasma coaxial resonator. *AIP Advances*, 11(10), 2021.
- [100] Karim Ouaras. *Mécanismes de formation et dynamique du transport des poussières de carbone et de tungstène dans un plasma Micro-Onde magnétisé et non-magnétisé*. PhD thesis, Université Sorbonne Paris Nord, 2016.
- [101] E Bisceglia, Swaminathan Prasanna, K Gazeli, X Aubert, CY Duluard, G Lombardi, and K Hassouni. Investigation of n (4s) kinetics during the transients of a strongly emissive pulsed ecr plasma using ns-talif. *Plasma Sources Science and Technology*, 30(9):095001, 2021.
- [102] B. Baudrillart, F. Bénédic, Th. Chauveau, A. Bartholomot, and J. Achard. Nanocrystalline diamond films grown at very low substrate temperature using a distributed antenna array microwave process: Towards polymeric substrate coating. *Diamond and Related Materials*, 75:44–51, 2017.
- [103] Chaimaa Mahi, Ovidiu Brinza, Riadh Issaoui, Jocelyn Achard, and Fabien Bénédic. Synthesis of high quality transparent nanocrystalline diamond films on glass substrates using a distributed antenna array microwave system. *Coatings*, 12(10):1375, 2022.
- [104] E. Timmermans. *Atomic molecular excitation processes in microwave induced plasmas: a spectroscopic study*. PhD thesis, Eindhoven University of Technology, 1999.
- [105] Michel Moisan and Jacques Pelletier. *Physique des plasmas collisionnels*. EDP Sciences, 2006.
- [106] Jaeho Kim, Makoto Katsurai, Dongmin Kim, and Hyroyuki Ohsaki. Microwave-excited atmospheric-pressure plasma jets using a microstrip line. *Applied Physics Letters*, 93(19):191505, 2008.
- [107] Jeffrey Hopwood, Alan R. Hoskinson, and José Gregório. Microplasmas ignited and sustained by microwaves. *Plasma Sources Science and Technology*, 23(6):064002, 2014.
- [108] J. J. Narendra, T. A. Grotjohn, and J. Asmussen. Microstripline applicators for creating microplasma discharges with microwave energy. *Plasma Sources Science and Technology*, 17(3):035027, 2008.
- [109] J. Hopwood, F. Iza, S. Coy, and D. B. Fenner. A microfabricated atmospheric-pressure microplasma source operating in air. *Journal of Physics D: Applied Physics*, 38(11):1698, 2005.
- [110] C. I. M. Beenakker. A cavity for microwave-induced plasmas operated in helium and argon at atmospheric pressure. *Spectrochimica Acta Part B: Atomic Spectroscopy*, 31(8-9):483–486, 1976.
- [111] M. Kamo, Y. Sato, S. Matsumoto, and N. Setaka. Diamond synthesis from gas phase in microwave plasma. *Journal of Crystal Growth*, 62:642–644, 1983.

- [112] P. K. Bachmann. Microwave plasma cvd and related techniques for low pressure diamond synthesis. In *Thin Film Diamond*, pages 31–53. Springer, 1994.
- [113] P. Bachmann, W. Drawl, D. Knight, R. Weimer, and R. Messier. Diamond nucleation and growth in bell jar microwave plasma cvd reactor. In G. H. Johnson, A. Badzian, and M. Geis, editors, *Extended abstracts: Diamond and Diamond-like Materials Synthesis*, page 99. MRS, Pittsburgh, 1988.
- [114] M. F  ner, C. Wild, and P. Koidl. Novel microwave plasma reactor for diamond synthesis. *Applied Physics Letters*, 72:1149–1151, 1998.
- [115] G. W. Faris, E. A. Brinkman, and J. B. Jeffries. Density measurements in a dc arcjet using scanned beam deflection tomography. *Opt. Express*, 7:447–460, 2000.
- [116] N. Ohtake, Y. Kuriyama, M. Yoshikawa, H. Obana, M. Kito, and H. Saito. Development of an arc-discharge plasma apparatus for the high-rate synthesis of diamond. *Bulletin of the Japan Society of Precision Engineering*, 25:5–10, 1991.
- [117] M. H. Loh and M. A. Cappelli. Diamond synthesis in supersonic direct-current arcjet plasma at subtorr pressures. *Surface and Coatings Technology*, 54:408–413, 1992.
- [118] K. Kurihara, K. Sasaki, M. Kawarada, and N. Koshino. High rate synthesis of diamond by dc plasma jet chemical vapor deposition. *Applied Physics Letters*, 52(6):437–438, 1988.
- [119] Y. A. Mankelevich, N. Suetin, M. Ashfold, W. Boxford, A. Orr-Ewing, J. Smith, and J. Wills. Chemical kinetics in carbon depositing dc-arc jet cvd reactors. *Diamond and Related Materials*, 12:383–390, 2003.
- [120] M. Cappelli, T. Owano, B. Dischler, and C. Wild. Low pressure synthetic diamond. In *Low Pressure Synthetic Diamond*, pages 59–84. Springer, Berlin, 1998.
- [121] University of Michigan. Wooldridge combustion facility. <http://wooldridge.engin.umich.edu/facilities/>, 2024.
- [122] E. Meeks, R. J. Kee, D. S. Dandy, and M. E. Coltrin. Computational simulation of diamond chemical vapor deposition in premixed $\text{C}_2\text{H}_2/\text{O}_2/\text{H}_2$ and CH_4/O_2 -strained flames. *Combustion and Flame*, 92:144–160, 1993.
- [123] G. V. E. Janssen, W. J. P. Schaminee, J. J. D. Vollenberg, W. Giling, and L. J. Seal. Rapid single crystalline diamond growth by acetylene-oxygen flame deposition. *Journal of Crystal Growth*, 104:752–757, 1990.
- [124] K. Ravi. Combustion synthesis: is it the most flexible of the diamond synthesis processes? *Diamond and Related Materials*, 4:243–249, 1995.
- [125] P. W. May. Diamond thin films: a 21st-century material. *Philosophical Transactions of the Royal Society of London A: Mathematical, Physical and Engineering Sciences*, 358: 473–495, 2000.

- [126] John C. Angus and Cliff C. Hayman. Low-pressure, metastable growth of diamond and "diamondlike" phases. *Science*, 241(4868):913–921, 1988.
- [127] James E. Butler and Anirudha V. Sumant. The cvd of nanodiamond materials. *Chemical Vapor Deposition*, 14(7-8):145–160, 2008.
- [128] Michael N. R. Ashfold, Paul W. May, James R. Petherbridge, Keith N. Rosser, James A. Smith, Yuri A. Mankelevich, and Nikolay V. Suetin. Unravelling aspects of the gas phase chemistry involved in diamond chemical vapour deposition. *Physical Chemistry Chemical Physics*, 3(17):3471–3485, 2001.
- [129] J. Achard, Vincent Jacques, and A. Tallaïre. Chemical vapour deposition diamond single crystals with nitrogen-vacancy centres: a review of material synthesis and technology for quantum sensing applications. *Journal of Physics D: Applied Physics*, 53(31):313001, 2020.
- [130] Nianjun Yang, Siyu Yu, Julie V Macpherson, Yasuaki Einaga, Hongying Zhao, Guohua Zhao, Greg M Swain, and Xin Jiang. Conductive diamond: synthesis, properties, and electrochemical applications. *Chemical Society Reviews*, 48(1):157–204, 2019.
- [131] Li Yang, Caiyi Jiang, Shenghui Guo, Libo Zhang, Jiyun Gao, Jinhui Peng, Tu Hu, and Liang Wang. Novel diamond films synthesis strategy: methanol and argon atmosphere by microwave plasma cvd method without hydrogen. *Nanoscale Research Letters*, 11: 1–6, 2016.
- [132] AA Emelyanov, VA Pinaev, M Yu Plotnikov, AK Rebrov, NI Timoshenko, and IB Yudin. Effect of argon on microwave plasma chemical vapor deposition of diamond coatings from an $\text{h}_2 + \text{ch}_4 + \text{ar}$ mixture activated in a microwave discharge. *Thermophysics and Aeromechanics*, 30(3):393–401, 2023.
- [133] G. Lombardi, K. Hassouni, G.-D. Stancu, L. Mechold, J. Röpcke, and A. Gicquel. Modeling of microwave discharges of h_2 admixed with ch_4 for diamond deposition. *Journal of Applied Physics*, 98(5), 2005.
- [134] Khaled Hassouni, Francis Mohasseb, Fabien Bénédic, Guillaume Lombardi, and Alix Gicquel. Formation of soot particles in $\text{ar}/\text{h}_2/\text{ch}_4$ microwave discharges during nanocrystalline diamond deposition: A modeling approach. *Pure and Applied Chemistry*, 78(6): 1127–1145, 2006.
- [135] Q. Zhang, H. D. Li, S. H. Cheng, Q. L. Wang, L. A. Li, X. Y. Lv, and G. T. Zou. The effect of co_2 on the high-rate homoepitaxial growth of cvd single crystal diamonds. *Diamond and Related Materials*, 20(4):496–500, 2011.
- [136] Stephen J. Harris and Anita M. Weiner. Effects of oxygen on diamond growth. *MRS Online Proceedings Library*, 162:103–107, 1989.

- [137] Soumen Mandal. Nucleation of diamond films on heterogeneous substrates: a review. *RSC Advances*, 11:10159–10182, 2021.
- [138] Jean-Charles Arnault and Hugues A. Girard. Diamond nucleation and seeding techniques: Two complementary strategies for the growth of ultra-thin diamond films. In *Nanodiamond*, pages 221–252. Royal Society of Chemistry, 2014.
- [139] Jakob Hees, Armin Kriele, and Oliver A. Williams. Electrostatic self-assembly of diamond nanoparticles. *Chemical Physics Letters*, 509(1-3):12–15, 2011.
- [140] Oliver A. Williams, Olivier Douhéret, Michael Daenen, Ken Haenen, Eiji Osawa, and Makoto Takahashi. Enhanced diamond nucleation on monodispersed nanocrystalline diamond. *Chemical Physics Letters*, 445(4-6):255–258, 2007.
- [141] Michael Daenen, Oliver Aneurin Williams, Jan D’Haen, Ken Haenen, and Milos Nesládek. Seeding, growth and characterization of nanocrystalline diamond films on various substrates. *physica status solidi (a)*, 203(12):3005–3010, 2006.
- [142] Henry A. Bland, Evan L. H. Thomas, Georgina M. Klemencic, Soumen Mandal, David J. Morgan, Andreas Papageorgiou, Tyrone G. Jones, and Oliver A. Williams. Superconducting diamond on silicon nitride for device applications. *Scientific Reports*, 9(1):2911, 2019.
- [143] S. T. T. T. Yugo, T. Kanai, T. Kimura, and T. Muto. Generation of diamond nuclei by electric field in plasma chemical vapor deposition. *Applied Physics Letters*, 58(10):1036–1038, 1991.
- [144] J. Gerber, M. Weiler, O. Sohr, K. Jung, and H. Ehrhardt. Investigations of diamond nucleation on ac films generated by dc bias and microwave plasma. *Diamond and Related Materials*, 3(4-6):506–509, 1994.
- [145] B. R. Stoner, G.-H. M. Ma, S. D. Wolter, and J. T. Glass. Characterization of bias-enhanced nucleation of diamond on silicon by in vacuo surface analysis and transmission electron microscopy. *Physical Review B*, 45(19):11067, 1992.
- [146] Shlomo Rotter. Applications of conformal cvd diamond films. *Israel Journal of Chemistry*, 38(1-2):135–140, 1998.
- [147] Shlomo Zalka Rotter and Joana Catarina Madaleno. Diamond cvd by a combined plasma pretreatment and seeding procedure. *Chemical Vapor Deposition*, 15(7-9):209–216, 2009.
- [148] Rajanish N. Tiwari and Li Chang. Growth, microstructure, and field-emission properties of synthesized diamond film on adamantane-coated silicon substrate by microwave plasma chemical vapor deposition. *Journal of Applied Physics*, 107(10), 2010.
- [149] K. Tsugawa, M. Ishihara, J. Kim, Y. Koga, and M. Hasegawa. Nucleation enhancement of nanocrystalline diamond growth at low substrate temperatures by adamantane seeding. *The Journal of Physical Chemistry C*, 114(9):3822–3824, 2010.

- [150] Sven Stauss, Chikako Ishii, David Z. Pai, Keiichiro Urabe, and Kazuo Terashima. Diamondoid synthesis in atmospheric pressure adamantane–argon–methane–hydrogen mixtures using a continuous flow plasma microreactor. *Plasma Sources Science and Technology*, 23(3):035016, 2014.
- [151] A Michau, P Swaminathan, S Longo, and K Hassouni. Particle charge fluctuation and its consequences on aerosol dynamics in dusty plasmas: from continuous to discrete statistical models. *Plasma Physics and Controlled Fusion*, 62(1):014002, 2019.
- [152] Kathleen De Bleecker, Annemie Bogaerts, and Wim Goedheer. Detailed modeling of hydrocarbon nanoparticle nucleation in acetylene discharges. *Physical Review E—Statistical, Nonlinear, and Soft Matter Physics*, 73(2):026405, 2006.
- [153] Eric Herbst and Chun Ming Leung. Gas-phase production of complex hydrocarbons, cyanopolynes, and related compounds in dense interstellar clouds. *Astrophysical Journal Supplement Series*, 69:271–300, 1989.
- [154] Gautier Tetard. *Modélisation de la formation de nanoparticules et des effets 'dusty plasma' dans les décharges radio-fréquence d'argon-acétylène*. PhD thesis, Université Sorbonne Paris Nord, July 2022.
- [155] Ch. Deschenaux, A. Affolter, D. Magni, Ch. Hollenstein, and P. Fayet. Investigations of CH_4 , C_2H_2 , and C_2H_4 dusty rf plasmas by means of FIR absorption spectroscopy and mass spectrometry. *Journal of Physics D: Applied Physics*, 32(15):1876, 1999.
- [156] Gautier Tetard, Armelle Michau, Swaminathan Prasanna, Jonathan Mougenot, Pascal Brault, and Khaled Hassouni. Molecular growth paths and dust-particles nucleation precursors in $\text{Ar}/\text{C}_2\text{H}_2$ low pressure discharges. *Plasma Processes and Polymers*, 19(5):2100204, 2022.
- [157] K. Ouaras, L. Colina Delacqua, G. Lombardi, J. Röpcke, M. Wartel, X. Bonnin, M. Redolfi, and K. Hassouni. In-situ diagnostics of hydrocarbon dusty plasmas using quantum cascade laser absorption spectroscopy and mass spectrometry. *Journal of Plasma Physics*, 80(6):833–841, 2014.
- [158] Kungen Teii, Tomohiro Ikeda, Atsushi Fukutomi, and Kiichiro Uchino. Effect of hydrogen plasma exposure on the amount of trans-polyacetylene in nanocrystalline diamond films. *Journal of Vacuum Science & Technology B: Microelectronics and Nanometer Structures Processing, Measurement, and Phenomena*, 24(1):263–266, 2006.
- [159] F. Piazza, A. Golanski, S. Schulze, and Gary Relihan. Transpolyacetylene chains in hydrogenated amorphous carbon films free of nanocrystalline diamond. *Applied Physics Letters*, 82(3):358–360, 2003.
- [160] Ralf I. Kaiser. Experimental Investigation on the Formation of Carbon-Bearing Molecules in the Interstellar Medium via Neutral–Neutral Reactions. *Chemical Reviews*, 102(5):

- 1309–1358, May 2002. ISSN 0009-2665, 1520-6890. doi: 10.1021/cr970004v. URL <https://pubs.acs.org/doi/10.1021/cr970004v>.
- [161] Alexander M Mebel and Ralf I Kaiser. Formation of Resonantly Stabilized Free Radicals via the Reactions of Atomic Carbon, Dicarbon, and Tricarbon with Unsaturated Hydrocarbons: Theory and Crossed Molecular Beams Experiments.
- [162] Bikau Shukla and Mitsuo Koshi. A novel route for pah growth in haca based mechanisms. *Combustion and Flame*, 159(12):3589–3596, 2012.
- [163] Hartwell F. Calcote. Mechanisms of soot nucleation in flames—a critical review. *Combustion and Flame*, 42:215–242, 1981.
- [164] Michael Frenklach, Ravi I. Singh, and Alexander M. Mebel. On the low-temperature limit of haca. *Proceedings of the Combustion Institute*, 37(1):969–976, 2019.
- [165] Michael Frenklach and Alexander M. Mebel. On the mechanism of soot nucleation. *Physical Chemistry Chemical Physics*, 22(9):5314–5331, 2020.
- [166] Ming Mao, Jan Benedikt, Angelo Consoli, and Annemie Bogaerts. New pathways for nanoparticle formation in acetylene dusty plasmas: a modelling investigation and comparison with experiments. *Journal of Physics D: Applied Physics*, 41(22):225201, 2008.
- [167] Kathleen De Bleecker, Annemie Bogaerts, and Wim Goedheer. Aromatic ring generation as a dust precursor in acetylene discharges. *Applied Physics Letters*, 88(15), 2006.
- [168] Mohammad Reza Kholghy. *The evolution of soot morphology in laminar co-flow diffusion flames of the surrogates for Jet A-1 and a synthetic kerosene*. PhD thesis, University of Toronto Toronto, Canada, 2012.
- [169] Saeed Ahmad, Hua Jiang, Kimmo Mustonen, Qiang Zhang, Aqeel Hussain, Abu Taher Khan, Nan Wei, Mohammad Tavakkoli, Yongping Liao, and et al. Er-Xiong Ding. Gas-phase synthesis of carbon nanotube-graphene heterostructures. *arXiv preprint arXiv:1904.08323*, 2019.
- [170] Jerome Perrin, Ch Bohm, Roxana Etemadi, and Antoni Lloret. Possible routes for cluster growth and particle formation in rf silane discharges. *Plasma Sources Science and Technology*, 3(3):252, 1994.
- [171] JS Knight, CG Freeman, MJ McEwan, VG Anicich, and WT Huntress. A flow tube study of ion-molecule reactions of acetylene. *Journal of Physical Chemistry*, 91(14): 3898–3902, 1987.
- [172] M. Y. Gamarnik. Size-related stabilization of diamond nanoparticles. *Nanostructured Materials*, 7(6):651–658, 1996.

- [173] Nong M. Hwang, Jun H. Hahn, and Duk Y. Yoon. Charged cluster model in the low pressure synthesis of diamond. *Journal of Crystal Growth*, 162(1):55–68, April 1996.
- [174] A. S. Barnard, S. P. Russo, and I. K. Snook. Modeling of stability and phase transformations in quasi-zero dimensional nanocarbon systems. *Journal of Computational and Theoretical Nanoscience*, 2(2):180–201, June 2005.
- [175] V. Yu Dolmatov, V. Myllymäki, and A. Vehanen. A possible mechanism of nanodiamond formation during detonation synthesis. *Journal of Superhard Materials*, 35(3):143–150, 2013.
- [176] Chikako Ishii, Sven Stauss, Koichi Kuribara, Keiichiro Urabe, Takehiko Sasaki, and Kazuo Terashima. Atmospheric pressure synthesis of diamondoids by plasmas generated inside a microfluidic reactor. *Diamond and Related Materials*, 59:40–46, 2015.
- [177] Swaminathan Prasanna, Armelle Michau, Cathy Rond, Khaled Hassouni, and Alix Gicquel. Self-consistent simulation studies on effect of methane concentration on microwave assisted $\text{H}_2\text{-CH}_4$ plasma at low pressure. *Plasma Sources Science and Technology*, 26(9): 097001, 2017.
- [178] David Warren Ball. *Field guide to spectroscopy*, volume 8. Spie Press Bellingham, Washington, 2006.
- [179] Kristaq Gazeli, Guillaume Lombardi, Xavier Aubert, Corinne Y. Duluard, Swaminathan Prasanna, and Khaled Hassouni. Progresses on the use of two-photon absorption laser induced fluorescence (talif) diagnostics for measuring absolute atomic densities in plasmas and flames. *Plasma*, 4(1):145–171, 2021.
- [180] Laurent Invernizzi, Corinne Y. Duluard, Hans Höft, Khaled Hassouni, Guillaume Lombardi, Kristaq Gazeli, and Swaminathan Prasanna. Peculiarities of measuring fluorescence decay times by a streak camera for ps-talif experiments in reactive plasmas. *Measurement Science and Technology*, 34(9):095203, 2023.
- [181] Hamamatsu. Universal streak camera. <https://www.hamamatsu.com/jp/en/product/photometry-systems/streak-camera/universal-streak-camera/applications.html>.
- [182] Wikipedia contributors. Raman scattering. https://en.wikipedia.org/wiki/Raman_scattering, 2024.
- [183] Horiba Scientific. Raman spectrometer presentation. <https://www.horiba.com/int/scientific/technologies/raman-imaging-and-spectroscopy/raman-spectrometer-presentation/>, n.d.
- [184] Laser Focus World. How to choose a laser: How to choose a laser for raman spectroscopy. <https://www.laserfocusworld.com/lasers-sources/article/16555207/>

- how-to-choose-a-laser-how-to-choose-a-laser-for-raman-spectroscopy, n.d.
- [185] S. Praver, K. W. Nugent, D. N. Jamieson, J. O. Orwa, L. Al Bursill, and J. L. Peng. The raman spectrum of nanocrystalline diamond. *Chemical Physics Letters*, 332(1-2):93–97, 2000.
- [186] S. A. Solin and A. K. Ramdas. Raman spectrum of diamond. *Physical Review B*, 1(4):1687, 1970.
- [187] James Birrell, J. E. Gerbi, O. Auciello, J. M. Gibson, J. Johnson, and J. A. Carlisle. Interpretation of the raman spectra of ultrananocrystalline diamond. *Diamond and Related Materials*, 14(1):86–92, 2005.
- [188] Stephanie Reich and Christian Thomsen. Raman spectroscopy of graphite. *Philosophical Transactions of the Royal Society of London. Series A: Mathematical, Physical and Engineering Sciences*, 362(1824):2271–2288, 2004.
- [189] F. Tuinstra and Jack L. Koenig. Raman spectrum of graphite. *The Journal of Chemical Physics*, 53(3):1126–1130, 1970.
- [190] Andrea Carlo Ferrari and John Robertson. Raman spectroscopy of amorphous, nanostructured, diamond-like carbon, and nanodiamond. *Philosophical Transactions of the Royal Society of London. Series A: Mathematical, Physical and Engineering Sciences*, 362(1824):2477–2512, 2004.
- [191] Andrea C. Ferrari and John Robertson. Interpretation of raman spectra of disordered and amorphous carbon. *Physical Review B*, 61(20):14095, 2000.
- [192] Andrea Carlo Ferrari and John Robertson. Resonant raman spectroscopy of disordered, amorphous, and diamondlike carbon. *Physical Review B*, 64(7):075414, 2001.
- [193] S. Lefrant, E. Perrin, and E. Mulazzi. Study of the properties of trans-polyacetylene through the raman spectra analysis. *Synthetic Metals*, 28(3):D295–D302, 1989.
- [194] E. Mulazzi, G. P. Brivio, E. Faulques, and S. Lefrant. Experimental and theoretical raman results in trans polyacetylene. *Solid State Communications*, 46(12):851–855, 1983.
- [195] Alexander M. Zaitsev. *Optical Properties of Diamond: A Data Handbook*. Springer Science & Business Media, 2013.
- [196] V. G. Ralchenko, V. S. Sedov, A. A. Khomich, V. S. Krivobok, S. N. Nikolaev, S. S. Savin, I. I. Vlasov, and V. I. Konov. Observation of the ge-vacancy color center in microcrystalline diamond films. *Bulletin of the Lebedev Physics Institute*, 42:165–168, 2015.
- [197] Core Tech Integratd Limited. Theory of x-ray photoelectron spectroscopy. https://www.coretechint.com/zh-hans/technical_info/theory_detail/1/.

- [198] ITODYS. Xps-ups-magcis. <https://www.itodys.univ-paris-diderot.fr/fr/services/xps-ups-magcis-2>, .
- [199] Younes Boukellal. *Contribution à la mise en place d'un microscope à force atomique métrologique (mAFM): Conception d'une tête AFM métrologique et caractérisation métrologique de l'instrument*. PhD thesis, École normale supérieure de Cachan-ENS Cachan, 2015.
- [200] MAX IV. Afm scanning modes. <https://www.maxiv.lu.se/beamlines-accelerators/support-labs/microscopy-labs/atomic-force-microscope/afm-scanning-modes/>.
- [201] Haithem Mansour. *Caractérisation des défauts cristallins au MEB par canalisation d'électrons assistée par diagrammes pseudo-Kikuchi haute résolution: application à l'acier IF, UO₂ et TiAl*. PhD thesis, Université de Lorraine, 2016.
- [202] ThermoFischer Scientific. What is sem? scanning electron microscopy explained. <https://www.thermofisher.com/blog/materials/what-is-sem-scanning-electron-microscopy-explained/>, 2023.
- [203] Ray F. Egerton. *Physical Principles of Electron Microscopy*, volume 56. Springer, 2005.
- [204] ResearchTweet. What is electron microscopy? principle, types, and importance. <https://researchtweet.com/what-is-electron-microscopy-principle-types/>.
- [205] David B Williams, C Barry Carter, David B Williams, and C Barry Carter. *The transmission electron microscope*. Springer, 1996.
- [206] Jeanne Ayache, Luc Beaunier, Jacqueline Boumendil, Gabrielle Ehret, and Danièle Laub. The different observation modes in electron microscopy (sem, tem, stem). In *Sample Preparation Handbook for Transmission Electron Microscopy: Methodology*, pages 33–55. Springer, 2010.
- [207] David M Pozar. *Microwave engineering: theory and techniques*. John wiley & sons, 2021.
- [208] P. J. Bruggeman, N. Sadeghi, D. C. Schram, and V. Linss. Gas temperature determination from rotational lines in non-equilibrium plasmas: a review. *Plasma Sources Science and Technology*, 23(2):023001, 2014.
- [209] S. A. Astashkevich, M. Käning, E. Käning, N. V. Kokina, B. P. Lavrov, A. Ohl, and J. Röpcke. Radiative characteristics of 3p σ , π ; 3d π^- , δ^- states of h₂ and determination of gas temperature of low pressure hydrogen containing plasmas. *Journal of Quantitative Spectroscopy and Radiative Transfer*, 56(5):725–751, 1996.
- [210] Se Youn Moon and Wonho Choe. A comparative study of rotational temperatures using diatomic oh, o₂ and n₂⁺ molecular spectra emitted from atmospheric plasmas. *Spectrochimica Acta Part B: Atomic Spectroscopy*, 58(2):249–257, 2003.

- [211] M. M. Vasiljevic, G. Lj. Majstorovic, D. J. Spasojevic, and N. Konjevic. Application of $gk^1\sigma_g, \nu = 0 \rightarrow b^1\sigma, \nu = 0$ hydrogen band for the axial temperature measurement in the cathode sheath region of an abnormal glow discharge. *European Physical Journal D*, 75: 112, 2021.
- [212] Mario Capitelli. *Nonequilibrium vibrational kinetics*, volume 39. Springer Science & Business Media, 2012.
- [213] I. Kovacs. *Rotational Structure in the Spectra of Diatomic Molecules*. Academic Press, 1969.
- [214] G. Lj. Majstorović and N. M. Šišović. On the use of two hydrogen bands for spectroscopic temperature measurement in a low-pressure gas discharge. *Journal of Research in Physics*, 36(1):1–12, 2012.
- [215] Gerhard Herzberg. *Molecular Spectra and Molecular Structure - Vol I*. Read Books Ltd, 2013.
- [216] H. N. Chu, E. A. Den Hartog, A. R. Lefkow, J. Jacobs, L. W. Anderson, M. G. Lagally, and J. E. Lawler. Measurements of the gas kinetic temperature in a $\text{ch}_4\text{-h}_2$ discharge during the growth of diamond. *Physical Review A*, 44(6):3796, 1991.
- [217] A. N. Goyette, W. B. Jameson, L. W. Anderson, and J. E. Lawler. An experimental comparison of rotational temperature and gas kinetic temperature in a discharge. *Journal of Physics D: Applied Physics*, 29(5):1197, 1996.
- [218] Tian-Liang Zhao, Yong Xu, Yuan-Hong Song, Xiao-Song Li, Jing-Lin Liu, Jin-Bao Liu, and Ai-Min Zhu. Determination of vibrational and rotational temperatures in a gliding arc discharge by using overlapped molecular emission spectra. *Journal of Physics D: Applied Physics*, 46(34):345201, 2013.
- [219] J. Röpcke, M. Käning, and B. P. Lavrov. Spectroscopical diagnostics of molecular microwave plasmas. *Journal de Physique IV France*, 08(PR7):Pr7–216, October 1998.
- [220] R. K. Garg, T. N. Anderson, R. P. Lucht, T. S. Fisher, and J. P. Gore. Gas temperature measurements in a microwave plasma by optical emission spectroscopy under single-wall carbon nanotube growth conditions. *Journal of Physics D: Applied Physics*, 41(9):095206, 2008.
- [221] Zhou Qing, D. K. Otorbaev, G. J. H. Brussaard, M. C. M. van de Sanden, and D. C. Schram. Diagnostics of the magnetized low-pressure hydrogen plasma jet: Molecular regime. *Journal of Applied Physics*, 80(3):1312–1324, August 1996.
- [222] Gerhard Heinrich Dieke. Hydrogen molecule wavelength tables of gerhard heinrich dieke. Technical report, Wiley-Interscience, 1972.

- [223] L. Wolniewicz and K. Dressler. The ef and gk $1g^+$ states of hydrogen: Adiabatic calculation of vibronic states in h_2 , hd , and d_2 . *Journal of Molecular Spectroscopy*, 67(1): 416–439, September 1977.
- [224] A. Gicquel, K. Hassouni, Y. Breton, M. Chenevier, and J. C. Cubertaon. Gas temperature measurements by laser spectroscopic techniques and by optical emission spectroscopy. *Diamond and Related Materials*, 5(3):366–372, April 1996.
- [225] Xavier Duten, Antoine Rousseau, Alix Gicquel, Khaled Hassouni, and Philippe Leprince. Time-resolved measurements of the gas temperature in a h_2/ch_4 medium pressure microwave 915 mhz pulsed plasma. *Journal of Physics D: Applied Physics*, 35(16):1939, 2002.
- [226] J. Krištof, A. Anušová, M. Anguš, P. Veis, X. Yang, T. Angot, P. Roubin, and G. Cartry. Diagnostics of low-pressure hydrogen discharge created in a 13.56 mhz rf plasma reactor. *Physica Scripta*, 91(7):074009, July 2016.
- [227] Marco Antonio Gigosos. Stark broadening models for plasma diagnostics. *Journal of Physics D: Applied Physics*, 47(34):343001, August 2014.
- [228] J. M. Palomares, S. Hübner, E. A. D. Carbone, N. de Vries, E. M. van Veldhuizen, A. Sola, A. Gamero, and J. J. A. M. van der Mullen. H stark broadening in cold plasmas with low electron densities calibrated with thomson scattering. *Spectrochimica Acta Part B: Atomic Spectroscopy*, 73:39–47, July 2012.
- [229] Marco A. Gigosos, Manuel Á. González, and Valentín Cardeñoso. Computer simulated balmer-alpha, -beta and -gamma stark line profiles for non-equilibrium plasmas diagnostics. *Spectrochimica Acta Part B: Atomic Spectroscopy*, 58(8):1489–1504, August 2003.
- [230] B. N. Sismanoglu, J. Amorim, J. A. Souza-Corrêa, C. Oliveira, and M. P. Gomes. Optical emission spectroscopy diagnostics of an atmospheric pressure direct current microplasma jet. *Spectrochimica Acta Part B: Atomic Spectroscopy*, 64(11-12):1287–1293, 2009.
- [231] Hans R. Griem and Ralph H. Lovberg. *Plasma Physics*. Academic Press, 1971.
- [232] N. Konjević, M. Ivković, and N. Sakan. Hydrogen balmer lines for low electron number density plasma diagnostics. *Spectrochimica Acta Part B: Atomic Spectroscopy*, 76:16–26, 2012.
- [233] J. Torres, J. Jonkers, M. J. van de Sande, J. J. A. M. van der Mullen, A. Gamero, and A. Sola. An easy way to determine simultaneously the electron density and temperature in high-pressure plasmas by using stark broadening. *Journal of Physics D: Applied Physics*, 36(13):L55–L59, June 2003.
- [234] J. Torres, J. M. Palomares, A. J. A. M. Sola, J. J. A. M. Van der Mullen, and A. Gamero. A stark broadening method to determine simultaneously the electron temperature and

- density in high-pressure microwave plasmas. *Journal of Physics D: Applied Physics*, 40(19):5929, 2007.
- [235] N. Derkaoui, C. Rond, Thomas Gries, Gérard Henrion, and A. Gicquel. Determining electron temperature and electron density in moderate pressure h_2/ch_4 microwave plasma. *Journal of Physics D: Applied Physics*, 47(20):205201, 2014.
- [236] N. Zhang, F. Sun, L. Zhu, M. P. Planche, H. Liao, C. Dong, and C. Coddet. Electron temperature and density of the plasma measured by optical emission spectroscopy in vlpps conditions. *Journal of Thermal Spray Technology*, 20:1321–1327, 2011.
- [237] K. Hassouni, M. Capitelli, F. Esposito, and A. Gicquel. State to state dissociation constants and non-equilibrium vibrational distributions under microwave hydrogen plasmas. *Chemical Physics Letters*, 340(3-4):322–327, 2001.
- [238] Jounayd Bentounes. *Étude expérimentale de la production d'un courant d'ions négatifs appliquée à la fusion thermonucléaire contrôlée par utilisation de techniques spectroscopiques et confrontation des résultats expérimentaux à un modèle numérique*. PhD thesis, Université de Mostaganem (Algérie), September 2018.
- [239] Sandra Schröter, Jérôme Bredin, Andrew R. Gibson, Andrew West, James P. Dedrick, Erik Wagenaars, Kari Niemi, Timo Gans, and Deborah O'Connell. The formation of atomic oxygen and hydrogen in atmospheric pressure plasmas containing humidity: picosecond two-photon absorption laser induced fluorescence and numerical simulations. *Plasma Sources Science and Technology*, 29(10):105001, 2020.
- [240] S. Zhang, A. F. H. Van Gessel, S. C. Van Grootel, and P. J. Bruggeman. The effect of collisional quenching of the $\text{o}(3\text{p}3\text{p})$ state on the determination of the spatial distribution of the atomic oxygen density in an appj operating in ambient air by talif. *Plasma Sources Science and Technology*, 23(2):025012, 2014.
- [241] Corinne Y. Duluard, Laurent Invernizzi, Khaled Hassouni, Guillaume Lombardi, Kristaq Gazeli, and Swaminathan Prasanna. Depopulation mechanisms of atomic hydrogen in the $n = 3$ level following two-photon excitation by a picosecond laser. *Plasma Sources Science and Technology*, 33(1):015003, 2024.
- [242] K. Hassouni, A. Gicquel, M. Capitelli, and J. Loureiro. Chemical kinetics and energy transfer in moderate pressure h_2 plasmas used in diamond mpacvd processes. *Plasma Sources Science and Technology*, 8(3):494–512, 1999.
- [243] W. L. Wiese and J. R. Fuhr. Accurate atomic transition probabilities for hydrogen, helium, and lithium. *Journal of Physical and Chemical Reference Data*, 38(3):565–720, 2009.
- [244] F. Brouillard and Xavier Urbain. Associative ionisation in low energy collisions. *Physica Scripta*, 2002(T96):86, 2002.

- [245] Akhilesh K Arora, T. R. Ravindran, G. L. N. Reddy, Arun K. Sikder, and D. S. Misra. Nature of confinement of phonons in nanocrystalline cvd diamond. *Diamond and Related Materials*, 10(8):1477–1485, 2001.
- [246] Vitaly I Korepanov, Hiro o Hamaguchi, Eiji Osawa, Vladimir Ermolenkov, Igor K Lednev, Bastian J. M. Etzold, Olga Levinson, Boris Zousman, Chandra Prakash Epperla, and Huan-Cheng Chang. Carbon structure in nanodiamonds elucidated from raman spectroscopy. *Carbon*, 121:322–329, 2017.
- [247] Kien-Wen Sun, J. Y. Wang, and T. Y. Ko. Photoluminescence and raman spectroscopy of single diamond nanoparticle. *Journal of Nanoparticle Research*, 10:115–120, 2008.
- [248] Denis Bogdanov, Alexander Bogdanov, Vladimir Plotnikov, Sergey Makarov, Alexander Yelissev, and Aleksei Chepurov. Core growth of detonation nanodiamonds under high-pressure annealing. *RSC Advances*, 11(21):12961–12970, 2021.
- [249] Leyong Hu, Yang Guo, Shuo Du, Shibing Tian, Junjie Li, and Changzhi Gu. Probing trans-polyacetylene segments in a diamond film by tip-enhanced raman spectroscopy. *Diamond and Related Materials*, 116:108415, 2021.
- [250] K. Ganesan, P. K. Ajikumar, S. K. Srivastava, and P. Magudapathy. Structural, raman and photoluminescence studies on nanocrystalline diamond films: Effects of ammonia in feedstock. *Diamond and Related Materials*, 106:107872, 2020.
- [251] M. Veres, S. Tóth, and M. Koós. Grain boundary fine structure of ultrananocrystalline diamond thin films measured by raman scattering. *Applied Physics Letters*, 91(3), 2007.
- [252] R Pfeiffer, H Kuzmany, N Salk, and B Günther. Evidence for trans-polyacetylene in nanocrystalline diamond films from h–d isotropic substitution experiments. *Applied Physics Letters*, 82(23):4149–4150, 2003.
- [253] R Thomas and DK Voznyak. Raman studies on zircon from the koffiefontein mine, free state province, south africa. *Geol Earth Mar Sci*, 6(2):1–3, 2024.
- [254] M Reinoso, F Álvarez, and H Huck. Hard carbon coatings deposited on steel. *Applied surface science*, 254(1):181–184, 2007.
- [255] Elhadji Cheikh Talibouya Ba, Marcello Rosa Dumont, Paulo Sérgio Martins, Bárbara da Silva Pinheiro, Matheus Philippe Martins da Cruz, and Jorge Wanderson Barbosa. Deconvolution process approach in raman spectra of dlc coating to determine the sp³ hybridization content using the id/ig ratio in relation to the quantification determined by x-ray photoelectron spectroscopy. *Diamond and Related Materials*, 122:108818, 2022.
- [256] Oleg S Kudryavtsev, Rustem H Bagramov, Dmitrii G Pasternak, Arkady M Satanin, Oleg I Lebedev, Vladimir P Filonenko, and Igor I Vlasov. Raman fingerprints of ultrasmall nanodiamonds produced from adamantane. *Diamond and Related Materials*, 133:109770, 2023.

- [257] Robert John Nemanich and SA Solin. First-and second-order raman scattering from finite-size crystals of graphite. *Physical Review B*, 20(2):392, 1979.
- [258] Ziyao Yuan, Yuning Guo, Cuihong Li, Lusheng Liu, Bing Yang, Haozhe Song, Zhaofeng Zhai, Zhigang Lu, Hong Li, Thorsten Staedler, et al. New multilayered diamond/ β -sic composite architectures for high-performance hard coating. *Materials & Design*, 186: 108207, 2020.
- [259] Anna Dychalska, Piotr Popielarski, Wojciech Franków, Kazimierz Fabisiak, Kazimierz Paprocki, and Mirosław Szybowicz. Study of cvd diamond layers with amorphous carbon admixture by raman scattering spectroscopy. *Mater. Sci.-Pol*, 33(4):799–805, 2015.
- [260] L Himics, S Tóth, M Veres, and M Koós. Spectral properties of the zero-phonon line from ensemble of silicon–vacancy center in nanodiamond. *Optical and Quantum Electronics*, 48:1–11, 2016.
- [261] Frederik Klauser, Doris Steinmüller-Nethl, Reinhard Kaindl, Erminald Bertel, and Norbert Memmel. Raman studies of nano-and ultra-nanocrystalline diamond films grown by hot-filament cvd. *Chemical Vapor Deposition*, 16(4-6):127–135, 2010.
- [262] X. B. Yan, T. Xu, S. R. Yang, H. W. Liu, and Q. J. Xue. Characterization of hydrogenated diamond-like carbon films electrochemically deposited on a silicon substrate. *Journal of Physics D: Applied Physics*, 37(17):2416, 2004.
- [263] T. Y. Leung, W. F. Man, P. K. Lim, W. C. Chan, F. Gaspari, and S. Zukotynski. Determination of the sp^3/sp^2 ratio of a-c:h by xps and xaes. *Journal of Non-Crystalline Solids*, 254(1-3):156–160, 1999.
- [264] J. F. Zhao, P. Lemoine, Z. H. Liu, J. P. Quinn, and J. A. McLaughlin. The effects of si incorporation on the microstructure and nanomechanical properties of dlc thin films. *Journal of Physics: Condensed Matter*, 12(44):9201, 2000.
- [265] Se Youn Moon, Dan-Bee Kim, B Gweon, and W Choe. Temperature measurement of an atmospheric pressure arc discharge plasma jet using the diatomic cn ($b\sigma + 2-\chi\sigma + 2$, violet system) molecular spectra. *Journal of applied physics*, 105(5), 2009.
- [266] Kosuke Kurosawa, Seiji Sugita, Kazuhisa Fujita, Ko Ishibashi, Toshihiko Kadono, Sohsuke Ohno, and Takafumi Matsui. Rotational-temperature measurements of chemically reacting cn using band-tail spectra. *Journal of Thermophysics and Heat Transfer*, 23(3):463–472, 2009.
- [267] J Krelowski, G Galazutdinov, and Piotr Gnaciński. Cn rotational excitation. *Astronomische Nachrichten*, 333(7):627–633, 2012.
- [268] J Luque, W Juchmann, and JB Jeffries. Spatial density distributions of c 2, c 3, and ch radicals by laser-induced fluorescence in a diamond depositing dc-arcjet. *Journal of applied physics*, 82(5):2072–2081, 1997.

- [269] Pengfei Zhang, Weidong Chen, Longhui Zhang, Shi He, Hongxing Wang, Shufang Yan, Wen Ma, Chunxia Guo, and Yanfeng Wang. Evolution of high-quality homoepitaxial cvd diamond films induced by methane concentration. *Coatings*, 11(8):888, 2021. doi: 10.3390/coatings11080888. URL <https://www.mdpi.com/2079-6412/11/8/888>.
- [270] RS Mason, PD Miller, and IP Mortimer. Anomalous loss of ionization in argon-hydrogen plasma studied by fast flow glow discharge mass spectrometry. *Physical Review E*, 55(6): 7462, 1997.
- [271] Panagiotis Grammatikopoulos, Theodoros Bouloumis, and Stephan Steinhauer. Gas-phase synthesis of nanoparticles: current application challenges and instrumentation development responses. *Physical Chemistry Chemical Physics*, 25(2):897–912, 2023.
- [272] Evangelos Skotadis, Evangelos Aslanidis, Maria Kainourgiaki, and Dimitris Tsoukalas. Nanoparticles synthesised in the gas-phase and their applications in sensors: A review. *Applied Nano*, 1(1):70–86, 2020.
- [273] Michael E Coltrin, Robert J Kee, and Greg H Evans. A mathematical model of the fluid mechanics and gas-phase chemistry in a rotating disk chemical vapor deposition reactor. *Journal of the Electrochemical Society*, 136(3):819, 1989.
- [274] K Hassouni, X Duten, A Rousseau, and A Gicquel. Investigation of chemical kinetics and energy transfer in a pulsed microwave h₂/ch₄ plasma. *Plasma Sources Science and Technology*, 10(1):61, 2001.
- [275] Guillaume Lombardi. *Diagnostics spectroscopiques d'espèces carbonées et modélisation physico-chimique de plasmas micro-ondes dans les mélanges H₂/CH₄ et Ar/H₂/CH₄ utilisés pour le dépôt de diamant*. PhD thesis, Université Paris Sud-Paris XI, 2003.
- [276] Kh Hassouni, O Leroy, S Farhat, and A Gicquel. Modeling of h₂ and h₂/ch₄ moderate-pressure microwave plasma used for diamond deposition. *Plasma chemistry and plasma processing*, 18:325–362, 1998.

List of Reactions

Reaction (R2.1)	32
Reaction (R2.2)	32
Reaction (R2.3)	32
Reaction (R2.4)	32
Reaction (R2.5)	32
Reaction (R2.6)	32
Reaction (R2.7)	32
Reaction (R2.8)	32
Reaction (R2.9)	32
Reaction (R2.10)	32
Reaction (R2.11)	32
Reaction (R2.12)	34
Reaction (R2.13)	34
Reaction (R2.14)	34
Reaction (R2.15)	34
Reaction (R2.16)	34
Reaction (R2.17)	34
Reaction (R2.18)	34
Reaction (R3.1)	41
Reaction (R4.1)	74
Reaction (R4.2)	74
Reaction (R4.3)	74
Reaction (R4.4)	74
Reaction (R4.5)	74
Reaction (R4.6)	74
Reaction (R4.7)	74
Reaction (R4.8)	76
Reaction (R4.9)	76
Reaction (R4.10)	76
Reaction (R4.11)	76